

**Study of collagen organization in cell-laden hydrogels and animal tissue
samples for effective tissue engineering scaffolds**

by

Anuraag Boddupalli

A dissertation submitted to the graduate faculty

in partial fulfillment of the requirements for the degree of

DOCTOR OF PHILOSOPHY

Major: Chemical Engineering

Program of Study Committee:
Kaitlin Bratlie, Major Professor
Andrew Hillier
Surya Mallapragada
Ian Schneider
Shan Jiang

The student author, whose presentation of the scholarship herein was approved by the program of study committee, is solely responsible for the content of this dissertation. The Graduate College will ensure this dissertation is globally accessible and will not permit alterations after a degree is conferred.

Iowa State University

Ames, Iowa

2018

Copyright © Anuraag Boddupalli, 2018. All rights reserved.

TABLE OF CONTENTS

| | Page |
|---|------|
| ACKNOWLEDGMENTS | vi |
| ABSTRACT | vii |
| CHAPTER 1. GENERAL INTRODUCTION | 1 |
| CHAPTER 2. METHODS FOR IMPLANT ACCEPTANCE AND WOUND HEALING: MATERIAL SELECTION AND IMPLANT LOCATION MODULATE MACROPHAGE AND FIBROBLAST PHENOTYPES | 4 |
| 2.1. Introduction | 4 |
| 2.2. Influence of Material Selection on the Host Response..... | 8 |
| 2.2.1. Natural Materials | 8 |
| 2.2.1.1. Alginate | 9 |
| 2.2.1.2. Chitosan..... | 10 |
| 2.2.1.3. Hyaluronic Acid | 14 |
| 2.2.2. Synthetic Materials..... | 15 |
| 2.2.2.1. Biodegradable Synthetic Materials | 16 |
| 2.2.2.2. Non-Biodegradable Synthetic Materials | 18 |
| 2.2.2.3. Hybrid Materials..... | 20 |
| 2.2.3. Summary of Material Selection | 21 |
| 2.3. Effect of Surface Topology and Functionalization on the FBR and Biocompatibility | 22 |
| 2.3.1. Effect of decellularized scaffolds | 22 |
| 2.3.2. Surface shapes and coatings | 24 |
| 2.3.3. Effect of pore size..... | 26 |
| 2.3.3. Study of mechanotransduction and cell signaling pathways | 29 |
| 2.4. Location and biocompatibility response | 30 |
| 2.4.1. Lungs..... | 31 |
| 2.3.2. Bones..... | 33 |
| 2.3.3. Heart..... | 35 |
| 2.3.4. Liver | 37 |
| 2.3.5. Skin | 38 |
| 2.3.6. Design principles for disparate implant locations..... | 41 |
| 2.5. Summary Table..... | 42 |
| 2.6. Conclusions | 43 |
| 2.7. References | 45 |
| CHAPTER 3. SECOND HARMONIC GENERATION IMAGING | 56 |
| 3.1. Introduction | 56 |
| 3.2. State of the art..... | 59 |
| 3.3. Analysis Techniques..... | 63 |

| | |
|---|----|
| 3.3.1. Susceptibility Measurements..... | 63 |
| 3.3.2. Polarization Resolved SHG imaging..... | 66 |
| 3.3.3. Fast Fourier Transform Analysis..... | 67 |
| 3.3.4. F/B Ratio Measurements..... | 68 |
| 3.3.5. Grey Local Correlation Matrix..... | 69 |
| 3.3.6. Second Harmonic to Autofluorescence Aging Index of Dermis..... | 71 |
| 3.3.7. Depth Dependent Decay Measurements..... | 73 |
| 3.4. Different Cancer Staging Methods..... | 74 |
| 3.4.1. Metavir Scoring system..... | 74 |
| 3.4.2. TNM system..... | 74 |
| 3.4.3. Tumor Associated Collagen Signatures..... | 75 |
| 3.5. Future Perspectives and Conclusions..... | 77 |
| 3.6. References..... | 78 |

CHAPTER 4. COLLAGEN ORGANIZATION OF FIBROBLASTS ENCAPSULATED IN PH RESPONSIVE METHACRYLATED ALGINATE

| | |
|---|-----------|
| HYDROGELS..... | 84 |
| 4.1. Introduction..... | 85 |
| 4.2. Experimental..... | 87 |
| 4.2.1. Materials..... | 87 |
| 4.2.2. Methacrylated Alginate (ALGMA) Synthesis..... | 87 |
| 4.2.3. Hydrogel Fabrication and Characterization..... | 89 |
| 4.2.4. In vitro Degradation..... | 89 |
| 4.2.5. Cell Culture and Viability Assay..... | 90 |
| 4.2.6. SHG Microscopy Imaging of the gels..... | 90 |
| 4.2.7. Statistical analysis..... | 92 |
| 4.3. Results..... | 92 |
| 4.3.1. Characterization of ALGMA hydrogels..... | 92 |
| 4.3.2. Compressive Moduli..... | 93 |
| 4.3.4. Swelling Response..... | 94 |
| 4.3.4. Degradation Kinetics..... | 94 |
| 4.3.5. Cytocompatibility of ALGMA hydrogels..... | 95 |
| 4.3.6. SHG Microscopy..... | 96 |
| 4.3.7. PCA..... | 100 |
| 4.4. Discussion..... | 103 |
| 4.5. Conclusions..... | 108 |
| 4.6. References..... | 108 |

CHAPTER 5. POLY-L-ARGININE MODIFICATIONS ALTER THE ORGANIZATION AND SECRETION OF COLLAGEN IN SKH1-E MICE.....

| | |
|---------------------------------|-----|
| 5.1. Introduction..... | 114 |
| 5.2. Materials and Methods..... | 117 |
| 5.2.1. Materials..... | 117 |
| 5.2.2. PLR Modification..... | 118 |
| 5.2.3. Ethics Statement..... | 118 |

| | |
|--|-----|
| 5.2.4. Animals | 118 |
| 5.2.5. Subcutaneous Injections | 119 |
| 5.2.6. Collagen Gel Preparation | 119 |
| 5.2.7. Second Harmonic Generation (SHG)..... | 120 |
| 5.2.8. Image Processing..... | 120 |
| 5.2.9. Statistics and Data Analysis | 122 |
| 5.3. Results | 122 |
| 5.3.1. Collagen Signal | 122 |
| 5.3.2. Collagen Organization..... | 124 |
| 5.3.3. Collagen III Secretion | 128 |
| 5.3.4. Statistical Analysis | 130 |
| 5.4. Discussion..... | 134 |
| 5.4.1. Collagen Signal Comparisons | 134 |
| 5.4.2. Collagen Organization Response | 135 |
| 5.4.3. Collagen III Response | 136 |
| 5.4.4. PCA | 138 |
| 5.5. Conclusions | 141 |
| 5.6. References | 141 |

| | |
|---|------------|
| CHAPTER 6. SECOND HARMONIC GENERATION IMAGING OF COLLAGEN FIBER ORIENTATION AS A MARKER FOR SCARRING | 146 |
| 6.1. Introduction | 146 |
| 6.2. Materials and Methods | 148 |
| 6.2.1. Materials..... | 148 |
| 6.2.2. Second Harmonic Generation (SHG)..... | 149 |
| 6.2.3. Image Processing..... | 149 |
| 6.2.4. Statistics and Data Analysis | 150 |
| 6.3. Results | 151 |
| 6.3.1. Fibrin Scaffold Treatment | 151 |
| 6.3.2. Partial Thickness Scaffold Treatments applied for 4 days | 152 |
| 6.3.3. Full Thickness Scaffold Treatments compared over 14 and 21 days..... | 154 |
| 6.3.4. Full Thickness scaffold Treatments compared over 14 and 21 days— Set II | 155 |
| 6.3.5. Full Thickness Scaffold Treatments compared over 21 and 42 days..... | 157 |
| 6.4. Discussion..... | 159 |
| 6.4.1. Fibrin Scaffold Treatment | 160 |
| 6.4.2. Partial Thickness Scaffold Treatments applied for 4 days | 160 |
| 6.4.3. Full Thickness Scaffold Treatments compared over 14 and 21 days..... | 161 |
| 6.4.4. Full Thickness Scaffold Treatments compared over 14 and 21 days— Set II | 162 |
| 6.4.5. Full Thickness Scaffold Treatments compared over 21 and 42 days..... | 162 |
| 6.5. Conclusions | 163 |
| 6.6. References | 164 |

| | |
|--|------------|
| CHAPTER 7. SECOND HARMONIC GENERATION MICROSCOPY OF COLLAGEN ORGANIZATION IN TUNABLE, ENVIRONMENTALLY RESPONSIVE ALGINATE HYDROGELS | 167 |
| 7.1. Introduction | 168 |
| 7.2. Experimental..... | 171 |
| 7.2.1. Materials..... | 171 |
| 7.2.2. Methacrylated Alginate (ALGMA) Synthesis | 171 |
| 7.2.3. Hydrogel Fabrication and Characterization | 172 |
| 7.2.4. In Vitro Degradation | 173 |
| 7.2.5. Cell Culture and Viability Assay..... | 173 |
| 7.2.6. Second Harmonic Generation Microscopy of the gels..... | 174 |
| 7.2.7. Statistical analysis | 176 |
| 7.3. Results | 176 |
| 7.3.1. Characterization of ALGMA Hydrogels..... | 176 |
| 7.3.2. Compressive Moduli | 177 |
| 7.3.3. Swelling Response | 178 |
| 7.3.4. Degradation Kinetics..... | 179 |
| 7.3.5. Cytocompatibility of ALGMA hydrogels | 180 |
| 7.3.6. SHG Microscopy..... | 182 |
| 7.4. Discussion..... | 185 |
| 7.5. Conclusions | 192 |
| 7.6. References | 192 |
| | |
| CHAPTER 8. PHOTOMASK-TUNED AND FIBRONECTIN-MODIFIED ALGINATE HYDROGELS FOR STUDYING FIBROBLAST MORPHOLOGY AND COLLAGEN ORGANIZATION | 200 |
| 8.1. Introduction | 201 |
| 8.2. Experimental..... | 203 |
| 8.2.1. Materials..... | 203 |
| 8.2.2. Methacrylated Alginate (ALGMA) Synthesis | 203 |
| 8.2.3. Hydrogel Fabrication and Characterization | 204 |
| 8.2.5. Cell Culture and Proliferation Assay..... | 205 |
| 8.2.6. Second Harmonic Generation Microscopy of the gels..... | 206 |
| 8.2.7. Immunocytochemical Staining..... | 207 |
| 8.2.8. Statistical Analysis | 208 |
| 8.3. Results | 208 |
| 8.3.1. Compressive Moduli | 208 |
| 8.3.2. Cell Viability | 209 |
| 8.3.3. Immunocytochemistry..... | 210 |
| 8.3.4. Secreted Collagen Levels | 211 |
| 8.3.5. Collagen Organization..... | 212 |
| 8.4. Discussion..... | 215 |
| 8.5. Conclusions | 222 |
| 8.6. References | 222 |
| | |
| CHAPTER 9. GENERAL CONCLUSION | 230 |

ACKNOWLEDGMENTS

I would like to thank my major professor, Dr. Kaitlin Bratlie for her patience and guidance throughout the course of my graduate studies here at Iowa State University. I would also like thank Dr. Andrew Hillier, Dr. Surya Mallapragada, Dr. Ian Schneider and Dr. Shan Jiang for their vital inputs, and for serving on my advisory committee. I am grateful for the support of my friends and group members, Hannah Bygd, Lida Zhu, Zhuqing Li, and Zihao Xu for their support in working long hours at the labs. I am also grateful for the support of Jake Nuhn, Juan Wang and Eric Hare for their valuable advice and productive collaboration.

Finally, I would like to thank my family for their unconditional and unconventional love and support. For my parents, Prasanna and Radha, who have always encouraged me to pursue my academic ambitions and instilled in me the love for science and reading. For my brother, Aravind who has been a reliable sounding board for ideas and advice. And last but not the least, my wife, Nadia for her immense support, patience and encouragement to never give up on my dreams, no matter how tough they seemed.

This work was supported by the National Science Foundation under Grant No. CBET 1227867, the Roy J. Carver Charitable Trust Grant No. 13-4265, and the Mike and Denise Mack faculty fellowship to Dr. Kaitlin Bratlie.

ABSTRACT

The interaction of biomaterials with biological systems is a complex process, that is triggered in response to implants and wounds. It is essential to understand the phases of wound healing response, particularly the interactions of immune cells such as macrophages and fibroblasts, with the local extracellular matrix which can influence implant acceptance or the restoration of the damaged wound site. Materials properties such as compressive modulus, surface geometry, functionalization, and topology can be tuned to modulate the inflammatory and fibrotic responses to wounds and implants.

Naturally derived materials, such as alginate, are widely used biomaterials owing to their biocompatibility and the diverse crosslinking strategies that can be used for fabrication. Soft alginate gels can be synthesized after methacrylation to be relatively stable under physiological conditions, while retaining pH sensitivity, which can be useful in the treatment of chronic wounds. Studying the collagen response to NIH/3T3 fibroblasts encapsulated in these soft hydrogels can develop wound healing strategies to promote faster wound healing. The transition of collagen organization from aligned to isotropic states in the dually crosslinked stiffer methacrylated alginate (ALGMA) hydrogels shows promise towards the development of topical gels for wound care.

Modifying the surface properties using arginine-like derivatives is effective in modulating the fibroblast response to implanted glass beads in SKH1-E mice. Collagen response to modified glass beads using SHG microscopy was evaluated using several factors such as collagen amount, secretion of collagen III, and organization of collagen. The albizziin modification showed both isotropic collagen organization as well similar collagen type III as unwounded skin. Furthermore, statistical analysis uncovered

correlations between SHG derived parameters and the materials properties of the chemical modifiers. Collagen type III was correlated with the surface tension of the modifier, and an empirical equation was derived relating materials parameters with the observed collagen measurements.

The effectiveness of diverse wound care strategies on shallow and deep wounds on porcine subjects was conducted using SHG microscopy. Treatment duration, as well as scaffold preparation were instrumental in reducing a scarring response and accelerating wound closure rates. By combining the understanding of wound healing in diverse tissue environments, with environmentally responsive wound dressings, it is possible to improve the quality of life for millions of patients across the world.

CHAPTER 1

GENERAL INTRODUCTION

There is an urgent need to understand the challenges of designing biocompatible materials. All materials used in tissue engineering trigger some level of biological responses upon implantation. Common challenges associated with the host response are failures due to chronic inflammatory responses as well as the formation of the avascular, fibrotic sheath around the implant. The avascular, chronic inflammatory host response can thus contribute to incomplete healing of percutaneous wounds for dermal implants and higher rates of infection from opportunistic pathogens.^{1,2} In the United States alone, over 25% of the GDP will be expended on research and development of novel biomaterials by 2040.³ Our main motivation for these research projects was to conceptualize a rational design for tissue engineering scaffolds that could incorporate influences of material properties, biochemical responses and biological activity.

The Advanced Healthcare Materials paper submitted in this thesis as Chapter 2 addresses the challenges associated with understanding the key role played by material characteristics that can influence implant compliance within natural tissue environments. By considering diverse types of material scaffolds as well as cellular responses from macrophages and fibroblasts, detailed insight was obtained on the need to elucidate cell-matrix interactions from a biomedical engineering perspective.

Second Harmonic Generation microscopy has enabled sensitive label-free detection and analysis of collagen response from cells proliferating in diverse biological environments. Chapters 3 focuses on the current state of the art techniques that have been studied using similar high content imaging platforms for analyzing biomedical scaffolds and their applications. With the combined insight from multimodal imaging techniques and the need for rational design of scaffolds, research

was conducted on soft, tunable hydrogel materials that can be fabricated for diverse applications. As implant failures are commonly observed as a result of inflammatory responses or unfavorable fibrotic encapsulation. The host responses to implanted materials are similar to those following injury.^{4,5} Cells recruited to the wound play a key role in the series of inflammatory response based process. The normal wound-process is restored after the foreign objects such as pathogens, unrecognized proteins etc. are either dissolved, degraded or phagocytosed.⁵ Fibrous encapsulation of implants isolates the implant from the host tissue. Over the Chapters 4 and 5, we focus on the effect of modifying the surface topology of implants through diverse strategies as well as identify key parameters that can guide rational design of biomaterials.

The collaborative research carried out in conjunction with the Corporate Research Materials Lab at 3M, facilitated a detailed study into the effect of different scaffolds to avoid scarring responses in porcine subjects. By carefully analyzing the samples for collagen-related biomarkers, it was possible for this blind study to provide unbiased insight into wound healing. We have included some of the most interesting results from this collaboration as Chapter 6. The perspective obtained from this collaboration was critical us to understand the challenges for designing scaffolds for lungs, heart, liver, skin, and bone systems. For successfully tuning the *in vivo* fibrotic response and the non-specific adsorption of proteins that can foul the implant surface and trigger undesirable responses, it was essential to work with stiffer alginate hydrogels to have the NIH/3T3 fibroblasts interact with physiologically relevant stiffnesses. Stiffer substrates, such as musculoskeletal regions, often trigger inflammatory responses while those for softer tissues, like liver and lungs, incite an anti-inflammatory response from the native macrophages and fibroblasts.^{6,7} By evaluating the tunability of collagen organization to the different crosslinking

strategies for methacrylated alginate hydrogels, it was possible for us initiate decoupling of cell-matrix interaction cues in Chapter 7.

The combination of most of the research on tunable, soft hydrogels for tissue engineering applications is explained in greater detail in Chapter 8 through the study of photomask-tuned alginate hydrogels that can mimic natural tissue environments. Through decoupling the influence of crosslinking mechanism on the collagen and overall cell-matrix interaction, it was possible to selectively observe the influence of mechanical stiffness on how cells secrete and organize collagen. This study thus becomes a fitting culmination of our analysis techniques for visualizing how cells sense the local microenvironment which can inform design of effective tissue engineering scaffolds.

References

1. Bryers, J. D., Giachelli, C. M. & Ratner, B. D. Engineering biomaterials to integrate and heal: The biocompatibility paradigm shifts. *Biotechnology and Bioengineering* **109**, 1898–1911 (2012).
2. Ratner, B. D. A paradigm shift: biomaterials that heal. *Polym. Int.* **56**, 1183–1185 (2007).
3. Place, E. S., Evans, N. D. & Stevens, M. M. Complexity in biomaterials for tissue engineering. *Nat. Mater.* **8**, 457–470 (2009).
4. Mutsaers, S. E., Bishop, J. E., McGrouther, G. & Laurent, G. J. Mechanisms of tissue repair: From wound healing to fibrosis. *Int. J. Biochem. Cell Biol.* **29**, 5–17 (1997).
5. Avula, M. N., Rao, A. N., McGill, L. D., Grainger, D. W. & Solzbacher, F. Foreign body response to subcutaneous biomaterial implants in a mast cell-deficient Kitw-Sh murine model. *Acta Biomater.* **10**, 1856–1863 (2014).
6. Quinlan, A. M. T. & Billiar, K. L. Investigating the role of substrate stiffness in the persistence of valvular interstitial cell activation. *J. Biomed. Mater. Res. - Part A* **100 A**, 2474–2482 (2012).
7. Ali, M. Y., Chuang, C.-Y. & Saif, M. T. a. Reprogramming cellular phenotype by soft collagen gels. *Soft Matter* **10**, 8829–37 (2014).

CHAPTER 2

METHODS FOR IMPLANT ACCEPTANCE AND WOUND HEALING: MATERIAL SELECTION AND IMPLANT LOCATION MODULATE MACROPHAGE AND FIBROBLAST PHENOTYPES

Modified from a manuscript published in *Advanced Healthcare Materials*, 5(20) 2575-2594 (2016)

This review is focused on materials and methods used to induce phenotypic changes in macrophages and fibroblasts. Herein, we give a brief overview on how changes in the phenotypes of macrophages and fibroblasts are critical biomarkers for identification of implant acceptance, wound healing effectiveness and also essential for evaluating the regeneration capabilities of some hybrid strategies. The different types of cells present during FBR have been extensively studied for evaluating the response to different materials, and there are varied material approaches towards fabrication of biocompatible, and non-cytotoxic substrates. We discuss how natural and synthetic materials have been used to engineer desirable outcomes in lung, heart, liver, skin, and musculoskeletal implants, and it has been observed that certain properties such as rigidity, surface shapes and porosity play a key role in the progression of the immune response. Several fabrication strategies are discussed to control the phenotype of infiltrating macrophages and fibroblasts: decellularization of scaffolds, surface coatings, implant shape, and pore size apart from biochemical signaling pathways that can inhibit or accelerate unfavorable immune response. It is essential hence to factor all the different design principles, material fabrication criteria for evaluating the choice of implant materials or regenerative therapeutic strategies.

2.1. Introduction

The field of biomaterials is an evolving interface between different synergistic topics of science and engineering. The growth of the field of tissue engineering has a huge impact on the cost of healthcare all over the world, to the effect that by 2040 over 25% of the total US GDP shall be

invested in biomaterials research and development¹. There is hence clearly a growing need for technologies that can provide treatment, while promoting regeneration of healthy parenchymal and stromal tissue². This niche is met by applying transdisciplinary principles from fields such as biological engineering, biochemistry, materials science, and chemical engineering to fabricate implants or scaffolds. However, the innate and complex intricacies in biological responses to material properties are challenging to predict *a priori*, meaning that implant failure often occurs as a result of inflammation³ and fibrous encapsulation⁴. Abating or eliminating such host responses is of central importance in current bio-implant design. There are several key characteristics involved in the host response to biomaterials, two of which are activation of macrophages and fibroblasts.⁵ These cells are essential to tissue regeneration, with the former mediating inflammation and the latter can instigate fibrous encapsulation.

Macrophages are thought to exist on a spectrum of phenotypes bookended by classical activated M1 macrophages and alternatively activated M2 macrophage. Another description of macrophage activation uses an analogy of a color wheel, in which classically activated, wound-healing, and regulatory macrophages occupy the 'primary colors' that blend into 'shades' of macrophage activation. M1 macrophages can be activated by lipopolysaccharides (LPS) or interferon- γ (IFN- γ) and produce cytokines and chemokines such as tumor necrosis factors- α (TNF- α), interleukin-1 (IL-1), interleukin-6 (IL-6), and nitric oxide; while M2 macrophages can be induced by IL-4 and release cytokines including tumor growth factor- β (TGF- β) and IL-10⁶⁻⁹. M1 macrophages are also known as inflammatory macrophages, which aid in 'sterilizing' the wound environment after injury, such as implantation of a biomaterial; in contrast, M2 macrophages are often termed anti-inflammatory and relieve inflammation and aid in tissue formation. These two contrary functions allow macrophages to play critical roles in host responses⁹.

Despite in depth studies examining macrophage function in the implant milieu, their response and activation pathways are not completely understood. Macrophages function differently depending on their location¹⁰ and can be further polarized into several sub-phenotype base on their microenvironment⁶.

The substrate and chemically sensitive differentiation of fibroblasts into myofibroblasts has been confirmed to have dramatic influence on the reorganization of the extracellular matrix (ECM)¹¹. Myofibroblasts have been studied for their role in tumor stroma remodeling and their influence on modifications of the ECM. Their presence is mediated by two main factors: *de novo* stress due to contractile actin bundles being activated and through mechanical stress¹². Both these factors are also inherently linked to macrophage polarization towards acute or chronic responses. The contractile actin bundles mediated change in ECM activity has been observed to be responsible for the secretion of TGF- β or its latent form, which also results in classical activation of M1 macrophage response¹³. Similarly, the mechanical stress has been known to play a role in the activation of the matrix metalloproteinases (MMPs), which are themselves responsible for activating TGF- β , from its latent form. Both fibroblasts and myofibroblasts secrete collagen and exert mechanical influence to alter ECM organization as a function of the material properties of implants or wounds.

It is known that shortly after implantation, protein adsorption at the implant surface will take place in seconds, followed by neutrophils adhesion which last 1 or 2 days¹⁴. Generally, monocytes will be recruited to the site of injury and will differentiate into macrophage within one week after implantation. If the material is not able to be phagocytosed, macrophage presence will persist, and eventually culminates in macrophage fusion into multinucleate giant cells followed by fibrous encapsulation of the foreign body¹⁵. Initially, host responses to different implants were classified

primarily on the basis of the fibrotic capsule that was formed. Further studies have displayed a diversity of cytokines and growth factors that intricately influence the acceptance of the implant, and its long-term stability *in vivo*.

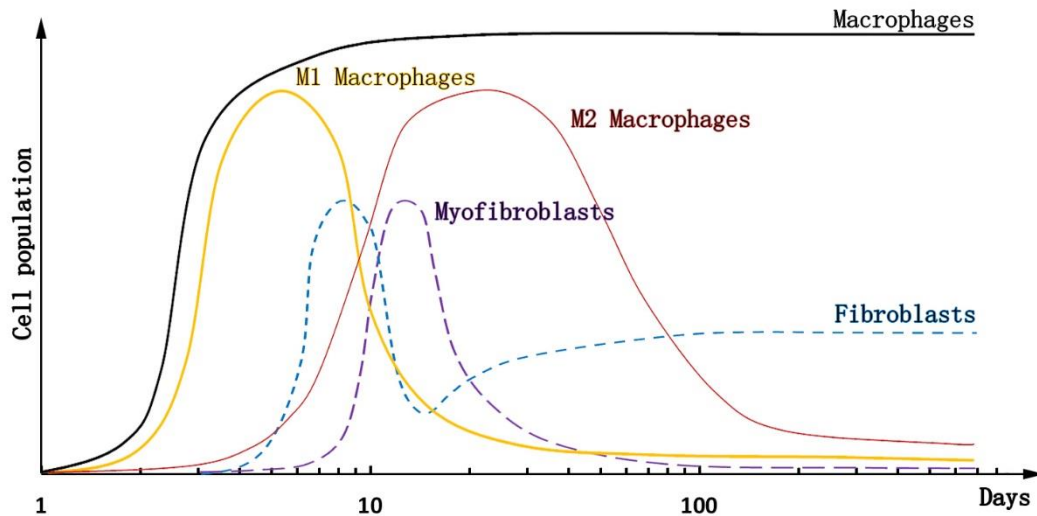


Figure 2.1. Time line of macrophage and fibroblast & myofibroblast population at the implant site.

Different growth factors and cytokines at the implant site are able to initiate complex pathways that differentiate monocytes into the various macrophage phenotypes. Based on the initial acceptance of the implants, these interactions can lead to the presence of fibroblasts, which are primarily responsible for the initiation of angiogenesis and the formation of ECM in the vicinity. Together, the changes in the phenotypes of the fibroblasts and macrophages responding to the wound or implant greatly influence the severity of the response.

Inflammation and formation of the fibrotic capsule^{16,17} were two of the first markers of the host response observed. Eventually it became essential to define the fibrotic response as beneficial or inflammatory. Depending on the location of the implants, surface properties, materials types,

and time-scales over which the studies were conducted, the extent of the host response was found to vary greatly.

Herein, we describe the macrophages and fibroblast response to bio implants with various materials, structures, and implant locations as a result of FBR. The purpose of this review is to organize current effort in modulating macrophage and fibroblast response to reduce FBR caused by bio implant and analysis how material selection and implant geometry structure can reduce FBR. This review provided the design principle of biocompatible implant with different implant locations.

2.2. Influence of Material Selection on the Host Response

Material selection is one of the primary factors for consideration in designing biomedical implants. Here, we have classified biomaterials into three main types: natural, synthetic, and hybrid materials. Natural materials derive from living sources and are generally bio-friendly. Synthetic materials have potentially infinite diversity and are generally more amenable to sterilization and fabrication processes¹⁶. Hybrid materials aim to combine the advantages of both natural materials and synthetic materials through physical and/or chemical linkages of the two types of materials. This section will discuss...

2.2.1 Natural Materials

Natural materials can be either bioactive or bioinert. Dermatan sulfate injection could significantly reduce myofibroblast and macrophage concentration and collagen content in inflammation environment¹⁷. Conversely, silk is relatively inert to cell: silicone implant coated with spider silk protein was able to reduce cytokine release and inhibit monocytes differentiation into macrophages¹⁸. In other cases, less cell population was found on silk fibroin and human tropoelastin hybrid protein coated scaffolds¹⁹.

However, natural materials often have several functions with micro-environment dependence²⁰. Improper usage of natural materials can also lead to enhanced FBR. Material such as chondroitin sulfate proteoglycans were known to cause inflammation and delay healing process after spinal cord injury. On the contrast, chondroitinase ABC injection could cause large-scale digestion and restore healing process^{21,22}.

Because of the variability and uncertainty during natural synthesis, the same categories of natural material can also differ in size and functional groups. Correct understanding and appropriate application of natural materials are essential for reducing FBR. The following sections will analysis different cell response principles for alginate, chitosan, and hyaluronic acid.

2.2.1.1. Alginate

Alginate is a polysaccharide derived from algae. Alginate has been widely used for drug encapsulation or tissue engineering owing to its low toxicity, good biocompatibility, and gelation under mild conditions with divalent cations. In addition, the structure of alginate is similar to the ECM of living tissues and it provides a moist, inert microenvironment for encapsulated cells.

Alginate is generally considered to elicit an anti-inflammatory response and high molecular weight alginate (500 kDa) has been shown to reduce pro-inflammatory cytokines IL-1 β and IL-6²³. However, a recent study showed that cell responses can be modified through changing the ratio of guluronic acid (G block) to mannuronic acid (M block). Previous research has shown that alginate containing 94% M block leads to higher TNF- α secretion than LPS stimulation in RAW264.7 macrophages while polymannuronate (100% M block) of a similar molecular weight produces significantly less TNF- α ²⁴. Further research demonstrated that this effect was more pronounced when comparing alginate degradation products from the G block and M block^{25,26}. Alginate oligosaccharides, particularly unsaturated guluronate oligosaccharide prepared by

enzymatic degradation (GOS-ED), induce strong inflammatory responses, measured by nitrite production, in RAW264.7 cells with a concentration and molecular weight dependence²⁶. However, alginate oligosaccharides degraded either by acid hydrolysis or oxidation showed no significant effect on naïve RAW264.7 cells, and oxidative degraded G block (GOS-OD) can even reduce inflammatory response in LPS induced RAW264.7 macrophages in a concentration dependent manner²⁵. Pathway study found that GOS-OD can efficiently inhibit LPS binding to cell surface and reduce cell activation²⁵.

The material properties of alginate are highly affected by the G/M ratio. One obvious difference that arises from altering the G/M ratio is the mechanical properties of the resulting gel. The G block forms an ‘egg box’ structure in the presence of di- and tri-valent cations, resulting in improved crosslinking and higher stiffness compared to M block rich alginate hydrogels²⁷. There are a limited number of studies interrogating the relationship between the FBR and the G/M ratio of alginate. Many of the studies that have been performed have inconsistent results²⁸⁻³¹. One of the previous studies claimed alginate with MG blocks or M block only, but not G block only, could stimulate human monocytes derived macrophage to produce inflammation cytokines such as TNF- α , IL-1, and IL-6. The alginate with lower G/M ratio resulted in higher cytokines release.³⁰ However, other recent study showed alginate with 60% M block can induce higher amount of TNF- α than 75% M block alginate, and alginate with M block only didn’t show significant difference in TNF- α production compare with control group.²⁴ There is a clear need to better understand the how the G/M ratio influences host responses.

2.2.1.2. Chitosan

Another natural material whose material properties and host responses are impacted by the ratio of its monomers and molecular weight is chitosan. Chitosan is partially deacetylated chitin

(poly-N-acetylglucosamine), which is the main component of crustacean shells. Chitosan can be biodegradable with a degree of deacetylation (DD) ranging from 15% to 85%³². It is also insoluble in human body fluid at high molecular weights (MW>20kDa)³³. Cellular responses to chitosan change with differing DD³²⁻³⁵.

The effect of DD is known to provoke a stronger antimicrobial response in chitosan with a higher DD^{36,37}. Further studies have shown that high molecular weight chitosan scaffolds (MW=890-830 kDa) with 95% DD significantly reduce cellular adhesion and had a lower M1/M2 ratio, measured by surface receptors CD206 for M2 macrophages and CCR7 for M1 macrophages, compared to chitosan scaffolds with 85% DD³⁵. Further reducing the DD of high molecular weight chitosan (76% DD) resulted in high secretion of inflammatory cytokine IL-1 β in bone marrow derived mouse macrophages *in vitro*, while chitin (7% DD) was a less potent stimulator of the M1 response³⁴. Taken together, these responses suggest a non-linear relationship between inflammation response and DD.

Mechanistic studies have also been performed to ascertain the effect of the acylation on the inflammasome, with multiple pathways implicated. IL-1 β release in the presence of 76% DD chitosan inhibited in both peritoneal and bone marrow derived macrophages harvested from NLRP3^{-/-} mice compared to wild type (WT). Pathways including K⁺ efflux, reactive oxygen species generation, and lysosomal destabilization were also involved. All of these pathways are necessary for peak IL-1 β release in response to chitosan³⁴. Pathways were also varied by macrophage initial phenotype: in M0 and M2a macrophage, IL-1ra could be induced by 80% DD chitosan but not 98% DD chitosan without active IL-4/STAT-6 axis, while there was no significant difference in M1 macrophage³². Moreover, 80% DD chitosan at both medium and low molecular weight was reported to cause delayed STAT-1 activation, but 98% DD chitosan cannot.³²

Although the mechanisms of macrophage activation as a result of chitosan acylation have been widely studied, the results are not directly comparable owing to the use of different macrophage cell lines, different molecular weights, and sources of chitosan. Other difficulties in comparing chitosan activation of macrophages stem from limited studies comparing a variety of DD. Some studies have even compared the acylation effect on macrophages using chitosan with molecular weights that differ by orders of magnitude³⁶, which may lead to a less reliable conclusion since molecular weight of chitosan might also impact cellular responses and modulate the FBR. Since the inflammatory response is not linearly related to DD^{34,35}, there is a need for systematic studies over a range of DD for consistent molecular weight. The effect of chitosan on different macrophage polarization is also necessary to provide a better picture on how implanted chitosan would modulate the innate immune response.

Molecular weight of chitosan over the range of 50 to 300 kDa does not have a significant effect on macrophage response.³⁸ Similar to alginate, very low molecular weight chitosan, specifically degradation products termed chitosan oligosaccharide (COS), have been reported to induce a strong inflammatory response^{39,40}. Chitosan enzymatic hydrolyzed with a degree of polymerization of 3-6 was found to greatly enhance inflammatory responses by increasing TNF- α and NO production in RAW 264.7 macrophages. COS induced inflammation is caused mainly by activating toll like receptor-4.³⁹ Interestingly, 20 kDa chitosan has little to no effect on macrophage morphology and CD40 expression while COS with an average molecular weight 750 Da causes M1 activation.⁴⁰ Even though high molecular weight chitosan does not induce a strong inflammatory response, degradation of the implant may result in an undesirable M1 macrophages response at these later time points. Chitosan (80%DD) with molecular weights ranging from 150 to 10,000 Da were implanted into skeletally aged rabbits' knee trochlea. These low molecular

weight materials have a faster degrade rate.⁴¹ High degradation rates can lead to massive release of COS and further cause serious implant inflammation; conversely, low degradation rates may effect tissue regeneration.

Chitosan is generally known to induce a higher inflammatory response than glass slides and tissue culture plastic *in vitro*.⁴²⁻⁴⁴ Higher cell mobility was observed for human primary monocytes derived macrophages cultured on chitosan film compare to tissue culture polystyrene plates.⁴³ Other studies have shown increased M1 markers such as IL-6, TNF- α , and IL-1 β .⁴² Anti-inflammatory cytokines increased significantly after 10 days. Mechanistic studies have shown that macrophages recognize chitosan via CD206.⁴²

Loading chitosan with drug or chemokines can also modulate cellular responses. Chitosan nanoparticles loaded with the non-steroidal anti-inflammatory drug (NSAID) diclofenac reduces IL-6 and prostoglandin E2 (PGE₂) secretion from LPS activated human macrophages while increasing TNF- α release⁴⁵. In contrast, chitosan encapsulating the anticancer agent methylglyoxal leads to high inflammatory mRNA expression including IL-6, IL-1 β , TLR-4, and TNF- α in Sarcoma-180 tumor bearing mice⁴⁶. It has been reported that maleimide-streptavidin modified methacrylamide chitosan hydrogel can loaded with growth factors such as IFN- γ and remain at high concentration in chitosan scaffold with less than 20% release after one month *in vitro*. However, when these materials were implanted into ???, they did not show observable differences compared to chitosan implants without the growth factor⁴⁷.

2.2.1.3. Hyaluronic Acid

Native hyaluronic acid (HA) is a non-sulfated glycosaminoglycan (GAG) with molecular weights up to 10 million Da.⁴⁸ HA can be naturally degraded and re-synthesized *in vivo*.⁴⁹ HA is known to interact with several cell surface markers, such as CD44, and can influence the FBR in a molecular weight dependent manner.⁵⁰

HA has distinct biological functions at different molecular weights. High molecular weight HA often lead to anti-inflammation⁵¹ and low molecular weight HA can cause inflammation⁵². Recently, HA molecular weight effects on macrophage reprogramming and cytokine release have been demonstrated.⁵³ HA molecular weight spanning 10^{-1} to 10^3 kDa were tested in macrophages polarized with LPS/IFN- γ or IL-4 along with naïve cells. Very high (10^3 kDa) and very low molecular weight (10^{-1} kDa) HA has direct influence on macrophage polarization regardless of the initial phenotype⁵³. In different phenotypes, most anti-inflammatory cytokines increase logarithmically with molecular weight; in contrast, most pro-inflammatory decrease logarithmically⁵³. Similar studies were performed on LPS/IFN- γ activated human peripheral blood monocytes obtained from donors. IL-1 β production after incubation with 5 to 1,700 kDa HA showed a decrease with molecular weight without a clearly identifiable trend. Large variety was found between each donor, and was used to explain the lack of a trend⁴⁸.

Although numerous studies on cellular responses to HA have been conducted *in vitro*, there is large uncertainty in the effect of HA molecular weight *in vivo*. One interesting phenomenon found both *in vivo* and *in vitro* showed that LPS activated macrophage could increase HA synthase (HAS) 1 and HAS 2 mRNA expression and decrease hyaluronidases⁵⁴. However, despite the reduction in hyaluronidases, rapid degradation of HA was still observed in macrophages even

though the HA concentration increased in other tissues⁵⁴, which suggested LPS activated macrophage may be able to degrade HA without hyaluronidases. HA synthase is able to synthesize high molecular weight HA⁵⁰, thus upregulation of synthase will lead to high molecular weight HA and reduce the inflammatory response caused by HA. The rapid degradation of HA in macrophages may abrogate this effect since low molecular weight HA is pro-inflammatory. The mechanism behind this response is still unknown.

The main surface marker that recognizes HA is CD44, which is upregulated in inflammatory environments.⁵³ Although IL-4 and LPS/INF- γ activated macrophage have similar levels of CD44 expression, IL-4 induced M2 macrophage can cause CD44 sulfation by post-translational modifications such as increasing chondroitin sulfate, while TNF- α can significantly reduce the sulfation and HA binding to macrophages⁵⁵. Since inhibition of chondroitin sulfate adhesion on CD44 could increase HA binding, chondroitin sulfate also regulates HA binding⁵⁵. Considering these factors, HA with pre-sulfating treatment may also reduce macrophage adhesion and induce an anti-inflammatory response. In fact, collagen films coated with 16% sulfated hyaluronic acid cultured with macrophages *in vitro* lead to increased M2 cytokines such as IL-10 and lower M1 cytokines such as TNF- α and IL-12 compared to 6% sulfated HA followed by native HA^{56,57}.

2.2.2. Synthetic Materials

Compared to natural materials, synthetic materials are generally less biocompatibility. However, due to their high plasticity, synthetic materials can easily be fabricated to have tunable mechanical properties, controlled degradation, and various structures^{60,61}. Unlike natural materials, many synthetic materials are more resistant to increased temperature and can be processed or sterilized easily. Synthetic materials are generally divided into bio-degradable and non-biodegradable categories.

2.2.2.1. Biodegradable Synthetic Materials

Polymers such as poly(lactic acid) (PLA) and poly(lactic-co-glycolic acid) (PLGA) are commonly used biodegradable materials. An ideal biodegradable implant can maintain their function and degrade without releasing cytotoxic substances. One of the major advantages of using biodegradable implant is that a second surgical intervention is not required¹⁶. With controlled degradation kinetics, tissue regeneration rates ideally match the degradation process.

PLA has been used for clinical application and has a low *in vivo* degradation rate ranging from months to years⁶². Because PLA alone often induces relatively high inflammatory response in the early stage of implantation⁶³⁻⁶⁵, PLA copolymer or surface coated PLA have been synthesized to improve host responses. Cardiovascular stent implants composed of high molecular weight PLA blended with phospholipid polymer bearing phosphorylcholine groups was able to reduce thrombus formation and significantly decrease inflammatory cytokines, IL-6, IL-1 β , and TNF- α , released compared with PLA alone when implanted subcutaneously in rats and in arteries of rats or rabbits⁶⁴. Unlike most natural materials, which cannot be processed under harsh reaction conditions, PLA implants can be fabricated through various processes including hot-melt extrusion⁶² due to its thermal and chemical stability.

The degradation behavior of synthetic material implant is mainly determined by polymer structure, molecular weight, morphology, and implant environment. Shape memory material composed of polyhedral oligomeric silsesquioxane (POSS) and PLA star-shaped copolymers exhibited a relationship between delay in degradation and PLA chain length⁶³. Both *in vitro* and *in vivo* degradation studies on POSS-PLA found that there was a lag phase period preceding a rapid degradation phase, in which the lag phase showed less than 10% degradation in 2-6 months with a dependence on PLA chain length while 90% of the mass was lost in 2 months during the

degradation phase regardless of PLA chain length⁶³. Interestingly, longer PLA chain length extended the lag phase but showed no observable effect in changing the degradation rate in the later phase⁶³. This could be a result of the dense PLA chain in outermost layer that delayed body fluid interfusion. Relatively mild inflammatory responses were observed when implanted subcutaneously in rats comparing to PLA alone. Through controlling PLA chain length, POSS-PLA implants could be applied to mid or long-term therapy such as bone bridging.

One disadvantage of biodegradable synthetic materials is that, in many cases, degradation products are not biocompatible and will lead to inflammatory response. A secondary acute inflammation was often observed in the site of implant during the rapid degradation period⁶³. Thus, how to design a bio-implant that can stay functional as long as the therapy requires and then degrade at a controlled rate that will not lead to a strong acute inflammation becomes an issue. One common used method to reduce implant host response is combining implant with anti-inflammatory drug such as dexamethasone^{62,66}. Biodegradable materials can achieve diffusion and degradation mediated control release. Both PLA and PLGA based polymers can perform sustained drug release kinetics and have a reduction in the late stage of implantation^{62,66}.

One effective solution recently developed is, rather than avoiding release of harmful degradation products, combining a secondary material to degradable implant that can neutralize degradation product. Materials with buffer capabilities such as apatitic nanoparticles can significantly reduce the acidic environment in the implant site caused by PLA or PLGA degradation products⁶⁷. Reduced degradation rate and host responses, including macrophage infiltration and fibrous encapsulation have been reported⁶⁷.

Degradation product can also be active pharmaceutical ingredients⁶⁸⁻⁷¹. Calcium phosphate cement (CPC) implants containing PLGA microparticles have been developed recently as bone

implants⁶⁸. The research hypothesized that the acidic degradation product of PLGA could be neutralized by calcium phosphate, which would eliminate the inflammatory response caused by PLGA degradation while further releasing calcium and phosphate ions that favor bone regeneration⁶⁸. Although the degree of neutralization and amount of ion released was not tested, the implantation outcome in femoral condyle of rabbits showed enhanced bone formation without inflammation in CPC with PLGA comparing to CPC alone or CPC with other non-degradable microparticles⁶⁸. CPC has also been coupled to PLGA through end group modified PLGA.⁶⁹ Here, acid terminated PLGA showed a higher degradation and bone formation rate compared to end-capped PLGA⁶⁹. In addition, the degradation rate of CPC-PLGA was only slightly affected by PLGA molecular weight and microparticle size but was highly dependent on PLGA end group and particle morphology^{70,71}. With appropriate end group modification to control degradation rate, this CPC-PLGA implant could be applied to various situations. By combining different materials that can neutralize opponents' degradation products, these studies provided a novel strategy to reduce degradation induced inflammation.

2.2.2.2. Non-Biodegradable Synthetic Materials

Non-biodegradable materials are often used as permanent implants and can avoid cytotoxicity and inflammatory responses caused by degradation products. Titanium is the most commonly used permanent bone implant. Applications include dental implants and total joint arthroplasty implants. Although it has been reported that titanium alloy, compared to zirconium alloy, leads to a higher inflammatory response through increased IL-6 and TNF- α release in osteoblasts and fibroblasts⁷², titanium is still the first choice for bone implant due to its mechanical properties and chemical resistance. Several methods have been developed to reduce the inflammation caused by titanium implant such as modifying surface chemistry^{73,74} or surface

pattern modification⁷⁵. Hydrophilic surface modified titanium can significantly decrease inflammatory cytokines TNF- α , IL-1, and IL-1 β gene expression in THP-1 and RAW264.7 macrophages^{73,74}. Surface modifications with calcium or strontium ions also induces more anti-inflammatory M2 J774.A1 macrophages⁷⁶.

Non-biodegradable polymers are often used for surface modification of biodegradable or natural materials to change their chemical and physical properties. Poly(ethylene glycol) (PEG), a highly hydrophilic polymer widely used in hydrogel and drug implants, is often conjugated to implants or particle surfaces to increase their wettability or water solubility⁷⁷. PEG also has a 'stealth' capability⁷⁸ as it can avoid cell recognition and reduce protein and cell adhesion⁷⁹. Poly(propylene) (PP) is more generally used as a mesh implant. It was reported to activate both inflammatory IL-6 and anti-inflammatory cytokine IL-1RA⁷ and cause chronic inflammation⁸⁰. Such inflammation could be largely decreased by coating with a polyurethane based hydrogel⁸¹. Despite the improved mechanical properties of non-degradable biopolymers, biodegradable materials are often favored since they do not require secondary surgery and favor tissue regeneration. In addition, for permanent implant applications, it is important to note that non-biodegradable implant are susceptible to wear. Implant abrasion is one of the reasons for permanent implant failure, which was often found in joint implants. Wear mediated particles can lead to inflammation⁸², which can further cause perennial overexpression of TNF- α and IL-1 β ⁸³. Coating these materials with one that is lubricating could possibly reduce the abrasion.

2.2.3. Hybrid Materials

On the basis of the above studies, a compelling case can be made for the inclusion of hybrid materials for implants. Since most natural materials do not have the range of mechanical properties that synthetic materials⁸⁶ and many synthetic materials lead to inflammatory responses, there are increasing interests in developing hybrid materials that incorporate the advantages of both natural and synthetic materials to form biocompatible and mechanically tunable implant.

One of the most common hybrid implants are the type where synthetic scaffolds are coated with natural materials to reduce the host response. From its wide range of properties, silk fibroin protein, which is extracted from silkworm or spider-silk, is considered a potential candidate due to its mechanical resilience⁸⁷. Hybrid scaffolds can be created by combining electrospun silk fibers with tunable gelatin hydrogels to synthesize musculoskeletal implants⁸⁷. By dosing these scaffolds with nano-doses of hydroxyapatite, biomineralization was observed which can be further improved to combat bone degradation and resorption due to ailments such as arthritis⁸⁷. Naïve silicone implants with thin spider silk proteins show a minimal inflammatory response, reduced fibrosis, and inhibited differentiation of monocytes to macrophages²⁰. The hybrid surfaces abated the transition of fibroblasts to myofibroblasts⁸⁸. Those positive responses, which were also concurred by experiments conducted by other groups, such as Kundu et al. who used silk fibroin composite hydrogels derived from silkworm, and Mooney et al. who used fibroin extracted from spider silk⁸⁹⁻⁹¹, indicated that silk coated hybrid scaffolds had a better performance for reducing inflammatory responses as compared to purely natural implants. Through the studies conducted on silk proteins and their tunable or biocompatible nature⁹¹ these hybrid substrates can be used as rigorous models for understanding the immune response in different locations within the body.

Other than coating natural materials on synthetic scaffold surfaces for improved biocompatibility, the combination of natural and synthetic material was also developed for the

purpose of morphological modification. As some natural materials are pH sensitive, chitosan at pH lower than 6 is positive charged. This allows negative charged material, poly(γ -glutamic acid), to form self-assembled multi-layer structures with chitosan through electrostatic interactions⁹⁰. Such structures offer chitosan with drug delivery capability, and successfully reprogrammed macrophage response with drug loaded. Chitosan-PGA loaded with diclofenac was reported to decrease PGE2 released from LPS activated human monocytes derived macrophages⁴⁵.

The combination of synthetic and natural materials certainly increases the materials space for biomedical implants, but also results in high lab-to-lab differences. One example is alginate-polylysine (PLL) microcapsules. Alginate-PLL microcapsules have been developed since 1980⁹³. However, alginate-PLL microcapsules with different G/M ratios and molecular weights were fabricated, leading to results that are difficult to compare⁹⁴. Even with similar physiochemical properties, Alginate-PLL microcapsules could lead to various inflammatory responses due to differences in the G/M ratio⁹⁴. This effect was magnified *in vivo* as the zeta potential increases significantly for alginate-PLL particles with 53% G-block but remains unchanged for 43% G-block after 1 day implantation⁹⁴. Silk fibroins coated titanium particles were also reported to function differently dependent on the biological source of silk⁹⁵.

2.2.4. Summary of Material Selection

Both natural and synthetic materials exhibit distinct properties, in which natural materials generally are biocompatible while synthetic materials have higher plasticity and are more easily modified. Current efforts in material selection mostly lies in reducing the inflammatory response caused by the bioimplant. One overarching theme is that most materials can be modified through molecular weight, and both natural and synthetic materials with small molecular weight, particularly degradation products, can lead to inflammation. Moreover, host responses to natural materials are further influenced by factors such as surface modification and monomer ratio.

Currently, most cellular responses mechanisms have not been completely developed. Detailed host responses to different natural, synthetic, and hybrid materials are listed in **Table 2.1**.

2.3. Effect of Surface Topology and Functionalization on the FBR and Biocompatibility

The local geometry of nanoparticles and scaffolds show very interesting effects on the host response. Through subtle changes in the exposed surface area, the shape of the surface available for interaction, and the overall geometry of the material, it has been observed that the host response can be triggered towards biocompatibility or extended fibrosis. For different cell types such as macrophages, changes in the geometry greatly influence their ability to phagocytose and thereby limit their interactions with the material, which in turn influences the signaling pathways for polarization. On the other hand, the geometry and material characteristics as a whole have been shown to influence fibroblast activation and differentiation, based on the local stress observed. This section will focus on three main geometrical considerations for designing biomaterials implants. The first aspect is the effect of decellularized scaffolds, wherein the aim is to observe cell interactions in a noise-free microenvironment. The second is the shape of the implant, including the impact of the radius of curvature on macrophage and fibroblast phenotype. Finally, the impact of pore size will be discussed, including its impact on cell differentiation.

2.3.1. Effect of Decellularized Scaffolds

Macrophage presence and phenotype at the site of implantation is essential for vascularization. In this section, we aim to elucidate the influence of decellularized scaffolds on the FBR. Decellularized scaffolds are ones obtained from different sources such as the trachea, esophagus, lungs, etc. as well as through murine versions of the same. The intense degradation of the ECM allows for removal of most of the triggers for the inflammatory response apart from GAGs, proteoglycans, and smaller blood proteins. GAGs are highly polar polysaccharide

compounds that perform a wide range of functions such as tissue hydration, coagulation, and enzyme activation.⁹ By ensuring that there are no residual cytokines such as TGF- β present in the decellularized scaffolds,¹⁰⁻¹² macrophage responses can be studied in a tunable, noise-free microenvironment.

Another important facet of decellularized scaffolds is their ability to provide viable models to study invasive diseases, which show increased FBR type symptoms. Idiopathic pulmonary fibrosis (IPF) has been studied in depth for over 15 years.^{13,14} By treating healthy decellularized lung scaffolds with bleomycin, it is possible to model how IPF biopsies showed local regions of high rigidity. These regions when cultured with fibroblasts showed increased differentiation to myofibroblasts, and higher presence of CD68+ macrophages. The progression of fibrosis, and subsequent macrophage and fibroblast phenotypic changes, can be readily observed in the *de novo* environment with reduced interference from inherently present cellular receptors and cytokines.¹⁵

Surface coatings of these *de novo* scaffolds can be used for manipulating the host response for increased biocompatibility. Myofibroblast differentiation from fibroblasts are readily observed *in vitro* under these conditions, and further research has been detailed under specific case studies for the work done on improving the biocompatibility of lung implants.^{16,17}

Coating implant surfaces with NSAIDs can reduce the FBR and also the infiltration of macrophages into the drug-releasing implant.¹⁸ Different modes of inoculation, primarily oral or through implants, were compared, which showed that sustained oral doses of salicylic acid led to renal failure, as compared to an improved non-inflammatory response and acceptance of the implant itself. Furthermore, they compared the degraded by-products of scaffold hydrogels such as PLGA over longer periods of time compared to simpler poly-L-lactic acid (PLLA) hydrogels

coated with salicylic acid, which showed that there were no inflammatory response by-products produced by the NSAIDs coated implants.

2.3.2. Surface Shapes and Coatings

Hydrogel based treatments have gained traction over the past several decades as novel systems for drug delivery, regenerative therapeutics, and sustainable *in vitro* models.^{19,20} Their jelly like natural structure provides a moist and relatively inert microenvironment, which is necessary for tissue engineering and 3D cell culture applications. Hydrogels have proven biocompatibility especially when comprised of components such as collagen, hyaluronic acid, or alginate. These hydrogels can be easily functionalized to produce a tunable microenvironments for changing macrophage and fibroblast phenotypes in a controlled fashion.^{21,22} Anseth and co-workers²³ have demonstrated 3D cell culture as a necessary tool for understanding cellular behavior especially for the progression of the host response. Their work indicated that different types of cells had a preference for specific underlying shapes and symmetries which are intrinsically related to mechanotransduction signals.²³

As discussed previously, alginates are a popular material for biomedical implants due to low toxicity, easy tunability, and good biocompatibility in both liquid and hydrogel form. Coated alginates and hydrogels provide a similarly tunable environment. Kolhar *et al.*²⁴ demonstrated that the shape and coatings of different alginate microcapsules directly influences the adhesion and migration of RBE4 rat brain endothelial cells and the efficiency of drug delivery. Surface and shape effects of different biomaterial interactions have been found to vary greatly for different locations.²⁵ As macrophages are phagocytes, modifications in shapes and coatings have been observed to be valid parameters to study this aspect of the host response. Wolf *et al.*²⁶ described in detail the effect that different scaffold geometries have on the host response, and observed how the 2D sheets and powder scaffolds work best for a rapid wound healing response based on their

ease of phagocytosis, whereas multi-sheet or tubular implants show the most compatible response for bone tissue implants.

Based on the observation that most hydrophilic, non-coated synthetic materials, elicited a highly inflammatory response *in vivo*, it became essential to explore combinations of natural and synthetic substrates for FBR studies. Hashizume *et al.*²⁷ focused on polyester urethane urea (PEUU) combined with decellularized ECM scaffolds, the former contribute to the elastomeric properties while the latter contributed to its biocompatibility. The PEUU/ECM hybrid showed cellular infiltration by macrophages and better incorporation into the abdominal wall. However, both the naïve PEUU and the composite material showed myofibroblast differentiation. This study mentioned that longer time periods would be necessary for eventual scaffold degradation and further characterization of macrophage polarization, as compared to generally visualizing CD68+ macrophage infiltration, would be essential to determine the end result initiated by the scaffold.

The FBR is influenced by the topology of the underlying substrates on the innate host response. Many research groups studied this response mechanism, such as Mooney and co-workers,²⁸ who demonstrated the importance of material shape and surface chemistry for an improved adaptive immune system boost strategy using mesoporous, cylindrical silicon rods (MSRs) as a host for immune cells. This technique can be modified by tuning the size of pores and the length of these MSRs. Subcutaneous implants of the MSRs loaded with specific factors such as granulocyte macrophage colony-stimulating factor, were analyzed to see how effectively they resulted in proliferation of bone marrow-derived dendritic cells. The efficacy of this new system was tested against conventional methods and the results showed that MSR based adjuvant therapy was 2.5 times more effective with more scope for improvement based on optimization of the aspect

ratio of scaffolds. Further work is being conducted on controlling the degradation kinetics of the MSRs for clinical studies, which will allow for even better positive host responses.

Device geometry plays an important role in macrophage and fibroblast activation. Different sized and shaped materials have resulted in unabated inflammation, formation of FGBCs, fibrosis, and uncontrolled damage to neighboring tissues.²⁹ All of these events are significant in the FBR to different implants and dictate the phenotypes of macrophage and fibroblast in the surrounding ECM and tissue. The studies showed how 1.5 mm circular particles elicit the most optimal biocompatibility, irrespective of material composition. They also suggested potential strategies for improving the FBR to biomaterials by focusing on porosity-based influences.

2.3.3. Effect of Pore Sizes

Both natural and synthetic materials show varied biocompatibilities depending on their surface properties. One important factor is their pore size, which in the case of natural materials are not as rigidly controlled as it can be in synthetic materials. It is essential to observe the interaction of innate cell responses with these porous materials. This section of the review aims to distil the seminal papers, which demonstrate the variability of the FBR depending on the pore sizes of the underlying substrates and establish trends for macrophage and fibroblast phenotypic changes.

An early proof of concept regarding the macrophage effect on the FBR mediated by porous substrates was conducted by Sussman *et al.*³⁰ Their study showed a clear difference between the FBR towards porous and non-porous materials where the former showed a thinner fibrotic capsule, along with improved vascularization. They suggested a possible hypothesis for this difference could be attributed to a greater fraction of fibrous material in the pores, which affected the acceptance of the implant. In such systems, the acceptance of the implants was judged on the basis of greater vascularization, thinner fibrotic response, and an absence of both the inflammatory type

aspect of the M1 response as well as remodeling associated M2 macrophages. Down regulation of the M2 response could be attributed to cellular adhesion, which was markedly decreased in the case of the porous implant materials, with almost none for the 34 μm pores, and a negligible response for the 160 μm pores, as well. There was an interesting atypical non-inflammatory response observed for the adhered M1 macrophages, which has great potential in terms of sub-classifications of phenotype changes in the host response. Specifically, due to the combination of surface area, pore size, etc., the 34 μm porous implants produced a combined M1 and M2 response which should be further studied.

Decellularized organ models can be used to understand the mechanisms behind IPF, and showed how changes in pore size could provide treatments to alleviate the compromised lung capacity due to fibrosis.³¹ The role played by porous ECM substrates was analyzed where the L-TGF- β activation is improbable after stripping of such proteins during decellularization, thereby placing emphasis on mechanical and adhesion cues in the microenvironment. Organized healthy ECM versus chaotic and disordered ECM in IPF samples was observed, along with increased myofibroblast differentiation showing high α -smooth muscle actin (α -SMA) levels, a protein characteristic of myofibroblasts, as compared to healthy tissues. The similarity of TGF- β levels could also be extrapolated towards assuming that there was lesser M1 macrophage presence. On the basis of the images published, this area of research could benefit from multimodal imaging to simultaneously evaluate biochemical and mechanical factors. Similar studies were also carried by Phipps *et al.*³² where they used large pore sized (on the order of 10 μm) based scaffolds for better biomineralization for bone tissue regeneration.

Pore size effects on the progression of FBR, and vascularization of implants has been evaluated using different models. Studies on how pore size influences cellular responses were

conducted by Leight *et al.*²³ Their experiments showed how pores formed due to 3D clusters made of polydimethylsiloxane (PDMS) on which MCF10A, a mammary epithelial cell line, was found to proliferate variably depending directly on the geometry and cluster sizes of the PDMS stamps. The island sizes (on the order of 100 μm) formed due to these micropatterns related well to research conducted by Liu and coworkers^{33,34} on the effects of surface topological cues, mechanotransduction, and the substrate porosity to the changes in macrophage phenotypes and their activation processes as a part of the FBR. Their results concurred with Booth *et al.*,¹⁷ in which healthy lung models showed significantly lesser myofibroblast presence as compared to their bleomycin treated IPF mimicking models.

Table 2.1. Cell response to different pore size

| Pore Size | Surface Type | Shape of implants | Fibroblast + Macrophage response | Reference |
|--------------------|--|-------------------|--|----------------------|
| ~5 nm | Fibronectin based scaffolds | Circular | myofibroblast differentiation, macrophages based on cell implant location, and on compressive measures | Tse et al (2012) |
| | | Square | | |
| | | Star-shaped | | |
| 1-20 μm | Alginate microcapsules with different coatings | Circular | Increased sizes of capsules showed lesser myofibroblasts+macrophages differentiation | Vegas et al (2016) |
| 34 μm | PMMA beads on PHEMA scaffolds | Circular | Increased myofibroblasts+macrophages | Sussman et al (2013) |
| 160 μm | | | Decreased myofibroblasts+macrophages | |

Table 2.1 Continued

| Pore Size | Surface Type | Shape of implants | Fibroblast + Macrophage response | Reference |
|-----------------------|-------------------------------------|---------------------------------|---|---------------------|
| ~50-100 μm | Cytokine coatings on PLLA/Gelatin | Random | IGF, bFGF coated substrates had higher myofibroblasts+macrophages presence | Lee et al (2014) |
| 0.3-1.5 mm | Alginate, Steel, Glass, polystyrene | Triagonal, circular, pentagonal | Increased sizes, circular capsules showed lesser myofibroblasts+macrophages differentiation | Veiseh et al (2015) |

2.3.4. Study of Mechanotransduction and Cell Signaling Pathways

One of the most important characteristics, that differentiates the microenvironment within the many parts of the human body are ones related to the natural cell populations and the mechanical properties of the substrates within them. In recent years, research has been focused on understanding the role of the local mechanical properties that influence cell phenotypes and their responses. The role of this mechanotransduction response has been observed as the mechanical stress being converted to biochemical signals, and activation of certain cell signaling pathways.^{35,36} Two of these important pathways are Yes-associated protein (YAP) and transcriptional coactivator with PDZ binding motif (TAZ). Regulation of these pathways affects the proliferation of human mesenchymal cells (MSCs) and fibroblasts on substrates of different rigidities ranging from 0.7 to 40 kPa, where this higher rigidity environment was based on the stiffness of the fibronectin modified polyacrylamide hydrogel. Another often overlooked factor is focal adhesion kinase (FAK), which plays a crucial role in the wound healing response. The overexpression of FAK is

what results in the formation of hypertrophic scars or keloids in mammals.³⁷ Similar to the studies conducted on YAP/TAZ, the responses of certain FAK-inhibited mice, and their wound healing response has been evaluated. Interesting results were obtained when valvular interstitial cells (VICs) were used to understand the fibroblast and macrophage activating pathways such as PI3K/AKT pathways, after being cultured or co-cultured on soft or stiff PEG scaffolds.^{21,38} Up regulation of the pathway was obtained as a response to the local rigidities and cytokines coatings. Sadtler *et al.*³⁹ added to this theory through their observations of how biomaterial treated injuries responded differently, based on the treatment of the surface and rigidity of the scaffold in contact with the wound itself. The above factors affected the cell phenotype towards a quiescent or deactivated state for soft substrates, and towards a highly activated state on stiffer substrates. These cell-signaling and mechanotransduction studies thus motivated a detailed review of the host responses observed for different organs within the body, to understand what conditions could be modified in the implant or regeneration therapies to suit the purpose most efficiently.

2.4. Location and Biocompatibility response

Recent studies have shown the important role that macrophage and fibroblast phenotype play in the host response,⁴⁰ by affecting the level of fibrosis observed. It is essential to understand the changes in their expression of phenotypes, depending on their location. There is no one favored phenotype for both macrophages and fibroblasts that positively affects bioimplants throughout the human body. Over the course of this section we aim to address this concern, by examining different organs and how their host response varies for both *in vivo* and *in vitro* studies. In this section, we will give a brief overview of important cell signaling pathways that influence the host response.

Then we will focus on biomaterial interaction studies for the different locations of implants within the body for lungs, bones, liver, skin, and heart.

2.4.1. Lungs

The effect of inhibiting different prostaglandins, for identification of critical points leading to a fibrotic response, has been the focus of theories formulated and experiments conducted by Hinz and co-workers⁴¹ over the past 20 years. Liu *et al.*¹⁶ and Dearth *et al.*⁴² hypothesized that inhibition of specific prostaglandin receptors such as PGE₂ and the COX-1/2 (cyclooxygenase-1/2) pathways causes stiffness driven activation of macrophages, which further leads to fibrosis.

Bleomycin treated lungs are models for IPF affected lungs, and their stiffness was found to be significantly higher than healthy tissue, which showed a median stiffness range between 3 to 5 kPa. Certain collagen rich regions in the IPF model showed high stiffness ranging from 25.6 to 40 kPa. These locally pre-calcified regions were shown to increase CD68+ macrophage presence and resulted in high levels of α -SMA, indicating the alterations were connected to myofibroblast differentiation. Shifting lung fibroblasts from soft to stiff substrates and reversing this process was also studied for up to 5 weeks to analyze the reversibility of this myofibroblast conversion.⁴³⁻⁴⁵ Even after returning the cells to soft substrates, the cells showed active markers for myofibroblasts indicating that the effect of the initial substrate could have long term effects on cell phenotype, as seen in **Figure 2.2**.

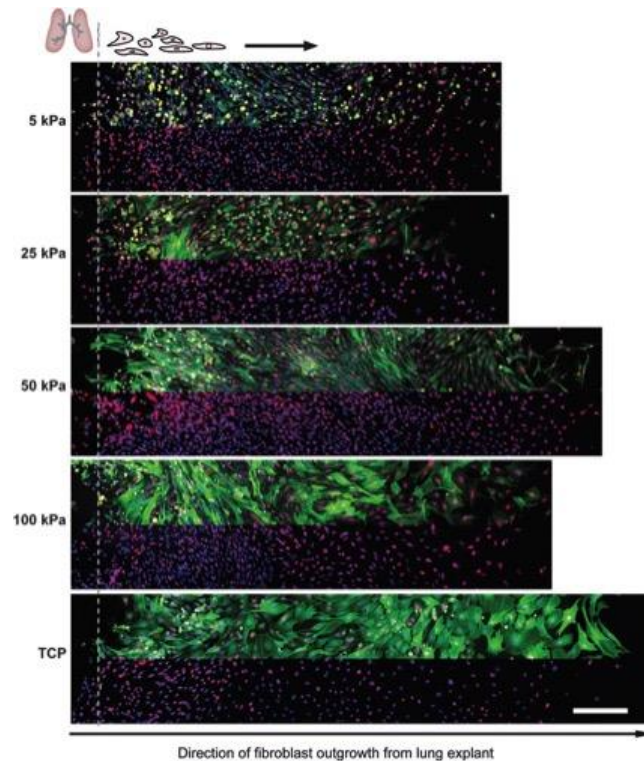


Figure 2.2: Effect of substrate stiffness on fibroblast differentiation to myofibroblasts. “Cell outgrowth on pathophysiologically stiff substrates. Lung parenchyma tissue explants (1 1 mm) were placed onto collagen-coated silicone substrates that were either 5, 25, 50, or 100 kPa in stiffness. After 6 days in culture, cells were paraformaldehyde fixed and examined by immunofluorescence for markers of cell proliferation (Ki67, red), myofibroblast presence (a-SMA, green) and distribution of cells (DAPI, blue). With increasing stiffness, myofibroblasts first appear on 25 kPa substrates and subsequently increase in number and distribution on 5–100 kPa models. Scale bar = 200 mm.” Reproduced with permission. Copyright 2012, The Royal Society of Chemistry

On the basis of these studies, we can suggest several integral design principles for implants or regeneration strategies in lung tissue (see Lungs section of **Figure 2.3**). These design principles would include soft substrates with rigidity less than 3 kPa, having greater than 30 μm sized pores, and decellularized scaffolds, all of which would show reduced macrophage and myofibroblast presence. These results link back to previous observations on the influence of pore sizes on macrophage phenotypes, and how sequestering adhesion of macrophages within them affect their regular behavior. It was observed for pores larger than 35 μm that the natural pro-inflammatory behavior of M1 macrophages was significantly reduced, as was the fibrotic capsule formation

mediated by M2 macrophages. These large pore size effects show host responses where there is inhibited fibroblast to myofibroblast differentiation, also contributing to a thinner fibrotic capsule, due to lower collagen secreted by the fibroblast cells. This is a very important aspect of modulating these material properties, as lower myofibroblast differentiation results in inhibited fibrosis alleviates and, in some cases, improves compromised lung capacity symptoms faced by patients suffering from IPF or cystic fibrosis.

2.4.2. Bone

The process of bone tissue engineering involves fabrication of constructs for culturing cells, delivering growth factors, and exerting mechanical stimuli.⁴⁶ There is limited information available regarding the effect different materials have on both macrophages and fibroblasts after implantation.⁴⁷ Two common strategies are generally employed for bone tissue engineering and dental implants. These were based on reprogramming stem cell lines^{12,48} into bone tissue using growth factors or using mechanotransduction to induce differentiation towards osteoblasts.⁴⁹

Hydroxyapatite coatings on scaffolds made of collagen I have been shown to improve MSC adhesion and differentiation into osteoblasts.^{32,46} Such coated scaffolds have significant advantages over previous stem cell based bone tissue engineering approaches. A popular addition to these scaffolds is the inoculation with MSCs instead of previously used embryonic stem cells, as the latter can result in teratomas.⁵⁰

Chemically modified hydrogels have been fabricated with different surface groups exposed to the ECM for interrogating their influence on bone regeneration pathways. The use of RGD-modified diacrylate hydrogels for improving biomineralization was studied by Eliseif *et al.*⁵¹ These RGD modified substrates stimulated the production of bone-production proteins such as osteocalcin, and they had a 2.5-fold increase in osteocalcin compared to non-RGD modified substrates. This response was a marker for regenerating healthy bone tissue around areas that have

suffered from debilitating diseases such as volumetric muscle loss (VML). VML has been studied in mammals as the loss of function and resorption of bone in areas that have previously been treated for other tumors or due to shock damage.⁵² Hybrid substrates and therapies to regenerate functional bone tissue in such areas with the help of decellularized mouse ECM scaffolds seeded with perivascular stem cells have been proposed.⁵³ These scaffolds have shown positive remodeling responses when transplanted into rat aortic valves by successfully recruiting M2 macrophages and myofibroblasts.

Another common technique for bone tissue engineering is based on growth factor mediated reprogramming.⁵⁴ For cases where there is severe muscle loss, there are several problems for treatment that include acceptance of new tissue and lack of available healthy tissue for implants. By pairing the ability of myofibroblasts to infiltrate gelatinous tissues and the acceptance of PLLA based scaffolds, a hybrid protocol was suggested to accelerate muscle regeneration at the site. Adding myogenic growth factors and observing their sustained presence within the implants activated STAT6 pathways, which resulted in both types of macrophages being differentiated at the site of the implants from freely circulating monocytes. The overall angiogenesis due to the activation of these pathways was a useful strategy showing the best empirical results for muscular regeneration, which was further modified using insulin-like growth factor treatment on gelatinous hydrogels.

On the basis of these studies on musculoskeletal implants and the innate response, we propose the following design principles: implants must be relatively stiff (>40 kPa), have small pores (~50 nm) or non-porous substrates, increased surface roughness to promote osteoblast differentiation, and a higher M2 macrophage and myofibroblast presence. The higher rigidity would be promoting the myofibroblast differentiation for the remodeling and initiation of M2

macrophages. The small pores would keep the macrophages non-adhered to the surface and exhibiting their standard host response.

2.4.3. Heart

Cardiomyocytes are specialized cardiac cells, which are integral for the synchronous involuntary muscle function in the heart. Novel strategies for the treatment of congenital heart diseases where tissue engineered heart valves (TEHVs) are fabricated using biocompatible scaffolds (made of fibrin and thrombin coated tissue culture plastic plates) containing VICs have been proposed.⁵⁵ Much like fibroblasts, VICs have a quiescent or dormant state where they freely circulate, and an activated state, which is initiated by certain cell signaling pathways (mostly GATA binding protein-4 and Tbox protein-5) that lead to ECM alterations. Neonatal human dermal fibroblasts can replace the VICs seeded in the scaffolds for TEHVs and the subsequent aortic remodeling. However, there are significant concerns that VICs in their activated state produce more ECM components and show high levels of α -SMA, which could result in fibrosis, leading to arterial blocking, rather than valve remodeling. To combat this concern, comparisons of pediatric VICs and dermal fibroblasts on different substrates were conducted to determine what components favor remodeling of the TEHVs, such that there are no adverse responses. Collagen type I was found to modulate the fibrosis to levels which would induce smooth angiogenesis around the fibrotic capsule. Wessels *et al.*⁵⁶ explored similar solutions using epicardially derived fibroblast cells (EPDCs), which have been transformed from cardiac fibroblasts to MSCs and can play a very important role in the process of valve healing *in vivo*. The formation of atrioventricular (AV) valves by these VICs can be potentially useful for providing treatment strategies for congenital heart defects in infants. Though the studies were unable to conclusively use EPDCs in scaffolds for AV rebuilding because of inconclusive myocardial staining, the process may yet be useful for studies of other heart diseases.

The biocompatibility of synthetically derived hyaluronic acid based hydrogels⁵⁷ has been well established. Chang *et al.*⁵⁷ injected blood-growth factor based solutions in hyaluronic acid based hydrogels and surmised that there is need to optimize several parameters: gelation time to avoid pulmonary embolisms during injection, pore sizes to allow for transport of metabolites, and degradation kinetics to avoid unwanted host responses to erosion products. These formulations promoted angiogenesis, improved cell function, and reduced CD44+ macrophages. The second approach for cardiac implants, analogous to pulmonary and musculoskeletal implants, was the strategy of reprogramming of fibroblasts into functional cardiomyocytes using a mixture of transcription factors and cytokines. Qian *et al.*⁵⁸ worked on treating quiescent fibroblasts with retroviral infection of Gata4, Mef2c, and Tbx4 doses that can potentially create techniques to heal organs *in vivo* by forming cardiomyocytes. These three genes are responsible for ECM alterations and activation of fibrocytes or quiescent fibroblasts to myofibroblasts, which concurs with their effectiveness in tracking VICs cell signaling responses. Lineage tracking was employed to monitor induced cardiomyocyte activity and their genetic signature was compared to native cardiomyocytes and non-infected heart cells.

Based on the above review, optimal material properties for cardiac reprogramming of myofibroblasts and repair are very similar to those identified for lung implants. The important factors are that the material be soft (<3 kPa), and have large pores (>30 μm), and reduce M2 macrophage and myofibroblast responses to avoid fibrosis and plaque to accumulate on the cardiac tissue. For heart implants it is essential to mediate a reduced fibrotic response to inhibit scarring of the cardiac tissue, which can disrupt its natural beatings. The adhesion of the macrophages within the pores of these surfaces would prevent an overall lower activated macrophage or myofibroblast response.

2.4.4. Liver

The mortality rates for diseases brought on by liver fibrosis is very high, at about 20% one month after diagnosis,⁵⁹ and can progress to non-treatable stages rapidly. It has been established that the hepatic stellate macrophages, known as Kupffer cells, play a key role in the progression of liver fibrosis.⁶⁰ The change in the phenotype of monocytes to polarized M1, M2, or Kupffer macrophages is mediated by different cell activated signaling pathways and are also linked to the inducible nitric oxide synthase and arginine stimulated classical M1/M2 polarization signals. The range of interactions between these different factors influencing the fibrotic capsule formation necessitates the need for liver fibrosis studies *in vitro* and *in vivo*.⁶¹

As fibrosis is a dynamic process, spanning multiple stages, it has been difficult to characterize based on the interactions of fibroblasts and macrophages. Macrophages play a critical role in the activation and differentiation of fibroblasts into myofibroblasts through the release of cytokines such as IL-13 and TGF- β .⁶² Modifying these cytokine release pathways in macrophages inhibited hepatic stellate cells, thereby reducing the fibrotic response. This key dynamic between macrophages and fibroblasts has perhaps been the best understood for liver fibrosis compared to other organs.⁶²

Different cell signaling pathways established for the progression of liver fibrosis and its inhibition have been widely studied. There are two major types of host responses that can be observed as a part of liver fibrosis progression, one for reducing liver scarring and the other for liver regeneration.⁶¹ It was logically concluded that different polarized responses of macrophages would be essential for these diametrically opposed roles in the host response, and this is further detailed in **Figure 2.3**. Macrophages are critically involved in both the injury and repair of the tissue, and it is possible to alter their polarizations to prevent fibrosis from progressing. These

findings illustrate the great need for clinical studies to observe the multi-cell participation in liver fibrosis.

Recruitment of GR1⁺ monocytes during liver injury is essential for the progression of liver fibrosis.⁶⁰ This study corroborates research conducted by Duffield *et al.*⁶¹ on macrophage phenotypic changes in liver injury or repair states. The activation of GR1⁺ at different stages of fibrosis through TGF- β was studied to evaluate the threshold levels of cytokine that activate the monocytes. The role played by different macrophage polarizations that can inhibit fibrosis was studied and identified the effect of arginase-1 expressing macrophages on a rat model, which was exhibiting schistosomiasis, via thioacetamide induction.⁶³

Key design principles for implants used for liver repair and fibrosis reduction have been identified based on the review above. For the purpose of reduction of liver scarring, there is a need for soft scaffolds or substrates (<2 kPa),⁶⁴ with large pores (>30 μ m), which can stimulate M1 macrophage response themselves or through classic activation via cytokines like IL-4. For the explicit purpose of liver repair and regeneration, it is essential to have stiff scaffolds (>40 kPa)¹⁶ which are non-porous or smooth, such that they can incite an increased M2 macrophage presence.

2.4.5. Skin

Skin undergoes a specific wound healing response. Macrophages are generally maintained at low levels in healthy skin, but can differentiate from monocytes in blood vessels shortly after implantation or injury and cause acute inflammation.⁶⁵ Fibrotic encapsulation of dermal implants is highly related to the interaction between M2 macrophages and fibroblasts. Cytokines released by M2 macrophages, including TGF- β and MMPs, are known to enhance collagen production and endothelial cell migration, respectively. This further results in FGF-2 and PDGF production, which have been reported to cause myofibroblast differentiation.⁶⁶

Several design principles have been found to reduce the FBR. From a mechanical aspect, dermal implants require larger pore sizes and lower stiffnesses to reduce the FBR. As previously mentioned, dermal implants with 34 μm pore sizes can significantly reduce the FBR by shifting macrophages to an M2 phenotype compared to the non-porous implant.³⁰ Additionally, poly(hydroxyethyl methacrylate) implanted into mice with 20 μm pore sizes has lower epithelial migration compared to 40 and 60 μm pore sizes, whereas no statistical difference was found between the 40 and 60 μm sized scaffolds.⁶⁷ Other research showed that titanium implants with larger pore sizes ranging from 40 to 160 μm did not have observable differences in cell ingrowth when implanted in rats,⁶⁸ which suggests a critical pore size around 30 μm may be able to appropriately modulate the host response. On the other hand, collagen hydrogel implants with a lower stiffness (elastic modulus 0.7 kPa) was reported to increase dermal fibroblast ingrowth compared to an implant with an elastic modulus of 1.6 kPa.⁶⁹

From the chemokine and cytokine aspect, one of the most significant factors influencing dermal implant acceptance is NO release. It has been previously reported that a silicone elastomer coated xerogel polymer implant that released NO could significantly reduce collagen encapsulation and chronic inflammation in rats.⁷⁰ The study suggested that NO release reduces both pro-inflammatory cytokine IL-6 and anti-inflammatory TGF- β release from macrophages. The former cytokine could lead to classical activation and the latter is known to enhance collagen production from dermal fibroblasts.⁷⁰

More recently, the effect of NO release kinetics on subcutaneous implants has been studied in Yorkshire-type piglets. Polyurethane-coated wire implants with longer release duration and improved NO loading were found to have a greater decrease in inflammation and fibrotic encapsulation.⁷¹ Thus, dermal implants capable of loading larger amounts of NO and maintaining long term *in vivo* NO concentration will reduce the FBR.

Other possible methods to modulate the FBR are through HA. HA naturally exists in skin at a high concentration.⁷² It plays an important role in skin regeneration and dermal fibroblasts cultured on an HA mesh has been shown to heal chronic wounds caused by skin loss clinically.⁷³ In skin wound healing, HA accumulation at the injury site is essential for macrophage recruitment.⁷⁴ As described above, sulfated HA can shift macrophage phenotype to an M2 state^{75,76} and enhance dermal fibroblast adhesion,⁷⁷ which favors wound healing. Implants coated with sulfated HA may reduce the FBR.

Based on the above review, the design principles for dermal implants would be using soft materials (~1 kPa) with large pores (>30 μm). Since skin contains high populations of resident fibroblasts, implants with long term NO release would further help reducing fibrotic encapsulation. M2 macrophage promoters or anti-inflammatory cytokines loaded into the scaffold can also decrease the host response.

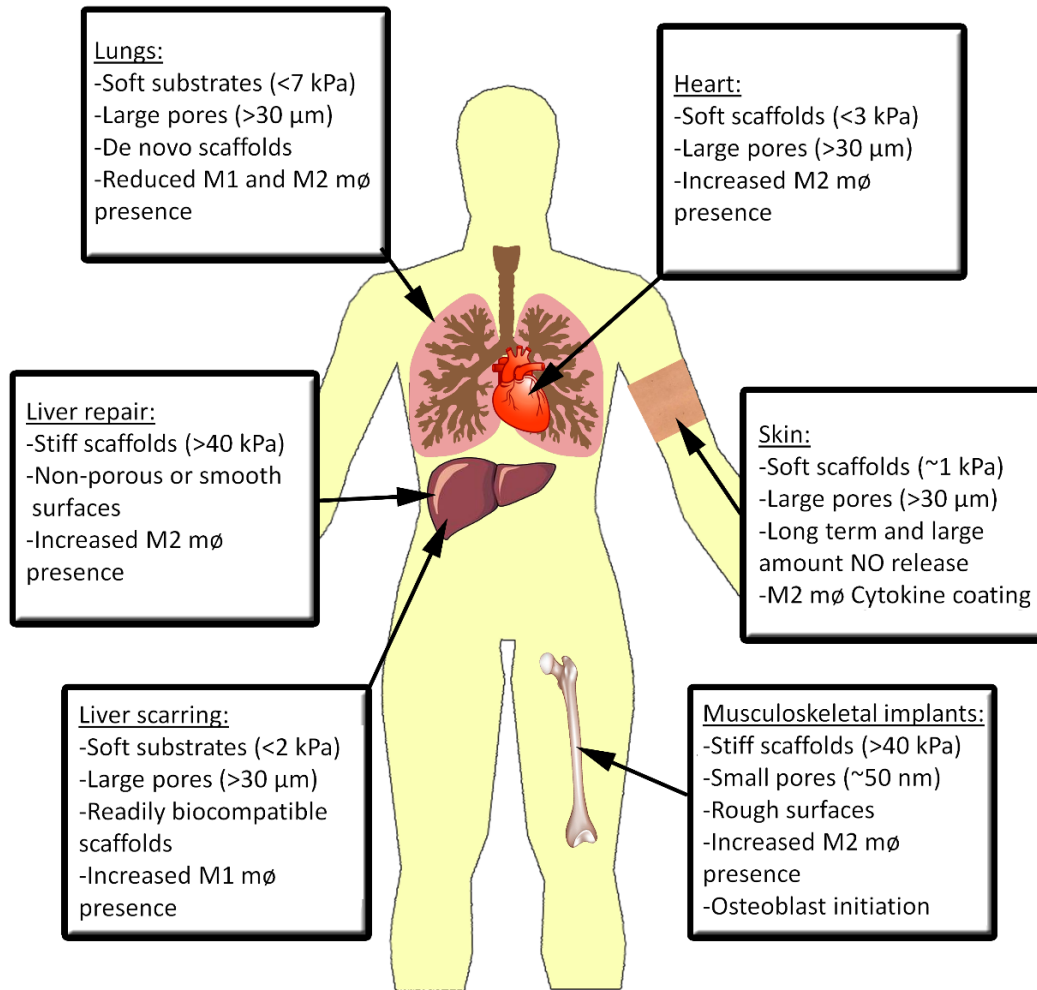


Figure 2.3: Design principles for bioimplants based on their location. These examples cover a range of microenvironments with unique material property requirements for appropriate macrophage and fibroblast responses. These descriptions are not comprehensive but illustrate some key aspects for eliciting appropriate outcomes.

2.4.6. Design Principles for Disparate Implant Locations

Figure 2.3 summarizes the design principles identified above for biomaterials to be implanted into different locations within the body. With the help of such summarization, it should be possible to understand the key roles played by different materials properties on host responses, and the changes in behavior of the cells that are integral to such a response. It is very likely that these design principles may be combined with multimodal imaging techniques capable of probing

the host response in real time to further understand the dynamic responses of macrophage and fibroblast phenotype to biomaterials.

2.5. Summary Table

Table 2.2. Summary of macrophages and fibroblasts response on bioimplant

| Material | Implant Site | Macrophage effect | Fibroblast effect | References |
|--------------------------|----------------|--|--|-----------------------------------|
| Bleomycin | Lungs | | Increased myofibroblast differentiation for stiff substrates | Liu ¹⁰⁴ (2010) |
| | | Hemosiderin staining | Higher myofibroblast differentiation + α SMA presence | Carnesechhi ¹⁵³ (2012) |
| Hyaluronan gel | Heart | Possibly both M1 and M2 | Positive FBR + decreased fibrosis over 7 days observation | Chang ¹⁴⁴ (2012) |
| | | Sulfation degree dependent | Increased myofibroblast with increased dosage | Franz (2013) |
| | | MW dependent | Low MW-increased myofibroblast High MW-decreased myofibroblasts | Rayahin (2015) |
| Silk | Bones | Differentiation into FBGCs and infiltrating macrophages | Osteogenic differentiation of hMSCs into osteoblasts | Melke ⁸⁷ (2015) |
| | Skin | Reduced macrophage number and inflammatory response | Reduced fibroblast and myofibroblast diff | Liu ²¹ (2014) |
| | Dermal | Macrophage differentiation inhibited | Reduced myofibroblast diff and fibrotic response | Zeplin ²⁰ (2014) |
| Mesenchymal stromal cell | Abdominal wall | Enhanced M2 response compare to acellular hydrogel and MSC alone | Increased myofibroblast diff and fibrotic response | Stucky (2015) |
| | Hippocampal | | Reduced myofibroblast diff and fibrotic response | Ayala (2015) |

Table 2.2 Continued

| Material | Implant Site | Macrophage effect | Fibroblast effect | References |
|-------------------|-----------------|----------------------------|--|--|
| Alginate hydrogel | In Vitro | G/M ratio dependent | G/M ratio dependent | Berven (2013) |
| | | MW dependent | Reduced myofibroblast with increased dosage | Zhou (2015) |
| | Intraperitoneal | M2 | Increased myofibroblast diff and fibrotic response | Jain (2015) |
| Chitosan | In vitro | DD dependent M1 | Reduced myofibroblasts | Fong (2015) |
| | | MW dependent M1 | Reduced fibrosis response | Zhang (2014) |
| | Intraperitoneal | Increased M1 | Reduced myofibroblast diff and fibrotic response | Chakrabarti ⁴⁸ (2014) |
| | Knee trochlea | Fast degradation on Low MW | Reduced myofibroblast diff and fibrotic response | Lafantaisie-Favreau ⁴³ (2013) |
| | Subcutaneous | No significant difference | No significant difference | Li ⁴⁹ (2014) |

2.6. Conclusions

In summary, bioimplant material, modification, and design should be selected based on implant location. For biodegradable materials, degradation rates need to match tissue regeneration rates in order to avoid implant deformation and fibrous encapsulation. Eliminating secondary inflammation caused by degradation products is also an essential issue. On the other hand, non-degradable implants, especially for joint replacements, focus more on wear resistance and fibrotic encapsulation. In most situations, natural materials can reduce acute inflammation upon implantation, but are limited by mechanical properties and most natural materials' degradation products lead to secondary inflammation. In contrast, synthetic materials have high plasticity but are likely to cause acute or chronic inflammation after implantation. The host response mechanisms to most materials have not been fully elucidated at this point.

Several challenges remain for developing biomaterials with the appropriate host response for lungs, heart, liver, skin, and musculoskeletal implants. Depending on the natural mechanical properties of organ systems, the design principles differ greatly. For example, stiff substrates elicit an appropriate remodeling response for bone implants, while softer substrates incite an anti-inflammatory response from macrophages and fibroblasts participating at the site of the implant. Furthermore, by understanding the effect of certain geometric cues affecting macrophages phagocytosis and stress sensing mechanisms in fibroblasts, more considerations were listed. On the basis of all these cues, the design principles can be applied to tailor the host response in these organs based also on the nature of the system they are exposed to, namely for regeneration strategies.

On reviewing the research conducted on the role played by both these cell types, there is a need for concurrent studies in order to better understand the host response and evaluate the factors that polarize cells. With the focus in biomedical sciences shifting towards non-invasive techniques of observation, there is a strong case for popularizing non-linear optics and/or multi-modal imaging to elucidate the subtle changes in behavior of the cells that are present as a part of the FBR. Though there has been some research conducted on the timeline of such responses such as Langer and coworkers,^{40,89,139, 180-182} and Bratlie and coworkers,¹⁸³ the common factor lacking across many such studies has been the application of techniques for efficient internal imaging. Non-linear optics have shown themselves as a useful tool to have in many such systems. Through the application of second harmonic generation microscopy combined with other bio-chemical imaging techniques such as two photon electron fluorescence microscopy,¹⁶⁹ it has been shown that we can identify the progression of innate response in deep tissues.^{184, 185} Over the course of the next decade, these methods may improve in terms of spatial and temporal resolution such that

real-time observations of macrophages, fibroblasts, and myofibroblasts become more commonplace.

Acknowledgments

This review was co-authored by Lida Zhu and I. We co-wrote the Introduction and Conclusion sections. Lida Zhu wrote the majority of the Materials Selection sections and designed the summary figure.

2.7. References

- [1] E. S. Place, N. D. Evans, M. M. Stevens, *Nat. Mater.* 2009, 8, 457.
- [2] N. M. Vacanti, H. Cheng, P. S. Hill, J. D. T. Guerreiro, T. T. Dang, M. Ma, S. Watson, N. S. Hwang, R. Langer, D. G. Anderson, *Bio- macromolecules* 2012, 13, 3031.
- [3] A. J. Rao, C. Nich, L. S. Dhulipala, E. Gibon, R. Valladares, S. Zwingenberger, R. L. Smith, S. B. Goodman, *J. Biomed. Mater. Res. - Part A* 2013, 101 A, 1926.
- [4] H. C. Bygd, K. D. Forsmark, K. M. Bratlie, *Clin. Transl. Med.* 2014, 3.
- [5] D. F. Williams, *Biomaterials* 2008, 29, 2941. [6] A. Mantovani, S. K. Biswas, M. R. Galdiero, A. Sica, M. Locati, *J. Pathol.* 2013, 229, 176.
- [7] P. J. Murray, J. E. Allen, S. K. Biswas, E. A. Fisher, D. W. Gilroy, S. Goerdt, S. Gordon, J. A. Hamilton, L. B. Ivashkiv, T. Lawrence, M. Locati, A. Mantovani, F. O. Martinez, J.-L. Mege, D. M. Mosser, G. Natoli, J. P. Saeij, J. L. Schultze, K. A. Shirey, A. Sica, J. Suttles, I. Udalova, J. A. van Ginderachter, S. N. Vogel, T. A. Wynn, *Immunity* 2014, 41, 14.
- [8] D. M. Mosser, J. P. Edwards, *Nat. Rev. Immunol.* 2008, 8, 958. [9] N. B. Hao, M. H. Lü, Y. H. Fan, Y. L. Cao, Z. R. Zhang, S. M. Yang, *Clin. Dev. Immunol.* 2012, 2012, 948098.
- [10] S. J. Galli, N. Borregaard, T. A. Wynn, *Nat Immunol* 2011, 12, 1035.
- [11] G. S. A. Boersema, N. Grotenhuis, Y. Bayon, J. F. Lange, Y. M. Bastiaansen-Jenniskens, *Biores. Open Access* 2016, 5, 6.
- [12] T. a. Wynn, A. Chawla, J. W. Pollard, *Nature* 2013, 496, 445. [13] P. J. Murray, T. a. Wynn, *Nat. Rev. Immunol.* 2011, 11, 723. [14] B. Hinz, S. H. Phan, V. J. Thannickal, M. Prunotto, A. Desmoulière, J. Varga, O. De Wever, M. Mareel, G. Gabbiani, *Am. J. Pathol.* 2012, 180, 1340.
- [15] M. Otranto, V. Sarrazy, F. Bonte, B. Hinz, G. Gabbiani, A. Desmouliere, F. Bonté, B. Hinz, G. Gabbiani, A. Desmouliere, *Cell Adhes. Migr.* 2012, 6, 203.

- [16] B. Hinz, S. H. Phan, V. J. Thannickal, A. Galli, M.-L. Bochaton-Pia llat, G. Gabbiani, *Am. J. Pathol.* 2007, 170, 1807.
- [17] J. J. M. Anderson, *Annu. Rev. Mater. Res.* 2001, 31, 81. [18] M. T. Wolf, C. L. Dearth, C. A. Ranallo, S. T. LoPresti, L. E. Carey, K. A. Daly, B. N. Brown, S. F. Badylak, *Biomaterials* 2014, 35, 6838.
- [19] T. A. Wynn, L. Barron, *Semin. Liver Dis.* 2011, 30, 245.
- [20] L. Barron, T. a. Wynn, *Am. J. Physiol. Gastrointest. Liver Physiol.* 2011, 300, G723.
- [21] G. Zhou, M. S. Niepel, S. Saretia, T. Groth, *J. Biomed. Mater. Res. - Part A* 2015, 493.
- [22] D. Akilbekova, K. M. Bratlie, *PLoS One* 2015, 10, e0130386.
- [23] B. Rolfe, J. Mooney, B. Zhang, S. Jahnke, S. Jane Le, Y.-Q. Chau, Q. Huang, H. Wang, G. Campbell, J. Campbell, *Regenera- tive Medicine and Tissue Engineering - Cells and Biomaterials* (Ed.: D. Eberli), InTech, Croatia 2011, Ch. 23, DOI: 10.5772/21790.
- [24] M. F. Maitz, *Biosurface and Biotribology* 2015, 1, 161.
- [25] C. L. R. Belmiro, R. G. Gonçalves, E. O. Kozłowski, A. F. Werneck, C. M. Takyia, M. Leite-Jr., M. S. G. Pavão, *Brazilian J. Med. Biol. Res.* 2011, 44, 624.
- [26] P. H. Zeplin, N. C. Maksimovikj, M. C. Jordan, J. Nickel, G. Lang, A. H. Leimer, L. Römer, T. Scheibel, *Adv. Funct. Mater.* 2014, 24, 2658.
- [27] H. Liu, S. G. Wise, J. Rnjak-Kovacina, D. L. Kaplan, M. M. M. Bilek, A. S. Weiss, J. Fei, S. Bao, *Biomaterials* 2014, 35, 5138.
- [28] R. Tejero, E. Anitua, G. Orive, *Prog. Polym. Sci.* 2014, 39, 1406. [29] S. Y. Seo, G. H. Lee, S. G. Lee, S. Y. Jung, J. O. Lim, J. H. Choi, *Car- bohydr. Polym.* 2012, 90, 109.
- [30] L. Berven, R. Solberg, H. H. T. Truong, Ø. Arlov, F. Lill Lund Aachmann, G. Skjåk-Bræk, W. M. Egge-Jacobsen, H. Thidemann Johansen, A. B. C. Samuelsen, *Bioact. Carbohydrates Diet. Fibre* 2013, 2, 30.
- [31] R. Zhou, X. Shi, Y. Gao, N. Cai, Z. Jiang, X. Xu, 2015. [32] X. Xu, X. Wu, Q. Wang, N. Cai, H. Zhang, Z. Jiang, M. Wan, T. Oda, *J. Agric. Food Chem.* 2014, 62, 3168.
- [33] N. C. Hunt, A. M. Smith, U. Gbureck, R. M. Shelton, L. M. Grover, *Acta Biomater.* 2010, 6, 3649.
- [34] J. L. Drury, R. G. Dennis, D. J. Mooney, *Biomaterials* 2004, 25, 3187. [35] B. J. Spargo, A. S. Rudolph, F. M. Rollwagen, *Biomaterials* 1994, 15, 853.
- [36] I. Constantinidis, I. Rask, R. C. Long, A. Sambanis, R. C. Long Jr., R. C. L. Jr., *Biomaterials* 1999, 20, 2019.
- [37] M. Otterlei, K. Ostgaard, G. Skjåk-Braek, O. Smidsrød, P. Soon-Shiong, T. Espevik, *J. Immunother.* (1991). 1991, 10, 286.

- [38] G. Klöck, A. Pfeffermann, C. Ryser, P. Gröhn, B. Kuttler, H. J. Hahn, U. Zimmermann, *Biomaterials* 1997, 18, 707.
- [39] M. Tanihara, Y. Suzuki, E. Yamamoto, A. Noguchi, Y. Mizushima, *J. Biomed. Mater. Res.* 2001, 56, 216.
- [40] A. J. Vegas, O. Veiseh, J. C. Doloff, M. Ma, H. H. Tam, K. Bratlie, J. Li, A. R. Bader, E. Langan, K. Olejnik, P. Fenton, J. W. Kang, J. Hollister-Locke, M. A. Bochenek, A. Chiu, S. Siebert, K. Tang, S. Jhunjhunwala, S. Aresta-Dasilva, N. Dholakia, R. Thakrar, T. Vietti, M. Chen, J. Cohen, K. Siniakowicz, M. Qi, J. McGarrigle, S. Lyle, D. M. Harlan, D. L. Greiner, J. Oberholzer, G. C. Weir, R. Langer, D. G. Anderson, *Nat. Biotechnol.* 2016, 34, 345.
- [41] D. Fong, M. B. Ariganello, J. Girard-Lauziere, C. D. Hoemann, *Acta Biomater.* 2015, 12, 183.
- [42] T. Mori, M. Murakami, M. Okumura, T. Kadosawa, T. Uede, T. Fujinaga, *J. Vet. Med. Sci.* 2005, 67, 51.
- [43] M. I. Oliveira, S. G. Santos, M. J. Oliveira, A. L. Torres, M. A. Barbosa, *Eur. Cells Mater.* 2012, 24, 136.
- [44] Y. Gu, W. Zhang, H. Wang, W. Y. Lee, *Colloids Surfaces B Biointer- faces* 2014, 117, 42.
- [45] Z.-S. Wen, L.-J. Liu, Y.-L. Qu, X.-K. Ouyang, L.-Y. Yang, Z.-R. Xu, *Mar. Drugs* 2013, 11, 3582.
- [46] D. Silva, R. Arancibia, C. Tapia, C. Acuña-Rougier, M. Diaz-Dosque, M. Cáceres, J. Martínez, P. C. Smith, *J. Periodontal Res.* 2013, 48, 677.
- [47] H. Ueno, F. Nakamura, M. Murakami, M. Okumura, T. Kadosawa, T. Fujinaga, *Biomaterials* 2001, 22, 2125.
- [48] M. S. Benhabiles, R. Salah, H. Lounici, N. Drouiche, M. F. A. Goosen, N. Mameri, *Food Hydrocoll.* 2012, 29, 48
- [49] A. B. Vishu Kumar, M. C. Varadaraj, L. R. Gowda, R. N. Tharanathan, *Biochem. J.* 2005, 391, 167.
- [50] D. P. Vasconcelos, A. C. Fonseca, M. Costa, I. F. Amaral, M. a. Barbosa, A. P. Águas, J. N. Barbosa, *Biomaterials* 2013, 34, 9952.
- [51] C. L. Bueter, C. K. Lee, J. P. Wang, G. R. Ostroff, C. a. Specht, S. M. Levitz, *J. Immunol.* 2014, 192, 5943
- [52] G. I. Howling, P. W. Dettmar, P. A. Goddard, F. C. Hampson, M. Dornish, E. J. Wood, *Biomaterials* 2001, 22, 2959.
- [53] Y. Okamoto, A. Inoue, K. Miyatake, K. Ogihara, Y. Shigemasa, S. Minami, *Macromol. Biosci.* 2003, 3, 587.
- [54] T. C. Chou, E. Fu, E. C. Shen, *Biochem. Biophys. Res. Commun.* 2003, 308, 403.

- [55] P. Zhang, W. Liu, Y. Peng, B. Han, Y. Yang, *Int. Immunopharmacol.* 2014, 23, 254.
- [56] G. J. Wu, C. H. Wu, G. J. Tsai, *J. Funct. Foods* 2015, 12, 70. [57] Y. Lu, A. Shah, R. A. Hunter, R. J. Soto, M. H. Schoenfisch, *Acta Biomater.* 2015, 12, 62.
- [58] N. Yang, W. H. Li, *Mater. Lett.* 2015, 138, 154. [59] C.-H. Lafantaisie-Favreau, J. Guzmán-Morales, J. Sun, G. Chen, A. Harris, T. D. Smith, A. Carli, J. Henderson, W. D. Stanish, C. D. Hoemann, *BMC Musculoskelet. Disord.* 2013, 14, 27.
- [60] C. Ji, A. Khademhosseini, F. Dehghani, *Biomaterials* 2011, 32, 9719. [61] R. M. Gonçalves, A. C. L. Pereira, I. O. Pereira, M. J. Oliveira, M. A. Barbosa, *J. Mater. Sci. Mater. Med.* 2015, 26, 5496.
- [62] A. Chakrabarti, D. Talukdar, A. Pal, M. Ray, *Cell. Immunol.* 2014, 287, 27.
- [63] H. Li, A. M. Koenig, P. Sloan, N. D. Leipzig, *Biomaterials* 2014, 35, 9049.
- [64] L. F. Baeva, D. B. Lyle, M. Rios, J. J. Langone, M. M. Lightfoote, *J. Biomed. Mater. Res. A* 2014, 102, 305.
- [65] R. Stern, *Eur. J. Cell Biol.* 2004, 83, 317. [66] A. Fakhari, C. Berkland, *Acta Biomater.* 2013, 9, 7081. [67] J. M. Delmage, D. R. Powars, P. K. Jaynes, S. E. Allerton, *Ann. Clin. Lab. Sci.* 1986, 16, 303.
- [68] P. W. Noble, *Matrix Biol.* 2002, 21, 25. [69] J. E. Rayahin, J. S. Buhrman, Y. Zhang, T. J. Koh, R. a. Gemeinhart, *ACS Biomater. Sci. Eng.* 2015, 1, 481.
- [70] R. D. Price, M. G. Berry, H. A. Navsaria, *J. Plast. Reconstr. Aesthet. Surg.* 2007, 60, 1110.
- [71] M. a. Croce, K. Dyne, F. Boraldi, D. Quaglino, G. Cetta, R. Tiozzo, I. Pasquali Ronchetti, *Tissue Cell* 2001, 33, 326.
- [72] M. Y. Chang, Y. Tanino, V. Vidova, M. G. Kinsella, C. K. Chan, P. Y. Johnson, T. N. Wight, *C. W. Frevert, Matrix Biol.* 2014, 35, 162.
- [73] C. M. McKee, M. B. Penno, M. Cowman, M. D. Burdick, R. M. Strieter, C. Bao, P. W. Noble, *J. Clin. Invest.* 1996, 98, 2403.
- [74] B. Ruffell, G. F. T. Poon, S. S. M. Lee, K. L. Brown, S. L. Tjew, J. Cooper, P. Johnson, *J. Biol. Chem.* 2011, 286, 19179.
- [75] S. Franz, F. Allenstein, J. Kajahn, I. Forstreuter, V. Hintze, S. Möller, J. C. Simon, *Acta Biomater.* 2013, 9, 5621.
- [76] J. Kajahn, S. Franz, E. Rueckert, I. Forstreuter, V. Hintze, S. Moeller, J. C. Simon, *Biomater* 2012, 2, 226.
- [77] A. van der Smissen, V. Hintze, D. Scharnweber, S. Moeller, M. Schnabelrauch, A. Majok, J. C. Simon, U. Anderegg, *Biomaterials* 2011, 32, 8938.
- [78] P. A. Gunatillake, R. Adhikari, N. Gadegaard, *Eur. Cells Mater.* 2003, 5, 1.

- [79] A. R. Nectow, K. G. Marra, D. L. Kaplan, *Tissue Eng. Part B Rev.* 2012, 18, 40.
- [80] C. A. Sundback, J. Y. Shyu, Y. Wang, W. C. Faquin, R. S. Langer, J. P. Vacanti, T. A. Hadlock, *Biomaterials* 2005, 26, 5454.
- [81] Y. Wang, Y. M. Kim, R. Langer, *J. Biomed. Mater. Res. A* 2003, 66, 192. [82] R. A. Allen, W. Wu, M. Yao, D. Dutta, X. Duan, T. N. Bachman, H. C. Champion, D. B. Stolz, A. M. Robertson, K. Kim, J. S. Isenberg, Y. Wang, *Biomaterials* 2014, 35, 165.
- www.MaterialsViews.com
- [83] D. Li, G. Guo, R. Fan, J. Liang, X. Deng, F. Luo, Z. Qian, *Int. J. Pharm.* 2013, 441, 365.
- [84] T. M. Fillion, J. Xu, M. L. Prasad, J. Song, *Biomaterials* 2011, 32, 985. [85] H. Il Kim, K. Ishihara, S. Lee, J. H. Seo, H. Y. Kim, D. Suh, M. U. Kim, T. Konno, M. Takai, J. S. Seo, *Biomaterials* 2011, 32, 2241.
- [86] J. Zhou, Y. T. Tsai, H. Weng, L. Tang, *Free Radic. Biol. Med.* 2012, 52, 218.
- [87] P. S. C. Sacchetin, R. F. Setti, P. D. T. V. E. Rosa, Â. M. Moraes, *Mater. Sci. Eng. C* 2016, 58, 870.
- [88] Y. Lee, J. Kwon, G. Khang, D. Lee, *Tissue Eng. Part A* 2012, 18, 1967. [89] T. T. Dang, K. M. Bratlie, S. R. Bogatyrev, X. Y. Chen, R. Langer, D. G. Anderson, *Biomaterials* 2011, 32, 4464.
- [90] W. Ji, F. Yang, H. Seyednejad, Z. Chen, W. E. Hennink, J. M. Anderson, J. J. J. P. van den Beucken, J. A. Jansen, *Biomaterials* 2012, 33, 6604.
- [91] H. Liao, X. F. Walboomers, W. J. E. M. Habraken, Z. Zhang, Y. Li, D. W. Grijpma, A. G. Mikos, J. G. C. Wolke, J. A. Jansen, *Acta Biomater.* 2011, 7, 1752.
- [92] R. P. Felix Lanao, S. C. G. Leeuwenburgh, J. G. C. Wolke, J. A. Jansen, *Biomaterials* 2011, 32, 8839.
- [93] R. P. Felix Lanao, S. C. G. Leeuwenburgh, J. G. C. Wolke, J. A. Jansen, *Acta Biomater.* 2011, 7, 3459.
- [94] J. W. M. Hoekstra, J. Ma, A. S. Plachokova, E. M. Bronkhorst, M. Bohner, J. Pan, G. J. Meijer, J. A. Jansen, J. J. J. P. Van Den Beucken, *Acta Biomater.* 2013, 9, 7518.
- [95] J. Kang, S. P. Schwendeman, *Biomaterials* 2002, 23, 239. [96] G. Zhu, S. R. Mallery, S. P. Schwendeman, *Nat. Biotechnol.* 2000, 18, 52.
- [97] A. Dalal, V. Pawar, K. McAllister, C. Weaver, N. J. Hallab, *J. Biomed. Mater. Res. - Part A* 2012, 100 A, 2147.
- [98] S. Hamlet, M. Alfarsi, R. George, S. Ivanovski, *Clin. Oral Implants Res.* 2012, 23, 584.
- [99] M. A. Alfarsi, S. M. Hamlet, S. Ivanovski, *J. Biomed. Mater. Res. - Part A* 2014, 102, 60.

- [100] S. Lee, J. Choi, S. Shin, Y. M. Im, J. Song, S. S. Kang, T. H. Nam, T. J. Webster, S. H. Kim, D. Khang, *Acta Biomater.* 2011, 7, 2337.
- [101] C.-H. Lee, Y.-J. Kim, J.-H. Jang, J.-W. Park, *Nanotechnology* 2016, 27, 085101.
- [102] A. J. Krych, F. Wanivenhaus, K. W. Ng, S. Doty, R. F. Warren, S. A. Maher, *J. Mater. Sci. Mater. Med.* 2013, 24, 2429.
- [103] C. Gong, X. Wei, X. Wang, Y. Wang, G. Guo, Y. Mao, F. Luo, Z. Qian, *Nanotechnology* 2010, 21, 215103.
- [104] Y. (Chezy) Barenholz, *J. Control. Release* 2012, 160, 117.
- [105] I. C. Saldarriaga Fernandez, J. F. da Silva Domingues, T. G. van Kooten, S. Metzger, D. W. Grainger, H. J. Busscher, H. C. van der Mei, *Eur. Cells Mater.* 2011, 21, 73.
- [106] S. Roman, I. Urbánková, G. Callewaert, F. Lesage, C. Hillary, N. I. Osman, C. R. Chapple, J. Deprest, S. MacNeil, *J. Urol.* 2016, 196, 261.
- [107] D. P. Poppas, J. J. Sung, C. M. Magro, J. Chen, J. P. Toyohara, B. J. Ramshaw, D. Felsen, *Hernia* 2016, 20, 623.
- [108] D. Weyhe, P. Hoffmann, O. Belyaev, K. Mros, C. Muller, W. Uhl, F. Schmitz, *Regul. Pept.* 2007, 138, 10.
- [109] M. L. Konstantinovic, E. Pille, M. Malinowska, E. Verbeken, D. Ridder, J. Deprest, *Int. Urogynecol. J. Pelvic Floor Dysfunct.* 2007, 18, 619.
- [110] E. M. Greenfield, M. a. Beidelschies, J. M. Tatro, V. M. Goldberg, A. G. Hise, *J. Biol. Chem.* 2010, 285, 32378.
- [111] E. Jacobi-Gresser, K. Huesker, S. Schutt, *Int. J. Oral Maxillofac. Surg.* 2013, 42, 537.
- [112] E. M. Engelhardt, L. A. Micol, S. Houis, F. M. Wurm, J. Hilborn, J. A. Hubbell, P. Frey, *Biomaterials* 2011, 32, 3969.
- [113] J. Melke, S. Midha, S. Ghosh, K. Ito, S. Hofmann, *Acta Biomater.* 2015, 31, 2015.09.005.
- [114] A. E. Thurber, F. G. Omenetto, D. L. Kaplan, *Biomaterials* 2015, 71, 145
- [115] D. Naskar, S. Nayak, T. Dey, S. C. Kundu, *Sci. Rep.* 2014, 4, 4745.
- [116] B. Kundu, N. E. Kurland, S. Bano, C. Patra, F. B. Engel, V. K. Yadavalli, S. C. Kundu, *Prog. Polym. Sci.* 2014, 39, 251.
- [117] J. R. Mauney, G. M. Cannon, M. L. Lovett, E. M. Gong, D. Di Vizio, P. Gomez, D. L. Kaplan, R. M. Adam, C. R. Estrada, *Biomaterials* 2011, 32, 808.
- [118] A. P. Cardoso, R. M. Gonçalves, J. C. Antunes, M. L. Pinto, A. T. Pinto, F. Castro, C. Monteiro, M. A. Barbosa, M. J. Oliveira, *Acta Biomater.* 2015, 23, 157.

- [119] D. An, Y. Ji, A. Chiu, Y. C. Lu, W. Song, L. Zhai, L. Qi, D. Luo, M. Ma, *Biomaterials* 2015, 37, 40.
- [120] P. De Vos, B. De Haan, R. Van Schilfgaarde, *Biomaterials* 1997, 18, 273.
- [121] P. de Vos, M. Spasojevic, B. J. de Haan, M. M. Faas, *Biomaterials* 2012, 33, 5552.
- [122] T. J. Keane, I. T. Swinehart, S. F. Badylak, *Methods* 2015, 84, 25.
- [123] B. N. Brown, R. Londono, S. Tottey, L. Zhang, K. a. Kukla, M. T. Wolf, K. a. Daly, J. E. Reing, S. F. Badylak, *Acta Biomater.* 2012, 8, 978.
- [124] K. E. M. Benders, P. R. van Weeren, S. F. Badylak, D. B. F. Saris, W. J. A. Dhert, J. Malda, *Trends Biotechnol.* 2013, 31, 169.
- [125] Y. Hong, A. Huber, K. Takanari, N. J. Amoroso, R. Hashizume, S. F. Badylak, W. R. Wagner, *Biomaterials* 2011, 32, 3387.
- [126] T. J. Keane, R. Londono, N. J. Turner, S. F. Badylak, *Biomaterials* 2012, 33, 1771.
- [127] American Thoracic Society, *International Multidisciplinary Consensus Classification of the Idiopathic Interstitial Pneumonias* 2002.
- [128] G. Raghu, H. R. Collard, J. J. Egan, F. J. Martinez, J. Behr, K. K. Brown, T. V. Colby, J. F. Cordier, K. R. Flaherty, J. A. Lasky, D. A. Lynch, J. H. Ryu, J. J. Swigris, A. U. Wells, J. Ancochea, D. Bouros, C. Carvalho, U. Costabel, M. Ebina, D. M. Hansell, T. Johkoh, D. S. Kim, T. E. King, Y. Kondoh, J. Myers, N. L. Müller, A. G. Nicholson, L. Richeldi, M. Selman, R. F. Dudden, B. S. Griss, S. L. Protzko, H. J. Schünemann, *Am. J. Respir. Crit. Care Med.* 2011, 183, 788.
- [129] F. Liu, J. D. Mih, B. S. Shea, A. T. Kho, A. S. Sharif, A. M. Tager, D. J. Tschumperlin, *J. Cell Biol.* 2010, 190, 693.
- [130] A. J. Booth, R. Hadley, A. M. Cornett, A. A. Dreffs, S. A. Matthes, J. L. Tsui, K. Weiss, J. C. Horowitz, V. F. Fiore, T. H. Barker, B. B. Moore, F. J. Martinez, L. E. Niklason, E. S. White, *Am. J. Respir. Crit. Care Med.* 2012, 186, 866.
- [131] Y. Chandorkar, N. Bhaskar, G. Madras, B. Basu, *Biomacromolecules* 2015, 16, 636.
- [132] J. A. Burdick, K. S. Anseth, *Biomaterials* 2002, 23, 4315. [133] H. Wang, M. W. Tibbitt, S. J. Langer, L. a. Leinwand, K. S. Anseth, *Proc. Natl. Acad. Sci. USA* 2013, 110, 19336.
- [134] M. W. Tibbitt, K. S. Anseth, *Biotechnol. Bioeng.* 2009, 103, 655. [135] J. L. Leight, W. F. Liu, R. R. Chaturvedi, S. Chen, M. T. Yang, S. Raghavan, C. S. Chen, *Cell. Mol. Bioeng.* 2012, 5, 299.
- [136] J. A. Champion, S. Mitragotri, *Pharm. Res.* 2009, 26, 244. [137] M. T. Wolf, C. L. Dearth, S. B. Sonnenberg, E. G. Lobo, S. F. Badylak, *Adv. Drug Deliv. Rev.* 2015, 84, 208.

- [138] J. Kim, W. A. Li, Y. Choi, S. A. Lewin, C. S. Verbeke, G. Dranoff, D. J. Mooney, *Nat. Biotechnol.* 2015, 33, 64.
- [139] O. Veiseh, J. C. Doloff, M. Ma, A. J. Vegas, H. H. Tam, A. R. Bader, J. Li, E. Langan, J. Wyckoff, W. S. Loo, S. Jhunjhunwala, A. Chiu, S. Siebert, K. Tang, J. Hollister-Lock, S. Aresta-Dasilva, M. Bochenek, J. Mendoza-Elias, Y. Wang, M. Qi, D. M. Lavin, M. Chen, N. Dholakia, R. Thakrar, I. Lacić, G. C. Weir, J. Oberholzer, D. L. Greiner, R. Langer, D. G. Anderson, *Nat. Mater.* 2015, 14, 643.
- [140] E. M. Sussman, M. C. Halpin, J. Muster, R. T. Moon, B. D. Ratner, *Ann. Biomed. Eng.* 2014, 42, 1508.
- [141] M. C. Phipps, W. C. Clem, J. M. Grunda, G. A. Clines, S. L. Bellis, *Biomaterials* 2012, 33, 524.
- [142] W. F. Liu, *Cardiovasc. Res.* 2012, 95, 215.
- [143] T. U. Luu, S. C. Gott, B. W. K. Woo, M. P. Rao, W. F. Liu, *ACS Appl. Mater. Interfaces* 2015, 7, 28665.
- [144] S. Dupont, L. Morsut, M. Aragona, E. Enzo, S. Giulitti, M. Cordenonsi, F. Zanconato, J. Le Digabel, M. Forcato, S. Bicciato, N. Elvassore, S. Piccolo, *Nature* 2011, 474, 179.
- [145] F. Calvo, N. Ege, A. Grande-Garcia, S. Hooper, R. P. Jenkins, S. I. Chaudhry, K. Harrington, P. Williamson, E. Moeendarbary, G. Charras, E. Sahai, *Nat. Cell Biol* 2013, 15, 637.
- [146] V. W. Wong, K. C. Rustad, S. Akaishi, M. Sorkin, J. P. Glotzbach, M. Januszyk, E. R. Nelson, K. Levi, J. Paterno, I. N. Vial, A. a. Kuang, M. T. Longaker, G. C. Gurtner, *Nat. Med.* 2011, 18, 148.
- [147] H. Wang, S. M. Haeger, A. M. Kloxin, L. A. Leinwand, K. S. Anseth, *PLoS One* 2012, 7, e39969.
- [148] K. Sadtler, K. Estrellas, B. W. Allen, M. T. Wolf, H. Fan, A. J. Tam, C. H. Patel, B. S. Lubner, H. Wang, K. R. Wagner, J. D. Powell, F. Housseau, D. M. Pardoll, J. H. Elisseeff, *Biomaterials* 2016, 352, 366.
- [149] C. L. Dearth, P. F. Slivka, S. A. Stewart, T. J. Keane, J. K. Tay, R. Londono, Q. Goh, F. X. Pizza, S. F. Badylak, *Acta Biomater.* 2015, 31, 50.
- [150] C. Yang, M. W. Tibbitt, L. Basta, K. S. Anseth, *Nat. Mater.* 2014, 13, 645.
- [151] C. M. Kirschner, K. S. Anseth, *Acta Mater.* 2013, 61, 931. [152] A. M. Kloxin, A. M. Kasko, C. N. Salinas, K. S. Anseth, *Science* 2009, 324, 59.
- [153] S. A. Park, S. H. Lee, W. D. Kim, *Bioprocess Biosyst. Eng.* 2011, 34, 505.
- [154] L. Vi, G. S. Baht, H. Whetstone, A. Ng, Q. Wei, R. Poon, S. Mylvaganam, M. Grynblas, B. A. Alman, *J. Bone Miner. Res.* 2015, 30, 1090.

- [155] B. DUAN, L. A. Hockaday, S. Das, C. Y. Xu, J. T. Butcher, *Tissue Eng. Part C Methods* 2015, 21, 150127064141008.
- [156] L. Bao, L. He, J. Chen, Z. Wu, J. Liao, L. Rao, J. Ren, H. Li, H. Zhu, L. Qian, Y. Gu, H. Dai, X. Xu, J. Zhou, W. Wang, C. Cui, L. Xiao, *Nat. Publ. Gr.* 2011, 21, 600.
- [157] F. Yang, C. G. Williams, D. A. Wang, H. Lee, P. N. Manson, J. Elisseeff, *Biomaterials* 2005, 26, 5991.
- [158] B. T. Corona, X. Wu, C. L. Ward, J. S. McDaniel, C. R. Rathbone, T. J. Walters, *Biomaterials* 2013, 34, 3324.
- [159] M. T. Wolf, K. A. Daly, J. E. Reing, S. F. Badylak, *Biomaterials* 2012, 33, 2916.
- [160] Y. M. Ju, A. Atala, J. J. Yoo, S. J. Lee, *Acta Biomater.* 2014, 10, 4332.
- [161] M. Fahrenholtz, H. Liu, D. Kearney, L. Wadhwa, C. Fraser, K. Grande-Allen, *J. Cardiovasc. Dev. Dis.* 2014, 1, 146.
- [162] A. Wessels, M. J. B. van den Hoff, R. F. Adamo, A. L. Phelps, M. M. Lockhart, K. Sauls, L. E. Briggs, R. A. Norris, B. van Wijk, J. M. Perez-Pomares, R. W. Dettman, J. B. E. Burch, *Dev. Biol.* 2012, 366, 111.
- [163] C. Y. Chang, A. T. Chan, P. A. Armstrong, H. C. Luo, T. Higuchi, I. A. Strehin, S. Vakrou, X. Lin, S. N. Brown, B. O'Rourke, T. P. Abraham, R. L. Wahl, C. J. Steenbergen, J. H. Elisseeff, M. R. Abraham, *Biomaterials* 2012, 33, 8026.
- [164] L. Qian, Y. Huang, C. I. Spencer, A. Foley, V. Vedantham, L. Liu, S. J. Conway, J.-D. Fu, D. Srivastava, *Nature* 2012, 485, 593.
- [165] Q. Peng, S. Zhuo, P. T. C. So, H. Yu, *Appl. Phys. Lett.* 2015, 106, 083701.
- [166] K. R. Karlmark, R. Weiskirchen, H. W. Zimmermann, N. Gassler, F. Ginhoux, C. Weber, M. Merad, T. Luedde, C. Trautwein, F. Tacke, *Hepatology* 2009, 50, 261.
- [167] J. S. Duffield, S. J. Forbes, C. M. Constandinou, S. Clay, M. Partolina, S. Vuthoori, S. Wu, R. Lang, J. P. Iredale, *J. Clin. Invest.* 2005, 115, 56.
- [168] J. T. Pesce, T. R. Ramalingam, M. M. Mentink-Kane, M. S. Wilson, K. C. El Kasmi, A. M. Smith, R. W. Thompson, A. W. Cheever, P. J. Murray, T. a. Wynn, *PLoS Pathog.* 2009, 5, e1000371.
- [169] L. Gailhouste, Y. Le Grand, C. Odin, D. Guyader, B. Turlin, F. Ezan, Y. Désille, T. Guilbert, A. Bessard, C. Frémin, N. Theret, G. Baffet, Y. Le Grand, *J. Hepatol.* 2010, 52, 398.
- [170] G. C. Gurtner, S. Werner, Y. Barrandon, M. T. Longaker, *Nature* 2008, 453, 314.
- [171] B. M. Delavary, W. M. van der Veer, M. van Egmond, F. B. Niessen, R. H. J. Beelen, *Immunobiology* 2011, 216, 753.

- [172] R. Kalluri, E. G. Neilson, *J. Clin. Invest.* 2003, 112, 1776.
- [173] R. a. Underwood, M. L. Usui, G. Zhao, K. D. Hauch, M. M. Takeno, B. D. Ratner, A. J. Marshall, X. Shi, J. E. Olerud, P. Fleckman, *J. Biomed. Mater. Res. - Part A* 2011, 98, 499.
- [174] B. J. Farrell, B. I. Prilutsky, J. M. Ritter, S. Kelley, K. Popat, M. Pitkin, *J. Biomed. Mater. Res. - Part A* 2014, 102, 1305.
- [175] J. H. Jeong, Y. Liang, M. Jang, C. Cha, C. Chu, H. Lee, W. Jung, J. W. Kim, S. a. Boppart, H. Kong, *Tissue Eng. Part A* 2013, 19, 1275.
- [176] E. M. Hetrick, H. L. Prichard, B. Klitzman, M. H. Schoenfisch, 2009, 28, 4571.
- [177] S. P. Nichols, A. Koh, N. L. Brown, M. B. Rose, B. Sun, D. L. Slomberg, D. A. Riccio, B. Klitzman, M. H. Schoenfisch, *Bio- materials* 2012, 33, 6305.
- [178] J. Necas, L. Bartosikova, P. Brauner, J. Kolar, *Vet. Med. (Praha)*. 2008, 53, 397.
- [179] D. A. Hollander, C. Soranzo, S. Falk, J. Windolf, *J. Trauma* 2001, 50, 1125.
- [180] W. F. Liu, M. Ma, K. M. Bratlie, T. T. Dang, R. Langer, D. G. Anderson, *Biomaterials* 2011, 32, 1796.
- [181] M. Ma, W. F. Liu, P. S. Hill, K. M. Bratlie, D. J. Siegwart, J. Chin, M. Park, J. Guerreiro, D. G. Anderson, *Adv. Mater.* 2011, 23, H189.
- [182] K. M. Bratlie, T. T. Dang, S. Lyle, M. Nahrendorf, R. Weissleder, R. Langer, D. G. Anderson, *PLoS One* 2010, 5, e10032.
- [183] H. C. Bygd, K. D. Forsmark, K. M. Bratlie, *Biomaterials* 2015, 56, 187.
- [184] Y. Zhang, M. L. Akins, K. Murari, J. Xi, M.-J. Li, K. Luby-Phelps, M. Mahendroo, X. Li, *Proc. Natl. Acad. Sci. USA* 2012, 109, 12878.
- [185] H. Bao, A. Boussioutas, R. Jeremy, S. Russell, M. Gu, *Opt. Express* 2010, 18, 1255.
- [186] J. L. Balestrini, S. Chaudhry, V. Sarrazy, A. Koehler, B. Hinz, *Integr. Biol.* 2012, 4, 410.
- [187] C. Lee, J. Shin, J. S. Lee, E. Byun, J. H. Ryu, S. H. Um, D.-I. Kim, H. Lee, S.-W. Cho, *Biomacromolecules* 2013, 14, 2004.
- [188] C. A. McCaslin, D. N. Petrusca, C. Poirier, K. A. Serban, G. G. Anderson, I. Petrache, *J. Cyst. Fibros.* 2015, 14, 70.
- [189] K. B. Fonseca, D. B. Gomes, K. Lee, S. G. Santos, A. Sousa, E. A. Silva, D. J. Mooney, P. L. Granja, C. C. Barrias, *Biomacro- molecules* 2014, 15, 380.
- [190] S. Jain, M. Amiji, *Biomacromolecules* 2012, 13, 1074.
- [191] S. Jain, T.-H. Tran, M. Amiji, *Biomaterials* 2015, 61, 162.

- [192] S. Carnesecchi, C. Deffert, Y. Donati, O. Basset, B. Hinz, O. Preynat-Seauve, C. Guichard, J. L. Arbiser, B. Banfi, J.-C. Pache, C. Barazzzone-Argiroffo, K.-H. Krause, *Antioxid. Redox Signal.* 2011, 15, 607.
- [193] K. Bartus, N. D. James, A. Didangelos, K. D. Bosch, J. Verhaagen, R. J. Yanez-Munoz, J. H. Rogers, B. L. Schneider, E. M. Muir, E. J. Bradbury, *J. Neurosci.* 2014, 34, 4822.
- [194] A. Didangelos, M. Iberl, E. Vinsland, K. Bartus, E. J. Bradbury, *J. Neurosci.* 2014, 34, 16424.
- [195] P. Korn, M. C. Schulz, V. Hintze, U. Range, R. Mai, U. Eckelt, M. Schnabelrauch, S. Müller, J. Becher, D. Scharnweber, B. Stadlinger, *J. Biomed. Mater. Res. - Part A* 2014, 102, 2334.
- [196] G. K. Tan, Y. Tabata, *Acta Biomater.* 2014, 10, 2684. [197] S. M. Van Putten, D. T. A. Ploeger, E. R. Popa, R. A. Bank, *Acta Bio- mater.* 2013, 9, 6502.
- [198] F. Wei, P. F. Slivka, C. L. Dearth, S. F. Badylak, *Biomaterials* 2015, 46, 131.
- [199] B. M. Sicari, J. L. Dziki, B. F. Siu, C. J. Medberry, C. L. Dearth, S. F. Badylak, *Biomaterials* 2014, 35, 8605.
- [200] B. N. Brown, J. E. Valentin, A. M. Stewart-akers, G. P. McCabe, S. F. Badylak, *Biomaterials* 2009, 30, 1482.
- [201] B. V. Fearing, M. E. Van Dyke, *Acta Biomater.* 2014, 10, 3136.
- [202] M. Borrelli, N. Joepen, S. Reichl, D. Finis, M. Schoppe, G. Geerling, S. Schrader, *Biomaterials* 2015, 42, 112.
- [203] L. A. Pace, J. F. Plate, T. L. Smith, M. E. Van Dyke, *Biomaterials* 2013, 34, 5907.
- [204] J. M. Tse, G. Cheng, J. A. Tyrrell, S. A. Wilcox-Adelman, Y. Boucher, R. K. Jain, L. L. Munn, *Proc. Natl. Acad. Sci. USA* 2012, 109, 911

CHAPTER 3

MULTIMODAL IMAGING OF HARMONOPHORES AND APPLICATION OF HIGH CONTENT IMAGING FOR EARLY CANCER DETECTION

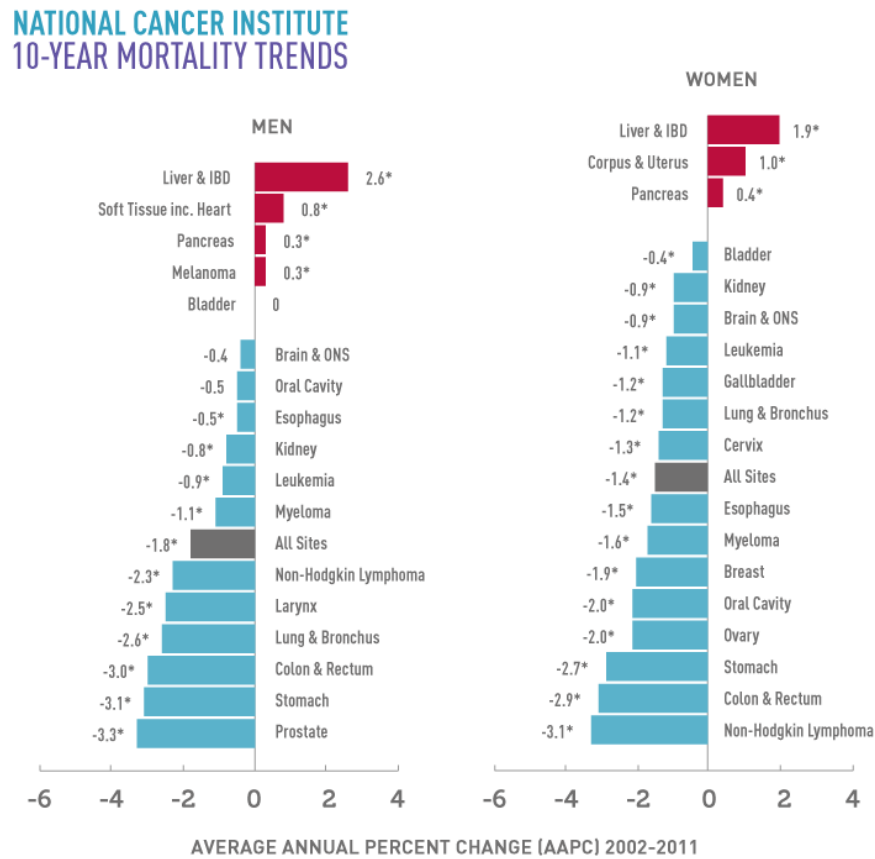
Modified from a manuscript published in *Materials Discovery*, 1, 10-20 (2015)

The importance of cancer detection has grown exponentially over the past few years, as medical costs and our demand for better quality of living rise. Multimodal imaging techniques aim to improve the efficiency of current diagnostic methods and provide greater insight into the mechanism of tumor metastasis. Second harmonic generation (SHG) microscopy is one such non-destructive imaging technique available to researchers for detecting the changes in the morphology of chiral molecules such as collagen, which are selectively imaged by this technique. Researchers aim to understand the role played by changes in collagen morphology in tumor development, by combining SHG with other non-linear optics instruments. Different cancer diagnoses have been shown to be detected efficiently by these methods, with higher clarity than the standard protocols available. This is a significant improvement, especially in the case of aggressive, invasive tumor types such as basal cell carcinoma (BCC) and invasive ductal carcinoma (IDC). Analyzing the data produced by such multimodal imaging methods is currently a nascent field. The aim of this review is to provide an overview of the analysis techniques currently used in this field of high content imaging and establish concurrence of methods to further improve the understanding and efficiency of cancer detection.

3.1 Introduction

The latest reports from the National Cancer Initiative show that Cancer has grown to become the 2nd largest cause for death in the United States, behind only heart disease. Beyond the emotional trauma suffered by families across countries worldwide, cancer also has a very high

economic impact on countries all over the world. [1, 2] A recent study by the Agency for Healthcare Research and Quality estimated that \$88.7 billion were spent just over 4 years back in 2011. With the rising costs, and the fragile state of the economy, cancer has progressed in importance and there remains a need for immediate action, in spite of mortality trends suggesting that the situation has improved, as can be seen in Figure 3.1.



* AAPC is significantly different from zero (p < .05).

www.cancer.gov

Source: Annual Report to the Nation on the Status of Cancer 1975-2011

Figure 3.1: Latest cancer trends report indicating the progress of cancer research in different types of cancer and their mortalities in men and women [1]

Multimodal imaging has sought to provide early diagnosis and a better understanding for several of the fast-acting types of cancers that are becoming a common fixture of the health-care

sector. Techniques such as second harmonic generation (SHG) microscopy have provided researchers a hybrid imaging technique which can offer biochemical insights into clinical samples, and yield information on a multitude of tumor diagnoses. SHG imaging uses two incoming photons having the same wavelength, scatter after interacting with a chiral molecule, and produce one photon of exactly half the incoming wavelength. The nature, intensity of this scattering phenomena can provide information into the internal structure of the tissues. [3, 4]

SHG imaging has been shown to have many advantages over traditional immunohistochemistry staining techniques or fluorescence microscopy. It is a non-linear optical approach toward imaging tissues both *in-situ* as well as being a part of endomicroscopy approaches [5, 6, 7] The SHG imaging approach is a non-staining, energy conservative technique. This is most suitable for non-destructive imaging of tissues, while simultaneously allowing for the internal visualization of the samples be clear. The most important prerequisite condition for SHG-active sites within the tissues is for there to be a non-centrosymmetric salient component within, which are selectively detected by the incident beam. Common examples of SHG active molecules, known as harmonophores are collagen types I and III, myosin (when present within acto-myosin complexes), and cholesterol crystals (ChC) which are chiral in nature. [8, 9, 10]

Studies conducted by Su *et al.* [11] have shown that extracellular matrix (ECM) alterations are a very important indicator for different kinds of tumor growth within corneal, colonic, cardiac, breast, and ovarian tissues. Intensity based SHG imaging can yield clear images of the modifications of the tissue structure, by elucidating collagen orientation changes in the ECM, as can be seen in Figure 3.2, which is an image taken of a sub-dermal tumor in a mouse, from the studies conducted by Brown. [12]

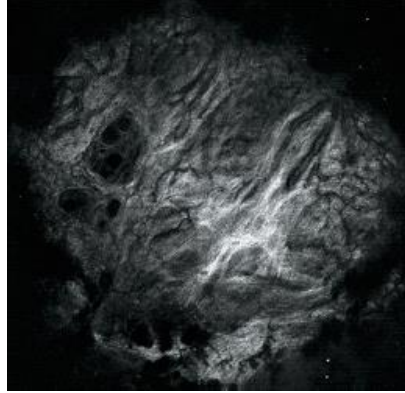


Figure 3.2: SHG image of a melanoma growth in sub-dermal tissue of a mouse. Image width was 6.6 mm. [12]

The most common challenge in methods such as SHG are that there is a complex amount of data generated for each tissue imaging, based on the fact that the harmonophores show varying intensity with polarization of the incident beams. These intensities, measurements of the forward, backward-scattering beams, and the variations of the angular pitch of the harmonophores necessitate a need for detailed analysis of the data generated. A significant concurrence needs to be achieved for the understanding of the results generated by this field of high content imaging.

2.2 State of the Art

It is interesting to note that the discovery of SHG as an imaging tool was by accident, and a consequence of experiments carried out to know more about piezoelectricity. Two young researchers Fukada and Yasuda, who were working on a piece of Achilles tendon observed that there observed to a macroscopic polarity to the sample. This polarity was hypothesized to be a consequence of charged repeating groups in crystal form, which was further confirmed by Lang a few years later to also show pyroelectric properties. [13] Together these created the breakthrough which allowed for biological molecules having chiral symmetry be visualized in a non-linear manner, without compromising on the structural or chemical integrity of the samples. One of the first examples shown to be easily differentiated on the basis of SHG imaging were rat tail tendons

and trachea cartilage, as they both contain collagen, but of different types [11]. These studies were gradually improved on to image differences in collagen morphology in mouse ovary, skin and bone samples [14].

It was observed that combining SHG with techniques such as two photon excitation fluorescence (TPEF) microscopy or coherent anti-Stokes Raman spectroscopy (CARS) can help provide biochemical specificity to the tissues being imaged. With the help of additional, non-destructive non-linear optics, further information about cancers such as basal cell carcinoma (BCC) were readily available, as shown by Vogler's group in 2010 [15]. The presence of fat reservoirs, collagen modifications, and fluorescing proteins was visualized by this multimodal imaging technique (as seen in Figure 2.3), providing new insight into BCC, which is an extremely fast acting cancer with a high mortality rate, as observed by Jamal's study in 2008 [16]. These studies further made the case for high content imaging, to be popularized all over the world. [17, 18, 19]

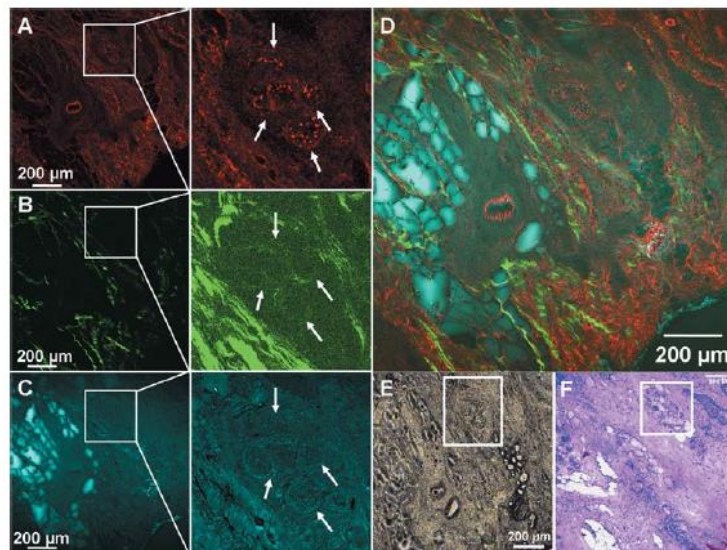


Figure 3.3: (A) TPEF highlighting the fluorescing proteins in the tissue, (B) SHG indicating the collagen organization around the carcinoma, (C) CARS showing the fat reservoirs around the carcinoma, (D) Hybrid image of all three techniques, (E) Brightfield image of the carcinoma, (F) H&E staining of the tissue to provide perspective, with insets highlighted for imaging [15]

As demonstrated for BCC, dermal tissues were one of the first to get imaged using SHG due to the ease of access and availability of samples [20, 21]. Chen and his group showed SHG and TPEF as a viable hybrid imaging tool [22], by simultaneously imaging collagen and elastin respectively. There was a clear difference observed on how the scars and normal dermis showed different levels of elastin and collagen presence.

Cicchi *et al.* demonstrated in 2010, how structurally different hypertrophic scarring in keloids is from healthy dermis at the micron scale [23, 9]. It was observed that normal dermis contained a randomly mixed presence of collagen and elastin, whereas keloids showed well aligned boundaries of collagen with very minimal presence of elastin. As keloids are present only in humans [22, 24, 25], and the nature of keloids have been shown to be influenced by the melanin content, studies such as these hold great promise in the fields of tissue engineering. These studies were further substantiated by independently analyzing the orientation of the collagen fibers formed, through fast Fourier transform (FFT) analysis. It was clear the isotropic nature of collagen fibers in keloids matched well with the visual observations made previously by Su *et al.* in 2011. [21, 23, 25, 26, 27]

The success of SHG imaging spurred interest in the early detection of breast cancer. In order to understand the significant difference between the clarity of tissue sections, Ambekar compared the hematoxylin & eosin stained (H&E) sections with the collagen mapped using SHG [28]. The sensitivity of SHG in detecting changes in collagen morphology has proved to be a game changer for this aspect of breast cancer detection at an early stage, as shown in Figure 2.4. Several groups such as Brown, Burke, Conklin, Ajeti have defined aspects of breast cancer types based on SHG [29, 20, 31, 32]

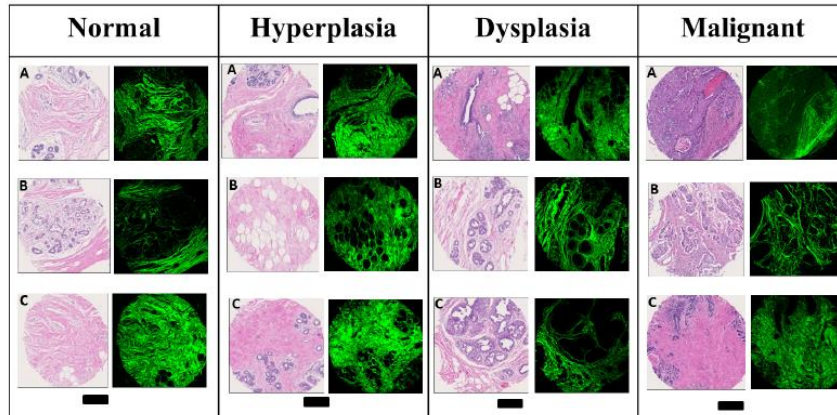


Figure 3.4: H&E and SHG imaging comparison for grades of breast cancer tissues [29]

The process of ECM modifications in cartilage and mammary tissues was studied in depth by Burke and co-workers in 2015 [29, 30]. In their studies they aimed to provide visual confirmation of the hypothesis put forward by Conklin in 2011 [31] regarding how collagen fibers re-align themselves from a randomly ordered state to that of structured form, as evidenced by their imaging of mammary tumors which is shown in Figure 2.5. Conklin defined his theory on tumor associated collagen signatures (TACs) on this basis, which we shall delve into later during this review. Here too, SHG imaging agrees with the standard pathology of improve the early diagnosis, detection of breast cancer.

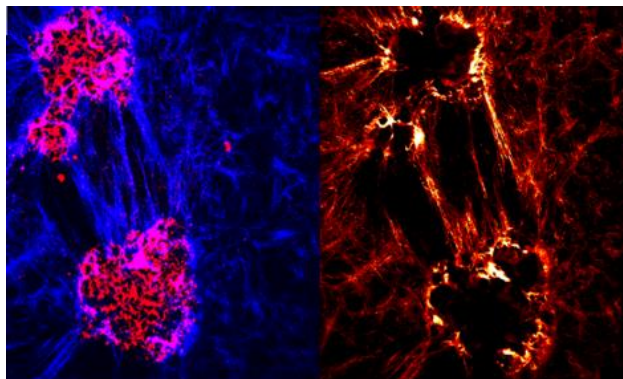


Figure 3.5: (left, red) Collagen organization at the onset of breast cancer, (left, blue) collagen alignment three days after onset. Changes in the forward and backward scattering of SHG signal. [30]

Another salient example of the application of SHG in cancer detection was towards the diagnosis of liver fibrosis. By combining TPEF with SHG, clear SHG-fibrosis indices were established, which were confirmed by the Metavir scoring of fibrosis [33, 34]. This correlation of fibrosis indices, developed by Gailhouse in 2011[35] is further vindication of the multimodal imaging process, using SHG and TPEF as a hybrid imaging platform, which also elucidates the difference in the mechanisms between the two methods [36].

3.3. Analysis Techniques

It is essential to understand that advanced imaging techniques such as SHG, two photon microscopy (TPM) and CARS are highly customizable. It is often up to the researcher to determine what data to extract from the imaging and how best to represent it in a coherent and effective way. These multimodal imaging techniques can produce vast amounts of data for a single image, and we will summarize the most common analysis techniques used by researchers all over the world. [37, 38, 39]

The growing requirement for quantitative SHG imaging resulted in the development of techniques which are used primarily for cancer detection and classification studies. We have given below some of the salient analysis methods observed:

3.3.1. Susceptibility Measurements (χ ratios)

The SHG signal obtained for any collagen containing sample is characterized by the second order nonlinear susceptibility tensor $\chi^{(2)}$. The relationship between the susceptibility, the Electrical field applied (E) and the polarization (P) is defined as:

$$P_{ijk} = \chi_{ijk} E_j E_k \quad (1)$$

For small molecules, it is understood that the main contributors to the susceptibility value are the C=O and the N-H groups present in the amide bonds. [40] Hence, this tensor is indicative of the collagen directionality within the imaged domains. For ease of analysis as well as approximation based on the point sized light source and the sample thickness not exceeding 5 μm , we consider the samples to observe cylindrical symmetry and follow the Kleinmann rules. The relation thus shall exhibit only two independent components: χ_{XXX} and $\chi_{XYX} = \chi_{XZZ} = \chi_{YXY} = \chi_{ZYZ} = \chi_{YYX} = \chi_{ZXX}$ where X is the direction of the collagen fibrils [4, 27]

An incident electric field E_0 then induces the following second harmonic wave in the fibril frame XYZ:

$$E_X^{2\omega} \propto [\chi_{XXX} \cos^2(\alpha - \varphi) + \chi_{XXX} \sin^2(\alpha - \varphi)] E_0^2 \quad (2a)$$

$$E_Y^{2\omega} \propto [\chi_{XYX} \sin 2(\alpha - \varphi)] E_0^2 \quad (2b)$$

In the above equations, α and φ stand for the laser excitation polarization angle and the fibril orientation angle, respectively, with respect to a fixed direction in the laboratory frame, usually taken as the X axis which is considered here to be the collagen fibril axis. This is valid because the lamellae within the collagen shall be parallel to the axis, and hence within plane of the electrical field E_0 . The total polarized collagen intensity is then given by:

$$I^{2\omega} = K (|\rho \cos^2(\alpha - \varphi) + \sin^2(\alpha - \varphi)|^2 + |\sin 2(\alpha - \varphi)|^2) \quad (3)$$

In the above equation, K is a constant merging the squared incident intensity and setup geometrical parameters. Two quantitative parameters appear in this expression: (i) the angle difference of α and φ , of the laser excitation polarization to the collagen fibrils axis within lamellar domains; (ii) the ratio ρ , which reflects the anisotropy of the nonlinear response of these lamellar domains and is calculated as $\rho = \chi_{XXX}/\chi_{XYX}$. This approach to calculate the polarization anisotropy

(p) and susceptibility (P) is valid for both forward scattered SHG as well as backward scattered SHG signals. [22]

In some cases, where the methylene contribution is considered separately, some of the above assumptions don't hold true for all the tensor elements. Some cases studies and theoretical models show the polarizability of the sample denoted by β in such cases. Resulting in the system getting defined by three related elements:

$$\chi_{XXX} = N^{(p)}\beta^{(p)} \cos^3 \theta^{(p)} + N^{(m)}\beta^{(m)} \cos \theta^{(m)} \quad (4a)$$

$$\chi_{XYY} = \frac{1}{2} N^{(p)}\beta^{(p)} \cos \theta^{(p)} \sin^2 \theta^{(p)} \quad (4b)$$

$$\chi_{YYX} = \frac{1}{2} N^{(p)}\beta^{(p)} \cos \theta^{(p)} \sin^2 \theta^{(p)} + N^{(m)}\beta^{(m)} \cos \theta^{(m)} \quad (4c)$$

In these above equations, $N^{(p)}$ and $N^{(m)}$ refer to the number of peptide and methylene groups in the system respectively. And the $\theta^{(p)}$ represents the pitch angle to which the collagen is oriented, and accordingly determined as per the following equations:

$$a = \chi_{XXX}/\chi_{XYY} \text{ and } b = \chi_{YYX}/\chi_{XYY}$$

$$\text{And, } \tan^2 \theta^{(p)} = \frac{2}{a - b + 1} \quad (5)$$

Studies conducted by Jung Su [11], on cartilage imaging relied on using these equations and susceptibility ratios in order to characterize differences between collagen type I and type II in rats, as shown in Figure 2.6 [27, 35, 41].

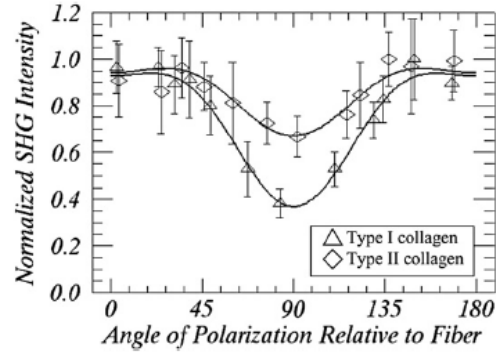


Figure 3.6: Normalized SHG intensity observed relative to the polarization angle [11]

Jung Su *et al.*, also demonstrated the clear change in intensity observed with respect to change in polarization. They highlighted one of the first examples of collagen morphologies being different in tendons and cartilage tissues, with the change in morphology from wavy, random signals to well aligned fibers.

3.3.2. Polarization Resolved SHG imaging

As the intensity of the SHG signal obtained for collagen presence is dependent on not just the concentration, but also the degree of ordering of the fibers, spacing, and the overall anisotropy of the collagen in the samples. This approach can be taken up in multiple applications, such as on the basis of the polarization anisotropy, or as separate measurements for each incident polarization angle. On the basis of polarization anisotropy, the images intensity was normalized over the following equation [42]:

$$PA = \frac{I_{\parallel} - I_{\perp}}{I_{\parallel} + I_{\perp}} \quad (6)$$

Here, the I_{\parallel} values were for those with horizontal polarization and I_{\perp} values for the vertically polarized imaging. PA values of 0 signify a high order of stochasticity, and those tending towards 1 or -1 are more uniaxial in orientation.

Polarization resolved imaging studies were conducted by the group of Ambekar *et al.*, to observe the differences in the intensity [28] for different incident polarization angles (from 0 to 180°), in various stages of breast cancer tissues. [5, 8, 27] This differentiation based on polarization was further elucidated by mapping the anisotropy of each of the 4 samples.

3.3.3. Fast Fourier Transform (FFT) Analysis

The images obtained by SHG microscopy can be analyzed using a FFT based model where each image is divided into user-defined regions of interest (ROI), according to which each part of the image is fit through an elliptical model [43]. The major and minor axis of this ellipse define the orientation of the collagen fiber within the ROI. Optimized ROIs are used in order to define the best collagen resolution and obtain an orientation map. The shapes of the collagen fibers are first approximated to that of an ellipse, and the FFT analysis further estimates the centroid of the ROI and calculates the distance of each point in the fiber from the centroid in order to obtain an overall orientation angle using radial vectors which sweep over 360° from the x-axis. [44] Hsin-Yuan Tan *et al.* [43] analyzed porcine cornea samples using FFT and obtained clearly demarcated orientation lines for different regions of the sample in Figure 3.7.

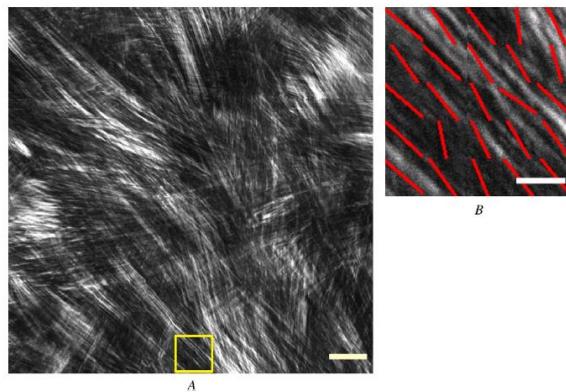


Figure 3.7: (A) Large area of porcine cornea (scale: 40 μm); (B): Collagen orientation lines mapped for the yellow inset box based on FFT analysis (scale: 10 μm) [43]

Akilbekova *et al.* used the FFT analysis in order to obtain resolved orientations of the collagen in the samples [45]. They were able to obtain shape description values for each of the samples, showing the different overall distribution of the collagen, differentiating between systems where the collagen was well-aligned to those which showed a random distribution [8, 31]

3.3.4. F/B Ratio Measurements

Another analysis technique used the nature of SHG measurements having a forward and backward scattering component, hitherto referred as F-SHG and B-SHG respectively. It has been understood that the F-SHG imaging is extremely sensitive to the presence of large collagen bundles which are of the order of the magnitude of the incoming SHG signal, whereas the B-SHG is sensitive to the septa and interstices created by randomly distributed small deposits of collagen, where the forward signal gets collected, but the backward signal is propagated stronger. The ratio of these two area percentages or intensities observed in the samples is often denoted as the F/B ratio, and taken as measure of the evolution of collagen alterations in the sample [46]

For each of the sample images, a stack is created, where a threshold is applied such that the signal to noise ratio is optimized for the individual F-SHG and B-SHG measurements. This threshold is used to create a mask, where all the non-collagen areas are automatically allotted a null value, with the collagen areas having value of 1. This sort of binary differentiation of the images brings the signal to the highest clarity. Depending on the types of cancer or tissue studied, the area percentage or the average intensity values are measured for each image in the F-SHG stack and divided by the corresponding images for the B-SHG one [47]

Groups such as Latour *et al.*, [41] took additional care to ensure the validity of such measurements by polarization resolving F/B ratio studies. As collagen is known to be anisotropic,

they were able to obtain even higher resolutions of the stromae observed in cornea samples, this analysis was combined with the direction maps created for the collagen alignment.

Another method of representing F/B ratio data is through statistically calculating the difference in the ratios, observed for different types of healthy and cancer tissues [46]. Many different types of non-parametric testing such as the Newman-Keuls test, help calculate the standard deviation and variances without compromising the integrity of the data. Kottman *et al.*, recently published their work on understanding the alteration in the ECM [48] as observed in different lung cancer tissues. Here, they studied an early detection strategy to differentiate between a highly invasive cryptogenic organizing pneumonia (COP) from usual interstitial pneumonia (UIP) and healthy tissue. UIP is characterized usually by decrease in lung volume and non-productive cough and is a common yet highly serious medical condition amongst smokers. UIP or idiopathic pulmonary fibrosis (IFP) patients often need to undergo lung transplantation after diagnosis. On the other hand, COP can be characterized by the presence of granular buds in the alveoli and bronchioles. Most cases of COP are cured within three months of treatment with corticosteroids unlike for UIP, where such treatments are largely ineffective [49, 50]. In cases such as these, an early detection method such as SHG F/B ratio analysis can potentially avoid fatalities.

3.3.5. Grey Local Correlation Matrix (GLCM)

GLCM is a statistical method to analyze texture in greyscale images [51]. It analyzes each ROI, with relation to its neighboring areas. This method can be set to analyze the images even on a pixel by pixel basis, by changing the offset, accounting for different channels within the image.

It can be classified largely on the basis of three applications:

- a. On the basis of weighted means which are multiplied to the GLCM values depending on distance from the main diagonal:

- i. For analyzing dissimilarity (D) where the weights multiplied to the GLCM values increase as you move away from the diagonal

$$\sum_{i,j=0}^{N-1} P_{i,j} |i - j| \quad (7)$$

- ii. For analyzing contrast (C) where the weights multiplied to the GLCM values decrease as you move away from the diagonal, also known as sum of squares variance.

$$\sum_{i,j=0}^{N-1} P_{i,j} (i - j)^2 \quad (8)$$

- iii. For analyzing homogeneity (H) where the weights multiplied to the GLCM values decrease exponentially as you move away from the diagonal. This is most applicable to images having a high contrast range.

$$\sum_{i,j=0}^{N-1} \frac{P_{i,j}}{1+(i-j)^2} \quad (9)$$

- b. On the basis of spatial matrix values, complete measurements based on orderliness. Similar to contrast wise measurements, Orderliness measures are calculated with GLCM weighted averages on the basis that:

- iv. Weights that increase with commonness shall increase with orderliness
- v. Weights that decrease with commonness shall increase with disorder

The three orderliness measures defined under the GLCM theory are:

- ASM or Energy mean which can be calculated by the following equation typically for cases where the matrix is highly orderly.

$$\sum_{i,j=0}^{N-1} P_{i,j}^2$$

- Max Probability (MAX): Simply records the highest value of the matrix in the center

- Entropy measurement based completely on the disorderliness of the system, and calculated by:

$$\sum_{i,j=0}^{N-1} P_{i,j} (-\ln P_{i,j})$$

- c. On the basis of statistics, calculating the GLCM mean, median and variance

The correlation (R) of each pixel to its neighboring ones are calculated as:

In these equations, the expectation values are denoted by μ and the standard deviations are denoted by σ .

$$R = \sum_{i,j} \frac{(i - \mu_i)(j - \mu_j) p_{i,j}}{\sigma_i \sigma_j} \quad (10a)$$

$$\mu_i = \sum_{i=1}^N i \cdot p_{i,j} ; \mu_j = \sum_{i=1}^N i \cdot p_{i,j} \quad (10b)$$

$$\sigma_i = \sqrt{\frac{1}{N-1} \cdot \sum_{i=1}^N i \cdot p_{i,j}} ; \sigma_j = \sqrt{\frac{1}{N-1} \cdot \sum_{i=1}^N j \cdot p_{i,j}} \quad (10c)$$

By modifying the offset values and studying the correlation, more information about the texture can be measured, as the offset directly influences the distance between each neighboring ROI taken into consideration. The group of Cicchi *et al.* [23] did important work on imaging and understanding the structural differences between keloids (K) and normal human dermis (HD) using the GLCM data analysis techniques. On the basis of calculating the homogeneity, correlation, and energy for different ROI values, they obtained a clear trend to tell apart normal dermis samples from excessively scarred keloid tissue.

3.3.6. Second Harmonic to Autofluorescence Aging Index of Dermis (SAAID)

In the field of dermatology, it became necessary to be able to image collagen for a variety of applications. Tissue engineering [9, 23, 42] also benefited from the studies conducted on quantifying the collagen density, especially when it could give more information on the proportions of elastin present alongside it. Such multimodal imaging studies were carried out by

researchers all over the world, where SHG was combined with any autofluorescence imaging technique which targeted the elastin present in the tissue samples.

SAAID has been devised as a measure of the collagen fiber intensity based on the hybrid TPEF imaging done along with SHG. The combined intensity values are used to calculate SAAID as per the following formula:

$$SAAID = \frac{I_{SHG} - I_{TPEF}}{I_{SHG} + I_{TPEF}} \quad (11)$$

It can be used as a measure of the collagen to elastin ratio in the dermal samples, as the elastin can be tagged with TPEF-active fluorescent markers, and the SHG will specifically only show collagen density. The SAAID is a very useful tool hence to determine the difference between normal skin, keloids and normal scars. As humans are the only mammals who exhibit the presence of keloids in response to physical trauma or at times surgery [21, 52], this analysis technique helps evaluate the tendency of certain tissues to develop to the keloids stage, where the elastin is significantly higher than for normal skin or scars.

Using these notations, the SAAID value hence approaches -1 when the collagen present in the sample is completely replaced by the elastin. In 2014, the group of Cicchi and Pavone [42], used the SAAID values to evaluate the effectiveness of laser ablative treatment in removing scarred tissue from normal dermis. In this study, they evaluated over three age groups of patients. Group I consisted of those less than 35 years of age, Group 2 had age between 35 and 60, whereas the last group had age above 60. Their images and results indicated clear differences in the amounts of collagen and elastin present, after multimodal imaging pre and post laser treatment [9, 23]

The results showed clearly that the SAAID values for normal skin was close to -1 due to the high presence of elastin, whereas the scores for keloids and scar tissues were closed to 1 owing to the higher concentration of collagen in the samples. The SAAID value measurements are often

accompanied in every study by two-sample parametric test, to be sure of statistical differences observed for the different sample types and also evaluate the standard deviation and means.

3.3.7. Depth Dependent Decay Measurements

In order for techniques such as SHG and TPEF to be comparably applicable to imaging different kinds of tumors, research groups devised the depth dependent decay (DDD) studies analysis method, which helps quantify the SHG signal differing from the change in the focal plane. It was observed that the signal intensity would exponentially increase with the increase in depth, and such a system could be easily represented by a first order equation where ‘x’ represented the imaging depth, and ‘y’ represented the SHG collagen intensity. For such systems, A is the pre-exponential scaling factor, C is the proportionality constant which ensures the non-collagen areas to have a null value. [22, 53, 54]

$$y = Ae^{-kx} + C \quad (12)$$

The k value obtained from the above equation is the DDD factor which is completely dependent on the sample absorption and composition. It can be easily obtained the collagen intensities against the different focal plane depths and extrapolated as per the exponential equation to obtain the k values for different samples.

Many groups such as Chen *et al.*, [22] in Taiwan have studied the differences between cartilage, tendons, and normal skin using SHG. They applied the DDD model to identify the difference between hypertrophic scars and normal dermis in this study.

These DDD studies can also be utilized for differentiating between collagen mixtures of different proportions due the sensitivity of the k values observed. Ajeti *et al.*, [32] used the DDD study to identify how collagen type I and V showed very different absorption and scattering

properties, the results of which could go a long way in analyzing different artificial tissue samples and their preparation.

3.4. Different Cancer Staging methods

Imaging methods such as SHG, have been shown to have a significant number of advantages over traditional cancer scoring systems. The different data analysis approaches that can be applied to the SHG data provide greater details about the sample [56], and at the same time, they do not damage the sample or use stains of any kind. It is essential though to see how the standard scoring systems can be combined with SHG analysis to provide concurrence for cancer diagnoses. We shall discuss below, some commonly used oncological scoring systems:

3.4.1. Metavir Scoring system

In this system, the severity of the liver cancer diagnosis, observed through histopathological examination of a liver biopsy, is made on the basis of two levels [33, 34]. Firstly, on the basis of inflammation, where it is graded from A0 to A4—ranging from ‘no activity’ to ‘severe activity’. And secondly, on the basis of the stage of fibrosis observed as:

- F0—No fibrosis
- F1—Portal fibrosis without septa
- F2—Portal fibrosis with few septa
- F3—Numerous septa without cirrhosis
- F4—Cirrhosis

3.4.2. TNM system

The TNM system for classifying severity of cancer is one of the most commonly accepted and used to differentiate between different stages of cancer. Unlike the Metavir Scoring system,

the TNM scoring applies to a wide range of cancer diagnoses.

In this system, each letter signifies a different key characteristic of the cancer diagnosis [55]. Starting with T, which denotes the size and hence reach of the primary tumor. For invasive cancer types, it is essential to know whether the cancer has spread to the nearby lymph nodes, and is denoted by N. And lastly, M denotes whether the cancer has spread to other parts of the body, forming secondary tumors in a process defined as metastasis-denoted by M. The values assigned to each of the letters can hence reveal a lot of information about the cancer diagnosis in a short, clear manner.

For the primary tumor (T) classifications, TX represents that the tumor could not be evaluated. T0 indicates the absence of the primary tumor, whereas Tis shows that the tumor is non-invasive at this stage. T1, T2, T3 and T4 all denote the size of the tumor.

In the regional lymph nodes (N) scoring, similarly NX represents non-evaluable tumor presence lymph node, N0 shows absence of tumor in the nodes. And N1, N2 and N3 denote the severity of the lymph node involvement, indicating the number of lymph nodes affected.

For the metastasis (M) scoring, MX shows that the metastasis could not be evaluated, M0 denotes absence of the invasiveness, and M1 shows its presence [56].

3.4.3. Tumor Associated Collagen Signatures (TACS)

For the purpose of understanding and defining key characteristics observed in collagen morphologies in cancer tissues, the group of Provenzano *et al.* [57] introduced the nomenclature of TACS. Studies had shown that in the cases of hyperplasia, adenocarcinoma and ductal carcinoma observed in mice, there were consistent epithelial clusters surrounded by an increased presence of collagen. These collagen morphologies were observed to always be one of three types, which helped classify the severity and invasiveness of the cancer diagnosis in the subjects [31].

- TACS 1-is recognized by highly dense and intense signal imaged for the small tumor detected
- TACS 2-is recognized by a smooth tumor boundary, within which the collagen fibers are majorly aligned parallel to the tumor boundary
- TACS 3-is recognized by collagen fibers being tangentially or perpendicularly aligned to the tumor boundary

Figure 3.8 from the study conducted by Conklin, shows the visual differences between the three TACS classifications.

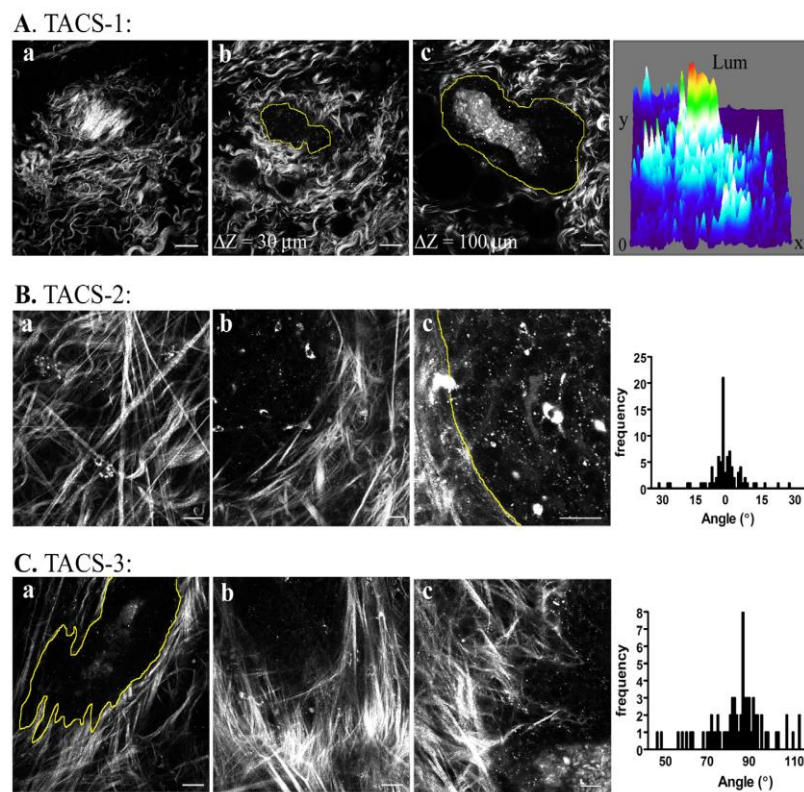


Figure 3.8: Tumor Associated Collagen Signature types in A, B, C, along with associated bar graph profiles for intensity of collagen signatures for that TACS orientation [31]

3.5. Future Perspectives and Conclusions

Positive trends have been observed for many of the cancer detection techniques, which have shown that these multimodal imaging techniques using SHG in combination with TPEF or CARS, have concurred with the standard pathology in place. This is a very important step in the establishment of protocol for early cancer detection, which shall improve the quality of living for the families affected by these deadly diseases, [57] which are often based on genetic traits

We have discussed the varied applications of SHG and the different high content imaging approaches towards cancer research [57, 58, 59]. It is evident that these methods, produce highly complex data, and it thus requires the need for big data analysis. Over the course of our survey of the latest work using SHG analysis, we tried to observe certain trends and preferences for using set techniques for the treatment of data, but it was very difficult to do so. Consensus established for optimized methods of testing which satisfy researchers across borders can help in global benefits. A possible step forward to this goal would be to encourage inter-disciplinary research projects to combat cancer types in laboratories and universities across the world. With the advancements, in the field of analytics, it would surely not be very long before non-parametric testing of data [59] as recommended in this review become the norm. Thereby reducing any bias of the data, based on the technique themselves, and establishing concurrence sooner with the existing clinical pathologies.

3.6. References

1. American Cancer Society. Cancer Facts & Figures 2015. Atlanta, Ga. 2015.
2. Rahib, L., Smith, B. D., Aizenberg, R., Rosenzweig, A. B., Fleshman, J. M., & Matrisian, L. M. (2014). Projecting cancer incidence and deaths to 2030: The unexpected burden of thyroid, liver, and pancreas cancers in the United States. *Cancer Research*, 74(11), 2913–2921. doi:10.1158/0008-5472.CAN-14-0155
3. Burke, K., Tang, P., & Brown, E. (2013). Second harmonic generation reveals matrix alterations during breast tumor progression. *Journal of Biomedical Optics*, 18(3), 31106. doi:10.1117/1.JBO.18.3.031106
4. Golaraei, A., Cisek, R., Krouglov, S., Navab, R., Niu, C., Sakashita, S., Barzda, V. (2014). Characterization of collagen in non-small cell lung carcinoma with second harmonic polarization microscopy. *Biomedical Optics Express*, 5(10), 3562. doi:10.1364/BOE.5.003562
5. Bao, H., Boussioutas, A., Jeremy, R., Russell, S., & Gu, M. (2010). Second harmonic generation imaging via nonlinear endomicroscopy. *Optics Express*, 18(2), 1255–1260. doi:10.1364/OE.18.001255
6. Zhang, Y., Akins, M. L., Murari, K., Xi, J., Li, M.-J., Luby-Phelps, K., ... Li, X. (2012). A compact fiber-optic SHG scanning endomicroscope and its application to visualize cervical remodeling during pregnancy. *Proceedings of the National Academy of Sciences*, 109(32), 12878–12883. doi:10.1073/pnas.1121495109
7. Rivera, D. R., Brown, C. M., Ouzounov, D. G., Pavlova, I., Kobat, D., Webb, W. W., & Xu, C. (2011). Compact and flexible raster scanning multiphoton endoscope capable of imaging unstained tissue. *Proceedings of the National Academy of Sciences*, 108(43), 17598–17603. doi:10.1073/pnas.1114746108
8. Suhaim, J. L., Chung, C.-Y., Lilledahl, M. B., Lim, R. S., Levi, M., Tromberg, B. J., & Potma, E. O. (2012). Characterization of Cholesterol Crystals in Atherosclerotic Plaques Using Stimulated Raman Scattering and Second-Harmonic Generation Microscopy. *Biophysical Journal*, 102(8), 1988–1995. doi:10.1016/j.bpj.2012.03.016
9. Cicchi, R., Matthäus, C., Meyer, T., Lattermann, A., Dietzek, B., Brehm, B. R., ... Pavone, F. S. (2014). Non-linear imaging and characterization of atherosclerotic arterial tissue using combined two photon fluorescence, second-harmonic generation and CARS microscopy. *Multiphoton Microscopy in the Biomedical Sciences XIV*, 9329, 894807. doi:10.1117/12.2037018
10. Liu, H., Qin, W., Shao, Y., Liu, Q., Ma, Z., Borg, T. K., & Gao, B. Z. (2012). Live Cardiomyocyte Imaging via Hybrid TPEF-SHG Microscopy. *Proceedings of SPIE*, 8225, 822524–822524–7. doi:10.1117/12.908381

11. Su, P. J., Chen, W. L., Li, T. H., Chou, C. K., Chen, T. H., Ho, Y. Y., ... Dong, C. Y. (2010). The discrimination of type I and type II collagen and the label-free imaging of engineered cartilage tissue. *Biomaterials*, 31(36), 9415–9421. doi:10.1016/j.biomaterials.2010.08.055
12. Brown, E., McKee, T., diTomaso, E., Pluen, A., Seed, B., Boucher, Y., & Jain, R. K. (2003). Dynamic imaging of collagen and its modulation in tumors in vivo using second-harmonic generation. *Nature Medicine*, 9(6), 796–800. doi:10.1038/nm879
13. Freund, I., Deutsch, M., & Sprecher, A. (1986). Optical Second-harmonic Microscopy, Crossed-beam Summation, and Small-angle Scattering in Rat-tail Tendon. *Biophysical Journal*, 50, 693–712.
14. Chen, X., Nadiarynkh, O., Plotnikov, S., & Campagnola, P. J. (2012). Second harmonic generation microscopy for quantitative analysis of collagen fibrillar structure. *Nature Protocols*, 7(4), 654–69. doi:10.1038/nprot.2012.009
15. Vogler, N., Meyer, T., Akimov, D., Latka, I., Krafft, C., Bendsoe, N., ... Popp, J. (2010). Multimodal imaging to study the morphochemistry of basal cell carcinoma. *Journal of Biophotonics*, 3(10-11), 728–736. doi:10.1002/jbio.201000071
16. Jemal, A., Siegel, R., Ward, E., Hao, Y., Xu, J., Murray, T., & Thun, M. J. (2008). Cancer statistics, 2008. *CA: A Cancer Journal for Clinicians*, 58(2), 71–96. doi:10.3322/CA.2007.0010
17. Seidenari, S., Arginelli, F., Dunsby, C., French, P., König, K., Magnoni, C., ... Ponti, G. (2012). Multiphoton laser tomography and fluorescence lifetime imaging of basal cell carcinoma: Morphologic features for non-invasive diagnostics. *Experimental Dermatology*, 21(11), 831–836. doi:10.1111/j.1600-0625.2012.01554.x
18. Seidenari, S., Arginelli, F., Bassoli, S., Cautela, J., Cesinaro, A. M., Guanti, M., ... König, K. (2013). Diagnosis of BCC by multiphoton laser tomography. *Skin Research and Technology*, 19(1), 297–304. doi:10.1111/j.1600-0846.2012.00643.x
19. Heuke, S., Vogler, N., Meyer, T., Akimov, D., Kluschke, F., Röwert-Huber, H.-J., ... Popp, J. (2013). Detection and Discrimination of Non-Melanoma Skin Cancer by Multimodal Imaging. *Healthcare*, 1(1), 64–83. doi:10.3390/healthcare1010064
20. Sun, C.-K., Chen, C.-C., Chu, S.-W., Tsai, T.-H., Chen, Y.-C., & Lin, B.-L. (2003). Multiharmonic-generation biopsy of skin. *Optics Letters*, 28(24), 2488–2490. doi:10.1364/OL.28.002488
21. Lilledahl, M., Olderøy, M., Finnøy, A., Olstad, K., & Brinchman, J. E. (2015). Second harmonic generation imaging in tissue engineering and cartilage pathologies, 9329, 93291C. doi:10.1117/12.2081583

22. Chen, G., Chen, J., Zhuo, S., Xiong, S., Zeng, H., Jiang, X., ... Xie, S. (2009). Nonlinear spectral imaging of human hypertrophic scar based on two-photon excited fluorescence and second-harmonic generation. *British Journal of Dermatology*, 161(1), 48–55. doi:10.1111/j.1365-2133.2009.09094.x
23. Cicchi, R., Kapsokalyvas, D., De Giorgi, V., Maio, V., Van Wiechen, A., Massi, D., ... Pavone, F. S. (2010). Scoring of collagen organization in healthy and diseased human dermis by multiphoton microscopy. *Journal of Biophotonics*, 3(1-2), 34–43. doi:10.1002/jbio.200910062
24. Linares, H. A., Kischer, C. W., Dobrkovsky, M., & Larson, D. L. (1972). The histotypic organization of collagen of the hypertrophic scar in humans. *The Journal of Investigative Dermatology*, 59(4), 323–332.
25. English, R. S., & Shenefelt, P. D. (1999). Keloids and hypertrophic scars. *Dermatologic Surgery*, 25(8), 631–638. doi:10.1046/j.1524-4725.1999.98257.x
26. Thrasivoulou, C., Virich, G., Krenacs, T., Korom, I., & Becker, D. L. (2011). Optical delineation of human malignant melanoma using second harmonic imaging of collagen. *Biomedical Optics Express*, 2(5), 1282–1295. doi:10.1364/BOE.2.001282
27. Su, P. J., Chen, W. L., Chen, Y. F., & Dong, C. Y. (2011). Determination of collagen nanostructure from second-order susceptibility tensor analysis. *Biophysical Journal*, 100(8), 2053–2062. doi:10.1016/j.bpj.2011.02.015
28. Ambekar, R., Lau, T.-Y., Walsh, M., Bhargava, R., & Toussaint, K. C. (2012). Quantifying collagen structure in breast biopsies using second-harmonic generation imaging. *Biomedical Optics Express*, 3(9), 2021. doi:10.1364/BOE.3.002021
29. Burke, R. M., Madden, K. S., Perry, S. W., Zettel, M. L., & Brown, E. B. (2013). Tumor-associated macrophages and stromal TNF- α regulate collagen structure in a breast tumor model as visualized by second harmonic generation. *Journal of Biomedical Optics*, 18(8), 86003. doi:10.1117/1.JBO.18.8.086003
30. Burke, K. A., Dawes, R. P., Cheema, M. K., Benoit, D. S. W., Perry, S. W., & Brown, E. (2015). Second-harmonic generation scattering directionality predicts tumor cell motility in collagen gels. *Journal of Biomedical Optics*, 20(5), 051024–1–051024–9. doi:10.1117/1.JBO.20.5.051024
31. Conklin, M. W., Eickhoff, J. C., Riching, K. M., Pehlke, C. a., Eliceiri, K. W., Provenzano, P. P., ... Keely, P. J. (2011). Aligned collagen is a prognostic signature for survival in human breast carcinoma. *American Journal of Pathology*, 178(3), 1221–1232. doi:10.1016/j.ajpath.2010.11.076
32. Ajeti, V., Nadiarnykh, O., Ponik, S. M., Keely, P. J., Eliceiri, K. W., & Campagnola, P. J. (2011). Structural changes in mixed Col I/Col V collagen gels probed by SHG microscopy: implications for probing stromal alterations in human breast cancer. *Biomedical Optics Express*, 2(8), 2307–2316. doi:10.1364/BOE.2.002307

33. Poynard, T., Bedossa, P., & Opolon, P. (1997). Natural history of liver fibrosis progression in patients with chronic hepatitis C. *The Lancet*, 349(9055), 825-832.
34. Bedossa, P., Dargère, D., & Paradis, V. (2003). Sampling variability of liver fibrosis in chronic hepatitis C. *Hepatology*, 38(6), 1449-1457.
35. Gailhouste, L., Grand, Y. Le, Odin, C., Guyader, D., Turlin, B., Ezan, F., ... Baffet, G. (2010). Fibrillar collagen scoring by second harmonic microscopy: A new tool in the assessment of liver fibrosis. *Journal of Hepatology*, 52(3), 398-406. doi:10.1016/j.jhep.2009.12.009
36. Strupler, M., Pena, a-M., Hernest, M., Tharaux, P.-L., Martin, J.-L., Beaufrepaire, E., & Schanne-Klein, M.-C. (2007). Second harmonic imaging and scoring of collagen in fibrotic tissues. *Optics Express*, 15(7), 4054-4065. doi:10.1364/OE.15.004054
37. Breunig, H. G., Weinigel, M., Bückle, R., Kellner-Höfer, M., Lademann, J., Darvin, M. E., ... König, K. (2013). Clinical coherent anti-Stokes Raman scattering and multiphoton tomography of human skin with a femtosecond laser and photonic crystal fiber. *Laser Physics Letters*, 10(2), 025604. doi:10.1088/1612-2011/10/2/025604
38. Hovhannisyanyan, V. a., Su, P. J., Lin, S. J., & Dong, C. Y. (2009). Quantifying thermodynamics of collagen thermal denaturation by second harmonic generation imaging. *Applied Physics Letters*, 94(23), 2007-2010. doi:10.1063/1.3142864
39. Meyer, T., Chemnitz, M., Baumgartl, M., Gottschall, T., Pascher, T., Matthäus, C., ... Popp, J. (2013). Expanding multimodal microscopy by high spectral resolution coherent anti-stokes Raman scattering imaging for clinical disease diagnostics. *Analytical Chemistry*, 85(14), 6703-6715. doi:10.1021/ac400570w
40. Plotnikov, S. V., Millard, A. C., Campagnola, P. J., & Mohler, W. A. (2006). Characterization of the myosin-based source for second-harmonic generation from muscle sarcomeres. *Biophysical Journal*, 90(2), 693-703. doi:10.1529/biophysj.105.071555
41. Latour, G., Gusachenko, I., Kowalczyk, L., Lamarre, I., & Schanne-Klein, M. (2012). In vivo structural imaging of the cornea by polarization-resolved second harmonic microscopy. *Biomedical Optics Express*, 3(1), 1. doi:10.1364/BOE.3.000001
42. Cicchi, R., Kapsokalyvas, D., Troiano, M., Campolmi, P., Morini, C., Massi, D., ... Pavone, F. S. (2014). In vivo non-invasive monitoring of collagen remodelling by two-photon microscopy after micro-ablative fractional laser resurfacing. *Journal of Biophotonics*, 7(11-12), 914-925. doi:10.1002/jbio.201300124
43. Tan, H. Y., Chang, Y. L., Lo, W., Hsueh, C. M., Chen, W. L., Ghazaryan, A. a., ... Dong, C. Y. (2013). Characterizing the morphologic changes in collagen crosslinked-treated corneas by Fourier transform-second harmonic generation imaging. *Journal of Cataract and Refractive Surgery*, 39(5), 779-788. doi:10.1016/j.jcrs.2012.11.036

44. Chen, T., Hilton, M. J., Brown, E. B., Zuscik, M. J., & Awad, H. A. (2013). Engineering superficial zone features in tissue engineered cartilage. *Biotechnology and bioengineering*, 110(5), 1476-1486. doi: 10.1002/bit.24799
45. Akilbekova, D., & Bratlie, K. M. (2015). Quantitative Characterization of Collagen in the Fibrotic Capsule Surrounding Implanted Polymeric Microparticles through Second Harmonic Generation Imaging. *Plos One*, 10(6), e0130386. doi:10.1371/journal.pone.0130386
46. Peng, Q., Zhuo, S., So, P. T. C., & Yu, H. (2015). Improving liver fibrosis diagnosis based on forward and backward second harmonic generation signals. *Applied Physics Letters*, 106(8), 083701. doi:10.1063/1.4913907
47. Nadiarnykh, O., LaComb, R. B., Brewer, M. a, & Campagnola, P. J. (2010). Alterations of the extracellular matrix in ovarian cancer studied by Second Harmonic Generation imaging microscopy. *BMC Cancer*, 10, 94. doi:10.1186/1471-2407-10-94
48. Kottmann, R. M., Sharp, J., Owens, K., Salzman, P., Xiao, G.-Q., Phipps, R. P., ... Perry, S. W. (2015). Second harmonic generation microscopy reveals altered collagen microstructure in usual interstitial pneumonia versus healthy lung. *Respiratory Research*, 16(1), 1–13. doi:10.1186/s12931-015-0220-8
49. Cordier, J. F. (2006). Cryptogenic organising pneumonia. *European Respiratory Journal*, 28(2), 422–446. doi:10.1183/09031936.06.00013505
50. Lynch 3rd, J. P., Sagar, R., Weigt, S. S., Zisman, D. A., & White, E. S. (2006, December). Usual interstitial pneumonia. In *Seminars in respiratory and critical care medicine* (Vol. 27, No. 6, pp. 634-651).doi:10.1055/s-2006-957335
51. Linke, J., McDermid, G. J., Pape, A. D., McLane, A. J., Laskin, D. N., Hall-Beyer, M., & Franklin, S. E. (2009). The influence of patch-delineation mismatches on multi-temporal landscape pattern analysis. *Landscape Ecology*, 24(2), 157-170. doi: 10.1007/s10980-008-9290-z
52. Rudolph, R. (1987). Wide spread scars, hypertrophic scars, and keloids. *Clinics in plastic surgery*, 14(2), 253-260. PMID: 3581659
53. Zhuo, S., Yan, J., Chen, G., Shi, H., Zhu, X., Lu, J., ... Xie, S. (2012). Label-free imaging of basement membranes differentiates normal, precancerous, and cancerous colonic tissues by second-harmonic generation microscopy. *PLoS ONE*, 7(6), 4–7. doi:10.1371/journal.pone.0038655
54. Zhuo, S., Zhu, X., Wu, G., Chen, J., & Xie, S. (2011). Quantitative biomarkers of colonic dysplasia based on intrinsic second-harmonic generation signal. *Journal of Biomedical Optics*, 16(12), 120501. doi:10.1117/1.3659715

55. Perry, S. W., Burke, R. M., & Brown, E. B. (2012). Two Photon and Second Harmonic Microscopy in Clinical and Translational Cancer Research. *Annals of Biomedical Engineering*, 40(2), 277–291. doi:10.1007/s10439-012-0512-9.
56. Sobin, L. H., & Fleming, I. D. (1997). TNM classification of malignant tumors, fifth edition (1997). *Cancer*, 80(9), 1803–1804. doi:10.1002/(SICI)1097-0142(19971101)80:9<1803::AID-CNCR16>3.0.CO;2-9
57. Provenzano, P. P., Eliceiri, K. W., Campbell, J. M., Inman, D. R., White, J. G., & Keely, P. J. (2006). Collagen reorganization at the tumor-stromal interface facilitates local invasion. *BMC Medicine*, 4(1), 38. doi:10.1186/1741-7015-4-38
58. Jiang, X., Zhong, J., Liu, Y., Yu, H., Zhuo, S., & Chen, J. (2011). Two-photon fluorescence and second-harmonic generation imaging of collagen in human tissue based on multiphoton microscopy. *Scanning*, 33(1), 53–56. doi:10.1002/sca.20219
59. Birk, J. W., Tadros, M., Moezardalan, K., Nadyarnykh, O., Forouhar, F., Anderson, J., & Campagnola, P. (2014). Second harmonic generation imaging distinguishes both high-grade dysplasia and cancer from normal colonic mucosa. *Digestive Diseases and Sciences*, 59(7), 1529–1534. doi:10.1007/s10620-014-3121-7

CHAPTER 4

COLLAGEN ORGANIZATION OF FIBROBLASTS ENCAPSULATED IN PH RESPONSIVE METHACRYLATED ALGINATE HYDROGELS

Modified from a manuscript published in Journal of Biomedical Materials Research Part A (2018)

The pH of dermal wounds shifts from neutral during the inflammatory phase to slightly basic in the tissue remodeling phase. Stage specific wound treatment can be developed using environmentally responsive alginate hydrogels. The chemistry of these networks dictates swelling behavior. Here, we fabricated alginate hydrogels using chain growth, step growth, and combined mixed mode gelation methods to crosslink methacrylated alginate (ALGMA) and gain control over swelling responses. Methacrylation of the alginate network was confirmed through NMR spectroscopy. Strontium cations were introduced to fabricate stiffer, dually crosslinked hydrogels. Dual crosslinking significantly decreased the swelling response over the pH range of 3 to 9 for step growth and chain growth hydrogels, with no impact on mixed mode hydrogels. The extent of crosslinking altered the hydrogel degradation profiles under accelerated degradation conditions. Encapsulated NIH/3T3 fibroblasts in the different ALGMA hydrogels remained viable with greater cell proliferation in the stiffer gels. Collagen organization deposited by the NIH/3T3 fibroblasts was monitored using second harmonic generation (SHG) microscopy and was influenced by the crosslinking mechanism. Ionic chain growth and ionic mixed mode crosslinked ALGMA hydrogels caused relatively isotropic collagen organization, particularly 10 days post-cell encapsulation. Principal component analysis (PCA) was employed to uncover correlations between the observed properties. The ability of these environmentally responsive gels to induce isotropic collagen and respond to pH changes means they hold promise as phase specific wound dressings.

4.1. Introduction

Wound healing responses are dynamic processes with both cell types and their populations changing throughout the process.¹ The sequence of events following injury can be divided into four overlapping phases: hemostasis, inflammation, proliferation, and remodeling.² Depending on the physiological response from the inflammatory phase to proliferation, wounds can be classified as acute or chronic.³ Chronic wounds can result from a compromised immune response, as is common in diabetes.⁴ Diabetic foot ulcers occur in over 15 to 25% of diabetics, with an annual incidence rate of over 10%.⁵ A recent study showed that there has been an approximately three fold increase in the cost of skin disease related medical expenses from \$29 to 75 billion in the past 13 years.^{6,7} The economic burden and high incidence rate of chronic wounds demonstrates the need for rapid and effective treatments for these afflictions.

Alginate has been widely used as a biomaterial for applications in wound healing and tissue engineering as it is naturally occurring, relatively inexpensive, can provide a moist environment suitable for encapsulated cells, and can be gelled under mild conditions. Divalent cations are typically used to ionically crosslink alginate *in situ*.⁸ However, these physical interactions are weak, meaning that divalent cations can be easily displaced by physiologically abundant monovalent sodium.⁹ Chain and step growth crosslinked hydrogels have been used to encapsulating cells for drug release and tissue engineering applications.¹⁰ Thiol-ene chemistry is a facile and selective reaction that can be used to crosslink a wide variety of naturally and synthetic polymers.¹¹ This method is a viable modification strategy to chemically crosslink biological molecules using thiodendrimers, which is a significant improvement on previous copper based crosslinking reactions which caused cytotoxicity.¹² Alginate hydrogels covalently crosslinked

through chain growth and click chemistry are cytocompatible, mechanically tunable hydrogels that are capable of providing a good approximation for studying *in vivo* biomaterial interactions.

In situ photocrosslinkable polymers are a promising construct for fabricating hydrogel for varied applications such as drug release systems, as well as tunable sensors for biomedical applications.¹³ Ultraviolet (UV) light can be used to initiate free radical polymerization to covalently crosslink functional methacrylate groups on the polymer chain and induce liquid-solid transitions of cell-gel formulations. Previous studies showed successful crosslinking of alginate and hyaluronic acid based hydrogels using methacrylate functional groups to prepare tissue engineering constructs.¹⁴ These functional hydrogels were used to encapsulate chondrocytes in an osteochondral defect model.¹⁵ Increased collagen secretion, swelling responses, and biocompatibility of encapsulated cells were some of the key parameters identified in these studies that can be further studied for the development of environmentally responsive hydrogels synthesized from methacrylated polysaccharides.^{15,16}

An integral aspect of developing topical formulations to aid in the wound healing response is to synthesize environmentally responsive hydrogels.¹⁷ The chemical structure of the polymer network plays a major role in the response to different environmental cues. Many properties such as ionization equilibrium, counterion species, and ion concentration can control the pH response of ionically crosslinked hydrogels.^{16,18} However, less focus has been paid to pH responses of covalently crosslinked hydrogels. In this study, we present a method for functionalizing very low viscosity alginate using methacrylic anhydride to improve the mechanical properties and degradation kinetics of the hydrogel. This allows us to photo-crosslink ALGMA through step growth, chain growth, or a combination of the two, termed mixed mode to form soft yet biocompatible hydrogels. We investigated the mechanical properties, swelling responses under

diverse pH conditions, degradation kinetics, cytocompatibility, and collagen deposition by encapsulated NIH/3T3 fibroblasts in the hydrogels. With the use of statistical analytical techniques such as PCA, we aimed to identify key factors that can improve rational design for the synthesis of a hydrogel formulation that can be used for tissue engineering applications pertinent to the treatment of chronic wounds.

4.2. Experimental

4.2.1. Materials

Very low viscosity alginic acid (CAS 9005-38-3) was obtained from Alfa Aesar (Tewksbury, MA). Other materials were purchased through Sigma Aldrich (St. Louis, MO) and were used as received, unless otherwise stated. Fresh deionized water (Milli-Q, Thermo Scientific Nanopure, Waltham, MA) was used throughout this study.

4.2.2. Methacrylated Alginate (ALGMA) Synthesis

ALGMA was prepared as previously described.¹⁹ Briefly, a 1% (w/v) solution of very low viscosity alginic acid in DI water was prepared. While the solution was mixing, 16 mL of methacrylic anhydride was slowly added. The pH was maintained between 8 to 9 using 5 M NaOH while reacting at 4 °C for 24 h. The solution was dialyzed for 48 h against water using a molecular weight cutoff membrane of 13,000 Da. The dialysate was changed twice daily. The solution was lyophilized (4.5L, Labconco, Kansas City, MO) and the ALGMA was collected as a white, soft solid. This reaction is illustrated in **Figure 4.1**.

NMR was used to confirm methacrylation of the alginic acid. Solutions of alginate and ALGMA were prepared using standard protocols.^{20,21} Briefly, ALGMA was dissolved in D₂O and lyophilized three times to replace all protons with deuterium before ~12.5 mg of polymer was

dissolved a final time in 600 μl of D_2O . The ^1H spectra were recorded on a Bruker Avance III Spectrometer at 70°C using a sweep width of 6602.1 Hz, a 90° pulse, and an acquisition time of 2.48 s. A total of 128 repetitive scans with 64 k points were acquired and the data were processed in MNova with 128k points, zero filling, and exponential line broadening of 1.0 Hz. The extent of methacrylation was calculated by the relative integrations of the protons from the methacrylate groups (I_{CH_2} at $\delta = 6.0$ and 5.6 ppm, and the methyl peak (I_{CH_3}), at $\delta = 1.8$ ppm) to the carbohydrate proton peaks (I_{H})_{polymer}.

$$\text{Methacrylation}\% = \frac{\left(\frac{I_{\text{CH}_2}}{n_{\text{CH}_2}} + \frac{I_{\text{CH}_3}}{n_{\text{CH}_3}}\right)}{\frac{I_{\text{polymer}}}{n_{\text{H}_{\text{polymer}}}}} \quad (1)$$

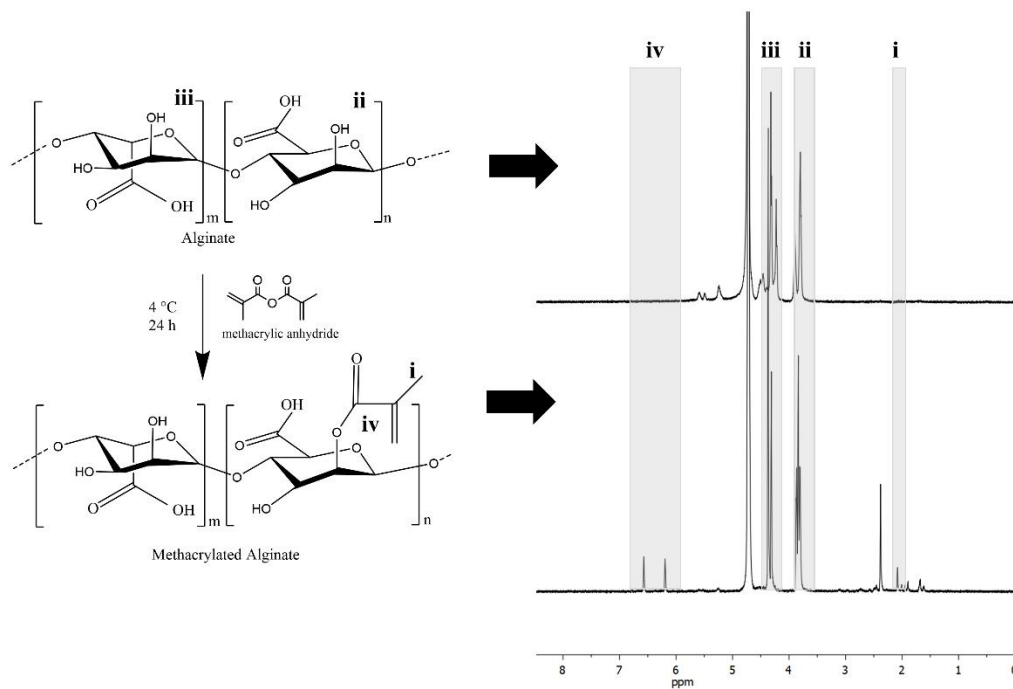


Figure 4.1. Synthesis and characterization of ALGMA. (A) Schematic representation of chemical modification of alginate. (B) ^1H NMR spectra of alginate and methacrylated alginate. The guluronate (ii) and mannuronate (iii) peaks are located at $\delta = 3.7$ and 4.7 ppm. Methacrylation of alginate polymer from unmodified to methacrylated with respective ^1H NMR spectra confirming the presence of (ii) guluronate and (iii) mannuronate. The methylene was found at $\delta = 6.2$ and $\delta = 5.6$ ppm (iv) and the methyl peaks at $\delta = 1.8$ ppm (i). The degree of methacrylation was calculated as a percentage of hydroxy group substitution with the methacrylate groups per repeating unit.

4.2.3. Hydrogel Fabrication and Characterization

To 10 ml of DI water, 300 mg of ALGMA was dissolved to obtain a 3% (w/v) solution. Irgacure 2959 (10 mg) was added to the stock solution. Three different gelation reactions, step growth, chain growth, and mixed mode polymerization were used to obtain different hydrogels. For chain growth gels, an aliquot of the stock solution was degassed under vacuum. For step growth polymerization, 250 μ l of 4 mg/ml dithiothreitol (DTT) was added to the stock solution. For the mixed mode polymerization, 250 μ l of 4 mg/ml DTT was added to the stock solution and it was degassed. All three pre-gels were exposed to UV light (365 nm, 2 W/cm²) for 10 minutes. For preparation of dually crosslinked ALGMA hydrogels, 100 μ l of 0.2 M SrCl₂ was added after the gels were exposed to UV light.

Hydrogel pegs (6 mm thick, 16 mm diameter, $n = 4$) were placed between two glass slides on top of which weights were added. Height changes and cross-section areas of the hydrogel pegs were measured through Image-J (NIH, Bethesda, MD). The compressive modulus was defined as the slope of the linear region in the stress-strain curve in the 5 – 15% strain range.

To measure the swelling ratios, the hydrogels ($n = 3$) were dried at room temperature in a desiccator. The solid was then swelled in 1 mM acetate buffer solution at pH 3, 5, 7.4, or 9 for 2 days. The wet and dry weights were recorded, and the swelling ratios were calculated using equation (1), where M_w is the wet mass and M_d is the dry mass.

$$S = \frac{M_w - M_d}{M_d} \quad (2)$$

4.2.4. *In Vitro* Degradation

For each gelation method, 1 ml of hydrogel was exposed to UV light and placed in 0.1 mM NaOH to determine how the crosslinking mechanisms affected gel stability and degradation

profiles. The hydrogels were first equilibrated for 24 h in water before measuring the initial mass to eliminate swelling effects. The mass of the hydrogel ($n = 3$) was measured every 24 h and compared with the initial mass.

4.2.5. Cell Culture and Viability Assay

NIH/3T3 fibroblasts (ATCC, Manassas, VA) were cultured at 37°C with 5% CO₂ in complete medium (CM, Dulbecco's modified Eagle's medium (Thermo Scientific) supplemented with 10% bovine calf serum, 100 U/L penicillin, and 100 µg/ml streptomycin). To 48 well plates, 200 µl of cell solution at 1×10^7 cells/ml was mixed with 300 µl hydrogel. Both live and dead controls were made in which the cells were plated directly on the tissue culture plastic in the absence of hydrogel. After 48 h, the dead control was aspirated and 300 µl of 70% ethanol was added for 10 minutes to kill the cells. The supernatant in each well was then aspirated and replaced with 150 µl phosphate buffered saline (PBS) with 0.3 µl of 1 mg/ml calcein-AM and 1.12 µl of 1 mg/ml 7-aminoactinomycin D (7-AAD) and incubated for 40 mins. Images were taken with a EVOS Flouid Cell Image Station (Thermo Scientific) using the red (excitation/emission 586/646 nm) and the green channels (482/532 nm).

4.2.6. SHG Microscopy Imaging of the gels

NIH/3T3 fibroblasts were suspended at a concentration of 1×10^7 cells/ml and mixed with an equal volume of hydrogel precursor solution. This solution (100 µl) was pipetted between two glass coverslips, exposed to UV light for crosslinking, and placed in Petri dishes containing CM. The cells were fed every three days. Negative controls consisting of gels without cells were also prepared. After 5, 7, or 10 days, the samples were fixed in 10% formalin solution and imaged.

All samples were imaged using a mode-locked Ti:Sapphire laser (100 fs pulse width, 1 kHz repetition rate, Libra, Coherent, Santa Clara, CA) that produces an 800 nm fundamental. The

average power at the sample image plane was controlled using a combination of a half-wave plate and a Glan-Thompson polarizer (Thorlabs, Newton, NJ). Second harmonic signal was collected in the transmission mode. For this setup, an inverted microscope (AmScope, Irvine, CA) and Nikon Plan Fluorite objective (20 ×, 0.50 NA, 2.1 mm WD, Nikon, Melville, NY) was used to focus the beam and the SHG transmission was collected with a Nikon water immersion objective (40 ×, 0.8 NA, 3.5 mm WD, Nikon). The transmitted SHG signal was reflected by a dichroic mirror (DMLP425T, Thorlabs) and separated from the fundamental beam with two short pass filters < 450nm (FGB37M, Thorlabs) and 808 nm notch filter (NF-808.0-E-25.0M, Melles Griot, Rochester, NY), before detection by an intensified CCD (iCCD, iStar 334T, Andor, Belfast, UK). Polarized SHG imaging was conducted using a Glan-Thompson polarizer and a half-wave plate mounted on a motor driven rotational stage (Thorlabs) to achieve linear polarization. Images of the samples were collected every 10° from 0° to 350°. A minimum of three images for each experimental condition was taken. From this collection of images, regions of interest (ROI) were fit using the following equation:

$$I_{SHG} = c \cdot \left\{ \left[\sin^2(\theta_e - \theta_o) + \left(\frac{\chi_{zzz}}{\chi_{zxx}} \right) \cos^2(\theta_e - \theta_o) \right]^2 + \left(\frac{\chi_{xzx}}{\chi_{zxx}} \right)^2 \sin^2(2(\theta_e - \theta_o)) \right\} \quad (3)$$

where $\frac{\chi_{zzz}}{\chi_{zxx}}$ and $\frac{\chi_{xzx}}{\chi_{zxx}}$ are second-order susceptibility tensor element ratios, θ_e and θ_o are incident polarization angle and collagen fiber angle, respectively, and c is a normalization constant. The orientation angle of collagen in each ROI was calculated and a histogram was generated. Collagen organization was measured by fitting the orientation angle histogram with a Gaussian fit over a 180° profile and full-width at half maximum (FWHM) values were obtained. Collagen types were identified using a previously described method.²² Briefly, collagen gels with varying collagen type III concentrations were imaged using SHG microscopy and the data was fit using equation 2.

Histograms of $\frac{\chi_{zzx}}{\chi_{xxx}}$ revealed the present of two peaks: one at ~ 0.8 , which is assigned to collagen type III and the second at ~ 1.2 , corresponding to collagen type I. The ratios of these integrated peaks were plotted against collagen type III concentration to yield a standard curve. This curve was used to estimate collagen type III concentrations in the imaged hydrogels.

4.2.7. Statistical Analysis

All data was subjected to statistical analysis and values are reported as mean \pm standard deviation (SD). Statistical significance of the mean comparisons was determined by a two-way ANOVA. Pair-wise comparisons were analyzed with Tukey's honest significant difference test. Differences were considered statistically significant for $p < 0.05$. Principal component analysis was conducted to uncover the correlations between the characterized properties of the gels and the collagen response from the encapsulated fibroblasts.

4.3 Results

4.3.1. Characterization of ALGMA Hydrogels

ALGMA was characterized using ^1H NMR spectroscopy (**Figure 4.1**), using a previously described protocol.²³ The mannuronic acid content of the unmodified alginate was determined to be $45 \pm 2\%$, with ii and iii labeling the guluronate and mannuronate residue peaks.²⁴ Two peaks appear in the ALGMA spectrum at 6.0 and 6.4 ppm, which are assigned to the methylene and methacrylamide protons, labeled as iv (**Figure 4.1**). The extent of methacrylation was calculated through the relative integration of the methacrylate and methyl peak (at 1.8 ppm, labeled as i) to those from the protons of the modified alginate, as $25 \pm 2\%$, using a previously described procedure.²⁵

4.3.2. Compressive Moduli

The compression modulus can serve as an approximation for the extent of crosslinking when comparing polymers with similar backbones (similar branching, molecular weight, etc.) fabricated using different crosslinking methods.²⁶ The compressive moduli (**Figure 2**) increase from step growth to chain growth to mixed mode (0.71 ± 0.04 , 1.29 ± 0.07 , and 1.61 ± 0.03 kPa, respectively). Introducing ionic junctions through strontium ions further increased the moduli. Ionically crosslinked ALGMA has a modulus of 0.53 ± 0.03 kPa. The increase in the compressive moduli for dually crosslinked hydrogels are ~500 Pa higher than their counterparts that are not ionically crosslinked (1.21 ± 0.07 , 1.99 ± 0.11 , and 2.24 ± 0.12 kPa for step growth, chain growth, and mixed mode gels).

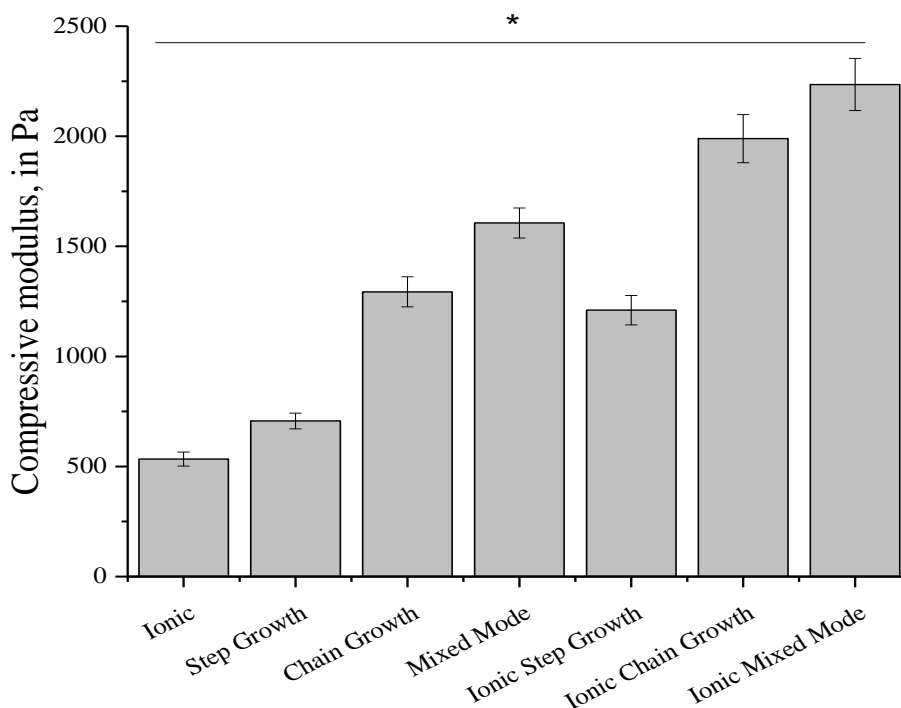


Figure 4.2. Compressive moduli of alginate hydrogels. Compressive moduli of methacrylated alginate hydrogels crosslinked through the different mechanisms. Data represents the mean \pm SD. $n = 3$. Statistical analysis through two-way ANOVA and Tukey's HSD post-hoc test. * $p < 0.05$.

4.3.3. Swelling Response

Significantly higher swelling responses were observed in basic conditions (pH 9) compared to the acidic conditions (pH 3, **Figure 4.3**). This trend was consistent for all crosslinked alginate hydrogels studied here. The swelling response (**Figure 4.3**) of the ionically crosslinked non-methacrylated alginate hydrogels was higher than covalently crosslinked hydrogels.

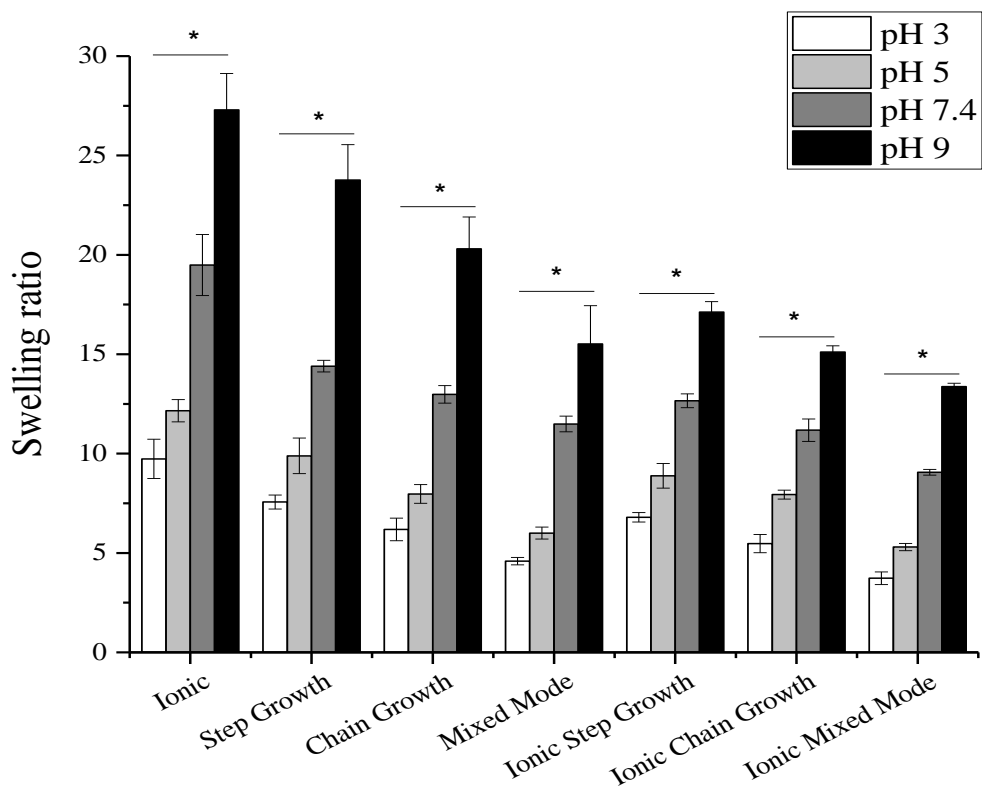


Figure 4.3. Swelling behavior of alginate hydrogels in different pH buffers. Hydrogels crosslinked through the different mechanisms were swelled in pH 3, 5, 7.4, and 9. Data represents the mean \pm SD. $n = 3$. Statistical analysis through two-way ANOVA and Tukey's HSD post-hoc test. * $p < 0.05$.

4.3.4 Degradation Kinetics

For efficient delivery of proteins, cells, or cytokines to wound sites,²⁷ it is essential to have well characterized degradation kinetics. These hydrogels were incubated in accelerated

degradation conditions (0.1 mM NaOH, **Figure 4.4**). Statistically, there was no difference for step growth, chain growth, and mixed mode gels with all three gels degrading to 50% of their original mass within 5-6 days. The ionically crosslinked hydrogels degraded completely within 6 h and are not shown. Dually crosslinked hydrogels were more stable than their covalently crosslinked counterparts with 50% of their original mass remaining after 13-16 days.

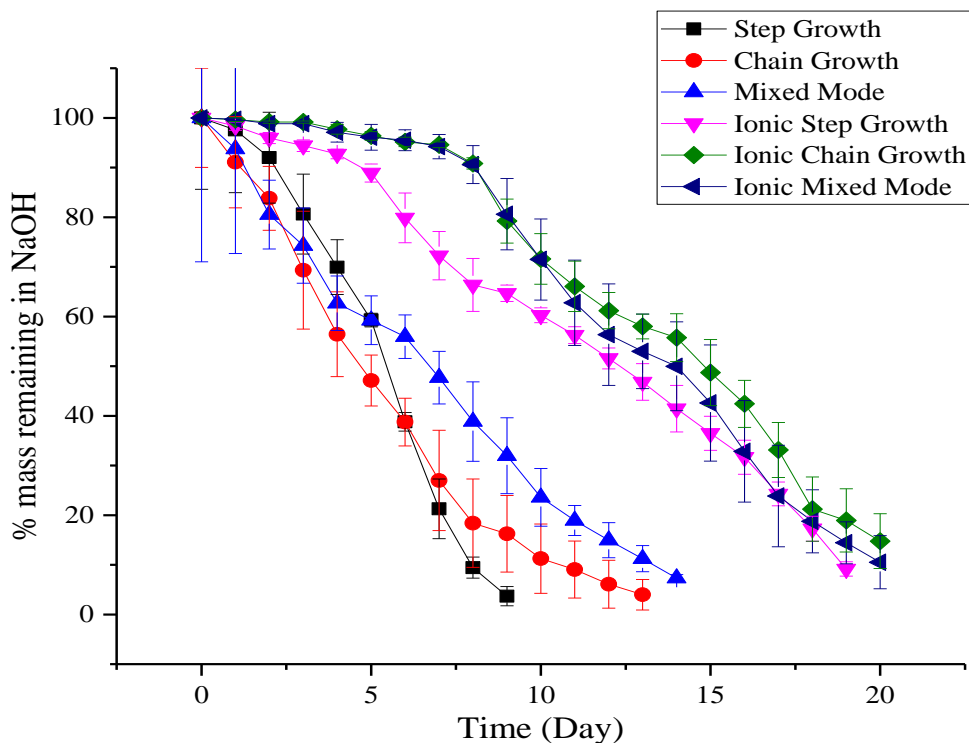


Figure 4.4. Alginate hydrogel degradation under accelerated conditions. Alginate hydrogels were immersed in 0.1 mM NaOH to mimic accelerated degradation conditions. Data represents the mean \pm SD. $n = 3$. Statistical analysis through two-way ANOVA and Tukey's HSD post-hoc test. * $p < 0.05$.

4.3.5. Cytocompatibility of ALGMA Hydrogels

Wound dressings must be cytocompatible. NIH/3T3 fibroblasts were encapsulated in the different ALGMA hydrogels and imaged using a live/dead assay. Cell proliferation after 48 h was normalized to the controls (cells cultured on tissue culture plastic) (**Figure 4.5**). Significant

differences were observed for the increase in cell proliferation with increasing compressive moduli of the ALGMA gels. The covalently crosslinked hydrogels showed proliferation of 24 ± 1 , 32 ± 2 , $44 \pm 1\%$ for the step growth, chain growth and mixed mode respectively. The dually crosslinked hydrogels showed significantly higher cell proliferation of 54 ± 4 , 62 ± 1 , $65 \pm 1\%$ for the ionic step growth, ionic chain growth and ionic mixed mode gel types respectively. The NIH/3T3 cells aggregated more for the dually crosslinked hydrogels compared to their covalently crosslinked counterparts. Overall, no dead cells were observed across all encapsulated conditions indicating minimal cytotoxicity of the alginate hydrogel solution. Cells were not encapsulated in non-methacrylated alginate hydrogels, due to their rapid breakdown under accelerated degradation conditions.

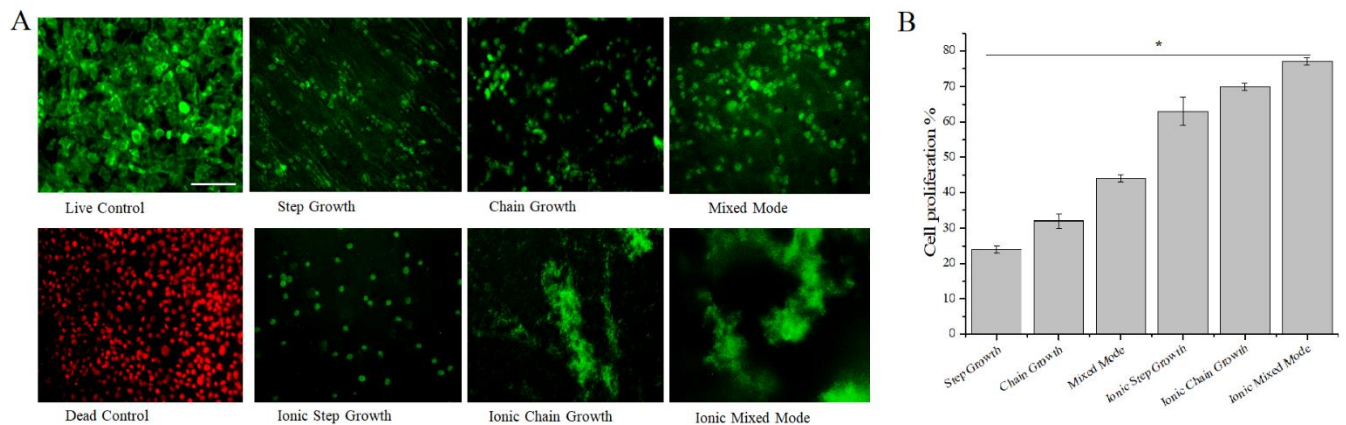


Figure 4.5. Proliferation of NIH/3T3 cells encapsulated in alginate hydrogels. NIH/3T3 fibroblasts were mixed with ALGMA and crosslinked. Cells seeded on tissue culture plastic served as the controls. (A) Representative micrographs of live (green) and dead (red) cells cultured for 48 h. (B) Quantification of live and dead cells. Data represents the mean \pm SD. $n = 6$. Statistical analysis through two-way ANOVA and Tukey's HSD post-hoc test. $*p < 0.05$.

4.3.6. SHG Microscopy

We used SHG microscopy to visualize the collagen deposition and remodeling in the cell-gel environment. Molecules must be non-centrosymmetric to be SHG active, which means that cell culture medium and the hydrogel network will not contribute to the signal. There was a clear

trend for collagen organization in the chain and step growth hydrogels. Initially, collagen was highly ordered on day 5 and became significantly more disordered on days 7 and 10 (**Figure 4.6**). We observed the same trend for dually crosslinked hydrogels (**Figure 4.6**). Mixed mode hydrogels, both covalently and dually crosslinked, showed no significant changes in collagen organization from days 5 to 10. The % collagen III calculated from the susceptibility tensor ratios (**Figures 4.7** and **4.8**) showed no trend for any of the hydrogel formulations, with their values varying from 1 to 36%.

Table 4.1. SHG analysis parameters for NIH 3T3 cells encapsulated in covalently crosslinked ALGMA hydrogels.

| Treatment | FWHM | Col III |
|---------------------|------------|--------------|
| Chain Growth Day 5 | 12 ± 2 | $25 \pm 5\%$ |
| Chain Growth Day 7 | 21 ± 4 | $4 \pm 1\%$ |
| Chain Growth Day 10 | 16 ± 3 | $9 \pm 1\%$ |
| Step Growth Day 5 | 18 ± 4 | $1 \pm 0\%$ |
| Step Growth Day 7 | 34 ± 7 | $19 \pm 6\%$ |
| Step Growth Day 10 | 33 ± 5 | $5 \pm 1\%$ |
| Mixed Mode Day 5 | 34 ± 9 | $8 \pm 2\%$ |
| Mixed Mode Day 7 | 23 ± 3 | $9 \pm 2\%$ |
| Mixed Mode Day 10 | 16 ± 4 | $7 \pm 2\%$ |

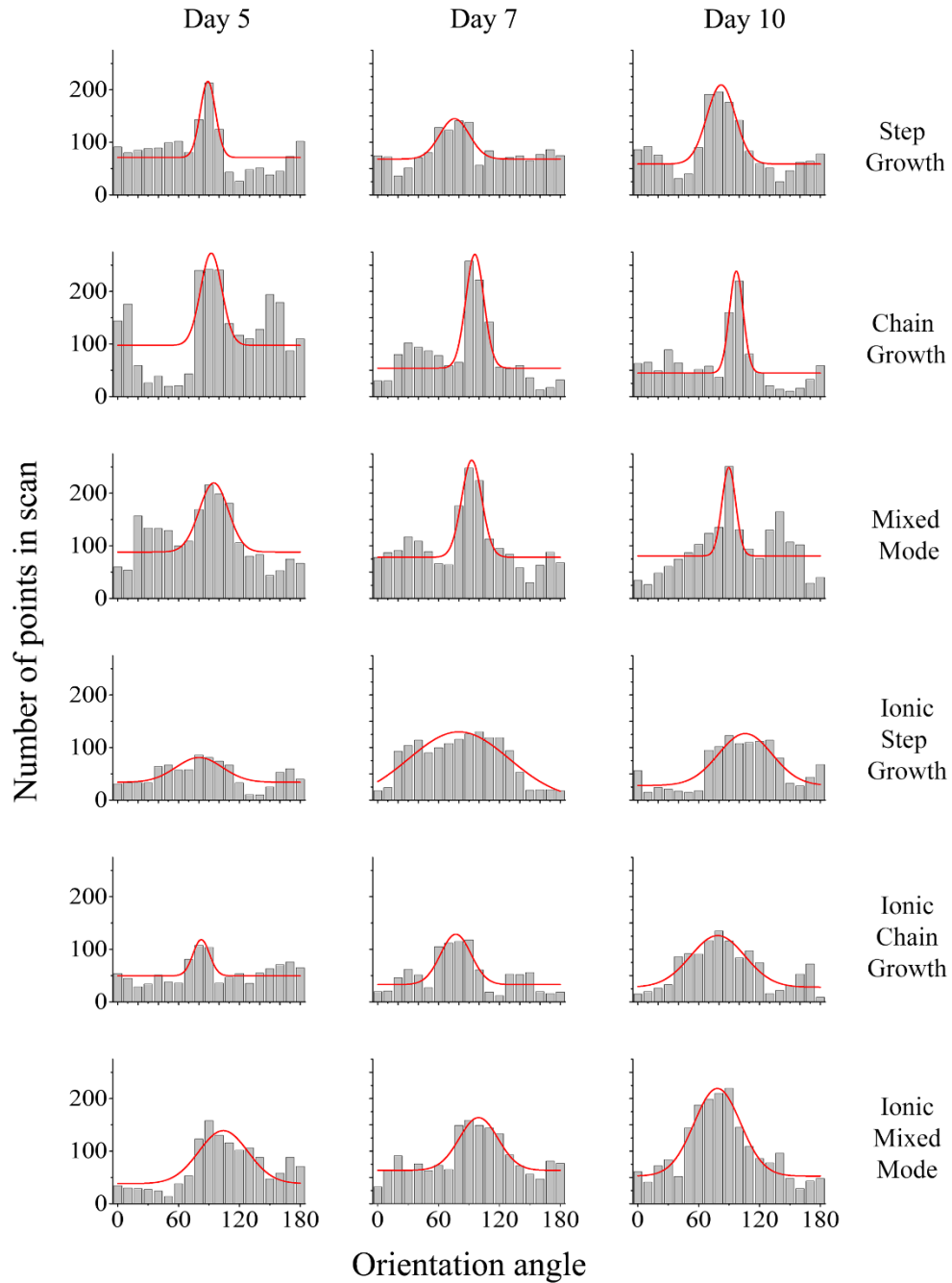


Figure 4.6. Organization of collagen secreted by encapsulated fibroblasts in alginate hydrogels. NIH/3T3 fibroblasts were mixed with ALGMA and crosslinked. Samples were imaged using SHG microscopy to observe the changes in collagen organization.

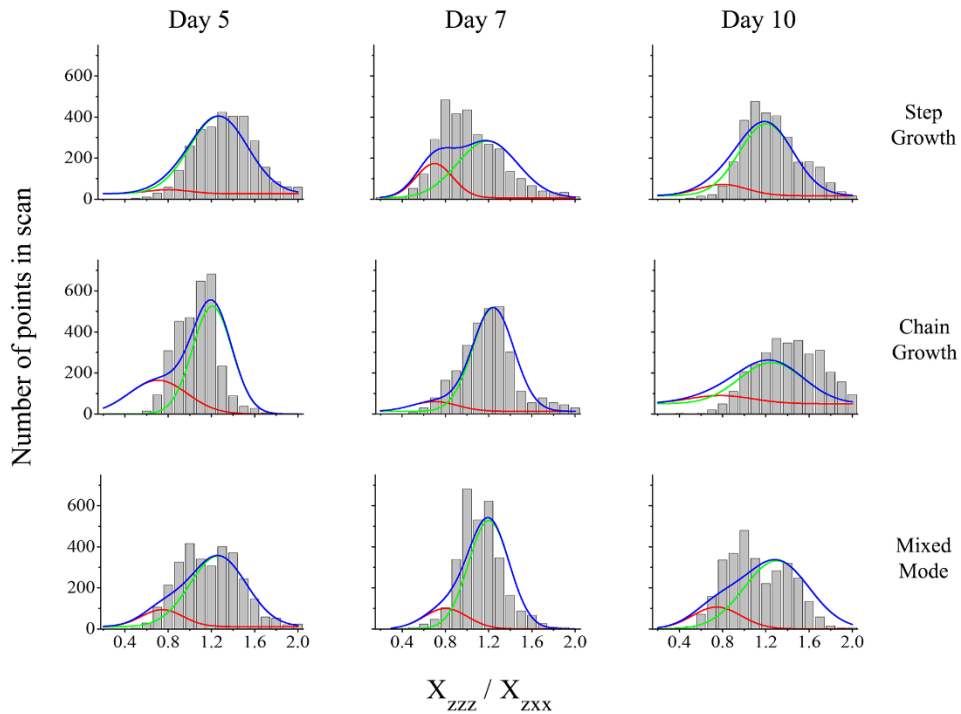


Figure 4.7. Collagen III secretion in covalently crosslinked ALGMA: Histograms of χ_{zzz}/χ_{zxx} values obtained for NIH 3T3 fibroblasts encapsulated in covalently crosslinked ALGMA hydrogels

Table 4.2. SHG analysis parameters for NIH 3T3 cells encapsulated in dually crosslinked ALGMA hydrogels.

| Treatment | FWHM | Col III |
|---------------------------|--------------|--------------|
| Ionic Chain Growth Day 5 | 19 ± 5 | $22 \pm 3\%$ |
| Ionic Chain Growth Day 7 | 35 ± 7 | $36 \pm 6\%$ |
| Ionic Chain Growth Day 10 | 63 ± 12 | $2 \pm 1\%$ |
| Ionic Step Growth Day 5 | 54 ± 17 | $9 \pm 2\%$ |
| Ionic Step Growth Day 7 | 117 ± 34 | $18 \pm 3\%$ |
| Ionic Step Growth Day 10 | 62 ± 12 | $5 \pm 1\%$ |
| Ionic Mixed Mode Day 5 | 57 ± 12 | $33 \pm 7\%$ |
| Ionic Mixed Mode Day 7 | 45 ± 7 | $6 \pm 1\%$ |
| Ionic Mixed Mode Day 10 | 54 ± 6 | $10 \pm 2\%$ |

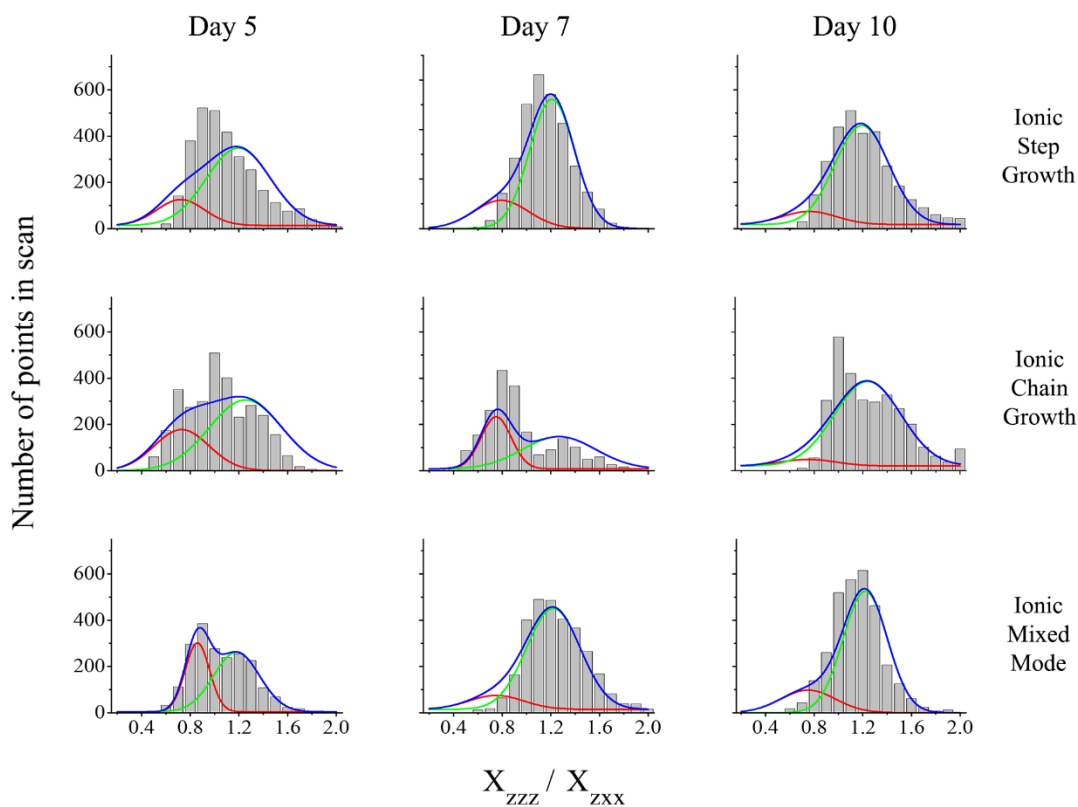


Figure 4.8. Collagen III secretion in dually crosslinked ALGMA: Histograms of χ_{zzz}/χ_{zxx} values obtained for NIH 3T3 fibroblasts encapsulated in dually crosslinked ALGMA hydrogels

4.3.7. PCA

Relationships between the collected data were analyzed using informatics analysis. For PCA, similar distances and angles of the projections indicates the data are correlated. Here, a Euclidean geometric map was used to uncover trends between the materials properties of the alginate gels and the collagen organization and type present in those gels. These have been plotted as PC1 and PC2 which are a linear combination of the different variables mapped on two new axes. In our study, PC1 explains 57.6% data variance and PC2 explains 23.4% data variance, which represents >80% of the original data information. Swelling ratios and compressive moduli were negatively correlated. Cell proliferation was strongly correlated to the mechanical modulus

(Figure 4.9). The Pearson correlation was $R = 0.86$ (Table 4.3). As expected, the compressive modulus was strongly negatively correlated ($R = -0.94$, Table 4.3) to the swelling under basic conditions (pH 9). Strong positive correlations were observed for the collagen FWHM (d10) with the cell proliferation ($R = 0.74$, Table 4.3) and degradation half-life ($R = 0.85$, Table 4.3) under accelerated conditions.

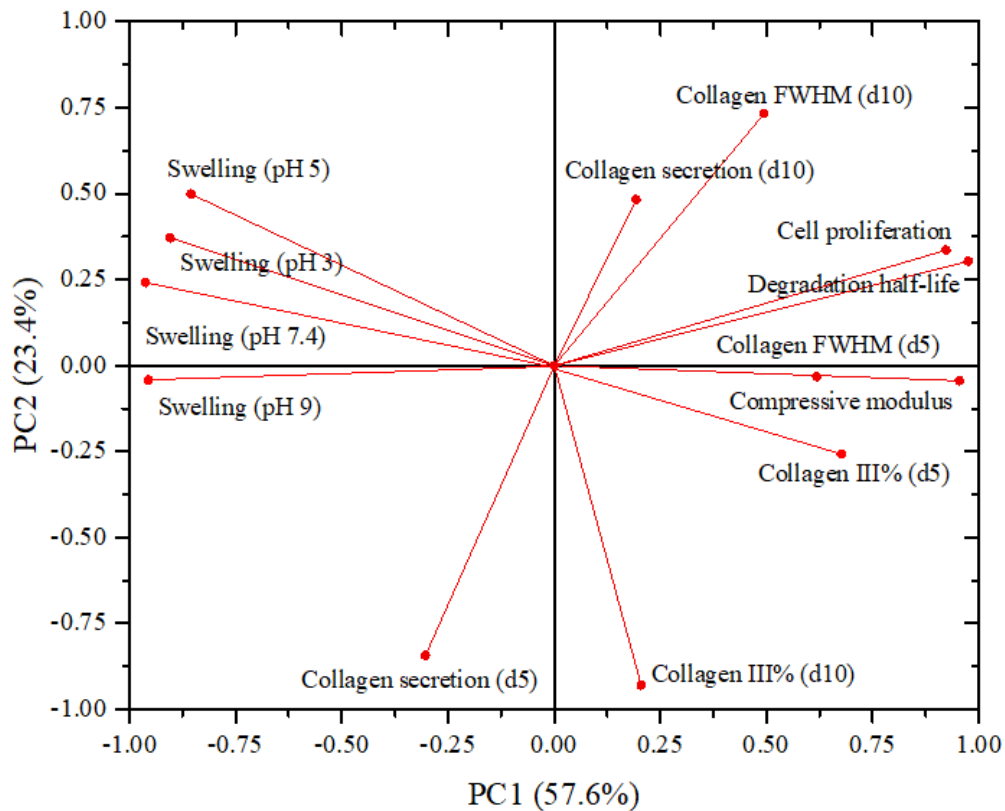


Figure 4.9. Loading plot of hydrogel parameters and their influence on cell proliferation and collagen secretion. PC1 explains 57.6% data variance and PC2 explains 23.4% data variance, which represents >80% of the original data information.

Table 4.3. Correlation matrix for the hydrogel properties and encapsulated cell responses.

| | Compressive Modulus | Swelling (pH 3) | Swelling (pH 5) | Swelling (pH 7.4) | Swelling (pH 9) | Degradation (half-life time) | Cell proliferation | Collagen secretion (d10) | Collagen FWHM (d10) | Col III % (d10) | Collagen secretion (d5) | Collagen FWHM (d5) | Col III% (d5) |
|------------------------------|---------------------|-----------------|-----------------|-------------------|-----------------|------------------------------|--------------------|--------------------------|---------------------|-----------------|-------------------------|--------------------|---------------|
| Compressive Modulus | 1.00 | -0.92 | -0.88 | -0.90 | -0.94 | 0.86 | 0.86 | 0.31 | 0.37 | 0.19 | -0.26 | 0.40 | 0.79 |
| Swelling (pH 3) | -0.92 | 1.00 | 0.99 | 0.97 | 0.94 | -0.81 | -0.67 | -0.23 | -0.04 | -0.46 | -0.12 | -0.44 | -0.66 |
| Swelling (pH 5) | -0.88 | 0.99 | 1.00 | 0.94 | 0.91 | -0.75 | -0.57 | -0.13 | 0.10 | -0.58 | -0.23 | -0.46 | -0.61 |
| Swelling (pH 7.4) | -0.90 | 0.97 | 0.94 | 1.00 | 0.95 | -0.92 | -0.86 | -0.17 | -0.36 | -0.34 | 0.11 | -0.58 | -0.74 |
| Swelling (pH 9) | -0.94 | 0.94 | 0.91 | 0.95 | 1.00 | -0.92 | -0.92 | -0.36 | -0.43 | -0.11 | 0.34 | -0.62 | -0.58 |
| Degradation (half-life time) | 0.86 | -0.81 | -0.75 | -0.92 | -0.92 | 1.00 | 0.98 | 0.14 | 0.85 | -0.10 | -0.60 | 0.66 | 0.58 |
| Cell proliferation | 0.86 | -0.67 | -0.57 | -0.86 | -0.92 | 0.98 | 1.00 | 0.28 | 0.74 | -0.08 | -0.56 | 0.65 | 0.58 |
| Collagen secretion (d10) | 0.31 | -0.23 | -0.13 | -0.17 | -0.36 | 0.14 | 0.28 | 1.00 | 0.11 | -0.66 | -0.32 | -0.24 | -0.20 |
| Collagen FWHM (d10) | 0.37 | -0.04 | 0.10 | -0.36 | -0.43 | 0.85 | 0.74 | 0.11 | 1.00 | -0.46 | -0.71 | 0.50 | 0.22 |
| Col III % (d10) | 0.19 | -0.46 | -0.58 | -0.34 | -0.11 | -0.10 | -0.08 | -0.66 | -0.46 | 1.00 | 0.62 | 0.30 | 0.47 |
| Collagen secretion (d5) | -0.26 | -0.12 | -0.23 | 0.11 | 0.34 | -0.60 | -0.56 | -0.32 | -0.71 | 0.62 | 1.00 | -0.08 | -0.19 |
| Collagen FWHM (d5) | 0.40 | -0.44 | -0.46 | -0.58 | -0.62 | 0.66 | 0.65 | -0.24 | 0.50 | 0.30 | -0.08 | 1.00 | 0.18 |
| Col III% (d5) | 0.79 | -0.66 | -0.61 | -0.74 | -0.58 | 0.58 | 0.58 | -0.20 | 0.22 | 0.47 | -0.19 | 0.18 | 1.00 |

4.4. Discussion

Here, ALGMA hydrogels were fabricated by methacrylating alginate using methacrylic anhydride.¹⁹ Characterization of the compressive moduli, degradation kinetics, and the swelling response to different pH conditions present ALGMA gels to be suitable for a variety of tissue engineering applications. The environmental response of the hydrogels to highly basic conditions, suggests that these gels could be used for controlled delivery applications of drugs to chronic wound environments.²⁸

ALGMA hydrogels were prepared through covalent crosslinking as well dual crosslinking using both ionic and covalent mechanisms. The mechanism of crosslinking has considerable influence on estimated compressive modulus.²⁹ Purely ionic crosslinking of these very low viscosity alginate resulted in extremely soft hydrogels with a modulus less than 1 kPa. Covalent crosslinking of the methacrylated alginate structure (**Figure 4.1**) resulted in stiffer hydrogels. This result is in line with previous studies that showed that the compressive moduli increased from step growth to chain growth to mixed mode crosslinking of polymers.^{29,30} The additional strontium ions increased the number of crosslinks, which increased the compressive moduli of the gels.³¹ Overall, the ALGMA hydrogels were tunable over the range of 0.6 to 2.5 kPa (**Figure 4.2**). Previous studies for the developing soft tissue scaffolds to encapsulate fibroblasts and hepatocytes have used hydrogels with compressive moduli from 1 to 15 kPa. The matrix remodeling activity of these encapsulated cells was observed through the analysis of their degradation activity in different conditions of hydrogel composition.^{32,33} Another study compared ionic and photocrosslinked cell-encapsulated hydrogels having similar mechanical moduli *in vivo*. The ionically crosslinked hydrogel did not retain structural integrity, whereas the stiffer covalently crosslinked hydrogels

remained intact with significant extracellular matrix (ECM) deposition on their surface, indicating successful biomaterial acceptance.³⁴

The propensity of a hydrogel to swell is inversely related to its crosslinking density. Theoretical models based on the Flory interaction parameter can be used to predict swelling behavior.³⁵ Since crosslinking density and mechanical moduli are correlated,³⁶ the softer gels were expected to degrade fastest, with stiffer gels degrading slower. Based on the compressive moduli, the step-growth gel was expected to have the largest swelling ratio, with the dually crosslinked mixed mode hydrogel swelling the least. This trend was observed for every pH condition (**Figure 4.3**). The carboxyl group on mannuronic acid has a pKa ~3.5. At pHs above the pKa, the charged carboxylate groups will repel one another, leading to a conformational change and volume increase of the hydrogel.³⁷ As such, significant increases were observed when the gels were exposed to increasingly alkali solutions. The swelling ratio was negatively correlated with compressive modulus ($R = -0.94$ with swelling ratios at pH 9) The purely ionic hydrogels with the lowest network density were observed to swell the most as expected at every pH condition, rising to 27 times their original dry weight at pH 9. The dually crosslinked hydrogels swelled significantly less than their covalently crosslinked hydrogel counterparts, with the ionic mixed mode hydrogel swelling to 13 times their original weight at the same condition. Crosslinking density and mechanism are important material properties that are correlated. As per the theory of rubber elasticity, an increase in the crosslinking density results in increased stiffness of the hydrogel.³⁶ Alginate, being an anionic polymer with carboxyl groups along its structure, is expected to swell more under basic conditions, while simultaneously being influenced by the stiffness of the hydrogel itself due to its network structure.³⁸ This propensity to swell more under basic conditions can be applied to delivery of cytokines to boost the immune response for chronic wound

treatments. Further transport phenomena characterization of optimal pore size and drug-matrix interactions can move this material towards use as a controlled release system.^{39,40}

As focus has shifted towards naturally derived hydrogels for biomedical applications for their improved biocompatibility and control of mechanical properties and degradation rates are important parameters for improved regenerative medicine applications.⁴¹ The crosslinking mechanism influences the mechanical strength with step growth being lowest and mixed mode being highest. Ionic crosslinks had a uniform impact on the compressive modulus and did not alter this trend for degradation kinetics (**Figure 4.4**). Since mechanical strength is expected to be related to degradation, the covalently crosslinked gels were anticipated to degrade faster than their dually crosslinked counterparts. The dually crosslinked hydrogels had a half-life approximated twice as long as their covalently crosslinked counterparts. The changes in swelling ratios were similar to the degradation trends, with the stiffest hydrogels swelling the least. This is in line with previous studies on photocrosslinked alginate hydrogels that showed strong correlations between increased stiffness, decreased swelling, and degradation rate characteristics.^{8,42}

Hydrogels used for tissue engineering applications must be cytocompatible. Live/dead staining images showed no cytotoxicity for NIH/3T3 cells encapsulated in the ALGMA hydrogels (**Figure 4.5**). Cell proliferation showed a strong correlation ($R = 0.86$) with the mechanical moduli. Cells encapsulated in ionic chain growth and ionic mixed mode hydrogels had cell proliferation > 60% (**Figure 4.5**). Typical monolayer cultures have reported cell viabilities of around 90% for surface-seeded chondrocytes and fibroblasts on stiffer methacrylated alginate substrates of 34 to 175 kPa elastic moduli.^{8,33}

SHG imaging of fibroblasts encapsulated in the ALGMA hydrogels showed the changes in the organization of secreted collagen. Collagen organization progressed from anisotropic to

significantly more isotropic distribution for covalently crosslinked step and chain growth gels (**Figure 4.6**). This trend continued for the dually crosslinked ALGMA hydrogels. One possible explanation for this observation is that excessive network entanglements for the mixed mode gels inhibited reorganization of the secreted collagen by the fibroblasts. Based on the swelling ratio and compressive modulus data, step growth and chain growth gels have a lower crosslinking density compared with the mixed mode gels, meaning that encapsulated cells are not restricted by the network. In one of the few studies using SHG microscopy to measure collagen organization in hydrogels, the formation and degradation of collagen fibrils appeared to be influenced positively by higher cell seeding density, however it was difficult to obtain direct cause-effect relationships.⁴³ Most studies relied on fluorescent tagging protocols for qualitative or quantitative estimation of the types of collagen secreted.^{44,45} The use of multimodal imaging, specifically polarization resolved SHG imaging is a relatively rare technique, yet it holds great promise for characterizing cell-biomaterial interactions without requiring dyes.

Factorial and Principal component analysis have been effective tools for evaluating correlations between material properties and biological responses. Studies previously conducted on modifying medium viscosity alginate with diverse functional groups sought to elucidate the macrophage-biomaterial interactions, particularly in identifying material and chemical properties that influence macrophage differentiation and reprogramming through PCA.^{20,46} Collagen secretion by fibroblasts is an integral aspect of the wound healing response, particularly with respect to the differentiation and activity of fibroblasts, which can be initiated by cytokines such as TGF- β .⁴⁷ Initiation of specific pathways such as Rho-associated protein kinase (ROCK), Yes-associated protein (YAP), TAZ (responsible for the coding of the Tafazzin gene) are often up-regulated on stiffer substrates.^{48,49} The feed-forward loop associated with stiffer substrates

influencing fibroblasts to secrete more collagen and other ECM proteins is a biomarker for cancer associated fibroblasts, as well.^{50,51} Thus, rational design of tunable hydrogels for chronic wound treatment may be improved through PCA analytical methods that examine multiple facets of materials design. The positive correlation between the swelling responses at different pH conditions and compressive moduli indicated that there was strong connection for all those trends driven by their shared negative correlation to the latter (all between $R = -0.88$ and -0.94). The initial collagen secretion showed a strong negative correlation with the FWHM of collagen organization on the final day of the cell-gel SHG observations. This suggests that cellular activity was driving these changes. Though it was difficult to ascertain an overall trend for the collagen type III levels, the PCA showed that there was a strong negative correlation between collagen type III levels and the collagen secretion levels.

The modulation of collagen secretion by fibroblasts in hydrogels for understanding mechanical cues that can alter wound healing, using non-linear optics is a relatively new approach for tissue engineering. Collagen gels have been studied in the past for their efficacy in hastening the wound healing progress towards granular tissue formation.⁵² The structure and orientation of collagen fibers have been studied for their influence on cell-mediated migration, which could play an important role in the remodeling of the wound site.⁵³ The relatively aligned collagen organization in response to the softer covalently crosslinked hydrogels, was in contrast to the relatively more isotropic response on the dually crosslinked hydrogel. Coupled with the moderately strong correlation of the FWHM at d5 to the compressive modulus in **Figure 4.7**, there is some basis for the hypothesis that the initial collagen organization being influenced by the mechanical properties of the encapsulating hydrogel. Histological studies have shown that collagen is highly aligned in hypertrophic and keloid scar tissues as compared to being stochastic

in normal skin.^{54,55} Highly aligned collagen fibers have been observed with increased collagen III % for inguinal hernia⁵⁶ Greater interest has been generated towards replicating isotropic collagen organization for improved wound healing, particularly for treatment of chronic wounds.⁵⁷ Dually crosslinked hydrogels show promise as hydrogels that promote isotropic collagen organization, and when combined with their moderately wide range of swelling responses, as viable drug delivery systems to promote chronic wound healing.

4.5. Conclusions

In this study, we successfully fabricated different methacrylated alginate hydrogels using covalent and ionic crosslinking strategies with tunable mechanical properties. Diverse polymerization mechanisms (such as step and chain growth) were used to fabricate alginate hydrogels ranging from very soft at 0.7 kPa to relatively stiffer gels prepared through dual ionic and covalent crosslinking. We demonstrated possible links between the increased swelling response and the crosslinking mechanisms for all hydrogel formulations under basic pH conditions, as expected from the anionic nature of the alginate polymer. Stiffer gels swelled to a lesser extent than softer gels across the same pH condition, possibly due to differences arising from the rubber elasticity theory. These ALGMA hydrogels were found to be cytocompatible when encapsulating NIH/3T3 fibroblasts. Stiffer gels were able to induce isotropic collagen organization, similar to that of healthy dermal tissues.

4.6. References

1. Diegelmann, R. F. & Evans, M. C. Wound healing: an overview of acute, fibrotic and delayed healing. *Front. Biosci.* **9**, 283–9 (2004).
2. Enoch, S., Leaper, D. J. & Beldon, P. Basic science of wound healing. *Surg.* **28**, 409–412 (2010).

3. Schneider, L. A., Korber, A., Grabbe, S. & Dissemond, J. Influence of pH on wound-healing: A new perspective for wound-therapy? *Arch. Dermatol. Res.* **298**, 413–420 (2007).
4. Edmonds, M., Bates, M., Doxford, M., Gough, A. & Foster, A. Topical treatment: Which dressing to choose. *Diabetes. Metab. Res. Rev.* **16**, 47–50 (2000).
5. Centers for Disease Control and Prevention [CDC]. National diabetes statistics report: Estimates of diabetes and its burden in the united states. 2009–2012 (2017). doi:10.1177/1527154408322560
6. Lim, H. W. *et al.* The burden of skin disease in the United States. *J. Am. Acad. Dermatol.* **76**, 958–972.e2 (2017).
7. Bickers, D. R. *et al.* The burden of skin diseases: 2004. A joint project of the American Academy of Dermatology Association and the Society for Investigative Dermatology. *J. Am. Acad. Dermatol.* **55**, 490–500 (2006).
8. Jeon, O., Bouhadir, K. H., Mansour, J. M. & Alsberg, E. Photocrosslinked alginate hydrogels with tunable biodegradation rates and mechanical properties. *Biomaterials* **30**, 2724–2734 (2009).
9. Baer, A. E., Wang, J. Y., Kraus, V. B. & Setton, L. A. Collagen gene expression and mechanical properties of intervertebral disc cell-alginate cultures. *J. Orthop. Res.* **19**, 2–10 (2001).
10. Crescenzi, V., Cornelio, L., Di Meo, C., Nardecchia, S. & Lamanna, R. Novel hydrogels via click chemistry: Synthesis and potential biomedical applications. *Biomacromolecules* **8**, 1844–1850 (2007).
11. Polizzotti, B. D., Fairbanks, B. D. & Anseth, K. S. Three-dimensional biochemical patterning of click-based composite hydrogels via thiolene photopolymerization. *Biomacromolecules* **9**, 1084–1087 (2008).
12. Dondoni, A. The emergence of thiol-ene coupling as a click process for materials and bioorganic chemistry. *Angew. Chemie - Int. Ed.* **47**, 8995–8997 (2008).
13. Peppas, N. A., Hilt, J. Z., Khademhosseini, A. & Langer, R. Hydrogels in biology and medicine: From molecular principles to bionanotechnology. *Adv. Mater.* **18**, 1345–1360 (2006).
14. Smeds, K. A. & Grinstaff, M. W. Photocrosslinkable polysaccharides for in situ hydrogel formation. *J. Biomed. Mater. Res.* **54**, 115–121 (2001).
15. Nettles, D. L., Vail, T. P., Morgan, M. T., Grinstaff, M. W. & Setton, L. A. Photocrosslinkable hyaluronan as a scaffold for articular cartilage repair. *Ann. Biomed. Eng.* **32**, 391–397 (2004).

16. Podual, K., Doyle, F. J. & Peppas, N. A. Preparation and dynamic response of cationic copolymer hydrogels containing glucose oxidase. *Polymer (Guildf)*. **41**, 3975–3983 (2000).
17. Peppas, N. A. & Khare, A. R. Preparation, structure and diffusional behavior of hydrogels in controlled release. *Adv. Drug Deliv. Rev.* **11**, 1–35 (1993).
18. Scott, R. A. & Peppas, N. A. Highly crosslinked, PEG-containing copolymers for sustained solute delivery. *Biomaterials* **20**, 1371–1380 (1999).
19. Chou, A. I. & Nicoll, S. B. Characterization of photocrosslinked alginate hydrogels for nucleus pulposus cell encapsulation. *J. Biomed. Mater. Res. - Part A* **91**, 187–194 (2009).
20. Bygd, H. C. & Bratlie, K. M. The effect of chemically modified alginates on macrophage phenotype and biomolecule transport. *J. Biomed. Mater. Res. - Part A* **104**, 1707–1719 (2016).
21. ASTM. *Standard Test Method for Bulk Properties of Textured Yarns*. **81**, 4–9 (2016).
22. Akilbekova, D. & Bratlie, K. M. Quantitative characterization of collagen in the fibrotic capsule surrounding implanted polymeric microparticles through second harmonic generation imaging. *PLoS One* **10**, 1–17 (2015).
23. Bygd, H. C., Forsmark, K. D. & Bratlie, K. M. Altering in vivo macrophage responses with modified polymer properties. *Biomaterials* **56**, 187–197 (2015).
24. Grasdalen, H. High-field, ¹H-n.m.r. spectroscopy of alginate: sequential structure and linkage conformations. *Carbohydr. Res.* **118**, 255–260 (1983).
25. Bae, H. *et al.* Cell-laden microengineered pullulan methacrylate hydrogels promote cell proliferation and 3D cluster formation. *Soft Matter* **7**, 1903–1911 (2011).
26. Rowley, J. A., Madlambayan, G. & Mooney, D. J. Alginate hydrogels as synthetic extracellular matrix materials. *Biomaterials* **20**, 45–53 (1999).
27. Paul, W. & Sharma, C. P. Chitosan and Alginate Wound Dressings : A Short Review. *Trends Biomater. Artif. Organs* **18**, 18–23 (2004).
28. Harding, K., Morris, H. & Patel, G. Science, Medicine, and the Future: Healing chronic wounds. *Br. Med. J.* **326**, 433–436 (2003).
29. Reddy, S. K., Anseth, K. S. & Bowman, C. N. Modeling of network degradation in mixed step-chain growth polymerizations. *Polymer (Guildf)*. **46**, 4212–4222 (2005).
30. Kharkar, P. M., Kloxin, A. M. & Kiick, K. L. Dually degradable click hydrogels for controlled degradation and protein release. *J. Mater. Chem. B* **2**, 5511–5521 (2014).

31. Samorezov, J. E., Morlock, C. M. & Alsberg, E. Dual Ionic and Photo-Crosslinked Alginate Hydrogels for Micropatterned Spatial Control of Material Properties and Cell Behavior. *Bioconjug. Chem.* **26**, 1339–1347 (2015).
32. Chan, A. W. & Neufeld, R. J. Tuneable semi-synthetic network alginate for absorptive encapsulation and controlled release of protein therapeutics. *Biomaterials* **31**, 9040–9047 (2010).
33. Hunt, N. C., Smith, A. M., Gbureck, U., Shelton, R. M. & Grover, L. M. Encapsulation of fibroblasts causes accelerated alginate hydrogel degradation. *Acta Biomater.* **6**, 3649–3656 (2010).
34. Chou, A. I., Akintoye, S. O. & Nicoll, S. B. Photo-crosslinked alginate hydrogels support enhanced matrix accumulation by nucleus pulposus cells in vivo. *Osteoarthr. Cartil.* **17**, 1377–1384 (2009).
35. Peppas, N. A., Huang, Y., Torres-Lugo, M., Ward, J. H. & Zhang, J. Physiochemical foundations and structural design of hydrogels in medicine and biology. *Annu. Rev. Biomed. Eng.* **2**, 9–29 (2000).
36. Anseth, K. S., Bowman, C. N. & Brannon-Peppas, L. Mechanical properties of hydrogels and their experimental determination. *Biomaterials* **17**, 1647–1657 (1996).
37. Chan, A. W. & Neufeld, R. J. Modeling the controllable pH-responsive swelling and pore size of networked alginate based biomaterials. *Biomaterials* **30**, 6119–6129 (2009).
38. Khare, A. R. & Peppas, N. A. Swelling/deswelling of anionic copolymer gels. *Biomaterials* **16**, 559–567 (1995).
39. Jeon, O., Powell, C., Solorio, L. D., Krebs, M. D. & Alsberg, E. Affinity-based growth factor delivery using biodegradable, photocrosslinked heparin-alginate hydrogels. *J. Control. Release* **154**, 258–266 (2011).
40. Drury, J. L. & Mooney, D. J. Hydrogels for tissue engineering: Scaffold design variables and applications. *Biomaterials* **24**, 4337–4351 (2003).
41. Nicodemus, G. D. & Bryant, S. J. Cell Encapsulation in Biodegradable Hydrogels for Tissue Engineering Applications. *Tissue Eng. Part B. Rev.* **14**, 149–165 (2008).
42. Jeon, O., Powell, C., Ahmed, S. M. & Alsberg, E. Biodegradable, photocrosslinked alginate hydrogels with independently tailorable physical properties and cell adhesivity. *Tissue Eng. Part A* **16**, 2915–2925 (2010).
43. Olderøy, M. *et al.* Biochemical and structural characterization of neocartilage formed by mesenchymal stem cells in alginate hydrogels. *PLoS One* **9**, (2014).
44. Stuart, K. & Panitch, A. Characterization of gels composed of blends of collagen I, collagen III, and chondroitin sulfate. *Biomacromolecules* **10**, 25–31 (2009).

45. Chen, X. G., Wang, Z., Liu, W. S. & Park, H. J. The effect of carboxymethyl-chitosan on proliferation and collagen secretion of normal and keloid skin fibroblasts. *Biomaterials* **23**, 4609–4614 (2002).
46. Bygd, H. C. & Bratlie, K. M. Investigating the synergistic effects of combined modified alginates on macrophage phenotype. *Polymers (Basel)*. **8**, 422 (2016).
47. Gabbiani, G. The myofibroblast in wound healing and fibrocontractive diseases. *J. Pathol.* **200**, 500–503 (2003).
48. Wynn, T. A. Cellular and molecular mechanisms of fibrosis. *J. Pathol.* **214**, 199–210 (2008).
49. Calvo, F. *et al.* Mechanotransduction and YAP-dependent matrix remodelling is required for the generation and maintenance of cancer-associated fibroblasts. *Nat Cell Biol* **15**, 637–646 (2013).
50. Mao, Y., Keller, E. T., Garfield, D. H., Shen, K. & Wang, J. Stromal cells in tumor microenvironment and breast cancer. *Cancer Metastasis Rev.* **32**, 303–315 (2013).
51. Grainger, D. W. All charged up about implanted biomaterials. *Nat. Biotechnol.* **31**, 507–509 (2013).
52. Tronci, G. *et al.* Protease-sensitive atelocollagen hydrogels promote healing in a diabetic wound model. *J. Mater. Chem. B* **4**, 7249–7258 (2016).
53. Yasui, T., Tohno, Y. & Araki, T. Determination of collagen fiber orientation in human tissue by use of polarization measurement of molecular second-harmonic-generation light. **43**, 10–14 (2004).
54. Verhaegen, P. D. H. M. *et al.* Differences in collagen architecture between keloid, hypertrophic scar, normotrophic scar, and normal skin: An objective histopathological analysis. *Wound Repair Regen.* **17**, 649–656 (2009).
55. Verhaegen, P. D. H. M. *et al.* Collagen bundle morphometry in skin and scar tissue: A novel distance mapping method provides superior measurements compared to Fourier analysis. *J. Microsc.* **245**, 82–89 (2012).
56. Klinge, U. *et al.* Synthesis of type I and III collagen, expression of fibronectin and matrix metalloproteinase 1 and 13 in hernias of patients with inguinal hernia. *Int J Surg Invest.* **1**, 219–227 (1999).
57. Greaves, N. S., Ashcroft, K. J., Baguneid, M. & Bayat, A. Current understanding of molecular and cellular mechanisms in fibroplasia and angiogenesis during acute wound healing. *J. Dermatol. Sci.* **72**, 206–217 (2013).

CHAPTER 5

POLY-L-ARGININE MODIFICATIONS ALTER THE ORGANIZATION AND SECRETION OF COLLAGEN IN SKH1-E MICE

Functionalized biomaterials interface with tissue upon implantation. There is a growing need to understand how materials properties influence this interaction so that efficient tissue engineering systems can be developed. In this study, we characterize collagen organization in response to functionalized glass beads implanted in SKH1-E mice. Poly-L-arginine (PLR) was modified with arginine derivatives to create a functionalized surface and was coated on glass beads. Tissue sections were removed 28 days post-implantation and were imaged using second harmonic generation (SHG) microscopy. These chemical modifications were able to alter the collagen distribution from highly aligned to disordered (~ 17 to 80° full width at half-maximum (FWHM)) and the collagen III/I ratio (0.02 to 0.42). Principal component analysis (PCA) comparing the physical properties of the modifiers (e.g. hydrophobicity, molar volume, freely rotating bonds, polarizability) with the SHG analytically derived parameters (e.g. collagen III/I ratio, collagen orientation) was performed. Chemical properties of the PLR-like modifications including lipophilicity, along with the number of freely rotating bonds and the polarizability had significant effects on collagen organization, both in terms of collagen orientation as well as the production of collagen III. These findings demonstrate the possibility of tuning the foreign body response in terms of collagen deposition and organization, to positively influence the acceptance of implanted biomaterials.

5.1. Introduction

The foreign body response is a complex series of processes initiated upon implantation of a biomaterial. The affected tissue responds to the implant through the secretion of chemokines, cytokines, and matrix metalloproteinases (MMPs) in an attempt to restore normal function at the implant site.¹ Different cell types participate in the foreign body response with specific roles as the tissue seeks to halt blood flow and repair the damaged extracellular matrix (ECM).²⁻⁴ The foreign body response interferes with the cascade of cell signaling pathways involved in normal wound closure by extending the inflammatory response phase.⁵ This hindered wound healing response to the implant consists of protein adsorption on the implant surface, recruitment of monocytes, monocyte differentiation from macrophages, macrophage fusion into foreign body giant cells, differentiation and activation of fibroblasts to myofibroblasts, and fibrotic encapsulation.⁶ Post inflammation fibroblasts and myofibroblasts secrete collagen, particularly types I and III, in the case of dermal tissues to synthesize a fibrotic layer in response to the implant. The organization of collagen in this fibrous collagen-rich layer can vary from well-aligned to a stochastic distribution of collagen fibrils.⁷ These deposited collagen fibrils become active components of the basement membrane reconstruction, by promoting the attachment of endothelial cells.⁸ During the remodeling phase of wound healing, collagen fibers are aligned stochastically similar to that of unwounded tissues.⁹ Healed tissues often do not recover their full mechanical strength, regaining only around 80% to the levels prior to the tissue damage.¹⁰ Scar tissue or incompletely healed tissue contain bundles of organized collagen fibers, compared to the isotropic organization in undamaged tissue.¹¹ In scar tissue, collagen type III is replaced by fibrillar collagen type III, as observed in fibrotic capsules around implant sites.¹² Isotropic collagen orientation with similar levels of collagen III as that in healthy dermal tissues, would be the ideal collagen response to implanted biomaterials.¹³

Multimodal imaging techniques such as second harmonic generation microscopy (SHG) enable sensitive, dye-free imaging of collagen in various clinical samples.¹⁴ In this non-linear microscopy process, two photons of the same wavelength are impinged spatially and temporally on a sample. When these photons interact with non-centrosymmetric moieties, they double in frequency.¹⁵ The non-centrosymmetric chemical structure of collagen arising from its triple helical structure, make it an SHG-active biomolecule. Changes in collagen density, organization, and type can be determined using SHG analysis. Other biomolecules that have been imaged using SHG are myosin in muscle tissue and cholesterol crystals in atherosclerotic plaques.^{16,17} SHG microscopy of triple helical collagen fibers can provide more information about the collagen response through susceptibility tensor analysis.^{14,15} These parameters are linked to the material properties, based on the molecular origins of the collagen signal arising from the ratio of their methylene to peptide bonds.¹⁸ Polarization resolved SHG microscopy is capable of differentiating between diverse types of collagen in dermal samples by generating a map of the susceptibility tensor components. Specifically, the ratio of collagen types I and III can be estimated by analyzing ratio of the nonlinear susceptibility tensor elements.¹⁴ Collagen type I is significantly more prevalent than type III in human skin, and the ratio of III/I is ~ 30% for unwounded adult dermis.¹⁹ As wound healing progresses, this ratio can rise to ~ 90% and gradually decreases during the re-epithelialization process.²⁰ Elevated levels of collagen type III are linked to a prolonged wound healing process. In some cases, these elevated levels are associated with hypertrophic scarring or internal injuries such as inguinal hernia.^{21,20,22} However, there is no consensus on the role played by collagen type III on the wound healing process, or the biomaterials properties that can induce different levels of collagen type III. It has been observed that as wound healing progresses towards the granulation phase, collagen I is replaced by collagen III particularly for tissues that undergo significant

mechanical stress, which indicates a difference in mechanotransductive signaling roles in the two types of collagen in the ECM^{23,24}. This change in significant tissue strength for higher collagen III is also observed for tissues prone to developing different types of hernias.²⁰ During scar tissue formation, collagen type III is organized with collagen type I in aligned bundles, while they are stochastically arranged in healthy tissue.¹³

Our study focuses on the analysis of the collagen response to functionalized glass beads implanted in SKH1-E mice. These mice are commonly used for studying dermal wound healing responses as they are hairless, making application and observation of topical treatments relatively easy.^{25,26} We used a library of chemical modifiers based off the amino acid arginine and its derivatives, which have been previously studied for their ability to influence the synthesis of collagen by fibroblasts in *in vitro*,²⁷ to examine how materials properties alter collagen organization. In another study examining collagen responses to materials, functionalized polystyrene microparticles were studied and it was found that dimethylamino functionalized particles resulted in isotropic collagen organization and a thin fibrotic capsule.²⁸ Poly-L-arginine (PLR) modified with arginine derivatives and coated on glass beads showed the influence of collagen directionality on the speed of fibroblast migration and secretion of angiogenic cytokines such as vascular endothelial growth factor.²⁹ Here, we have uncovered physicochemical properties of these materials that correlate with collagen organization and the ratio of collagen type III/I. Analyses such as this aim to improve rational design for biomaterials that can tune the fibrotic response towards better implant acceptance.

5.2. Materials and Methods

Experiments were performed with a minimum of three replicates. Results were compared to controls of unmodified PLR and uncoated glass beads. All materials were purchased from Sigma (St. Louis, MO) and used as received, unless otherwise indicated. Fresh deionized (DI) water (Milli-Q Nanopure, Thermo Scientific, Waltham, MA) and sterile 1X phosphate buffered saline (PBS, diluted from 10X solution (Fisher, Pittsburgh, PA), to 0.1 M, pH 7.4) was used throughout this study.

5.2.1. Materials

Surface modifiers were coupled to 29,000 Da PLR (Alamanda Polymers, Huntsville, AL). These modifiers are shown in **Figure 5.1** and include β -(1,2,4-triazol-3-yl)-alanine, 2-amino-3-guanidinopropionic acid (Matrix Scientific, Elgin, SC), 3-guanidinopropionic acid, nitroarginine, creatine (Acros Organics, Pittsburgh, PA), carnitine, citrulline, 5-hydroxylysine, acetylglutamine, N-carbamyl- α -aminoisobutyric acid, acetyl-carnitine, 2,4-diaminobutyric acid, acetylnornithine, albizziin, and arginine (Amresco, Solon, OH).

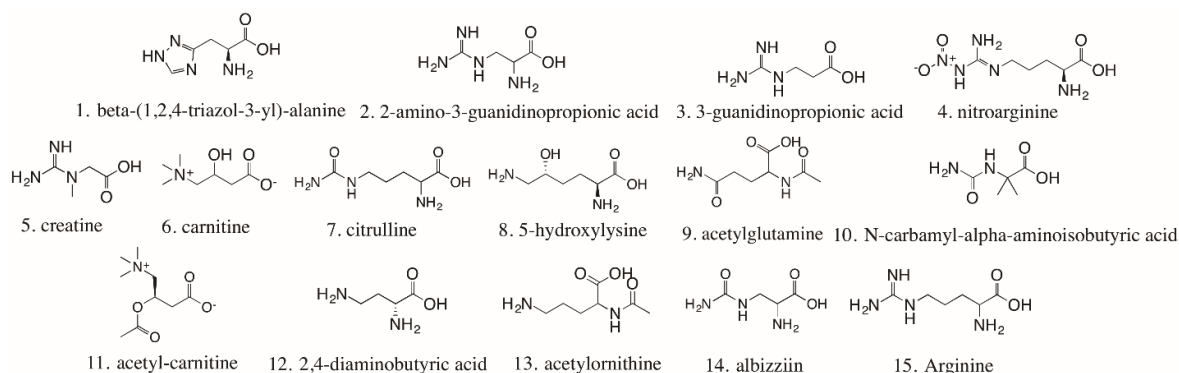


Figure 5.1. Chemical structures of the molecules used in the modification of poly-L-arginine (PLR). The arginine derivatives shown here are numbered for easier identification in experiments and discussion throughout the paper.

5.2.2. PLR Modification

The fifteen different modifiers (**Figure 5.1**) were coupled to PLR using 1-ethyl-3-(3-dimethylaminopropyl)carbodiimide (EDC, Oakwood Chemical, West Columbia, SC). These materials were modified as previously described²⁹ using 4 ml of a 2.5 mg/ml solution of PLR in PBS with 100 molar equivalents of arginine derivative. EDC (200 mg) was added to the scintillation vial and stirred for 4 h at room temperature. The modified polymers were dialyzed against H₂O for 24 h and subsequently lyophilized (4.5 L, Labconco, Kansas City, MO). The modified PLR was re-suspended in PBS at 0.1% w/v and stored at -20°C.

5.2.3. Ethics Statement

The research protocol was approved by the local animal ethics committees at Iowa State University (Institutional Animal Care and Use Committee) prior to initiation of the study.

5.2.4. Animals

6-week-old female SKH1-E mice were obtained from Charles River Laboratories (Wilmington, MA). The mice were maintained at the animal facilities in the College of Veterinary Medicine at Iowa State University, accredited by the American Association of Laboratory Animal care, and were housed under standard conditions with a 12-hour light/dark cycle. Both water and food were provided *ad libitum*.

5.2.5. Subcutaneous Injections

Animal tissue specimens previously obtained²⁹ were used here. Briefly, injections were performed according to ISO 10993-6:2007. Glass beads (105 – 150 μm , Warrington, PA) were sterilized via autoclave and were coated with each of the fifteen modified PLRs, PLL (poly-L-lysine), and unmodified PLR. Uncoated glass beads were also tested. Mice were anesthetized via isoflurane inhalation at a concentration of 1-4% isoflurane/balance O_2 to minimize movement. The backs of the mice were scrubbed with 70% isopropyl alcohol and five modified glass beads (10% v/v, 100 μl) were injected in an array format with a sixth injection of unmodified PLR coated beads. All experiments were conducted in quintuplicate. After 28 days, the mice were euthanized via CO_2 asphyxiation. The injected beads and surrounding tissue was excised. Sections were fixed in 10% formalin, embedded in paraffin, sectioned into 5 μm slides, and mounted on glass slides.

5.2.6. Collagen Gel Preparation

Collagen type I (BD Biosciences, Franklin Lakes, NJ) was solubilized in acetic acid (20 mM) at 10 mg/mL to prepare a stock solution. This solution was mixed on ice with 10 \times PBS, 1 M NaOH and deionized water to prepare aliquots of 1, 2, 4 and 6 mg/mL of collagen type I solutions. This solution was then pipetted on to glass coverslips and gelled at 37°C for 1 h.

5.2.7. Second Harmonic Generation (SHG)

The laser system is a mode-locked Ti:sapphire laser (100 fs pulse width, 1 kHz repetition rate, Libra, Coherent, Santa Clara, CA) that produces an 800 nm fundamental. The average power at the samples was kept at 1 – 10 mW to avoid tissue damage using a half-wave plate and a Glan-Thompson polarizer (Thorlabs, Newton, NJ). SHG images were collected in transmission mode. An inverted microscope stage (AmScope, Irvine, CA) and a 20× Nikon Plan Fluorite objective (0.50 NA, 2.1 mm) were used to focus the 800 nm beam. The second harmonic signal was collected with a 40× Nikon water immersion objective (0.8 NA, 3.5 mm). The signal was reflected with a dichroic mirror (Thorlabs) and the fundamental beam was removed using a short pass filter < 450 nm (Thorlabs) and an 808 nm notch filter (Melles Griot, Rochester, NY). The signal was detected using an intensified CCD camera (iCCD, iStar 334T, Andor, Belfast, UK) with 512 × 512 active pixels. The polarization of the incoming beam was changed using a Glan-Thompson polarizer and a half-wave plate mounted on a motor driven rotational stage (Thorlabs). These optics were inserted before the focusing objective.

Images of tissue sections and collagen standard curve samples were collected every 10° from 0 to 350°. A minimum of three sets of polarization images for each experimental condition were taken. Birefringence was calculated to be within the resolution of the polarization angles for the thickness of tissues (5 μm) used in this study.

5.2.8. Image Processing

The intensity of the second harmonic signal of collagen as a function of polarization angle of the incident laser beam can be written as:

$$I_{SHG} = c \cdot \left\{ \left[\sin^2(q_e - q_0) + \left(\frac{C_{zzz}}{C_{zxx}} \right) \cos^2(q_e - q_0) \right]^2 + \left(\frac{C_{xzx}}{C_{zxx}} \right)^2 \sin^2(2(q_e - q_0)) \right\} \quad (1)$$

where $\frac{C_{zzz}}{C_{zxx}}$ and $\frac{C_{xzx}}{C_{zxx}}$ are second-order susceptibility tensor element ratios; θ_e and θ_0 are the incident polarization angle and collagen fiber angle, respectively; and c is a normalization constant. Tensor elements can be used as a contrast mechanism for distinguishing sources of SHG signal.^{12,30} Images were filtered using a median noise filter (3×3) to attenuate the salt and pepper noise in the acquired images (ImageJ, NIH, Bethesda, MD). Images were binned to obtain regions of interest (ROIs) of 2×2 pixels. Collagen orientation angles and second-order susceptibility tensor element ratios were determined for every ROI by fitting to a Levenberg-Marquardt algorithm using Matlab (MathWorks, Natick, MA). Photon counts below 5 counts per pixel were excluded from the analysis as this was determined to be below the limit of detection for this setup. The limit of detection was determined by measuring ambient noise detected by the iCCD when the incoming light was blocked. The Matlab script generated images displaying the orientation angles of collagen determined for each ROI and heat maps for the second-order susceptibility tensor element ratios. Histograms for both were also obtained.

5.2.9. Statistics and Data Analysis

Statistical analysis was performed using JMP® statistical software (Cary, NC). Statistical significance of the mean comparisons was determined by a two-way ANOVA. Pair-wise comparisons were analyzed with Tukey's honest significant difference test. Differences were considered statistically significant for $p < 0.05$. Principal component analysis (PCA) was conducted to explain relationships between modifier properties and experimentally derived parameters. The principal components were calculated as linear combinations of the plotted parameters, to denote the directions of maximum variance. The correlations between different properties can be observed as projected values against the two principal components (PC1 and PC2).

5.3. Results

5.3.1. Collagen Signal

Collagen signal was measured and compared against a standard curve of collagen concentration versus SHG signal intensity which was fit using the equation below ($R^2 = 0.99$, **Figure 5.2A**).

$$I_{\text{SHG}} = (-7.75 \times 10^5)x^2 + (3.14 \times 10^7)x \quad (2)$$

where x is the collagen concentration in mg/mL

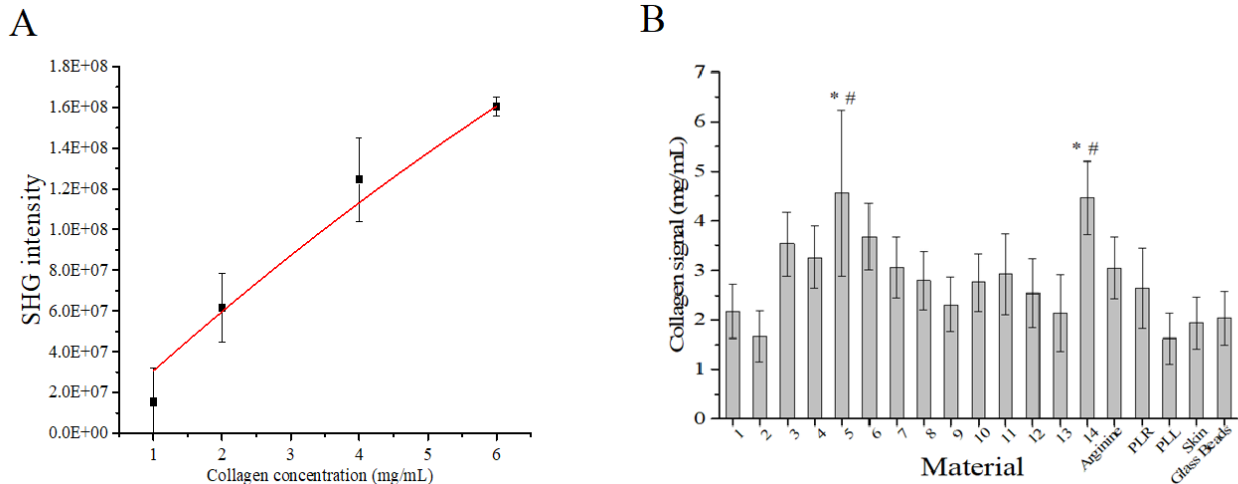


Figure 5.2. Quantification of collagen surrounding implanted glass beads coated with modified PLR. (A) Standard curve for collagen type I concentration. The SHG intensity is plotted against the known concentration of collagen concentration. (B) Quantification of collagen concentration surrounding implants. Data represents the mean \pm standard deviation (SD). $n = 15$. Statistical analysis through two-way ANOVA and Tukey's HSD post-hoc test. * $p < 0.05$.

There were no significant differences in the amount of collagen present in 16 of the 18 modifications tested *ex vivo* (Table 5.1). The collagen signal in response to the creatine and albizziin modifications were ~ 2 -fold higher than the control samples of naïve glass bead and untreated skin samples (Figure 5.2B).

Table 5.1. Approximated collagen concentration and collagen type III ratio surrounding implanted glass beads coated with modified PLR. Data represents the mean \pm standard error. $n = 3$

| Modification | Collagen signal | |
|---------------------------------------|-----------------|--------------------|
| | (in mg/ml) | Collagen III ratio |
| β -(1,2,4-triazol-3-yl)-alanine | 2.17 ± 0.54 | 0.16 ± 0.04 |
| 2-amino-3-guanidinopropionic acid | 1.67 ± 0.51 | 0.18 ± 0.04 |
| 3-guanidinopropionic acid | 3.53 ± 0.65 | 0.19 ± 0.05 |
| Nitroarginine | 3.27 ± 0.63 | 0.36 ± 0.08 |
| Creatine | 4.56 ± 0.75 | 0.05 ± 0.02 |

Table 5.1 continued

| Modification | Collagen signal (in mg/mL) | Collagen III ratio |
|--|---------------------------------------|---------------------------|
| Carnitine | 3.68 ± 0.66 | 0.05 ± 0.01 |
| Citrulline | 3.06 ± 0.61 | 0.02 ± 0.01 |
| 5-hydroxylysine | 2.80 ± 0.59 | 0.16 ± 0.03 |
| Acetyl glutamine | 2.31 ± 0.55 | 0.08 ± 0.02 |
| N-carbamyl- α -aminoisobutyric acid | 2.76 ± 0.59 | 0.07 ± 0.01 |
| Acetylcarnitine | 2.92 ± 0.81 | 0.10 ± 0.03 |
| 2,4-diaminobutyric acid | 2.54 ± 0.70 | 0.09 ± 0.02 |
| Acetyloronithine | 2.14 ± 0.77 | 0.09 ± 0.01 |
| Albizziin | 4.46 ± 0.74 | 0.42 ± 0.13 |
| Arginine | 3.05 ± 0.61 | 0.18 ± 0.03 |
| Poly-L-arginine | 2.64 ± 0.81 | 0.21 ± 0.03 |
| Poly-L-lysine | 1.62 ± 0.51 | 0.07 ± 0.03 |
| Skin | 1.94 ± 0.53 | 0.26 ± 0.07 |
| Glass Beads | 2.04 ± 0.54 | 0.14 ± 0.04 |

5.3.2. Collagen Organization

The collagen organization was quantified by fitting the obtained histograms with Gaussian curves (**Figure 5.3**). Using the full-width at half-maximum (FWHM) values of the Gaussian fits, there were clear differences for some modifiers (**Table 5.2**). Collagen organization in response to modifications carnitine (Mod 6), 5-hydroxylysine (Mod 8), acetylcarnitine (Mod 11), albizziin (Mod 14), Poly-L-lysine (PLL) and arginine (Mod 15) was relatively isotropic.

The isotropy for these modifications was confirmed by an algorithm referred to as an isotropy check, given below as Equation 3. The half-width of the confidence interval (CI_{Height}) was subtracted from the peak of the Gaussian fit (Height) of the histograms and if this peak was greater than 125 points than the Average plus the half-width of the confidence interval of the average (CI_{Average}), the peak was considered a false value.

$$\text{If } [\text{Height} - CI_{\text{Height}}] > [\text{Average} + CI_{\text{Average}} + 125] \quad (3)$$

Then Collagen Organization = Isotropic

This algorithm was applied to modifications where the peaks arose from only one or two bins, with the remaining bins being statistically similar. The FWHM for the nitroarginine modification ($25 \pm 4^\circ$) showed highly aligned collagen organization whereas organization for the arginine modification was relatively isotropic and failed the isotropy check test. Comparisons of citrulline ($55 \pm 11^\circ$) to albizziin (isotropic organization) and 2-amino-3-guanidinopropionic acid ($55 \pm 10^\circ$) to arginine (isotropic organization) modifications showed clear differences in collagen response. These modifications have similar chemical structure with the exception that citrulline and arginine contain two additional CH_2 groups, compared to their albizziin and 2-amino-3-guanidinopropionic acid counterparts. The most aligned collagen response was observed for N-carbamyl- α -aminoisobutyric acid ($15 \pm 3^\circ$) while the 3-guanidinopropionic acid modification elicited the widest, recognized (based on the isotropy check) collagen organization with a FWHM of $78 \pm 1^\circ$. The area under the curve was tabulated from the orientation angle curve fits (**Table 5.2**). The area under the curve was significantly higher for the citrulline modification (15099 ± 3508), compared to the response of all other modifications.

Table 5.2. Collagen organization (measured as FWHM) and the area under the fit for tissue surrounding implanted glass beads coated with modified PLR. Data represents the mean \pm standard error. n = 3

| Modification | FWHM | Angle Fit Area |
|--|-------------|-----------------------|
| β -(1,2,4-triazol-3-yl)-alanine | 17 \pm 2 | 4530 \pm 562 |
| 2-amino-3-guanidinopropionic acid | 55 \pm 10 | 6229 \pm 1306 |
| 3-guanidinopropionic acid | 78 \pm 1 | 7127 \pm 984 |
| Nitroarginine | 25 \pm 4 | 9298 \pm 1382 |
| Creatine | 16 \pm 3 | 4646 \pm 794 |
| Carnitine | -- | -- |
| Citrulline | 55 \pm 11 | 15099 \pm 3508 |
| 5-hydroxylysine | -- | -- |
| Acetyl glutamine | 17 \pm 6 | 2222 \pm 728 |
| N-carbamyl- α -aminoisobutyric acid | 15 \pm 3 | 3608 \pm 868 |
| Acetylcarnitine | -- | -- |
| 2,4-diaminobutyric acid | 23 \pm 5 | 3080 \pm 634 |
| Acetyloronithine | 19 \pm 4 | 4299 \pm 880 |
| Albizziin | -- | -- |
| Arginine | -- | -- |
| Poly-L-arginine | 29 \pm 3 | 7773 \pm 862 |
| Poly-L-lysine | -- | -- |
| Skin | 41 \pm 5 | 9292 \pm 1085 |
| Glass Beads | 24 \pm 2 | 7696 \pm 723 |

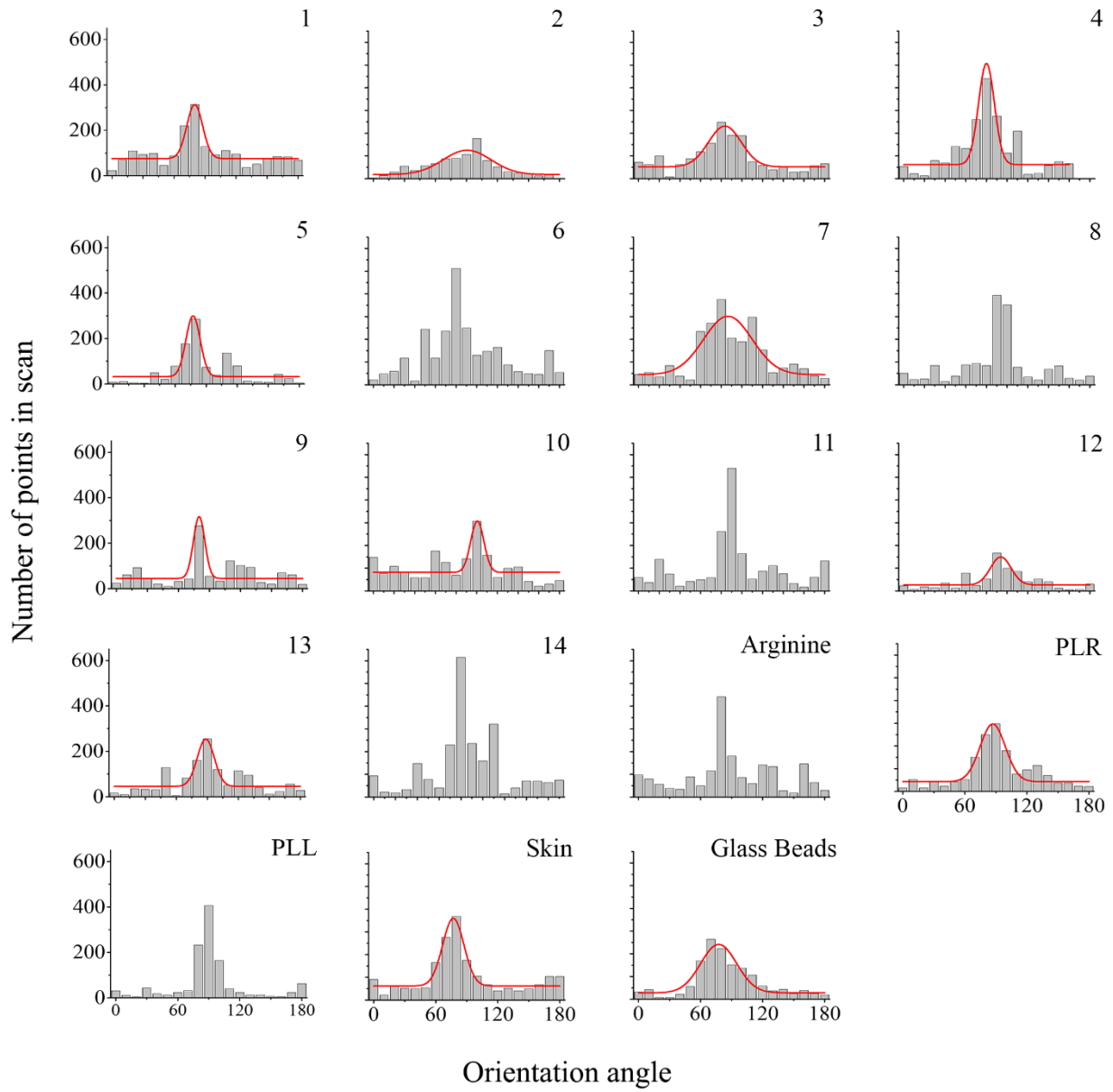


Figure 5.3. Histograms of collagen organization surrounding implanted glass beads coated with modified PLR. The bars represent experimentally acquired data. The red line is the Gaussian fit to the data.

5.3.3. Collagen III Secretion

The nonlinear susceptibility tensor ratios were calculated for each ROI and were plotted as histograms (**Figure 5.4**), which were then used to estimate the collagen III presence. A gradient curve previously obtained²⁸ for collagen III concentration was used to estimate the collagen III/I ratio, thus enabling comparisons of the type of collagen deposited surrounding the different chemical modifications (**Table 5.1**). Nitroarginine ($36 \pm 8 \%$) resulted in almost twice the amount of collagen III surrounding the implant compared to arginine ($18 \pm 3 \%$). As noted above, collagen surrounding the nitroarginine modification was also more isotropic than collagen surrounding the arginine modification. In comparing the 2-amino-3-guanidinopropionic acid and arginine modifications, which differ by two CH₂ groups, the fiber organization was significantly different, with the former being more oriented. In contrast, both modifications resulted in similar levels of collagen type III surrounding the implant (18% , $p > 0.05$). In the case of albizziin and citrulline modifications, citrulline was more isotropic than albizziin and resulted in twenty times less collagen type III than albizziin ($2 \pm 0 \%$ for citrulline and $42 \pm 13\%$ for albizziin) surrounding the implant. Citrulline has two additional CH₂ groups separating the urea and amine functional groups than albizziin. The PLL coating resulted in a third the amount of collagen type III ($7 \pm 2 \%$) surrounding the implant compared to the PLR coating ($21 \pm 3 \%$). Converting the urea functional group on albizziin to a guanidine (2-amino-3-guanidinopropionic acid) resulted in a two-fold decrease in the collagen type III levels in the neighboring tissue.

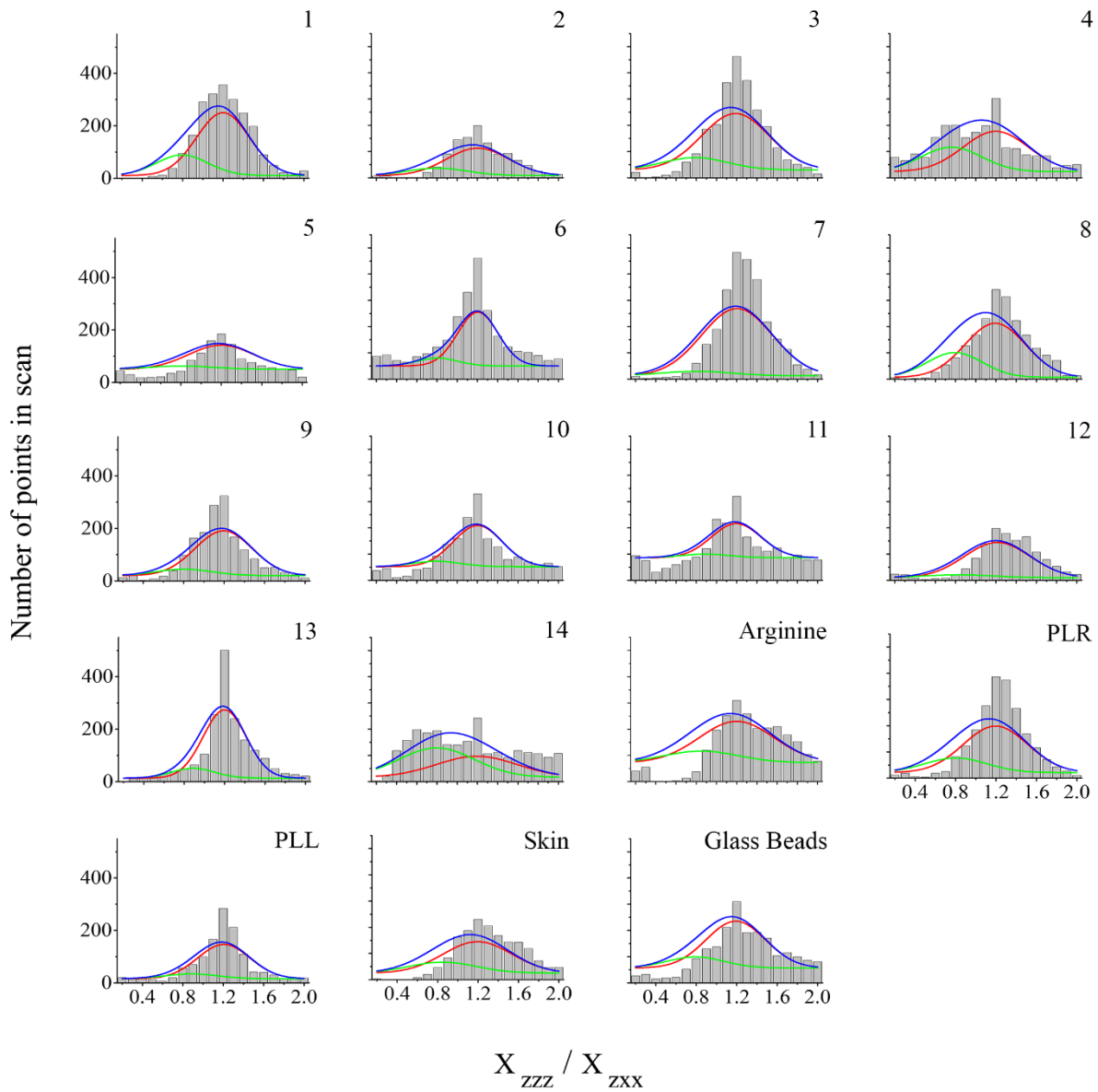


Figure 5.4. Histograms of $\frac{X_{zzz}}{X_{zxx}}$ values obtained for implanted glass beads coated with modified PLR. The bars represent experimentally acquired data. The blue line is the bimodal Gaussian fit to the data. The individual modes are represented as green (collagen type III) and red (collagen type I) lines.

5.3.4. Statistical Analysis

The correlation matrix (**Table 5.3**), and the PCA (**Figure 5.5**) were used to explain relationships between the experimentally observed second harmonic parameters and the chemical properties of the modifiers. Freely rotating bonds (r) of the modifiers was well correlated ($R = 0.47$, **Table 5.3**) with the FWHM of the collagen orientation. There were also strong correlations for the collagen III ratio with surface tension and the hydrogen bond acceptors (HBA) of the modifiers ($R = 0.72$ and 0.62 , respectively).

Based on the PCA of the collagen organization with the properties of the modifiers (**Figure 5.5**), the lipophilicity (LogD at pH 5.5), surface tension, and the number of HBA of the chemical modifier were correlated to the collagen III levels. These parameters were used to map an equation of for the explained collagen III ratio against the observed values, however the factorial equation obtained had insufficient goodness of fit ($R^2 = 0.56$) and was not included with the analyzed data.

Previously obtained cell responses to these PLR modifications²⁸ were also analyzed using PCA to uncover additional correlations. The speed of the cell migration on PLR modified surfaces was negatively correlated with polarizability ($R = -0.53$) and molar volume ($R = -0.50$), while having a positive correlation to the log P ($R = 0.48$) of the modifiers (**Figure 5.5**). The persistence of the cells in response to the modifiers was found to correlate positively to log D at pH 5.5 ($R = 0.58$).

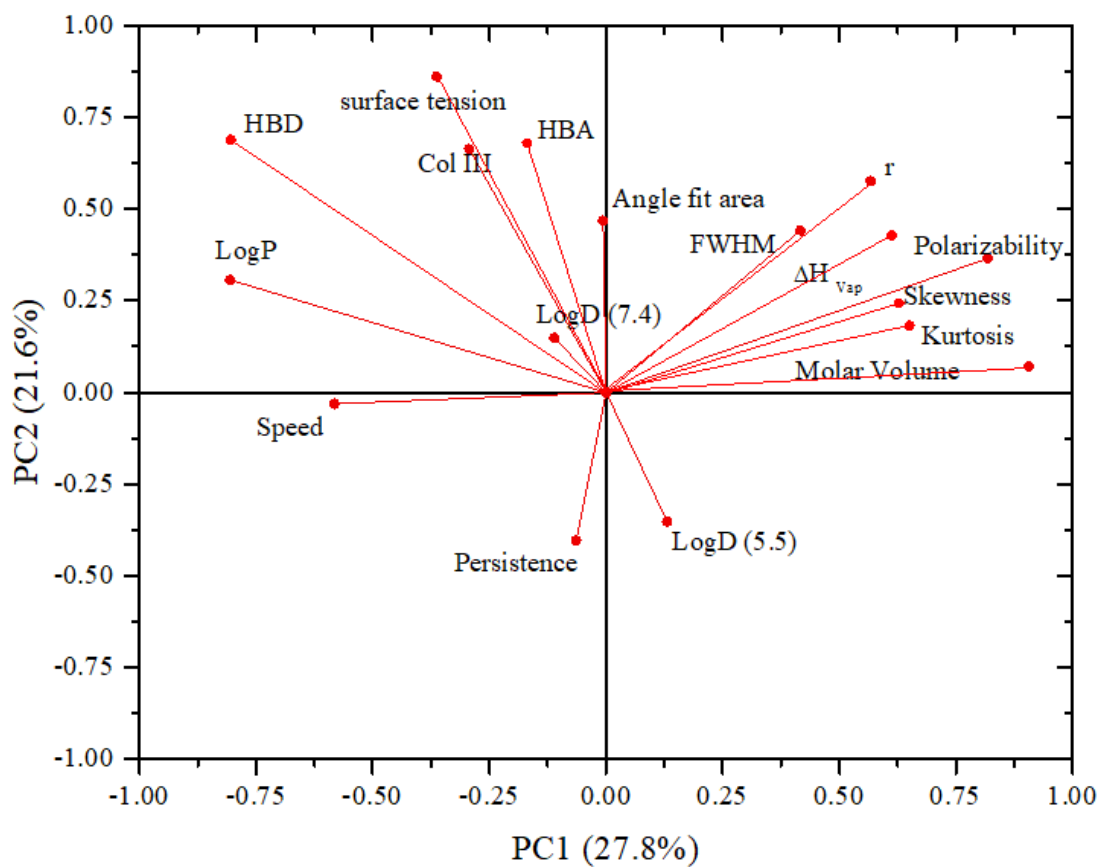


Figure 5.5. Loading plot of physicochemical materials properties and their influence on cell mobility and collagen organization. PC1 explains 27.8% data variance and PC2 explains 21.6% data variance. HBD = hydrogen bond donors, HBA = hydrogen bond acceptors, r = freely rotating bonds.

Table 5.3. Pearson's correlations for the chemical properties, SHG microscopy-based analysis and cell response parameters

| | | | | | | | | | | | | | | | | | |
|---------------|---------------|-------|-------|----------|----------|-------|-------------|-------|------------|------------|-------|--------------|----------------|-----------------|-------|-------|-------|
| | Col III ratio | FWHM | Area | Skewness | Kurtosis | Speed | Persistence | LogP | LogD (5.5) | LogD (7.4) | p | molar volume | ΔH Vap | surface tension | r | HBD | HBA |
| Col III ratio | 1.00 | 0.24 | 0.17 | 0.17 | 0.13 | 0.35 | 0.14 | 0.37 | -0.04 | 0.28 | -0.03 | -0.24 | 0.06 | 0.72 | 0.07 | 0.48 | 0.62 |
| FWHM | 0.24 | 1.00 | 0.41 | 0.59 | 0.56 | -0.17 | 0.06 | -0.51 | -0.31 | 0.09 | 0.26 | 0.20 | -0.03 | 0.46 | 0.47 | 0.01 | -0.12 |
| Area | 0.17 | 0.41 | 1.00 | -0.24 | -0.30 | 0.03 | -0.02 | -0.04 | 0.12 | 0.54 | 0.30 | 0.17 | -0.07 | 0.42 | 0.32 | 0.19 | 0.35 |
| Skewness | 0.17 | 0.59 | -0.24 | 1.00 | 0.97 | -0.16 | -0.08 | -0.43 | -0.27 | -0.24 | 0.34 | 0.35 | 0.13 | 0.03 | 0.32 | -0.24 | -0.09 |
| Kurtosis | 0.13 | 0.56 | -0.30 | 0.97 | 1.00 | -0.27 | -0.02 | -0.46 | -0.21 | -0.23 | 0.35 | 0.36 | 0.13 | 0.02 | 0.23 | -0.27 | -0.09 |
| Speed | 0.35 | -0.17 | 0.03 | -0.16 | -0.27 | 1.00 | 0.09 | 0.48 | -0.17 | -0.21 | -0.53 | -0.50 | -0.23 | -0.08 | -0.27 | 0.32 | 0.01 |
| Persistence | 0.14 | 0.06 | -0.02 | -0.08 | -0.02 | 0.09 | 1.00 | -0.15 | 0.58 | 0.23 | -0.12 | -0.02 | -0.36 | -0.19 | -0.45 | -0.30 | -0.20 |
| LogP | 0.37 | -0.51 | -0.04 | -0.43 | -0.46 | 0.48 | -0.15 | 1.00 | -0.17 | -0.13 | -0.42 | -0.54 | -0.27 | 0.50 | -0.22 | 0.79 | 0.48 |

Table 5.3 Continued

| | HBA | HBD | r | surface tension | ΔH Vap | molar vol. | p | LogD (7.4) | LogD (5.5) | |
|--|-------|-------|-------|-----------------|----------------|------------|-------|------------|------------|-----------------|
| | 0.62 | 0.48 | 0.07 | 0.72 | 0.06 | -0.24 | -0.03 | 0.28 | -0.04 | Col III ratio |
| | -0.12 | 0.01 | 0.47 | 0.46 | -0.03 | 0.20 | 0.26 | 0.09 | -0.31 | FWHM |
| | 0.35 | 0.19 | 0.32 | 0.42 | -0.07 | 0.17 | 0.30 | 0.54 | 0.12 | Area |
| | -0.09 | -0.24 | 0.32 | 0.03 | 0.13 | 0.35 | 0.34 | -0.24 | -0.27 | Skewness |
| | -0.09 | -0.27 | 0.23 | 0.02 | 0.13 | 0.36 | 0.35 | -0.23 | -0.21 | Kurtosis |
| | 0.01 | 0.32 | -0.27 | -0.08 | -0.23 | -0.50 | -0.53 | -0.21 | -0.17 | Speed |
| | -0.20 | -0.30 | -0.45 | -0.19 | -0.36 | -0.02 | -0.12 | 0.23 | 0.58 | Persistence |
| | 0.48 | 0.79 | -0.22 | 0.50 | -0.27 | -0.54 | -0.42 | -0.13 | -0.17 | LogP |
| | 0.13 | -0.56 | -0.34 | -0.21 | -0.07 | 0.37 | 0.30 | 0.58 | 1.00 | LogD (5.5) |
| | 0.26 | -0.19 | -0.18 | 0.56 | -0.41 | 0.00 | 0.10 | 1.00 | 0.58 | LogD (7.4) |
| | 0.38 | -0.34 | 0.67 | -0.02 | 0.75 | 0.93 | 1.00 | 0.10 | 0.30 | p |
| | 0.09 | -0.56 | 0.59 | -0.39 | 0.75 | 1.00 | 0.93 | 0.00 | 0.37 | molar volume |
| | 0.42 | -0.04 | 0.58 | -0.02 | 1.00 | 0.75 | 0.75 | -0.41 | -0.07 | ΔH Vap |
| | 0.63 | 0.80 | 0.12 | 1.00 | -0.02 | -0.39 | -0.02 | 0.56 | -0.21 | surface tension |
| | 0.18 | 0.12 | 1.00 | 0.12 | 0.58 | 0.59 | 0.67 | -0.18 | -0.34 | r |
| | 0.48 | 1.00 | 0.12 | 0.80 | -0.04 | -0.56 | -0.34 | -0.19 | -0.56 | HBD |
| | 1.00 | 0.48 | 0.18 | 0.63 | 0.42 | 0.09 | 0.38 | 0.26 | 0.13 | HBA |

5.4. Discussion

Collagen organization and type are indicators of implant acceptance as well as the stage of the wound healing processes. Collagen is secreted and remodeled by stromal cells such as fibroblasts and myofibroblasts to promote wound contraction.³¹ SHG microscopy is a high information, dye-less, non-linear optical technique that can visualize collagen organization and type in diverse tissues.^{15,28,32} By examining how chemical modifications alter collagen organization, rational design of biomaterials can be improved.

5.4.1. Collagen Signal Comparisons

The collagen signal for the 18 different modifications was estimated to be in the range of 2 to 5 mg/mL. Modification 5 (creatine) resulted in significantly higher collagen secretion at an estimated 4.56 ± 0.75 mg/mL, almost twice that of the control skin sample (1.94 ± 0.53 mg/mL). Creatine is a stimulant for promoting collagen secretion by fibroblasts in dermal tissues.³³ In another study, creatine supplements were observed significantly increase skin firmness through stimulating procollagen secretion and collagen alignment in young and aged humans, which was measured *in vivo* using multiphoton laser scanning microscopy.³⁴ The effect of the PLR-like modifications on the differentiation of fibroblasts associated with collagen synthesis and the wound healing response showed that it is possible to tune the modifier's chemical properties to enhance angiogenesis related biomarkers such as VEGF.²⁹ Statistical analysis on the chemical structure of the modifier and its influence on *in vivo* collagen organization indicated the modifier's hydrophobicity was positively correlated to the collagen type III deposition.

Studies on collagen organization in response to chemical modifications are uncommon, and there is a growing need to elucidate the materials properties responsible for collagen deposition and organization during the foreign body response. It is important to note here that there are limitations in SHG based collagen sensing as well, deriving from the limited z-axis depth of imaging, as well as significant differences arising from imaging fibrillar and non-fibrillar sources of collagen.³⁵

5.4.2. Collagen Organization Response

Collagen organization in response to *in vivo* implantation of PLR modified glass beads was quantified using Gaussian fit parameters of FWHM and area under the fit (**Figure 5.3**). For modifications that failed the isotropy check test, it was qualitatively observed that there was a relatively consistent amount of collagen imaged between 0 and 180°, with the presence of a few bins that were causing over-fitting of the histogram. In **Table 5.2**, the FWHM and area under the curve for the histograms of isotropic collagen organization response have been removed. Comparisons between the different collagen organization responses can be mapped using a few key factors such as the effect of shorter versus longer chain lengths. There was an inconsistent trend for carbon chain length with collagen organization. Citrulline and albizziin have almost the same chemical structure, with the former having an -CH₂ group making its chain length longer. Similarly, arginine has the longer chain with otherwise similar chemical structure as compared to amino-3-guanidinopropionic acid modification.

The comparison of the collagen organization response to albizziin and citrulline was interesting as the former is longer in chain length, and got a relatively aligned collagen response, with the shorter chain length containing albizziin resulting in an isotropic one. However, this trend was not continued for the case of comparing the shorter 2-amino-3-guanidinopropionic acid (aligned collagen response) to the longer modification of arginine (isotropic collagen response). There was also no consistent trend for the other modifications that elicited isotropic collagen organization responses. These observations support the hypothesis that the collagen organization response is a complicated process, which cannot be readily mapped on the basis of purely chemical structure comparisons of the modifications.

Unwounded dermal tissue contains disordered collagen and is considered a marker for implant acceptance.² Studies have shown the presence of the disordered collagen organization in dermal tissues, which is significantly different from the heavily aligned conformations shown for scarring and hypertrophic lesions.³⁶ There are clear differences in the collagen organization even between different types of scarring, such as between keloids and hypertrophic scars which are analogous in some cases to fibrotic responses to rejected implants.^{37,38} These organizational Tuning collagen organization thus plays a key role in the foreign body response⁶ and wound healing.²⁹

5.4.3. Collagen III Response

Secretion of collagen III is observed early in the wound healing process, with continued elevated levels of collagen III/collagen I ratios indicating prolonged healing as is seen in chronic wounds.²¹ Increased levels of collagen secretion is also observed in keloidal and hypertrophic scar samples, and are characterize by the formation of parallel collagen fibers.³⁹

Patients suffering from direct and indirect hernias were found to have significantly higher collagen type III levels than those without hernias.²² This could be either a consequence or instigation from abnormal angiogenesis at the injury site.²² Surface modifications showing lower levels of collagen III are potential treatments that could assist progression to the remodeling stage. As the wound healing process progresses, collagen III is steadily replaced with collagen I.⁴⁰ It is unclear to what extent surface modifications further facilitate the wound healing.⁴¹

We compared the collagen III response for the arginine derivative modifications with key differences in their chain length and compared their effects on instigating similar collagen III levels as that of the skin control sample (**Figure 5.4**). Collagen III levels for the skin control ($26.14 \pm 6.67\%$), matched previously reported values.¹⁹ Overlapping levels of collagen III signal to that of the skin control, such as those measured for nitroarginine ($36 \pm 8\%$) and albizzin ($42 \pm 13\%$), could indicate possible progression of the wound healing process towards reepithelialization.^{42,43} The collagen III levels had poor correlation with the FWHM of the collagen organization ($R = 0.24$). The estimated levels of collagen III varied greatly across the samples from 2 to 42%. Acute or chronic inflammatory responses to the implant can influence collagen III secretion.⁴⁴ Additionally, the interaction of platelet derived growth factor with the material surface can influence the deposition of different collagen types.^{45,46}

Integrins are transmembrane receptors that facilitate ECM deposition, which is a key phase of the host response to naïve and functionalized surfaces.⁴⁷ A specific integrin, $\alpha2\beta1$, has been observed on platelets, fibroblasts, and epithelial cells for its affinity to bind with collagen, which contains the GFOGER sequence.⁴⁸ It is possible that the arginine-like modifications studied here could be influencing the collagen deposition and organization^{47,48} through a similar mechanism.

Surface properties play a major role in how secreted types of collagen coalesce to form different network meshes on varied substrates.⁴⁹ The hydrophobicity of functionalized polymer substrates has been studied for its influence on the adsorption of secreted collagen in the presence of different biological sera.^{50,51} This link between hydrophobicity and collagen was further explored by a study in which terminal-group modified self-assembled monolayers of alkanethiols on gold were implanted in air pouches. The most hydrophobic surface coating of -CH₃ functionalized monolayers triggered the densest collagen secretion and fibrotic layer formation.⁵² Previous studies on functionalizing surfaces with PLR-like modifiers showed the significance of lipophilicity (logP) on the collagen secretion and organization.⁵³

5.4.4. PCA

The physicochemical properties of different surface modifications can influence the cellular response of fibroblasts.²⁹ Informatics analysis of this data using PCA (**Figure 5.5**) revealed correlations that can be used to explain relationships between chemical modifications and host responses to the implanted materials. Surface tension was well correlated with the collagen type III ratio surrounding the implant. It is important to note that the modifiers used here were relatively hydrophilic, with surface tensions ranging from 48 to 84 dyne/cm. Increased collagen III levels are essential in the earlier stages of wound healing. During later phases, collagen type III should be remodeled to collagen I.^{41,54}

Larger FWHM values indicate isotropic collagen organization. Unwounded skin is isotropic.⁵⁵ Kurtosis and skewness parameters are markers for the collagen organization. Skewness is considered a measure of symmetry for the statistical distribution and kurtosis is defined as a measure of whether the normal distribution is heavy or light-tailed. Together, these statistical parameters provide an analytical insight into the collagen organization beyond just the FWHM. In our study, we observed in the PCA (**Figure 5.5**) that unlike the FWHM, the skewness and kurtosis were positively correlated to the polarizability and molar volume of the modifiers. Polarizability has been studied as an intrinsic aspect to consider for the quantitative structure activity relationships (QSAR) analysis of diverse chemical structures influencing biological interactions such as nerve toxicity in frogs.⁵⁶ This influence of polarizability and its correlation to the fit parameters indicates that it could play a possible role in the alignment of collagen fibers as a part of biomaterial interactions.

Using PCA, we attempted to derive an empirical equation for the collagen III ratio in response to the implanted surfaces. However, this equation could not sufficiently explain the variability in the collagen III levels in response to the modification with a poor R^2 and Q^2 fit of 0.56 and 0.4 respectively. The FWHM of the deposited collagen was not determined for all of the modifiers since some of these failed the isotropy check. Therefore, an empirical equation for the FWHM was not determined. It is possible though to discuss the strong correlations of some of the chemical parameters of the modifier to the collagen organization response with respect to biomaterial interactions.

The number of HBD, HBA, and surface tension of the modifiers are closely linked to the hydrophobicity and surface charge of the functionalized substrate. Previous research on the hydrophobicity of surfaces showed that rat hepatocytes and schwannoma cells preferred hydrophobic surfaces with functionalized ECM proteins.⁵¹ Considering the salient observations from the collagen organization and the collagen III levels together, it can be stated that albizziin modification elicited the best collagen response under the *in vivo* conditions.

Altering the cell adhesion, migration, and proliferation on functionalized surfaces can improve wound healing and implant acceptance.^{57,58} Modifying the underlying substrates with different ligand chemistries influences cell attachment and the subsequent production of ECM proteins that are integral aspects of the foreign body response.⁵⁹ Migration studies on these surfaces indicated that NIH/3T3 fibroblasts migrated faster on creatine coated substrates.²⁹ In our SHG based analysis, we observed higher levels of collagen secretion and orientation in response to the creatine modified glass surface, which is in line with the aforementioned study. When the migration-based cell response parameters (i.e., speed and persistence) were combined with the *ex vivo* SHG analysis and chemical properties in a PCA plot, we uncovered correlations with the chemical properties of the modifier. The negative Pearson's correlations for the speed with polarizability ($R = -0.53$) and molar volume ($R = -0.50$) were noted from the PCA, as possible influences on how the cell migration can be influenced by the electrochemical and physical properties of the modifier (**Table 5.3**). The positive correlation of the cell persistence to the LogD (5.5) ($R = 0.58$) and negative correlation to the number of freely rotating bonds in the chemical modifier structure ($R = -0.45$), indicates the effect that the solubility of such chemical modifiers has on how cells migrate across functionalized surfaces.

5.5. Conclusions

The collagen response to functionalized glass beads coated with modified PLRs was studied to better understand how chemical modifications can impact implant acceptance. Tissue sections were removed 28 days post-implantation and showed some significant differences in the measured collagen signal intensity, in particular for the creatine and albizziin modifications. Increased collagen type III had a positive correlation with hydrogen bond acceptors in the modifier structure and surface tension. PCA also uncovered correlations between the freely rotating bonds, and the enthalpy of vaporization of the modifier on the organization of collagen response to modified PLR coated glass beads. The insights obtained from correlating the chemical properties of the PLR modifications to the SHG imaging derived parameters can further the design principles for improving implant acceptance.

5.6 References

1. Anderson, J. M., Rodriguez, A. & Chang, D. T. Foreign body reaction to biomaterials. *Semin. Immunol.* **20**, 86–100 (2008).
2. Boddupalli, A., Zhu, L. & Bratlie, K. M. Methods for Implant Acceptance and Wound Healing: Material Selection and Implant Location Modulate Macrophage and Fibroblast Phenotypes. *Adv. Healthc. Mater.* (2016). doi:10.1002/adhm.201600532
3. Trindade, R., Albrektsson, T., Tengvall, P. & Wennerberg, A. Foreign Body Reaction to Biomaterials: On Mechanisms for Buildup and Breakdown of Osseointegration. *Clin. Implant Dent. Relat. Res.* 1–12 (2014). doi:10.1111/cid.12274
4. Bryers, J. D., Giachelli, C. M. & Ratner, B. D. Engineering biomaterials to integrate and heal: The biocompatibility paradigm shifts. *Biotechnology and Bioengineering* **109**, 1898–1911 (2012).
5. Ziats, N. P., Miller, K. M. & Anderson, J. M. In vitro and in vivo interactions of cells with biomaterials. *Biomaterials* **9**, 5–13 (1988).
6. Kastellorizios, M., Tipnis, N. & Burgess, D. J. *Foreign body reaction to subcutaneous implants. Advances in Experimental Medicine and Biology* **865**, (2015).

7. Olderøy, M. *et al.* Biochemical and structural characterization of neocartilage formed by mesenchymal stem cells in alginate hydrogels. *PLoS One* **9**, (2014).
8. Singer, A. J. & Clark, R. a F. Cutaneous Wound Healing. *N. Engl. J. Med.* **341**, 738–746 (1999).
9. Martin, P. Wound Healing--Aiming for Perfect Skin Regeneration. *Science (80-.)*. **276**, 75–81 (1997).
10. Clark, J. a., Cheng, J. C. Y. & Leung, K. S. Mechanical properties of normal skin and hypertrophic scars. *Burns* **22**, 443–446 (1996).
11. Linares, H. A., Kischer, C. W., Dobrkovsky, M. & Larson, D. L. The histotypic organization of collagen of the hypertrophic scar in humans. *J. Invest. Dermatol.* **59**, 323–332 (1972).
12. Clore, J. N., Cohen, I. K. & Diegelmann, R. F. Quantitation of Collagen Types I and III during Wound Healing in Rat Skin. *Proc. Soc. Exp. Biol. Med.* **161**, 337–340 (1979).
13. Van Zuijlen, P. P. M. *et al.* Collagen morphology in human skin and scar tissue: No adaptations in response to mechanical loading at joints. *Burns* **29**, 423–431 (2003).
14. Chen, X., Nadiarynk, O., Plotnikov, S. & Campagnola, P. J. Second harmonic generation microscopy for quantitative analysis of collagen fibrillar structure. *Nat. Protoc.* **7**, 654–69 (2012).
15. Boddupalli, A. & Bratlie, K. M. Multimodal imaging of harmonophores and application of high content imaging for early cancer detection. *Mater. Discov.* **1**, 10–20 (2016).
16. Suhaimi, J. L. *et al.* Characterization of Cholesterol Crystals in Atherosclerotic Plaques Using Stimulated Raman Scattering and Second-Harmonic Generation Microscopy. *Biophys. J.* **102**, 1988–1995 (2012).
17. Plotnikov, S. V, Millard, A. C., Campagnola, P. J. & Mohler, W. a. Characterization of the myosin-based source for second-harmonic generation from muscle sarcomeres. *Biophys. J.* **90**, 693–703 (2006).
18. Su, P. J. *et al.* The discrimination of type I and type II collagen and the label-free imaging of engineered cartilage tissue. *Biomaterials* **31**, 9415–9421 (2010).
19. Velnar, T., Bailey, T. & Smrkolj, V. The Wound Healing Process: An Overview of the Cellular and Molecular Mechanisms. *J. Int. Med. Res.* **37**, 1528–1542 (2009).
20. Koruth, S. & Narayanaswamy Chetty, Y. V. Hernias- Is it a primary defect or a systemic disorder? Role of collagen III in all hernias- A case control study. *Ann. Med. Surg.* **19**, 37–40 (2017).

21. Zhang, K., Garner, W., Cohen, L., Rodriguez, J. & Phan, S. Increased Types I and III Collagen and Transforming Growth Factor- β 1 mRNA and Protein in Hypertrophic Burn Scar. *J. Invest. Dermatol.* **104**, 750–754 (1995).
22. Klinge, U. *et al.* Synthesis of type I and III collagen, expression of fibronectin and matrix metalloproteinase 1 and 13 in hernias of patients with inguinal hernia. *Int J Surg Invest.* **1**, 219–227 (1999).
23. Tomasek J. J., Gabbiani G., Hinz B., Chaponnier C., B. R. A. Myofibroblasts and mechano-regulation of connective tissue remodelling. *Nat. Rev. Mol. Cell Biol* **3**, 346–63 (2002).
24. Tomasek, J. J., Gabbiani, G., Hinz, B., Chaponnier, C. & Brown, R. a. Myofibroblasts and mechano-regulation of connective tissue remodelling. *Nat. Rev. Mol. Cell Biol.* **3**, 349–63 (2002).
25. Benavides, F., Oberyszyn, T. M., VanBuskirk, A. M., Reeve, V. E. & Kusewitt, D. F. The hairless mouse in skin research. *J. Dermatol. Sci.* **53**, 10–18 (2009).
26. Palero, J. A., de Bruijn, H. S., van der Ploeg van den Heuvel, A., Sterenberg, H. J. C. M. & Gerritsen, H. C. Spectrally Resolved Multiphoton Imaging of In Vivo and Excised Mouse Skin Tissues. *Biophys. J.* **93**, 992–1007 (2007).
27. Bygd, H. C., Forsmark, K. D. & Bratlie, K. M. Altering invivo macrophage responses with modified polymer properties. *Biomaterials* **56**, (2015).
28. Akilbekova, D. & Bratlie, K. M. Quantitative characterization of collagen in the fibrotic capsule surrounding implanted polymeric microparticles through second harmonic generation imaging. *PLoS One* **10**, 1–17 (2015).
29. Bygd, H. C., Akilbekova, D., Muñoz, A., Forsmark, K. D. & Bratlie, K. M. Poly-l-arginine based materials as instructive substrates for fibroblast synthesis of collagen. *Biomaterials* **63**, 47–57 (2015).
30. Gavin, H. P. *The Levenberg-Marquardt method for nonlinear least squares curve-fitting problems. Department of Civil and Environmental Engineering, Duke University* (2013).
31. Wynn, T. A. Cellular and molecular mechanisms of fibrosis. *J. Pathol.* **214**, 199–210 (2008).
32. Ajeti, V. *et al.* Structural changes in mixed Col I/Col V collagen gels probed by SHG microscopy: implications for probing stromal alterations in human breast cancer. *Biomed. Opt. Express* **2**, 2307–2316 (2011).
33. Knott, A. *et al.* A novel treatment option for photoaged skin. *J. Cosmet. Dermatol.* **7**, 15–22 (2008).
34. Fischer, F. *et al.* Folic acid and creatine improve the firmness of human skin in vivo. *J. Cosmet. Dermatol.* **10**, 15–23 (2011).

35. Gailhouste, L. *et al.* Fibrillar collagen scoring by second harmonic microscopy: A new tool in the assessment of liver fibrosis. *J. Hepatol.* **52**, 398–406 (2010).
36. Ehrlich, H. P. *et al.* Morphological and immunochemical differences between keloid and hypertrophic scar. *Am. J. Pathol.* **145**, 105–113 (1994).
37. English, R. S. & Shenefelt, P. D. Keloids and hypertrophic scars. *Dermatologic Surg.* **25**, 631–638 (1999).
38. Cicchi, R. *et al.* *In vivo* non-invasive monitoring of collagen remodelling by two-photon microscopy after micro-ablative fractional laser resurfacing. *J. Biophotonics* **7**, 914–925 (2014).
39. Verhaegen, P. D. H. M. *et al.* Differences in collagen architecture between keloid, hypertrophic scar, normotrophic scar, and normal skin: An objective histopathological analysis. *Wound Repair Regen.* **17**, 649–656 (2009).
40. Volk, S. W., Wang, Y., Mauldin, E. a, Liechty, K. W. & Adams, S. L. Diminished type III collagen promotes myofibroblast differentiation and increases scar deposition in cutaneous wound healing. *Cells. Tissues. Organs* **194**, 25–37 (2011).
41. Gabbiani, G. The myofibroblast in wound healing and fibrocontractive diseases. *J. Pathol.* **200**, 500–503 (2003).
42. Volk, S. W., Wang, Y., Mauldin, E. A., Liechty, K. W. & Adams, S. L. Diminished type III collagen promotes myofibroblast differentiation and increases scar deposition in cutaneous wound healing. *Cells Tissues Organs* **194**, 25–37 (2011).
43. Brisson, B. K. *et al.* Type III collagen directs stromal organization and limits metastasis in a murine model of breast cancer. *Am. J. Pathol.* **185**, 1471–1486 (2015).
44. Lee, Y., Kwon, J., Khang, G. & Lee, D. Reduction of inflammatory responses and enhancement of extracellular matrix formation by vanillin-incorporated poly(lactic-co-glycolic acid) scaffolds. *Tissue Eng. Part A* **18**, 1967–78 (2012).
45. Roberts, A. B. *et al.* Transforming growth factor type beta: rapid induction of fibrosis and angiogenesis in vivo and stimulation of collagen formation in vitro. *Proc. Natl. Acad. Sci.* **83**, 4167–4171 (1986).
46. Grotendorst, G. R., Seppä, H. E., Kleinman, H. K. & Martin, G. R. Attachment of smooth muscle cells to collagen and their migration toward platelet-derived growth factor. *Proc. Natl. Acad. Sci. U. S. A.* **78**, 3669–72 (1981).
47. Zeltz, C. & Gullberg, D. The integrin-collagen connection - a glue for tissue repair? *J. Cell Sci.* **129**, 1284–1284 (2016).
48. Emsley, J., Knight, C. G., Farndale, R. W., Barnes, M. J. & Liddington, R. C. Structural Basis of Collagen Recognition by Integrin $\alpha 2\beta 1$. *Cell* **101**, 47–56 (2000).

49. Brown, B. N. *et al.* Surface characterization of extracellular matrix scaffolds. *Biomaterials* **31**, 428–437 (2010).
50. Dewez, J., Berger, V., Schneider, Y. & Rouxhet, P. Influence of Substrate Hydrophobicity on the Adsorption of Collagen in the Presence of Pluronic F68, Albumin, or Calf Serum. *J. Colloid Interface Sci.* **191**, 1–10 (1997).
51. Dewez, J. L. *et al.* Adhesion of mammalian cells to polymer surfaces: From physical chemistry of surfaces to selective adhesion on defined patterns. *Biomaterials* **19**, 1441–1445 (1998).
52. Barbosa, J. N., Madureira, P., Barbosa, M. A. & Águas, A. P. The influence of functional groups of self-assembled monolayers on fibrous capsule formation and cell recruitment. *J. Biomed. Mater. Res. - Part A* **76**, 737–743 (2006).
53. Ma, L., Bygd, H. C. & Bratlie, K. M. Improving selective targeting to macrophage subpopulations through modifying liposomes with arginine based materials. *Integr. Biol.* **9**, 58–67 (2017).
54. Otranto, M. *et al.* The role of the myofibroblast in tumor stroma remodeling. *Cell Adhes. Migr.* **6**, 203–219 (2012).
55. Cicchi, R. *et al.* Scoring of collagen organization in healthy and diseased human dermis by multiphoton microscopy. *J. Biophotonics* **3**, 34–43 (2010).
56. Hansch, C. *et al.* On the role of polarizability in chemical - Biological interactions. *J. Chem. Inf. Comput. Sci.* **43**, 120–125 (2003).
57. Mann, B. K. & West, J. L. Cell adhesion peptides alter smooth muscle cell adhesion, proliferation, migration, and matrix protein synthesis on modified surfaces and in polymer scaffolds. *J. Biomed. Mater. Res.* **60**, 86–93 (2002).
58. Yang, Z. *et al.* Bioactive Plasma-Polymerized Bipolar Films for Enhanced Endothelial Cell Mobility. *Macromol. Biosci.* **11**, 797–805 (2011).
59. Luttikhuisen, D. T., Harmsen, M. C. & Van Luyn, M. J. A. Cellular and molecular dynamics in the foreign body reaction. *Tissue Eng.* **12**, 1955–1970 (2006).

CHAPTER 6

SECOND HARMONIC GENERATION IMAGING OF COLLAGEN FIBER ORIENTATION AS A MARKER FOR SCARRING

More than US\$25 billion was spent on costs related to chronic wound care treatment in the United States in 2008. In addition to the high cost, chronic wounds affect over 6.5 million people.¹ These slow-healing wounds are often seen in people suffering from diabetes and obesity. Wound care accounts for a significant economic expenditure in not just the US, but all over the world. The Corporate Research of Materials Lab at 3M collaborated with the Bratlie lab to understand the wound healing process from the perspective of changes in collagen that can be sensitively analyzed using Second Harmonic Generation (SHG) microscopy. By imaging tissues that have been subjected diverse treatment strategies, the Bratlie lab conducted a blind study on the effectiveness of the wound healing process. The ability of specific treatments to induce isotropic collagen organization, as well as similar collagen III % to unwounded tissue, were used to evaluate the efficacy of over 20 formulations spread across 272 tissue sections so far.

6.1. Introduction

A wound has been defined as a “a break in the epithelial integrity of the skin and may be accompanied by disruption of the structure and function of underlying normal tissue”.² They are not limited to physical trauma, but can also be caused by diseases that cause internal or external damage to organs. The disruption of the local tissue environment causes the instigation of a cascade of biological responses including blood coagulation, inflammatory, and chronic wound healing.³

The natural wound healing process is timely and ordered, seeking to restore anatomic functionality of damaged tissues.^{4,5} The wound healing response varies greatly depending on the health status of the subject, particularly when treating for acute versus chronic wounds.⁵ Stochastic collagen order occurs in unwounded dermis, while scar tissue from hypertrophic scars is more aligned in parallel arrays.⁶ Collagen III typically rapidly decreases once wound healing progresses towards granulation tissue formation. Sustained, elevated levels of the collagen type III are associated with delayed healing response.^{7,8} Isotropic collagen orientation⁶ with similar levels of collagen III⁸ as unwounded tissue would be the ideal outcome for a wound dressing.

Polarized SHG microscopy can sensitively visualize collagen organization in diverse clinical samples, without the use of dyes or complicated tagging protocols.⁹ SHG microscopy is a non-linear interaction between two incident laser beams with samples, resulting in the generation of photon that are frequency doubled.¹⁰ This technique can quantitatively characterize collagen organization in rat tail tendons and cartilage tissue.¹¹ As this technique is a second-order optical process, non-centrosymmetric molecules are SHG active under the electric dipole approximation, while non-centrosymmetric molecules do not contribute to the signal.

The susceptibility tensor elements measure using SHG are related to the material properties.^{9,12} Shifts in these susceptibility elements can be used to differentiate between different types of collagen signal based on differences in peptide or methylene binding.¹¹ By extracting these susceptibility tensors, a map of collagen type III to collagen type I can be obtained.⁹ The ratio of collagen III/I is approximately 30% for unwounded dermal tissues.^{13,14} Collagen III levels remain elevated in prolonged wound healing responses, as seen in hypertrophic scarring and inguinal hernias.^{7,15,16}

There is no consensus, however, on the exact role played by collagen III in the wound healing process. During the granulation tissue formation phase, the replacement of collagen I by collagen III is higher in tissues that undergo greater mechanical stress.¹⁷ This indicates possible differences for the role played by the two types of collagen in terms of how they respond to mechanotransductive cues. The up-regulation of collagen III indicates decreases in mechanical remodeling of the wound site.¹⁵ In injuries from burns, it is common to see well aligned collagen in scar tissue, compared to disorganized unwounded dermis.^{14,18}

Our study evaluates five different wound treatments provided by 3M, as a blind study. Considerable information regarding the wound healing formulations were proprietary to 3M, and thus the treatments are defined with the limited titles assigned to each of them.

6.2. Materials and Methods

All the imaging studies were conducted in triplicate for each sample. Results were compared to controls as provided by 3M. Preserved tissue samples from porcine subjects were used throughout this study.

6.2.1. Materials

Treatments were prepared under confidential conditions by the researchers at the Corporate Research Materials Laboratory at 3M.

6.2.2. Second Harmonic Generation (SHG)

SHG imaging was conducted using a mode-locked Ti:sapphire laser (100 fs pulse width, 1 kHz repetition rate, Libra, Coherent, Santa Clara, CA) that produces a fundamental of 800 nm fundamental. The samples were irradiated with a non-damaging power of 1 to 10 mW, which was tuned using a half-wave plate and a Glan-Thompson polarizer (Thorlabs, Newton, NJ). Images were collected in the transmission mode. The 800 nm beam was focused using an inverted microscope stage (AmScope, Irvine, CA) and a 20× Nikon Plan Fluorite objective (0.50 NA, 2.1 mm). The SHG signal was collected with a 40× Nikon water immersion objective (0.8 NA, 3.5 mm). The signal was reflected with a dichroic mirror (Thorlabs) and the noise from the fundamental beam was removed using a short pass filter < 450 nm (Thorlabs) and an 808 nm notch filter (Melles Griot, Rochester, NY). The signal was detected using an intensified CCD camera (iCCD, iStar 334T, Andor, Belfast, UK) with 512 × 512 active pixels. The polarization of the incident beam was tuned using a Glan-Thompson polarizer and a half-wave plate mounted on a motor driven rotational stage (Thorlabs). The focusing objective was placed after the optical elements. Images were acquired every 10° from 0 to 350°. Images were collected in triplicate.

6.2.3. Image Processing

The equation used for mapping the SHG signal of collagen in the imaged samples as a function of the polarization angle of the incident laser beam is as follows:

$$I_{SHG} = c \cdot \left\{ \left[\sin^2(q_e - q_0) + \left(\frac{C_{zzz}}{C_{zxx}} \right) \cos^2(q_e - q_0) \right]^2 + \left(\frac{C_{xzx}}{C_{zxx}} \right)^2 \sin^2(2(q_e - q_0)) \right\} \quad (1)$$

where $\frac{C_{zzz}}{C_{zxx}}$ and $\frac{C_{xzx}}{C_{zxx}}$ are second-order susceptibility tensor element ratios; θ_e and θ_0 are the incident polarization angle and collagen fiber angle, respectively; and c is a normalization constant. The susceptibility tensor element ratios have been used to distinguish sources of SHG signal.^{19,20} Images were compiled using ImageJ (NIH, Bethesda, MD) to prepare the image stacks for processing using MATLAB (MathWorks, Natick, MA). The SHG Images were binned to obtain regions of interest (ROIs) of 4×4 pixels. A Levenberg-Marquardt algorithm²¹ was used to estimate the orientation angle of the collagen and its associated susceptibility tensors for each ROI in the SHG image (MATLAB). A threshold signal of 5 photon counts per pixel was used for the analysis, based on the limit of detection for this setup. The analysis generated orientation maps superimposed on the SHG image stacks, which displayed the orientation angle determined for all ROI. Histograms of both the orientation angles and susceptibility tensor ratios were also obtained.

6.2.4. Statistics and Data Analysis

JMP® statistical software (Cary, NC) was used to perform the statistical analysis on all the obtained data. Statistical significance when comparing the means of the data sets was evaluated through a two-way ANOVA. Tukey's honest significant difference test was used for and the differences were considered significant only for $p < 0.05$.

6.3. Results

Collagen organization was analyzed by fitting the obtained histograms with Gaussian curves. Using the full-width at half-maximum (FWHM) values of the Gaussian fits, collagen organization was quantified. The collagen III % was estimated by measuring the area under the histogram curve. A gradient curve previously obtained by Akilbekova and Bratlie²⁰ for collagen III concentration was used to estimate the collagen III/I ratio, thus enabling comparisons of the type of collagen deposited in response to diverse treatment strategies.

6.3.1. Fibrin Scaffold Treatment

Thrice applied fibrin scaffolds were used as treatments for wounds for 14 days. The collagen response to this treatment and its corresponding controls were analyzed. For this treatment, both the sample and control (presumably wounded skin sample with no treatment) showed relatively low collagen order. There was no significant difference observed for the collagen organization in the control and treatment, with both samples having FWHM values above 60° (Figure 6.1).

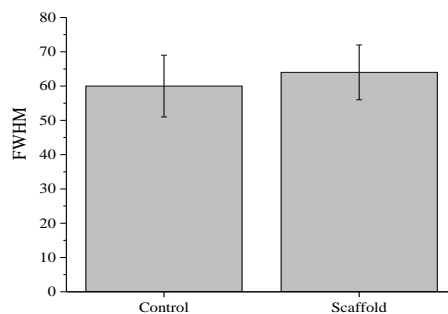


Figure 6.1. Comparing collagen organization response to thrice applied fibrin scaffold treatments. Data represents the mean \pm SD. $n = 4$. Statistical analysis through two-way ANOVA and Tukey's HSD post-hoc test. * $p < 0.05$

The collagen III % in response to the fibrin scaffold was significantly different from the control (**Figure 6.2**). Both the sample and control showed relatively low collagen III % compared to typical levels in human dermal tissues of around 30%.

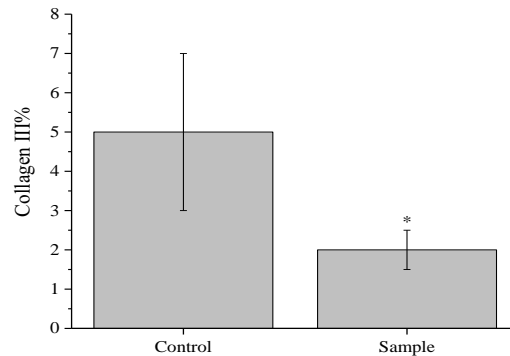


Figure 6.2. Comparing collagen III secretion response to thrice applied fibrin scaffold treatments. Data represents the mean \pm SD. n = 4. Statistical analysis through two-way ANOVA and Tukey's HSD post-hoc test. * p < 0.05

6.3.2. Partial Thickness Scaffold Treatments applied for 4 days

Scaffold treatments on shallow wounds termed partial thickness (PT) wounds were analyzed for their effectiveness. The scaffolds were maintained on the wound site for 4 days before excision. For this treatment, four different treatments named Promogran, Foam, Biostep and "Collagen" were compared. There was no significant difference between the four treatments, all of which showed moderately isotropic collagen organization, with FWHMs above 40° for all four treatments (**Figure 6.3**).

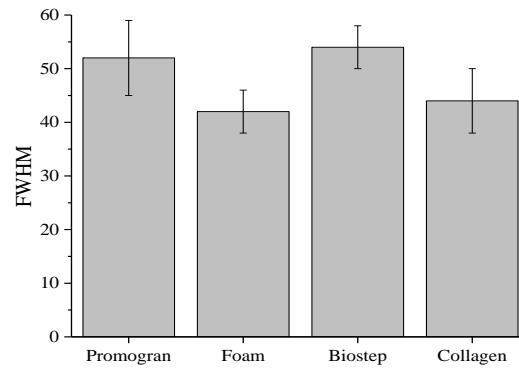


Figure 6.3. Comparing collagen organization response to PT scaffold treatments applied for four days. Data represents the mean \pm SD. $n = 4$. Statistical analysis through two-way ANOVA and Tukey's HSD post-hoc test. * $p < 0.05$

In contrast, there were significant differences in the collagen III % response to the Foam treatment, compared to the other three PT scaffold treatments. All the treatments showed relatively moderate levels of collagen III % compared to the thrice applied fibrin scaffold treatments (**Figure 6.4**).

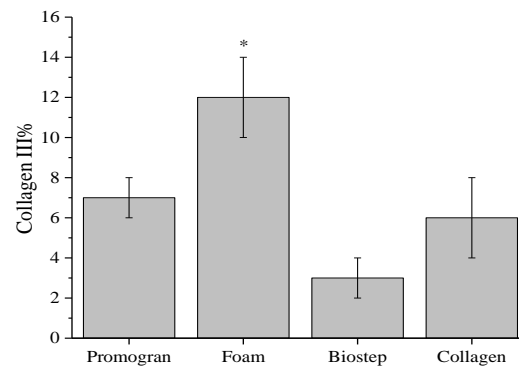


Figure 6.4. Comparing collagen III secretion response to PT scaffold treatments applied for four days. Data represents the mean \pm SD. $n = 4$. Statistical analysis through two-way ANOVA and Tukey's HSD post-hoc test. * $p < 0.05$

6.3.3. Full Thickness Scaffold Treatments compared over 14 and 21 days

Scaffolds applied to full Thickness (FT) wounds were also studied. These treatments were maintained on the wound site for 14 and 21 days before excision. Treatments labelled as C, P, TG and TS were analyzed for their efficacy in restoring the wound site to its original state by comparing the collagen organization and secretion responses. There was no significant difference for any of the treatments which showed moderately isotropic collagen organization on d14, all of which had FWHM values above 40° . (**Figure 6.5**). However, there were significant differences between the d21 and d14 sets for treatments C, TG and TS, which elicited a more disordered collagen response. Collagen organization was relatively unchanged over the treatment period only for treatment P, which remained around FWHM values of 60° across the three weeks of treatment.

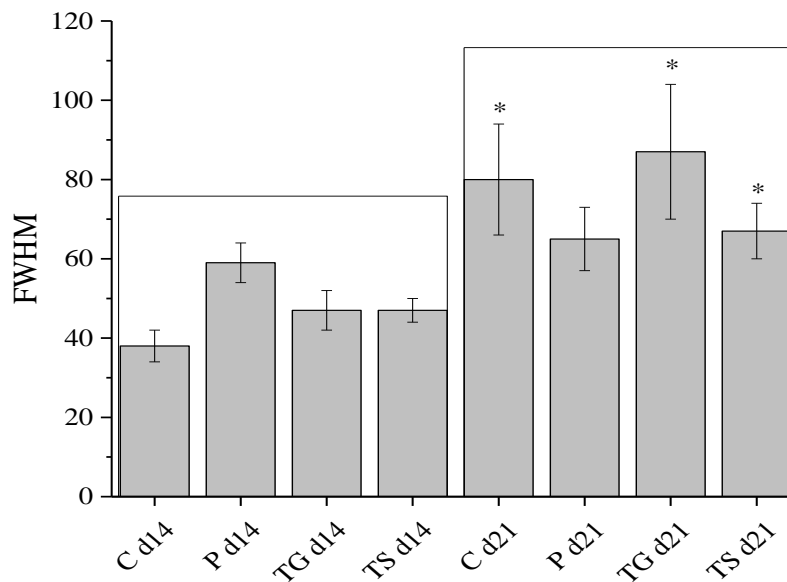


Figure 6.5. Comparing collagen organization response to FT scaffold treatments. Data represents the mean \pm SD. $n = 2$. Statistical analysis through two-way ANOVA and Tukey's HSD post-hoc test. * $p < 0.05$

The collagen III secretion followed the same trend as collagen organization with there being significant differences for the collagen III in response to the C, TG, and TS treatments when comparing their d14 and d21 levels. Furthermore, there were no significant differences across treatments when comparing treatments of the same application time. (**Figure 6.6**).

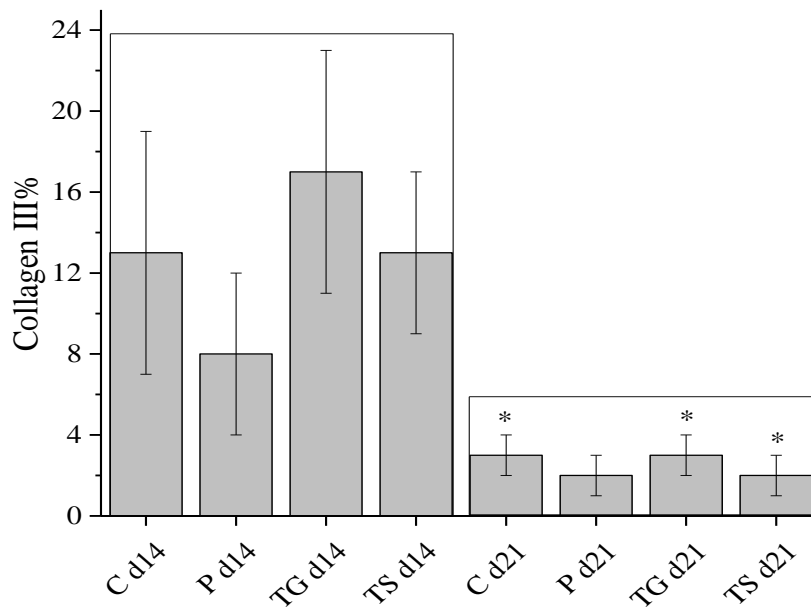


Figure 6.6. Comparing collagen III secretion response to FT scaffold treatments. Data represents the mean \pm SD. $n = 2$. Statistical analysis through two-way ANOVA and Tukey's HSD post-hoc test. * $p < 0.05$

6.3.4. Full Thickness Scaffold Treatments compared over 14 and 21 days — Set II

Scaffold formulations labeled as C, I, TG and TS were analyzed for their effectiveness in treating FT over 14 and 21 days before tissue excision. While TG and TS scaffolds initially resulted in more aligned collagen signal with FWHM of around 40° , the variation in collagen response across the samples meant that there were no statistically significant differences across the d14 sample set (**Figure 6.7**).

Two of the four treatments (C and I) showed significantly more aligned collagen after three weeks of treatment compared to the d14 samples. Treatment TG showed no significant difference for the collagen response after three weeks, remaining relatively isotropic. Only treatment TS showed significantly more isotropy in the collagen response after three weeks of application.

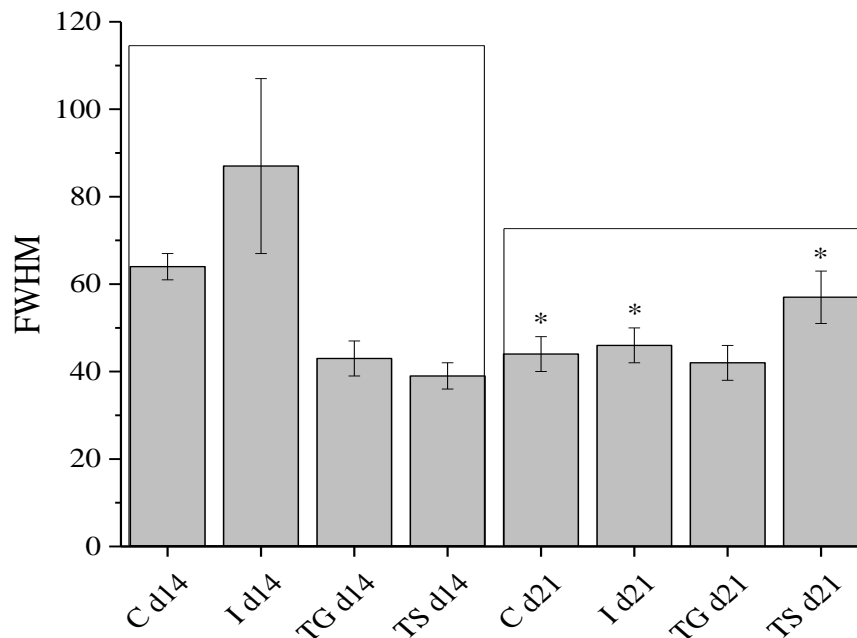


Figure 6.7. Comparing collagen organization response to FT scaffold treatments—Set II. Data represents the mean \pm SD. $n = 2$. Statistical analysis through two-way ANOVA and Tukey's HSD post-hoc test. * $p < 0.05$

There were significant differences for the collagen III levels in response to the I, TG, and TS treatments when comparing their d14 and d21 levels, with the latter eliciting significantly lower levels of collagen III secretion. There were no significant differences for any of the treatments when comparing samples across the same time point. Treatment C showed the least variation in collagen III% response across the two treatment times (**Figure 6.8**).

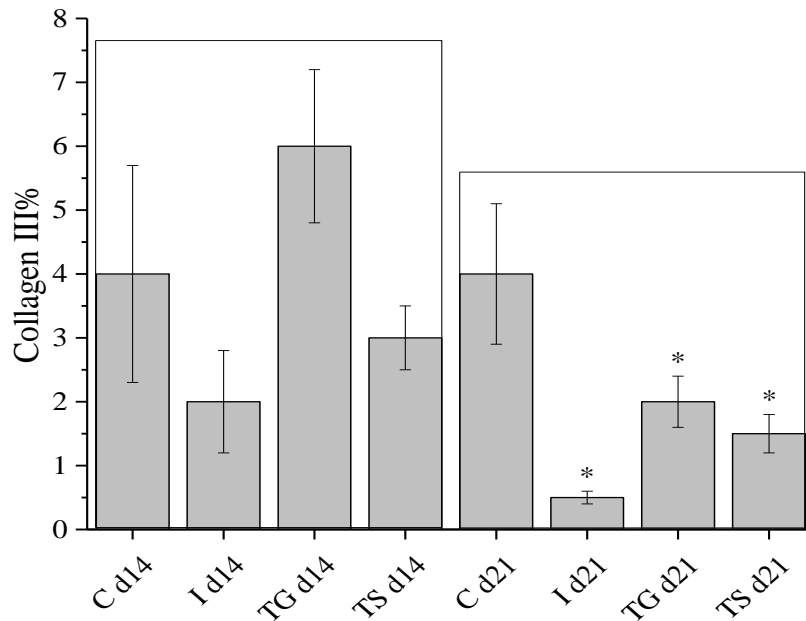


Figure 6.8. Comparing collagen III secretion response to FT scaffold treatments—Set II. Data represents the mean \pm SD. n = 4. Statistical analysis through two-way ANOVA and Tukey’s HSD post-hoc test. * p < 0.05

5.3.5. Full Thickness Scaffold Treatments compared over 21 and 42 days

Longer treatment times of 21 and 42 days were also analyzed. For this treatment, two treatments (A and B) were provided with respective controls for both the time-points.

The controls across d21 and d42 showed highly isotropic collagen organization which were significantly different from those in response to A and B treatments, which were moderately isotropic with FWHM around 50° (**Figure 6.9**). Only treatment B showed significantly more isotropic collagen on d42 compared to d21.

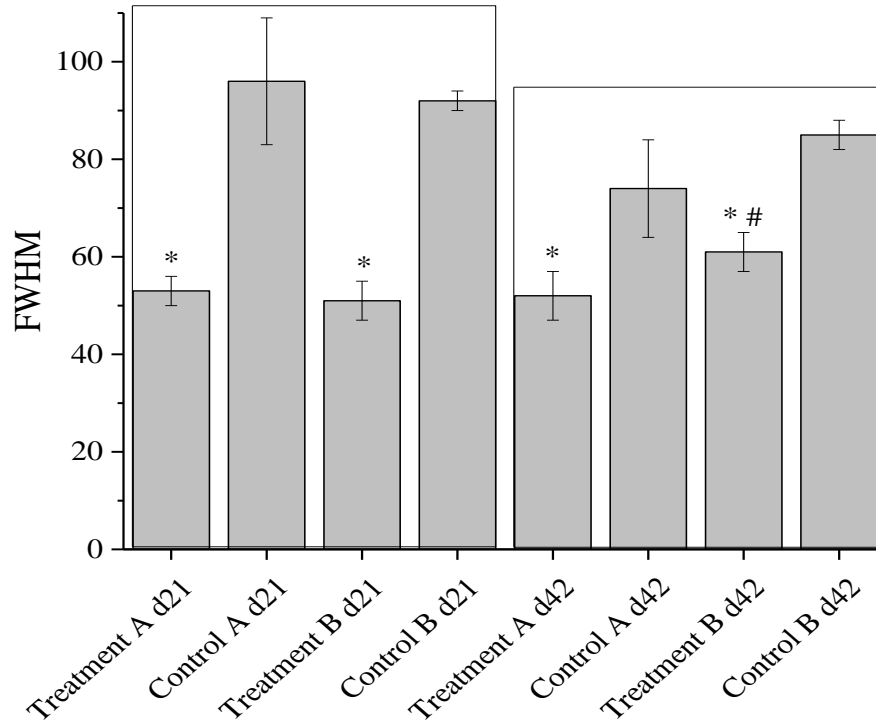


Figure 6.9. Comparing collagen organization response to FT scaffold treatments compared over d21 and d42. Data represents the mean \pm SD. $n = 4$. Statistical analysis through two-way ANOVA and Tukey's HSD post-hoc test. * $p < 0.05$ for comparison with control, # < 0.05 for comparison with d21 sample response

Similar to the comparisons for collagen organization, there were significant differences observed for collagen III in response to treatment A on d21 and for treatment B on d42. All the control samples showed a wide variation in collagen III %, ranging from 9 to 17% (**Figure 5.10**).

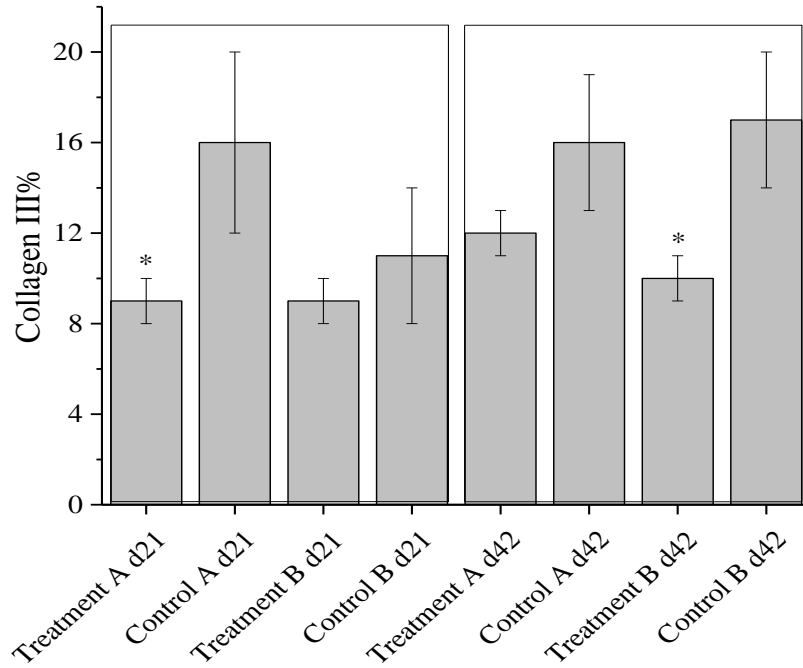


Figure 6.10. Comparing collagen III secretion response to FT scaffold treatments compared over d21 and d42. Data represents the mean \pm SD. $n = 4$. Statistical analysis through two-way ANOVA and Tukey's HSD post-hoc test. * $p < 0.05$

6.4. Discussion

Collagen plays a key role in the wound healing process. Its secretion and organization by fibroblasts and myofibroblasts as a response to implants and injuries is similar.²² SHG imaging of this collagen response, with a view towards identifying key biomarkers for scarring and delayed healing are important insights that can improve our understanding of the dynamics of tissue remodeling.^{23–25}

6.4.1. Fibrin Scaffold Treatment

Collagen organization in response to the thrice applied fibrin scaffold treatment was analyzed (**Figure 6.1**). The treatment efficacy can be considered good, as there were no significant differences in the collagen alignment compared to the control. Both showed isotropic collagen signal, with high FWHM values. The collagen secretion responses to the treatments indicated that the fibrin treatment elicited significantly lower collagen III% (**Figure 6.2**). Fibrin scaffold treatments have been studied for their ability to promote clotting by aiding the natural platelet response to stem the blood flow at the wound site.²⁶ Fibrin based scaffolds can controllably deliver cytokines such as basic fibroblast growth factor to promote wound healing for diabetic mice,²⁷ as well as for treatment of dermal wounds.²⁸ The efficacy of the 3M fibrin scaffold would undoubtedly have considered these successful design principles from previous studies for fabricating their product.

6.4.2. Partial Thickness Scaffold Treatment applied for 4 days

The effectiveness of the scaffolds for PT wounds was evaluated based on their ability to induce isotropic collagen organization within a short application period of 4 days. All four treatments showed relatively moderate levels of collagen disorder with similar FWHM values (**Figure 6.3**). Within these comparisons, it was only possible to acquire more information about the Promogran and Biostep wound dressings.

The Foam and Collagen named treatments appeared to be 3M test-products. As there were no control samples defined for these samples, it can only be speculated that the goal of this study was to compare the efficacy of the Foam and Collagen treatments as compared to commercially available treatments in Promogran and Biostep.^{29,30} The collagen III levels are difficult to compare for without controls, with the Foam showing significantly higher levels amongst the four sample sets (**Figure 6.4**).

6.4.3. Full Thickness Scaffold Treatments compared over 14 and 21 days

The effectiveness of the scaffolds for the FT wounds was evaluated for their ability to induce isotropic collagen organization over 2 and 3 weeks of application. All four treatments (C, P, TG and TS) showed relatively moderate levels of collagen disorder with comparable FWHM values when comparing their responses on d14 and d21 (**Figure 6.5**). The progression of moderately to highly isotropic collagen order by d21 was noted. This transition is in line with similar studies examining the timeline of wound healing across dermal wounds, which have shown that myofibroblast activity and its associated remodeling peaks by week 3, after which the extent of wound closure varies greatly over weeks to even months for the wound closure to be complete.² The P treatment showing no changes in collagen organization could be either a case of halted healing or a scarring response. The scarring response becomes more probable since the collagen III levels did not significantly change from d14 to d21 (**Figure 6.6**). Since these levels are lower than what has been reported for hypertrophic scarring, this would need to be confirmed through clinical observations.³¹ In the absence of controls, it was only possible to compare the relative efficacy of the different scaffold treatments as given.

6.4.4. Full Thickness Scaffold Treatments compared over 14 and 21 days—Set II

The effectiveness of the scaffolds for the FT wounds was evaluated based on their ability to induce isotropic collagen organization over 2 and 3 weeks of application. All four treatments (C, I, TG and TS) showed moderate to relatively aligned collagen when comparing between their responses on d14 and d21 (**Figure 6.7**). Unlike Set I, there was no progression of moderately isotropic to highly isotropic states of collagen order by d21 for two of the four formulations analyzed. This lack of collagen isotropic levels by three weeks of application for treatments C and I, can be presumed a marker for either limited healing or scar formation.¹⁸ The treatment TG having no changes in collagen organization is likely a result of scarring. Unlike treatment P from Set I, the scarring response cannot be judged by comparing the collagen III % levels across d14 and d21, as the only treatment that shows no statistical change was treatment C (**Figure 6.8**). There are some studies that examine other markers for wound healing, such as presence of myofibroblasts and the expression of alpha-smooth muscle actin for scarring responses.³² This study stands in good contrast to the previous scaffold study of the same time period showing salient differences in wound healing response with what can be speculated as similar formulations of 3M treatment.

6.4.5. Full Thickness Scaffold Treatments compared over 21 and 42 days

Treatments A and B compared with their controls over 3 and 6 weeks of treatment showed interesting variations in collagen organization. Even with both the controls and samples showing relatively elevated levels of isotropic collagen, there were statistically significant differences in the higher disorder of the control samples for both d21 and d42 sets.

This was less significant for the d42 sets, where collagen organization is remodeled to that of unwounded tissues.²² In the case of treatment B there were significant differences from d21 to d42 (**Figure 6.9**). The wide range of collagen III levels for the two treatments and their controls indicated that these treatments were not influencing the secretion of different collagen types as much as some of the above-mentioned treatments (**Figure 6.10**).

6.5. Conclusions

The analysis of wound healing samples from 3M provided valuable insight into the tunability of collagen organization and secretion in response to diverse treatments and formulations. Comparisons to the controls for some treatments were useful for understanding the extent of healing in the porcine subjects. Some treatments were statistically different compared to the other formulations within the same set. For most treatments studied over extended time periods, it was observed that collagen organization progressed to a more isotropic state and the collagen III % rose to similar levels as that of unwounded tissues. However, in the FT wound set II treated with scaffolds, the collagen response to treatments showed significantly higher alignment that could indicate scarring. Increased collagen type III was not commonly observed for most treatment sets as compared to their shorter time-point counterparts or controls.

Acknowledgements

This work was supported by the external collaboration between CRML and Dr. Kaitlin Bratlie, which started from December 2016. The research was also supported by National Science Foundation under Grant No. CBET-1227867 and the Roy J. Carver Charitable Trust Grant No. 13-4254. Dr. Kaitlin Bratlie is grateful for the Michael and Denise Mack Faculty Fellowship.

6.6 References

1. Sen, C. K. *et al.* Human skin wounds: A major and snowballing threat to public health and the economy: PERSPECTIVE ARTICLE. *Wound Repair Regen.* **17**, 763–771 (2009).
2. Enoch, S., Leaper, D. J. & Beldon, P. Basic science of wound healing. *Surg.* **28**, 409–412 (2010).
3. Singer, A. J. & Clark, R. a F. Cutaneous Wound Healing. *N. Engl. J. Med.* **341**, 738–746 (1999).
4. Martin, P. Wound Healing--Aiming for Perfect Skin Regeneration. *Science (80-.).* **276**, 75–81 (1997).
5. Morton, L. M. & Phillips, T. J. Wound healing and treating wounds Differential diagnosis and evaluation of chronic wounds. *J. Am. Acad. Dermatol.* **74**, 589–605 (2016).
6. Linares, H. A., Kischer, C. W., Dobrkovsky, M. & Larson, D. L. The histotypic organization of collagen of the hypertrophic scar in humans. *J. Invest. Dermatol.* **59**, 323–332 (1972).
7. Zhang, K., Garner, W., Cohen, L., Rodriguez, J. & Phan, S. Increased Types I and III Collagen and Transforming Growth Factor- β 1 mRNA and Protein in Hypertrophic Burn Scar. *J. Invest. Dermatol.* **104**, 750–754 (1995).
8. Clore, J. N., Cohen, I. K. & Diegelmann, R. F. Quantitation of Collagen Types I and III during Wound Healing in Rat Skin. *Proc. Soc. Exp. Biol. Med.* **161**, 337–340 (1979).
9. Chen, X., Nadiarynk, O., Plotnikov, S. & Campagnola, P. J. Second harmonic generation microscopy for quantitative analysis of collagen fibrillar structure. *Nat. Protoc.* **7**, 654–69 (2012).
10. P. J. Campagnola, Loew, L. M., Campagnola, P. J. & Loew, L. M. Second-harmonic imaging microscopy for visualizing biomolecular arrays in cells, tissues and organisms. *Nat Biotech* **21**, 1356–1360 (2003).
11. Su, P. J. *et al.* The discrimination of type I and type II collagen and the label-free imaging of engineered cartilage tissue. *Biomaterials* **31**, 9415–9421 (2010).
12. Chen, W. L. *et al.* Second harmonic generation ?? tensor microscopy for tissue imaging. *Appl. Phys. Lett.* **94**, 2007–2010 (2009).
13. Bailey, A. J., Sims, T. J., Le Lous, M. & Bazin, S. Collagen polymorphism in experimental granulation tissue. *Biochem. Biophys. Res. Commun.* **66**, 1160–1165 (1975).
14. Robson, M. C., Steed, D. L. & Franz, M. G. Wound Healing: Biologic Features and Approaches to Maximize Healing Trajectories. *Curr. Probl. Surg.* **38**, 1–140 (2001).

15. Koruth, S. & Narayanaswamy Chetty, Y. V. Hernias- Is it a primary defect or a systemic disorder? Role of collagen III in all hernias- A case control study. *Ann. Med. Surg.* **19**, 37–40 (2017).
16. Klinge, U. *et al.* Synthesis of type I and III collagen, expression of fibronectin and matrix metalloproteinase 1 and 13 in hernias of patients with inguinal hernia. *Int J Surg Invest.* **1**, 219–227 (1999).
17. Wei, S., Chow, L. T. C., Shum, I. O. L., Qin, L. & Sanderson, J. E. Left and right ventricular collagen type I/III ratios and remodeling post-myocardial infarction. *J. Card. Fail.* **5**, 117–126 (1999).
18. Van Zuijlen, P. P. M. *et al.* Collagen morphology in human skin and scar tissue: No adaptations in response to mechanical loading at joints. *Burns* **29**, 423–431 (2003).
19. Su, P. J., Chen, W. L., Chen, Y. F. & Dong, C. Y. Determination of collagen nanostructure from second-order susceptibility tensor analysis. *Biophys. J.* **100**, 2053–2062 (2011).
20. Akilbekova, D. & Bratlie, K. M. Quantitative characterization of collagen in the fibrotic capsule surrounding implanted polymeric microparticles through second harmonic generation imaging. *PLoS One* **10**, 1–17 (2015).
21. Gavin, H. The Levenberg-Marquardt method for nonlinear least squares curve-fitting problems. *Dep. Civ. Environ. Eng. Duke Univ.* 1–15 (2011).
22. Wynn, T. A. Cellular and molecular mechanisms of fibrosis. *J. Pathol.* **214**, 199–210 (2008).
23. Ajeti, V. *et al.* Structural changes in mixed Col I/Col V collagen gels probed by SHG microscopy: implications for probing stromal alterations in human breast cancer. *Biomed. Opt. Express* **2**, 2307–2316 (2011).
24. Bygd, H. C., Akilbekova, D., Muñoz, A., Forsmark, K. D. & Bratlie, K. M. Poly-l-arginine based materials as instructive substrates for fibroblast synthesis of collagen. *Biomaterials* **63**, 47–57 (2015).
25. Boddupalli, A. & Bratlie, K. M. Multimodal imaging of harmonophores and application of high content imaging for early cancer detection. *Mater. Discov.* (2015). doi:10.1016/j.md.2015.11.002
26. CLARK, R. A. F. Fibrin and Wound Healing. *Ann. N. Y. Acad. Sci.* **936**, 355–367 (2006).
27. Losi, P. *et al.* Fibrin-based scaffold incorporating VEGF- and bFGF-loaded nanoparticles stimulates wound healing in diabetic mice. *Acta Biomater.* **9**, 7814–7821 (2013).
28. Carriel, V. *et al.* Epithelial and stromal developmental patterns in a novel substitute of the human skin generated with fibrin-agarose biomaterials. *Cells Tissues Organs* **196**, 1–12 (2012).

29. Acelity, S. by. Promogran wound dressings.
30. Nephew, S. and. Biostep: Collagen Matrix Dressings.
31. Cameron, A. M., Adams, D. H., Greenwood, J. E., Anderson, P. J. & Cowin, A. J. A novel murine model of hypertrophic scarring using subcutaneous infusion of bleomycin. *Plast. Reconstr. Surg.* **133**, 69–78 (2014).
32. Darby, I. A., Laverdet, B., Bonté, F. & Desmoulière, A. Fibroblasts and myofibroblasts in wound healing. *Clin. Cosmet. Investig. Dermatol.* **7**, 301–311 (2014).

CHAPTER 7

SECOND HARMONIC GENERATION MICROSCOPY OF COLLAGEN ORGANIZATION IN TUNABLE, ENVIRONMENTALLY RESPONSIVE ALGINATE HYDROGELS

We synthesized photocrosslinked, environmentally responsive alginate hydrogels for tissue engineering applications. Methacrylated alginate (ALGMA) hydrogels were prepared across a variety and combination of ionic, covalent (chain growth, step growth, and mixed mode) crosslinking strategies to obtain a range of compressive moduli from 9.3 ± 0.2 kPa for the softest ionically crosslinked hydrogels to 22.6 ± 0.3 kPa for the dually crosslinked ionic mixed mode gels. The swelling behavior of the alginate hydrogels was significantly higher at basic pH conditions. Stiffer gels consistently swell to a lesser degree compared to softer gels for all conditions. These hydrogels were stable – retaining >80% of their original mass for three weeks – when incubated in a basic solution of diluted sodium hydroxide, which mimicked accelerated degradation conditions. Encapsulated NIH/3T3 fibroblasts remained viable and proliferated significantly more in stiffer hydrogel substrates compared to softer gels. Additionally, the collagen secreted by encapsulated fibroblasts was quantifiably comparable using second harmonic generation (SHG) microscopy imaging. Fibroblasts encapsulated in the softer hydrogels secreted significantly less collagen than the stiffer gels. The collagen in these softer gels was also more aligned than the stiffer gels. The ability to tune collagen organization using hydrogels has potential applications ranging from corneal wound healing where organized collagen is desired to epithelial wound scaffolds where a random organization is preferable.

7.1. Introduction

The human body contains natural tissue environments with dynamic and diverse mechanical properties.¹ Dynamic changes occur from regular maintenance of homeostasis, wound healing, or a response to implants.² Cells reside within these tissues ensconced in a three-dimensional scaffold known as the extracellular matrix (ECM), which responds to both macroscopic as well as microscopic perturbations.³ The ECM comprises of different combinations of proteins like collagen, glycosaminoglycans, and adhesive glycoproteins which vary from organ to organ.⁴ The macroscopic aspects derive from how the ECM provides structural integrity to the native tissue as well as a separation between different layers of tissue organization.⁵ On a smaller scale, there are biochemical cues provided by the proteins that comprise the ECM, such as collagen and fibronectin, that can instigate diverse cell signaling pathways,^{6,7} alter cell shape,⁸ as well as changes in cytoskeletal organization,^{1,9} and stress fiber formation,¹⁰ These aspects of the cell-matrix interactions are influential for several critical processes including angiogenesis,¹¹ organogenesis,¹² wound healing,¹³ as well as response to diseases¹⁴ and tumor metastasis.¹⁵

The goal of tissue engineering is to recapitulate the natural, dynamic *in vivo* environment in order to minimize unwanted host responses as well as replicate lost tissue.¹⁶ Tissue engineering covers not just the obvious motive of improving current healthcare solutions, but also to decrease costs associated with global healthcare, which is expected to rise to 8% of the US GDP by 2040.¹⁷ An ideal material for tissue engineering scaffolds would be biocompatible, mechanically tunable, and have degradation rates that match tissue regeneration rates.^{18,19} Natural polymers, with their similarity to the ECM are easy to obtain, modify, and apply to diverse tissue engineering applications.²⁰

Alginate is an anionic, polysaccharide which derives from seaweed or bacteria and has been effectively used as a supporting scaffold or tunable delivery system for tissue repair.²¹ It can be easily crosslinked using divalent cations, as well interact with a wide variety of proteoglycans and polyelectrolytes. The carboxylic acid moiety on alginate renders it pH-responsive and it can be used to deliver diverse payloads.²² Unlike conventional cationic crosslinking of hydrogels, we explored covalent crosslinking facilitated by methacrylation of the alginate backbone so that alginate could be chemically crosslinked through photoinitiated mechanisms.²³ Covalently crosslinked hydrogels are more stable *in vivo*, unlike ionically crosslinked alginate which degrades rapidly due to preferential replacement of divalent cations by monovalent ones.²⁴ UV-crosslinkable methacrylated alginate (ALGMA) hydrogel formulations show structural stability, tunability of crosslinking mechanisms as well as significant cytocompatibility for use as cell-encapsulation platforms to study secretion of ECM proteins *in vitro*.^{25,26} ECM proteins like collagen play a critical role in the structural integrity and cell-material interactions across a range of biological processes such as the host response.^{27,28} Both fibroblasts and myofibroblasts secrete collagen types I and III, as a critical part of their mechanotransduction processes.²⁹ It has been observed that there is a great need to understand the mechanisms through which stromal cells sense diverse materials and the kinetics of ECM protein secretion particularly as to how dysregulation in collagen deposition has been linked to rejected implants as shown by over the top fibrotic response.^{27,30} These studies inspired preparation of tunable alginate hydrogel environments that can be used for studying collagen organization under very soft, responsive conditions.³¹

Diverse crosslinking strategies can be employed to fabricate a range of materials properties of ALGMA hydrogels. Chain growth polymerization can be initiated using photoinitiators yja Irgacure 2959 in a degassed solution of the hydrogel to form dense chains of methacrylated alginate networks.^{32,33} Step growth polymerization occurs through thiol-ene photoclick chemistry wherein the free radical from cleavage of the photoinitiator abstracts a proton from the thiol crosslinker to create a thiyl radical. Subsequent propagation of the step growth mechanism takes place through the reaction of the thiyl radical and the vinyl group.³⁴ . A combination of step and chain growth termed mixed mode has been previously studied to prepare hybrid covalent crosslinks in the ALGMA solutions.^{31,35,36} To further increase the range of mechanical properties, ionic crosslinking of the covalently crosslinked hydrogels has been done using naturally derived polymers like alginate³⁷, carrageenan³⁸ and hyaluronan.³⁹ Collagen secretion levels from encapsulated fibroblasts has been largely evaluated using fluorescent tagging or SDS-PAGE.^{40,41} Second harmonic generation (SHG) microscopy allows for sensitive, high-content-imaging of not just secreted collagen, but also collagen organization.^{42,43} In this study, we use SHG microscopy and subsequent data analysis to examine how hydrogel stiffness can tune collagen organization from tuned to stochastic when encapsulating NIH/3T3 fibroblasts. The ability to influence collagen organization is a relatively unexplored are with previous research focused on visualizing the collagen alignment in neocartilage secreted by primary mesenchymal stem cells showing no direct cause-effect relationships.⁴⁴ We sought to decouple the effects of crosslinking density and compressive moduli, as well as crosslinking mechanism on how scaffolds influence remodeling by encapsulated fibroblasts. For specific applications such as skin grafts, cartilage repair, and corneal wound healing, being able to tune collagen organization to avoid compliance mismatch

from the local microenvironment will further improve scaffolds by better recapitulating the native environment.

6.2. Experimental

7.2.1. Materials

Medium viscosity alginic acid (CAS 9005-38-3) was obtained from MP Biomedicals Fisher Scientific (Hampton, NH) and methacrylic anhydride (CAS 760-93-00) was supplied by Sigma Aldrich (St. Louis, MO). 2-hydroxy-4'-(2-hydroxyethoxy)-2-methylpropiophenone (Irgacure 2959) was obtained from Sigma-Aldrich (St. Louis) and dithiothreitol (DTT) was obtained from VWR Chemicals (Batavia, IL). Other materials were purchased through Sigma Aldrich (St. Louis) and were used as received, unless otherwise stated. Fresh deionized water (Milli-Q, Thermo Scientific Nanopure, Waltham, MA) was used throughout this study.

7.2.2. Methacrylated Alginate (ALGMA) Synthesis

Methacrylated alginate solutions were prepared based on a previously described protocol.³¹ A 1% (w/v) solution of medium viscosity alginic acid in DI water was prepared by mixing 2 g alginic acid powder in 200 mL of DI water. Methacrylic anhydride (16 mL) was slowly added to the solution. The pH of the solution was maintained between 8 and 9 using aliquots of 5 M NaOH at 4 °C. After 24 h, the methacrylated alginate solution was dialyzed against water using a molecular weight cutoff membrane of 13,000 Da for two days with dialysate being refreshed twice daily. The final dialyzed product was lyophilized (4.5 L, Labconco, Kansas City, MO). NMR was used to confirm methacrylation of the alginic acid. Solutions of alginate and ALGMA were prepared using standard protocols.⁴⁵ The % methacrylation was calculated by the relative integration of the protons from the methacrylate group (I_{CH_2} at $\delta = 6.0$ and 5.6 ppm) and the

methyl group (I_{CH_3} at $\delta = 1.8$ ppm) to the protons from the carbohydrate peak ($I_{polymer}$) using equation 1 (**Figure 7.1**).

$$\% \text{Methacrylation} = \frac{\left(\frac{I_{CH_2}}{n_{CH_2}} + \frac{I_{CH_3}}{n_{CH_3}} \right)}{\frac{I_{polymer}}{n_{H_{polymer}}}} \quad (1)$$

7.2.3. Hydrogel Fabrication and Characterization

The stock solution for methacrylated alginate hydrogels was prepared by dissolving 300 mg of ALGMA and 10 mg of Irgacure 2959 in 10 mL of DI water. Step growth, chain growth and mixed mode polymerization was conducted to obtain a range of mechanically different hydrogels. The step growth polymerization was obtained by adding 250 μ L of 4 mg/mL dithiothreitol (DTT) to the stock solution. Chain growth polymerization was conducted by degassing the stock solution under vacuum. Mixed mode polymerization was obtained by adding the 250 μ L of 4 mg/mL DTT followed by degassing. All hydrogels were crosslinked by exposure to UV light (365 nm, 2 W/cm²) for 10 minutes. Dually crosslinked ALGMA hydrogels were fabricated by adding 100 μ L of 0.2 M SrCl₂ after exposure to UV light.

To measure the compressive modulus of the ALGMA hydrogels, plugs (6 mm thick, 16 mm diameter, $n = 4$) were prepared for testing. These hydrogel samples were placed between two glass slides, on which sequential series of weights were added. Image J (NIH, Bethesda, MD) was used to evaluate changes in height and cross-sectional area of the hydrogel samples in response to the weights. The slope of the linear region in the stress strain curve over a strain range of 5-15% was defined as the compressive modulus.

Swelling ratios of the different crosslinked hydrogels ($n = 3$) were measured after drying at room temperature. These hydrogels were swollen in acetate buffers (1 mM) and maintained at pH 3, 5, 7.4 and 9 for two days. The swelling ratios were subsequently calculated after analyzing

the recorded dry and wet weights using equation 2 where M_d is the dry mass and M_w is the wet mass.

$$\text{Swelling ratio} = \frac{M_w - M_d}{M_d} \quad (2)$$

7.2.4. *In Vitro* Degradation

To test the degradation of the hydrogels, the gels were placed in accelerated degradation conditions (0.1 mM NaOH). After equilibrating these gels for one day in solution, masses were recorded for each consecutive day. The % mass remaining was compared with the initial mass and recorded for each time-point.

7.2.5. Cell Culture and Proliferation Assay

NIH/3T3 fibroblasts (ATCC, Manassas, VA) were passaged at 37°C with 5% CO₂ in Dulbecco's modified Eagle's medium (Cellgro, Thermo Scientific) supplemented with 10% bovine calf serum, penicillin (100 U/L) and streptomycin (100 µg/mL), referred to as complete medium (CM). Cell suspension aliquots of 200 µL (1×10^7 cells/mL) were mixed 300 µL of the different hydrogel solutions and were pipetted into 48 well plates. For each plate, live and dead controls were made by plating cells directly on tissue culture plastic. The plates were incubated for 48 h. The medium in the dead control wells was aspirated and replaced with 300 µL of 70% ethanol for 10 minutes. Subsequently, the supernatant in all wells was aspirated. To each well 150 µL of working solution (2µM calcein AM (AnaSpec, Fremont, CA) and 7.5 µM of 7-aminoacino mycin D (Tonbo Biosciences, San Diego, CA) in phosphate buffered saline (PBS)) was added and the plates were incubated for 30 – 40 min at 37°C in 5% CO₂. Fluorescent images were taken using EVOS Flouid Cell Image Station (Thermo Scientific) with the red (excitation/emission 586/646 nm) and green channels (482/532 nm) set to visualize the dead and live cells respectively. Live and dead cells were quantified at an excitation/emission of 485/528

nm and 645/490 nm, respectively, using a plate reader (BioTek Synergy HT Multidetector Microplate Reader, Biotek, Winooski, VT). The percentage of live cells was determined using the following equation:

$$\% \text{ live cells} = \frac{F(528)_{\text{sample}} - F(528)_{\text{Dead Control}}}{F(528)_{\text{Live Control}} - F(528)_{\text{Dead Control}}} \times 100\% \quad (3)$$

where $F(528)_{\text{sample}}$ is the fluorescent signal at 528 nm from the cell laden samples, $F(528)_{\text{Dead Control}}$ is the fluorescent signal at 528 nm from the lysed control samples, and $F(528)_{\text{Live Control}}$ is the fluorescent signal at 528 nm from the control samples.

7.2.6. Second Harmonic Generation Microscopy of the gels

Equal volumes of suspended NIH/3T3 fibroblasts (1×10^7 cells/mL) were mixed with hydrogel solutions. The cell-gel suspension (100 μ L) was pipetted between two coverslips, which were exposed to UV light (365 nm, 2 W/cm²) for 10 min. These gelled samples were then placed in Petri dishes containing CM. Medium was replaced every three days. Negative controls were prepared by crosslinking the gels without cells. All samples were preserved in 10% formalin before imaging.

A mode-locked Ti: Sapphire laser (100 fs pulse width, 1 kHz repetition rate obtained from Libra, Coherent, Santa Clara, California) that operates with an 800 nm fundamental, was used to image all samples. A half-wave plate and Glan-Thompson polarizer (Thorlabs, Newton, New Jersey) was used to control the power at the sample stage. The second harmonic signal from the interaction with the samples was collected in transmission mode.

To image these samples, an inverted microscope (Amscope, Irvine, California) and a Nikon Plan Fluorite objective (20 \times , 0.50 NA, 2.1 mm WD, Nikon, Melville, New York) was used to focus the beam. The SHG transmission was collected using a Nikon water immersion objective (40 \times , 0.8 NA, 3.5 mm WD, Nikon, Melville, New York). This signal was reflected by a dichroic

mirror (DMLP425T, Thorlabs). Two short pass filters < 450 nm (FGB37M, Thorlabs) and an 808 nm notch filter (NF-808.0-E-25.0M, Melles Griot, Rochester, New York) were used to separate the signal from the fundamental beam prior to detection by the intensified charge couple device (iCCD, iStar 334T, Andor, Belfast, United Kingdom). A Glan-Thompson polarizer and a half-wave plate mounted on a motor-driven rotational stage (Thorlabs) was used to generate linear polarized light to conduct polarized SHG imaging. Images of the samples were acquired at every 10° from 0° to 350°. For every experimental condition, images were collected in triplicate. The regions of interest (ROIs) were analyzed and fit using the following equation:

$$I_{SHG} = c \cdot \left\{ \left[\sin^2(\theta_e - \theta_o) + \left(\frac{\chi_{zzz}}{\chi_{zzx}} \right) \cos^2(\theta_e - \theta_o) \right]^2 + \left(\frac{\chi_{xzx}}{\chi_{zzx}} \right)^2 \sin^2(2(\theta_e - \theta_o)) \right\} \quad (4)$$

where $\frac{\chi_{zzz}}{\chi_{zzx}}$ and $\frac{\chi_{xzx}}{\chi_{zzx}}$ are the second-order susceptibility tensor element ratios, θ_e and θ_o are the incident polarization angle and collagen fiber angle, respectively, and c is a normalization constant. Each ROI was individually analyzed for the orientation of collagen within it. A histogram was generated detailing the orientation of the collagen in the entire image. The organization of collagen was evaluated based on the full-width at half maximum (FWHM) of the Gaussian fit of the histogram. The types of collagen were identified using a previously described method.³⁰ Collagen gels of varying collagen III concentrations were fabricated and imaged using polarized SHG microscopy, and the resulting images were fit using equation 3. Histograms of $\frac{\chi_{xzx}}{\chi_{zzx}}$ showed the presence of a peak at ~0.8 which was assigned to collagen III, and one at ~1.2 that was assigned to collagen I. The ratio of the integrated peaks was plotted against the actual collagen III concentration in the gels to yield a standard curve. This standard curve allowed for estimation of collagen III levels in the imaged samples.

7.2.7. Statistical Analysis

Data generated was statistically analyzed and the values are reported as mean \pm standard deviation (SD). Mean comparisons were determined to be statistically significant via a two-way ANOVA. Tukey's honest significant difference test was used to evaluate the pair-wise comparisons. Statistically significant differences were identified for $p < 0.05$.

7.3. Results

7.3.1. Characterization of ALGMA Hydrogels

Characterization of the ALGMA was conducted using ^1H NMR spectroscopy (Figure 6.1), based on a previously described protocol.⁴⁶ Peaks appearing at 6.0 and 5.6 ppm were assigned to the methacrylamide protons confirming methacrylation of the alginic acid. The extent of methacrylation was calculated to be $27 \pm 2\%$ using equation 1. The mannuronic acid content was determined to be $50 \pm 2\%$.

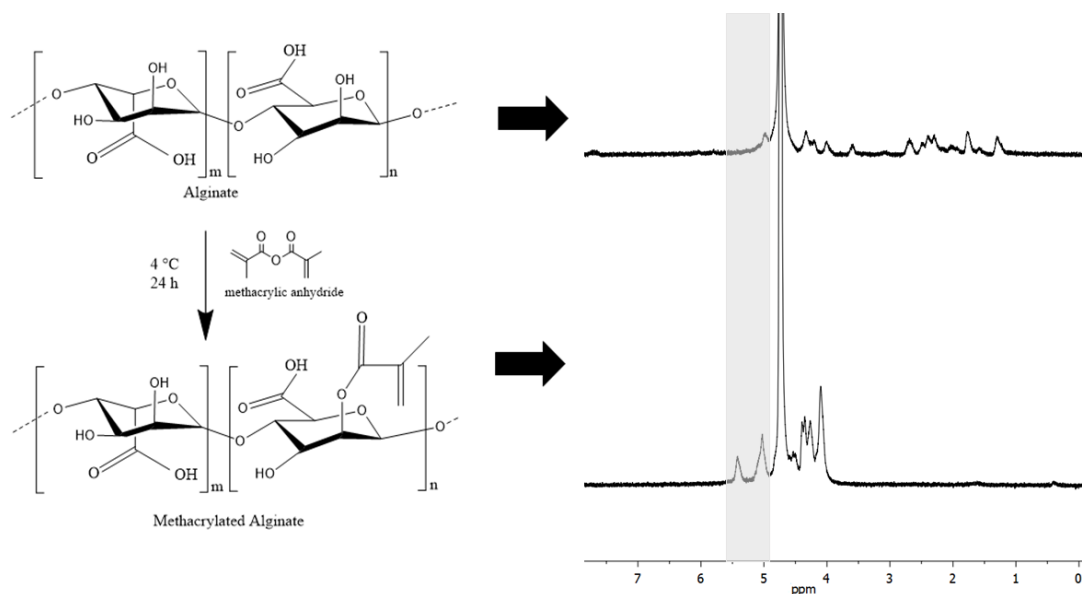


Figure 7.1 Synthesis and characterization of ALGMA. (Left) Schematic representation of chemical modification of alginate. (Right) ^1H NMR spectra of alginate and methacrylated alginate. Methacrylation of alginate polymer from unmodified to methacrylated with respective ^1H NMR spectra found at $\delta = 6.2$ and $\delta = 6.6$ ppm. The degree of methacrylation was calculated as a percentage of hydroxy group substitution with the methacrylate groups per repeating unit.

7.3.2. Compressive Moduli

The compressive modulus of medium viscosity ALGMA hydrogels was modulated via different crosslinking methods.³¹ Comparisons of the compressive moduli of the different hydrogel preparations are shown in **Figure 7.2**. Our previously published results using very low viscosity alginate are included.³¹ Stiffness significantly increased from 9.3 ± 0.2 kPa for step growth, 13.0 ± 0.3 kPa for chain growth, and 15.2 ± 0.2 kPa for the mixed mode conditions. Dually crosslinked hydrogels were formed by incubating the hydrogels in 0.2 M SrCl_2 and had compressive moduli ~ 7 kPa higher than the covalently crosslinked gels. These gels had compressive moduli of 16.7 ± 0.3 kPa for ionic step growth, 20.2 ± 0.4 kPa for ionic chain growth, and 22.6 ± 0.3 kPa for the relatively stiffest formulation of the ionic mixed mode condition. The non-methacrylated ionic alginate hydrogels had a compression modulus of 8.3 ± 0.3 kPa. In comparison to the very low viscosity ALGMA hydrogels which showed a range of 0.7 ± 0.1 to 2.24 ± 0.1 kPa, these medium viscosity-based gels were significantly stiffer, thus depicting two completely different ranges of mechanical environment. These distinct ranges of mechanotransductive cues provide us with a good comparison of cell responses to stiff substrates (similar to what is observed for musculoskeletal environments^{47,48}) and soft substrate (similar to fatty tissue in the liver⁴⁹ or healthy lung tissues^{48,50}).

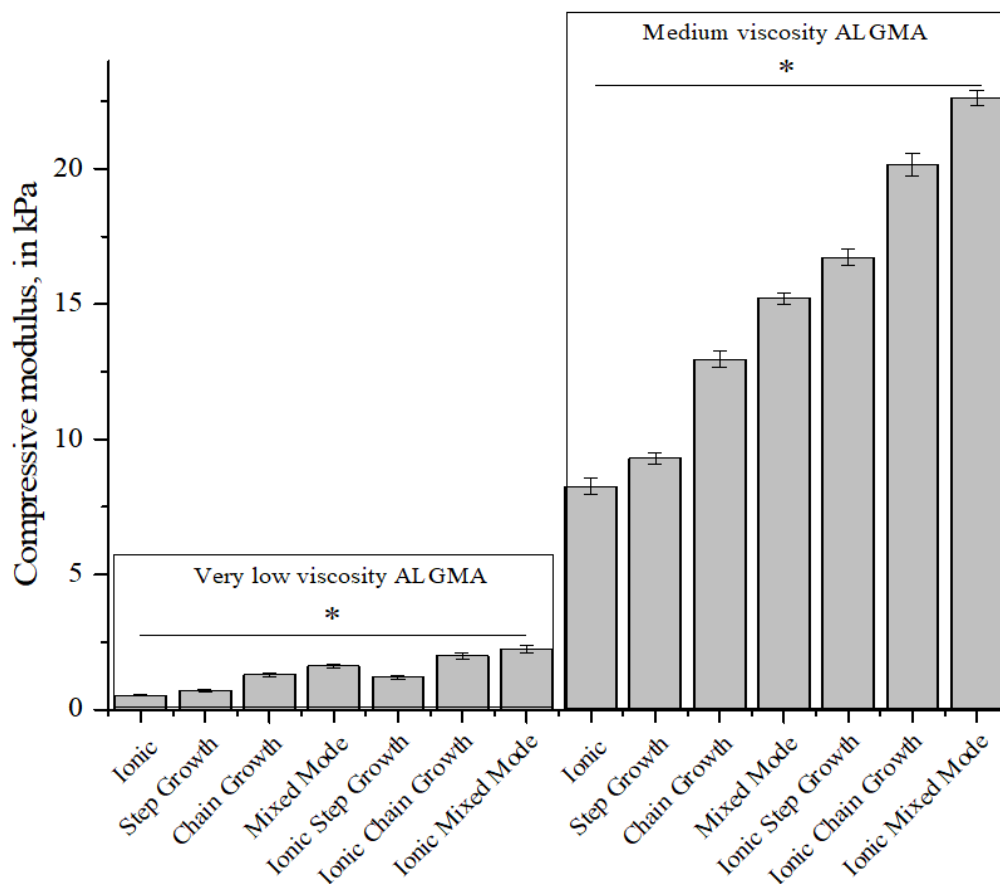


Figure 7.2. Compressive moduli of alginate hydrogels. Compressive moduli of methacrylated alginate hydrogels crosslinked through the different mechanisms and alginate precursor viscosities. Data represents the mean \pm SD. $n = 3$. Statistical analysis through two-way ANOVA and Tukey's HSD post-hoc test. * $p < 0.05$.

7.3.3. Swelling Response

The swelling response of these hydrogels was examined to evaluate their suitability as scaffolds for wound healing applications.^{45,51} By controlling the crosslinking density, swelling responses can be tuned and delivery kinetics of potential encapsulated drugs can be controlled.^{52,53} Softer hydrogels were able to swell to a greater extent than the stiffer hydrogels. Under basic conditions, the swelling response was significantly higher for all hydrogels compared to swelling in acidic conditions (**Figure 7.3**). This swelling response plateaued at pH 9 for the mixed mode and all three dually crosslinked hydrogels, which were the stiffer gels (>15 kPa). Swelling was not

statistically significant for the dually crosslinked hydrogels at pH 3 and at pH 5. One interesting finding was that at pH 7.4 and 9, the swelling response increased from the mixed mode gels to the ionic step growth gels and then decreased again. This may result from the Sr^{2+} interaction with the free carboxylic acid groups, mitigating the otherwise downward trend.

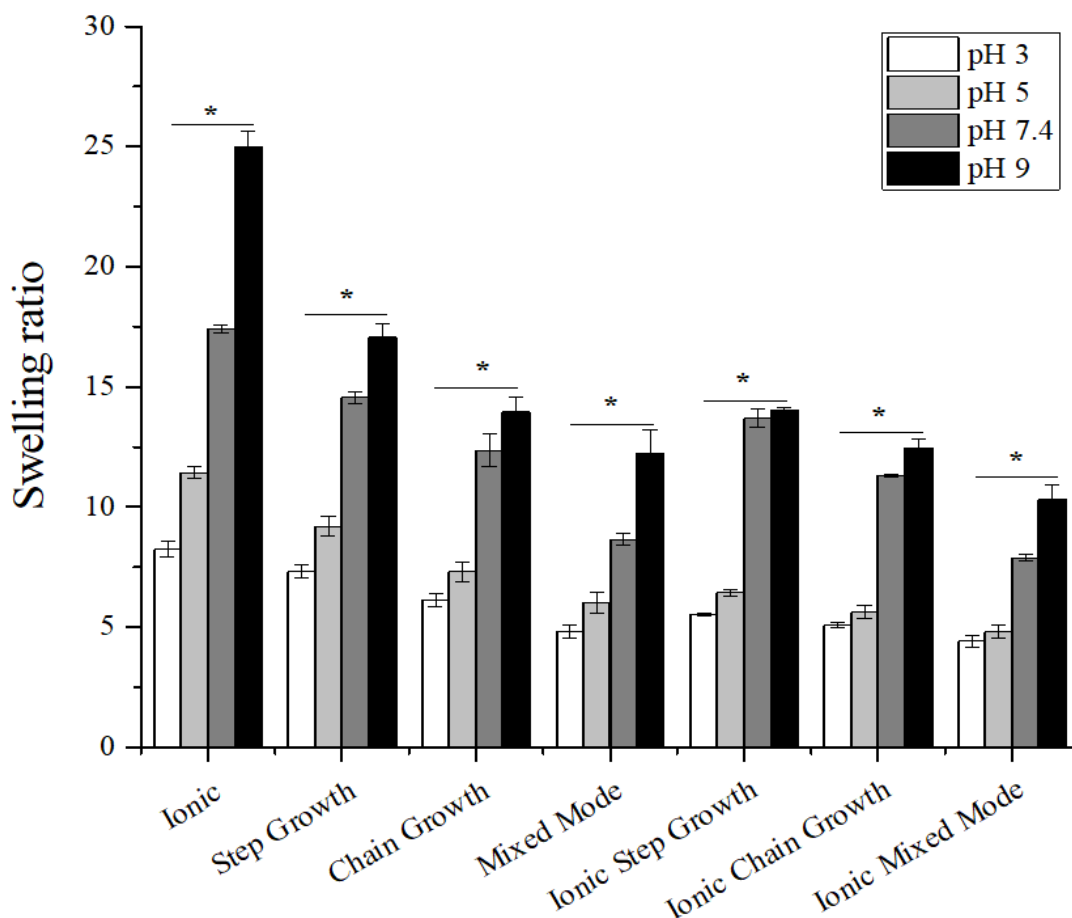


Figure 7.3. Swelling response of the medium viscosity alginate hydrogels in a range of pH buffers. Hydrogels crosslinked through different mechanisms were swelled in pH 3, 5, 7.4, and 9 sodium acetate buffers. Data represents the mean \pm SD. $n = 3$. Statistical analysis through two-way ANOVA and Tukey's HSD post-hoc test. * $p < 0.05$.

7.3.4. Degradation Kinetics

Hydrogels should have degradation kinetics that are similar to the tissue regeneration rate.^{54,55} All of the hydrogels in this study were incubated in 0.1 mM NaOH to mimic accelerated

degradation conditions (**Figure 7.4**). There were no statistical differences observed for the degradation kinetics of the covalently crosslinked hydrogels, with the three dually crosslinked hydrogels showing a relatively more stable response. The hydrogels degraded to 50% of their original mass over 31 ± 3 days for the former, while the half-life was extended to 25 ± 3 days for the latter.

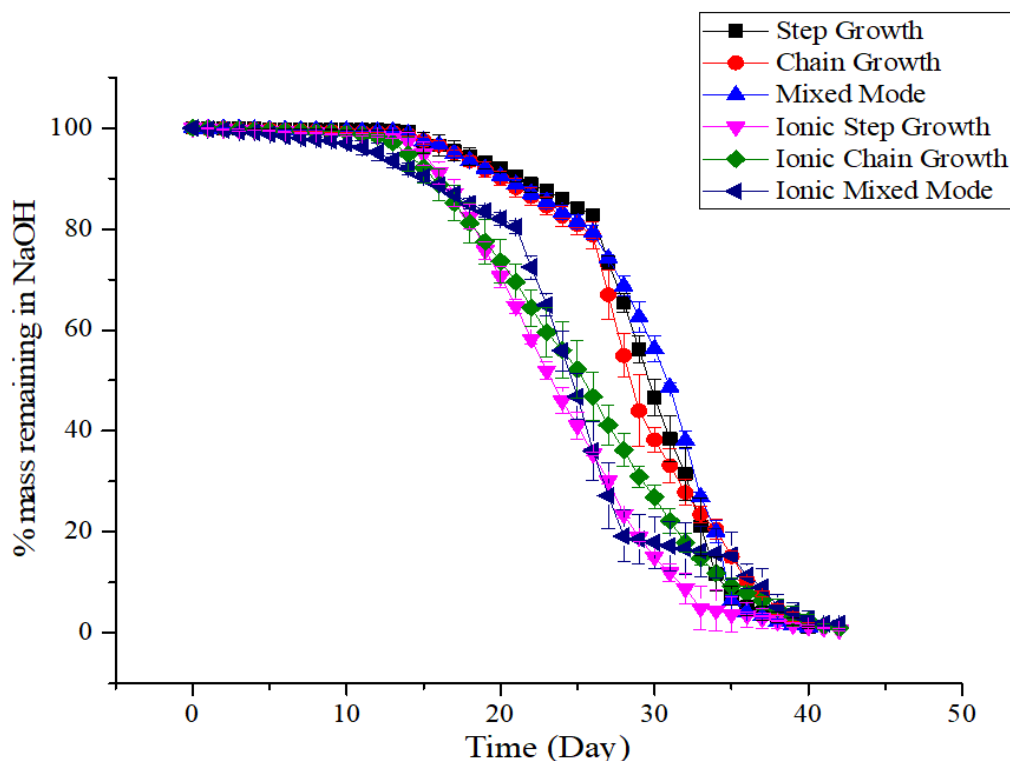


Figure 7.4. Degradation response of alginate hydrogels under accelerated conditions. Alginate hydrogels were immersed in 0.1 mM NaOH to mimic accelerated degradation conditions. Data represents the mean \pm SD. $n = 3$. Statistical analysis through two-way ANOVA and Tukey's HSD post-hoc test. * $p < 0.05$.

7.3.5. Cytocompatibility of ALGMA Hydrogels

One of the major prerequisites for any viable hydrogel used in biomedical applications is cytocompatibility.^{18,56} Live/Dead assays were conducted to evaluate the cytocompatibility of the different ALGMA hydrogels encapsulating NIH/3T3 fibroblasts. The encapsulated fibroblasts

were imaged and compared after 48 hours of incubation, and the proliferation was normalized to the cells cultured on tissue culture plastic (**Figure 7.5**). We have included cell proliferation on very low viscosity ALGMA gels³¹ for comparison. The low viscosity ALGMA gels showed a monotonic increase in cell proliferation with increasing stiffness. This trend did not carry forward for fibroblasts encapsulated in medium viscosity ALGMA studied here. Here there was a steep increase in cell proliferation from step growth (27 ± 4 %) to chain growth (51 ± 1 %). Cell proliferation plateaued at $\sim 60\%$ for the dually crosslinked hydrogels, with values of 56 ± 2 , 57 ± 1 and 62 ± 1 % for the ionic step growth, ionic chain growth, and ionic mixed mode hydrogels, respectively. These results indicated that there is a threshold hydrogel stiffness for the medium viscosity ALGMA hydrogels beyond which increased stiffness does not improve cell proliferation.

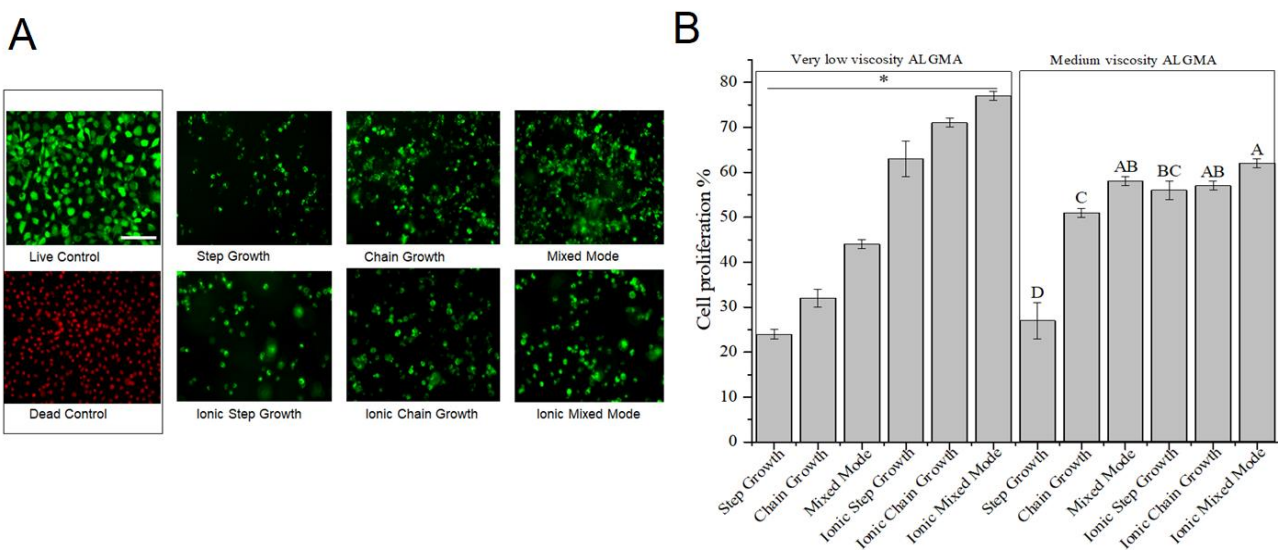


Figure 7.5. Proliferation of NIH/3T3 cells encapsulated in alginate hydrogels. NIH/3T3 fibroblasts were mixed with ALGMA hydrogel solutions made from very low and medium viscosity alginic acid and crosslinked under different mechanisms. Cells cultured on tissue culture plastic served as controls. (A) Representative micrographs of live (green) and dead (red) cells cultured for 48 h. (B) Quantification of live and dead cells. Data represents the mean \pm SD. $n = 6$. Statistical analysis through two-way ANOVA and Tukey's HSD post-hoc test. $*p < 0.05$.

7.3.6. SHG Microscopy

Encapsulated fibroblasts have been studied for their ability to synthesize collagen under diverse cell culture conditions.⁵⁷ SHG microscopy allows sensitive visualization of collagen secreted by these encapsulated cells as collagen is a non-centrosymmetric protein that is known to be SHG active. Collagen secretion levels were normalized to the background obtained by imaging non-cell laden hydrogel controls that had been incubated under identical conditions. Across the different hydrogel conditions there was an increase in collagen levels on day 7 compared to day 5 (Figure 7.6). For all but one of the cell-hydrogel samples (ionic chain growth), the collagen levels on day 10 were significantly lower than the day 5 values. Collagen levels were positively correlated ($R = 0.98$) to the modulus of the hydrogel for all materials studied here (Figure 7.7). Ionic chain growth and ionic mixed mode hydrogels caused the fibroblasts to produce more collagen after 5 days of culture than the other hydrogels. There were significant differences observed for the increase in normalized collagen levels particularly for measurements taken on day 7 and day 10.

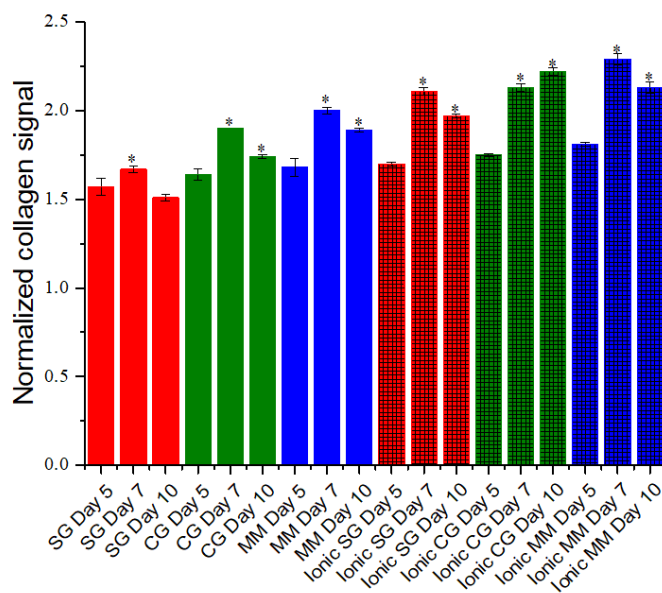


Figure 7.6. Collagen secretion by NIH/3T3 cells encapsulated in alginate hydrogels was evaluated using SHG microscopy. Encapsulated NIH/3T3 fibroblasts were mixed with ALGMA

and crosslinked. Collagen signal was normalized to the signal from the respective non-cell seeded hydrogel samples. Data represents the mean \pm SD. $n = 3$. Statistical analysis was conducted for each hydrogel type through two-way ANOVA and Tukey's HSD post-hoc test. $*p < 0.05$ for samples compared to day 5 results. Red, green and blue colored bars represent the step growth, chain growth and mixed mode crosslinking mechanisms. Dually crosslinked hydrogels shown with additional cross-hatch pattern on top of the original covalent crosslinking color.

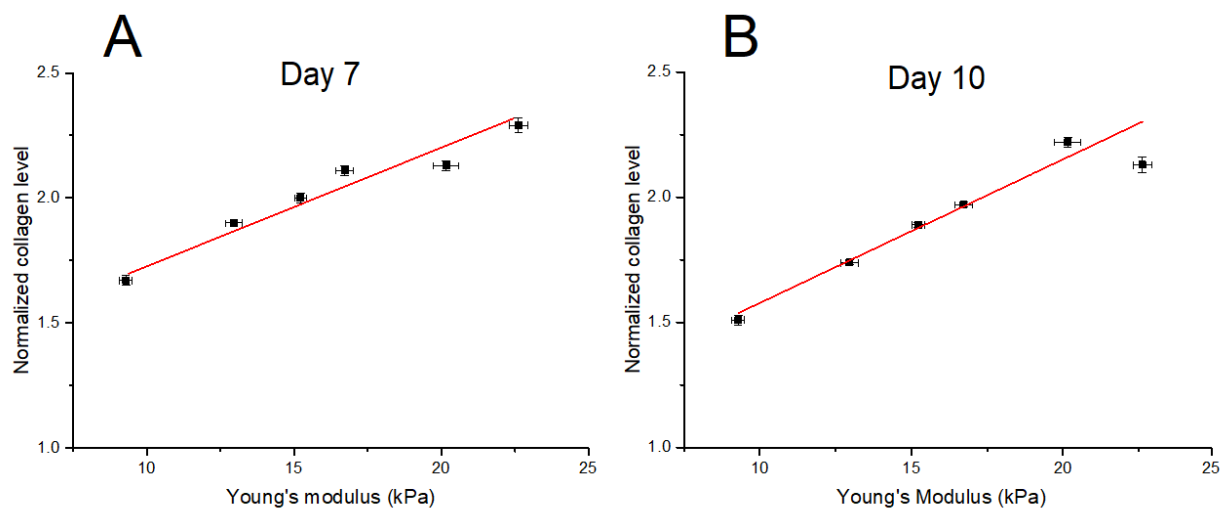


Figure 7.7: Correlation of collagen levels to Young's modulus. Normalized collagen levels plotted against the Young's modulus of the different ALGMA hydrogels, as measured on day 7 (A) and day 10 (B). Data represents the mean \pm SD. $n = 3$.

Collagen organization can influence on cell morphology and proliferation.^{58,59} It is also a biomarker for tumor progression.^{60,61} In comparing the organization of the collagen secreted, and possibly rearranged by the fibroblasts,^{61–64} there was an interesting trend in which softer gels resulted in more organized collagen, while stiffer gels resulted in less organized collagen (**Figure 7.8 and 7.9**). This trend appears to reach a plateau or possible decrease for ionic chain growth and ionic mixed mode gels, which have compressive moduli > 20 kPa. The line is a guide for the eye. Mechanical properties have previously been shown to influence cell proliferation in which stiffer substrates corresponded to upregulation of protein secretion.⁶⁵ Conversely, previous studies have shown that patterned protein presentation can be used to spatiotemporally tune stem cell differentiation, independent of the mechanics of the encapsulating hydrogel.⁶⁶ This is the first

report to our knowledge on mechanical properties influencing collagen organization. The empirical evidence presented on the influence of the hydrogel crosslinking method on collagen organization secreted by encapsulated fibroblasts adds demonstrates how materials can influence host responses to tissue engineered scaffolds.

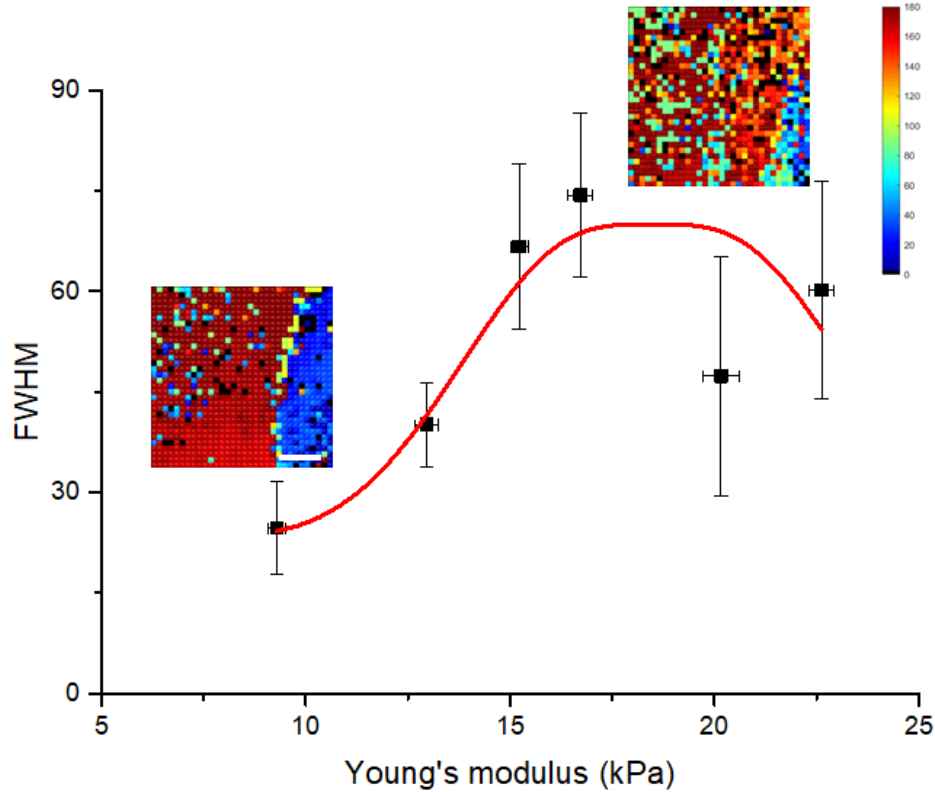


Figure 7.8. Organization of collagen secreted by encapsulated fibroblasts in alginate hydrogels. Collagen secreted by NIH/3T3 fibroblasts encapsulated in the different alginate hydrogels were analyzed using SHG microscopy on day 10 and are reported as FWHMs. Data represents the mean \pm SD. $n = 3$. The solid line is a guide for the eye indicating the trend for how collagen organization varies with changes in the modulus of crosslinked hydrogel. The legend to the organization of the collagen as seen in the heat-map is provided on the top right.

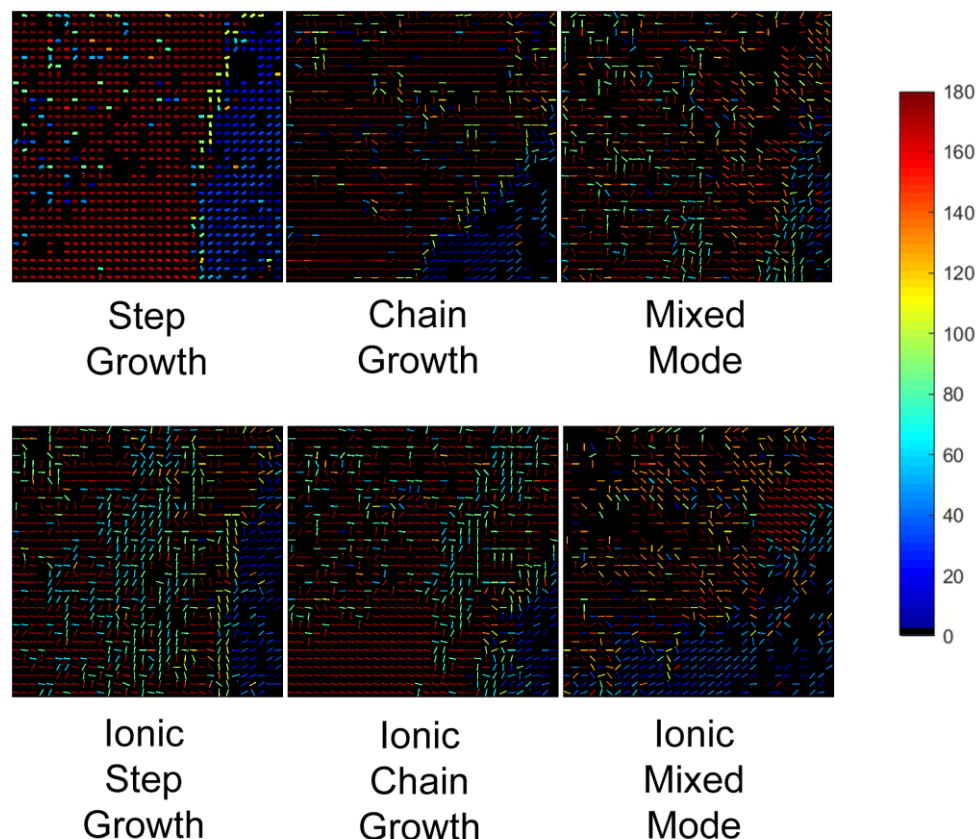


Figure 7.9. Effect of crosslinking mechanism on collagen organization. Collagen organization heat maps in response to the different ALGMA hydrogel environments showing clear changes with difference in crosslinked hydrogel environment. The legend for the heat map is on the right side of the figure.

7.4. Discussion

In this study, ALGMA hydrogels were synthesized through previously described protocols by reacting medium viscosity alginic acid precursor with methacrylic anhydride.³¹ Key properties of these tunable hydrogels were analyzed including the compressive moduli, degradation kinetics, and swelling responses to different pH environments. The resulting empirical observations indicated that the medium viscosity ALGMA hydrogels are suitable for fabrication of cytocompatible scaffolds for studying collagen secretion and organizational changes by encapsulated fibroblasts.

Most cells are anchorage dependent and adhere to underlying substrates forming focal adhesions. This cell-substrate interaction senses substrate stiffness by the cell reaching out through the actin-myosin cytoskeleton and is critical to the subsequent expression of secreted proteins as well as differentiation to activated phenotypes.^{8,49} Ionic, covalent, and a combination of the two (dual crosslinking) crosslinking mechanisms were employed to prepare medium viscosity ALGMA hydrogels with compressive moduli in the range of 8.3 ± 0.3 to 22.6 ± 0.3 kPa (**Figure 7.2**). From these measurements, it is evident that there is a considerable influence from both the alginic acid precursor as well the crosslinking mechanism on the compressive moduli with our previously studied very low viscosity based ALGMA hydrogels restricted within a range of 0.5 ± 0.1 to 2.2 ± 0.1 kPa,³¹ compared to the significantly stiffer ones synthesized here from medium viscosity precursors. The overall trend of the increase in compressive moduli conforms to the theory of rubber elasticity.^{31,67} We are primarily concerned with how hydrogel properties can influence collagen organization. As such, this range of mechanical environments will allow us to disentangle trends between hydrogel stiffness and collagen alignment as this range of moduli traverses previously observed thresholds for fibroblasts to express actin stress fibers and differentiate to myofibroblasts.^{68,69} Some studies have indicated the presence of an intermediate stage of proto-myofibroblasts that not express α -smooth muscle actin, while still showing significantly higher overall actin expression.^{70,71} Another study used chemically modified, soft alginate hydrogels with compressive moduli over the range of ~ 10 to 12 kPa, that showed low immune cell activation, and significantly reduced fibrotic response.⁷²

Acute wound sites show rapid transition in pH from slightly acidic immediately after injury to basic conditions during granulation tissue formation, to more neutral levels upon reepithelialization.^{73,74} Chronic wounds remain slightly alkali, which makes the wound site more

susceptible to opportunistic pathogens.^{74,75} Hence, an important aspect of designing biocompatible scaffolds from naturally derived, anionic polymers is utilizing their natural tendency to swell under basic pH conditions.^{76,77} Responsive scaffolds that swell in alkaline pH can be used to deliver payloads of cytokines and chemokines to boost the natural wound healing process, and dynamically mitigate the chronicity of the wound site.^{78,79} As the crosslinking density is inversely related to the swelling response,⁶⁷ it was expected that the softer purely ionically or covalently crosslinked hydrogels would swell more than the dually crosslinked gels. This trend held for previously studied very low viscosity ALGMA gels,³¹ as well as the gels prepared here from medium viscosity alginic acid (**Figure 7.3**). All the ALGMA hydrogels swelled the most at pH 9 condition, which makes these viable materials for preparing scaffolds for chronic wound treatments. Further studies can be conducted to evaluate the kinetics of using such responsive hydrogels for drug delivery to chronic wounds, by studying the transport of clinically relevant biomolecules from swollen hydrogels.²² To this end, there have been studies carried out using additional stages of wound treatment using acidified solutions,⁸⁰ allo-grafts derived from neonatal foreskin to instigate accelerated wound healing⁸¹ as well as synthetically derived scaffolds such as Apligraf®, which closely resembles the structure of natural skin.⁸² An environmentally responsive scaffold that can be tuned to deliver payloads of wound-healing relevant growth factors or patient-derived stromal cells could personalize wound care management with minimal immune rejection.^{83,84}

The degradation of hydrogels results in decreased crosslink density over time.⁸⁵ Alginate hydrogels are very stable in PBS. Thus, to measure hydrolytic degradation, the ALGMA gels were incubated in a basic solution of 0.1 mM sodium hydroxide.^{86,87} Covalently crosslinked ALGMA hydrogels derived from very low viscosity degraded to 50% of their original mass within 6 ± 1

days with dually crosslinking increasing the half-life to 13 ± 2 days. The gels fabricated here were almost 5 times as stable, with half-lives of 31 ± 3 days (**Figure 7.4**). However, dually crosslinking the medium viscosity gels did not increase the half-life (25 ± 3 days). Ideally, degradation kinetics of the scaffold should match tissue regeneration rates. Potential inflammatory or fibrotic responses can result if these rates are not equivalent.⁸⁸

Scaffolds must be cytocompatible.⁸⁹ NIH/3T3 cells showed no cell death when encapsulated in the different crosslinked ALGMA hydrogels (**Figure 7.5B**). Additionally, the encapsulated cells had cell proliferation above 50% compared to the controls of tissue culture plastic (TCP), with the exception of step-growth gels. When looking at the compressive moduli and cell proliferation (**Figure 7.5A**), it appears that there was a threshold compressive modulus beyond which the cell proliferation showed few significant changes with increased crosslinking density. 3D encapsulation of cells allows for relatively better approximations of the natural *in vivo* conditions, as compared to surface seeding studies.¹⁸ Comparing the cell morphology in the live/dead assay, there were no differences for the different hydrogel environments which agrees with Huebsch *et al.*⁶⁵ In an effort to decouple the mechanical effects of 3D modified alginate matrices on the morphology of human mesenchymal stem cells (hMSCs, which are similar in many ways to fibroblasts), the cells were encapsulated in alginate hydrogels of varying Young's modulus and fixed concentration of the RGD motif that was used to increase cell adhesion. There were no significant changes in morphology observed when cultured for 2h, 24h and even one week under encapsulated conditions. Such studies indicate the complexity in using nanoporous cell encapsulation hydrogels such as alginate for studying the changes in cell morphology responses. The plateaued trend of the cell proliferation to the dually crosslinked hydrogels introduces the possibility that once the ALGMA hydrogels are uniformly crosslinked above 20 kPa, would it be

possible to disentangle the effect of gelation mechanism and the rigidity to determine which factor holds greater significance on cellular responses.^{90,91}

Fibroblasts have mechanical memory regarding the stiffness of the substrates they are cultured on, particularly with respect to how they differentiate to myofibroblasts that has been positively correlated to over-secretion of collagen I.^{48,57,92} Qualitative as well as quantitative analysis of the secreted collagen using SHG microscopy has allowed for an informed rational design of biocompatible materials.^{30,93} Here, we see a significant increase of the collagen levels on day 7 for all hydrogel conditions compared to day 5 (**Figure 7.6**). This was expected as protein deposition typically increases with culture time. The overall timeline can vary based on several factors such size, shape and topography of the environment.⁹⁴ As such, the ionic chain growth gel may have a different timeline related to its crosslinking mechanism compared with the other gels. The positive correlation of the collagen levels to the modulus of the underlying substrate conformed to previous studies in which stiffer substrates cause stromal cells to secrete more ECM proteins particular around day 7 to day 10.^{56,95} The decrease in collagen levels beyond day 7 may result from an increase in MMP-13 (collagenase).⁹⁵ These results could also indicate an upregulation in overall cell activity which may be a precursor for fibroblast-to-myofibroblast differentiation, particularly in the stiffer microenvironments.⁹⁶ Similarly, Huebsch *et al.* found that alginate hydrogels encapsulating hMSCs instigated osteogenic differentiation when the gels were stiffer. Encapsulated, with a biphasic influence of the modulus on ECM secretion.⁶⁵ Beyond just the quantification of the collagen levels, it is of great importance to understand the influence of collagen organization.⁵⁸ There is a dearth of studies conducted on the tunability of local collagen organization using sensitive visualization techniques. As has been previously stated, the timeline of collagen secretion and its organization can determine the fate of implanted materials and

understanding how materials alter these responses will allow us to improve implant compatibility and prevent a fibrotic response.³⁰

The organization of collagen in the ECM influences the remodeling of wounds,⁹⁷ as well as acceptance of implants.³⁰ Aligned collagen is found in specific natural environments such as mammalian tendons as well as cornea.^{98,99} Stochastic collagen is present in natural dermis.¹⁰⁰ Keeping collagen alignment in mind, we can determine how materials properties will change cellular responses and this understanding can improve scaffold design for tissue repair in different organs.²² Collagen angles were measured using SHG and were plotted using a heat map to better visualize regions of organization. Softer step growth gels (~10 kPa) can be seen as having a lower FWHM, which the hydrogel resulted in more aligned collagen (**Figure 7.10**). This can be visualized in the heat map in which there are large regions of collagen having the same orientation angle. The FWHM of collagen decreases with increasing compressive modulus, which means the collagen is more isotropic. The heat map shows that there is a large variation in collagen angles for the ionic step growth condition (~15 kPa) (**Figures 7.8 and 7.9**). This suggests that not only mechanical stiffness of the underlying substrate influences collagen response, necessitating further research on disentangling the influence of crosslinking mechanism on cell interactions. As this study is limited to collagen based analysis, future studies on the expression of FAK and MAPK expression along with quantified immunocytochemical staining of cells cultured in or on such scaffolds could further elucidate the mechanism that is causing collagen organization.^{101,102} This study provides further development of SHG microscopy as a platform for visualizing the influence of materials properties in tunable hydrogels to how cells sense their local microenvironment.

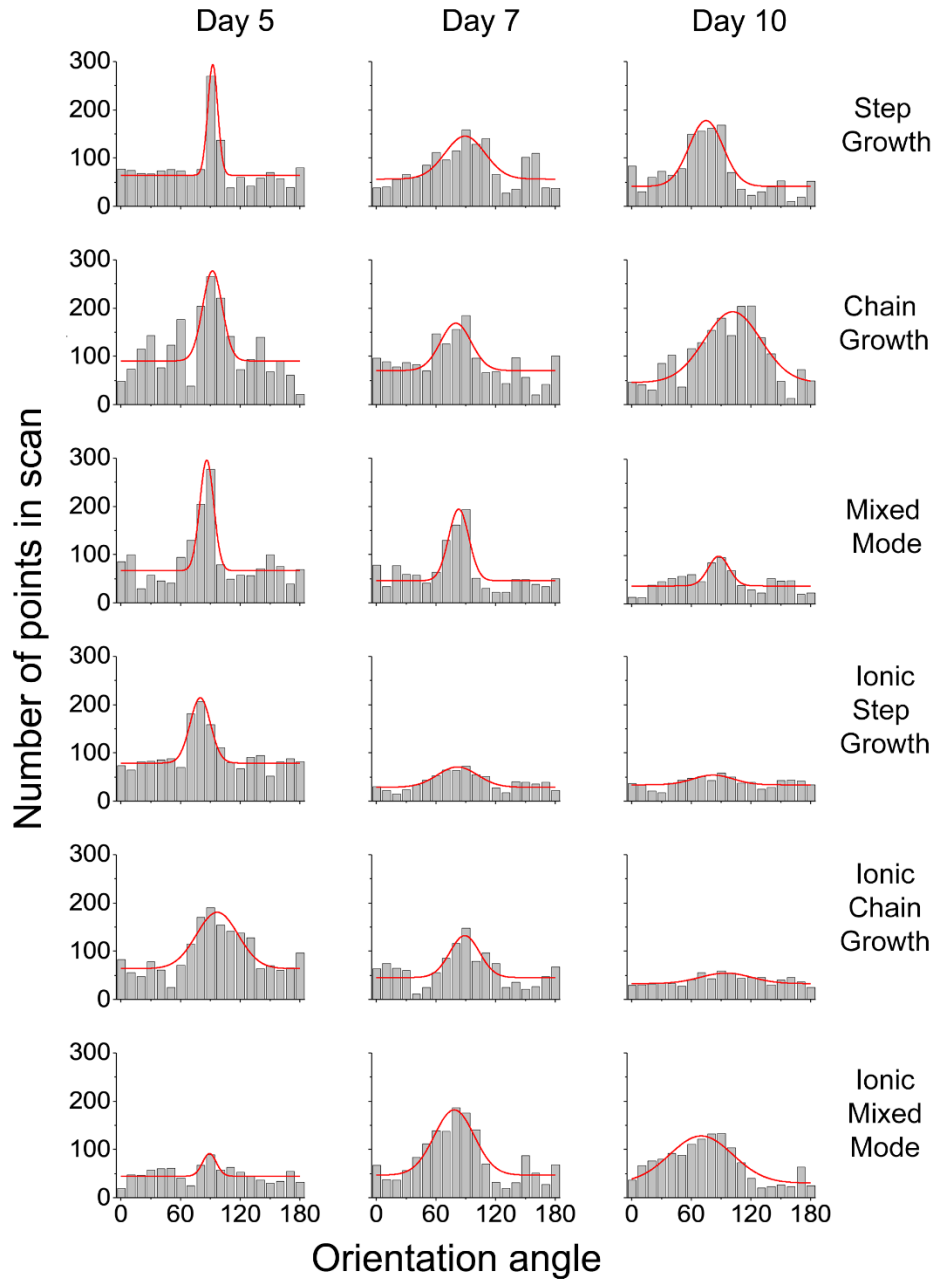


Figure 7.10: Comparing collagen alignment over 10 days. Histograms of collagen organization obtained for collagen secreted by NIH 3T3 fibroblasts encapsulated in the ALGMA hydrogels. The bars represent experimentally acquired data. The red line is the Gaussian fit to the data.

7.5. Conclusions

We successfully fabricated methacrylated alginate hydrogels from medium viscosity alginic acid through ionic, covalent, and a combination of ionic and covalent crosslinking mechanisms. These mechanisms yielded a range of hydrogels that were stiffer, pH responsive as well as significantly more robust under accelerated degradation conditions of incubation compared to hydrogels fabricated from very low viscosity alginate. NIH/3T3 fibroblasts encapsulated in these hydrogels showed no cell death and a preferred threshold stiffness above which cell proliferation was > 60 % compared to TCP controls. Collagen secretion in response to the encapsulation conditions was positively correlated with the modulus for all environments. Collagen was more isotropic for the mixed mode and ionic step growth conditions, whereas the softer gels resulted in more anisotropic organization. The detailed characterization of the influence of crosslinking mechanisms for these responsive ALGMA hydrogels indicates the need for including it as an important factor for the fabrication of tissue engineering scaffolds.

Acknowledgements

This work was supported by the Roy J. Carver Charitable Trust Grant No. 13-4265.

7.6 References

1. Discher, D. E., Janmey, P. A. & Wang, Y. Tissue Cells Feel and Respond to the Stiffness of Their Substrate. *Science* (80-.). **310**, 1139–1143 (2005).
2. Nelson, C. M. & Bissell, M. J. Of Extracellular Matrix, Scaffolds, and Signaling: Tissue Architecture Regulates Development, Homeostasis, and Cancer. *Annu. Rev. Cell Dev. Biol.* **22**, 287–309 (2006).
3. Tibbitt, M. W. & Anseth, K. S. Hydrogels as extracellular matrix mimics for 3D cell culture. *Biotechnol. Bioeng.* **103**, 655–663 (2009).
4. Rosso, F., Giordano, A., Barbarisi, M. & Barbarisi, A. From Cell-ECM Interactions to Tissue Engineering. *J. Cell. Physiol.* **199**, 174–180 (2004).

5. Aamodt, J. M. & Grainger, D. W. Extracellular matrix-based biomaterial scaffolds and the host response. *Biomaterials* **86**, 68–82 (2016).
6. Jikko, A., Harris, S. E., Chen, D., Mendrick, D. L. & Damsky, C. H. Collagen Integrin Receptors Regulate Early Osteoblast Differentiation Induced by BMP-2. *J. Bone Miner. Res.* **14**, 1075–1083 (1999).
7. Plikus, M. V *et al.* Regeneration of fat cells from myofibroblasts during wound healing. *Science* (80-.). **8792**, 1–12 (2017).
8. Yeung, T. *et al.* Effects of substrate stiffness on cell morphology, cytoskeletal structure, and adhesion. *Cell Motil. Cytoskeleton* **60**, 24–34 (2005).
9. Discher, D. E. *et al.* Matrix Mechanosensing: From Scaling Concepts in 'Omics Data to Mechanisms in the Nucleus, Regeneration, and Cancer. *Annu. Rev. Biophys.* **46**, 295–315 (2017).
10. Burridge, K. & Guilluy, C. Focal adhesions, stress fibers and mechanical tension. *Exp. Cell Res.* **343**, 14–20 (2016).
11. Lee, P. F., Bai, Y., Smith, R. L., Bayless, K. J. & Yeh, a. T. Angiogenic responses are enhanced in mechanically and microscopically characterized, microbial transglutaminase crosslinked collagen matrices with increased stiffness. *Acta Biomater.* **9**, 7178–7190 (2013).
12. Stamenkovic, I. Extracellular matrix remodelling: the role of matrix metalloproteinases. *J. Pathol.* **200**, 448–464 (2003).
13. Gurtner, G. C., Werner, S., Barrandon, Y. & Longaker, M. T. Wound repair and regeneration. *Nature* **453**, 314–321 (2008).
14. Bao, P. *et al.* The Role of Vascular Endothelial Growth Factor in Wound Healing. *J. Surg. Res.* **153**, 347–358 (2009).
15. Loeffler, M., Krüger, J. A., Niethammer, A. G. & Reisfeld, R. A. Targeting tumor-associated fibroblasts improves cancer chemotherapy by increasing intratumoral drug uptake. *J. Clin. Invest.* **116**, 1955–1962 (2006).
16. Bryers, J. D., Giachelli, C. M. & Ratner, B. D. Engineering biomaterials to integrate and heal: The biocompatibility paradigm shifts. *Biotechnology and Bioengineering* **109**, 1898–1911 (2012).
17. Harrison, R. H., St-Pierre, J.-P. & Stevens, M. M. Tissue Engineering and Regenerative Medicine: A Year in Review. *Tissue Eng. Part B Rev.* **20**, 1–16 (2014).
18. Kharkar, P. M., Kiick, K. L. & Kloxin, A. M. Designing degradable hydrogels for orthogonal control of cell microenvironments. *Chem. Soc. Rev.* **42**, 7335–7372 (2013).
19. Peyton, S. R., Raub, C. B., Keschrumrus, V. P. & Putnam, A. J. The use of poly (ethylene

- glycol) hydrogels to investigate the impact of ECM chemistry and mechanics on smooth muscle cells. *Biomaterials* **27**, 4881–4893 (2006).
20. Jeon, O., Powell, C., Ahmed, S. M. & Alsberg, E. Biodegradable, photocrosslinked alginate hydrogels with independently tailorable physical properties and cell adhesivity. *Tissue Eng. Part A* **16**, 2915–2925 (2010).
 21. Lee, K. Y. & Mooney, D. J. Alginate: Properties and biomedical applications. *Prog. Polym. Sci.* **37**, 106–126 (2012).
 22. Jeon, O., Powell, C., Solorio, L. D., Krebs, M. D. & Alsberg, E. Affinity-based growth factor delivery using biodegradable, photocrosslinked heparin-alginate hydrogels. *J. Control. Release* **154**, 258–266 (2011).
 23. Rowley, J. A., Madlambayan, G. & Mooney, D. J. Alginate hydrogels as synthetic extracellular matrix materials. *Biomaterials* **20**, 45–53 (1999).
 24. Baer, A. E., Wang, J. Y., Kraus, V. B. & Setton, L. A. Collagen gene expression and mechanical properties of intervertebral disc cell-alginate cultures. *J. Orthop. Res.* **19**, 2–10 (2001).
 25. Chen, W. L. *et al.* Second harmonic generation χ tensor microscopy for tissue imaging. *Appl. Phys. Lett.* **94**, (2009).
 26. Chou, A. I., Akintoye, S. O. & Nicoll, S. B. Photo-crosslinked alginate hydrogels support enhanced matrix accumulation by nucleus pulposus cells in vivo. *Osteoarthr. Cartil.* **17**, 1377–1384 (2009).
 27. Kastellorizios, M., Tipnis, N. & Burgess, D. J. *Foreign body reaction to subcutaneous implants. Advances in Experimental Medicine and Biology* **865**, (2015).
 28. Gay, S., Vijanto, J., Raekallio, J. & Penttinen, R. Collagen types in early phases of wound healing in children. *Acta Chir. Scand.* **144**, 205–211 (1978).
 29. Gabbiani, G. The myofibroblast in wound healing and fibrocontractive diseases. *J. Pathol.* **200**, 500–503 (2003).
 30. Akilbekova, D. & Bratlie, K. M. Quantitative characterization of collagen in the fibrotic capsule surrounding implanted polymeric microparticles through second harmonic generation imaging. *PLoS One* **10**, 1–17 (2015).
 31. Boddupalli, A. & Bratlie, K. M. Collagen organization deposited by fibroblasts encapsulated in pH responsive methacrylated alginate hydrogels. *J. Biomed. Mater. Res. Part A* (2018). doi:10.1002/jbm.a.36482
 32. Shih, H. & Lin, C.-C. Cross-Linking and Degradation of Step-Growth Hydrogels Formed by Thiol-Ene Photoclick Chemistry. *Biomacromolecules* **13**, 2003–2012 (2012).

33. Mironi-harpaz, I., Yingquan, D., Venkatraman, S. & Seliktar, D. Photopolymerization of cell-encapsulating hydrogels : Crosslinking efficiency versus cytotoxicity. *Acta Biomater.* **8**, 1838–1848 (2012).
34. Reddy, S. K., Anseth, K. S. & Bowman, C. N. Modeling of network degradation in mixed step-chain growth polymerizations. *Polymer (Guildf)*. **46**, 4212–4222 (2005).
35. Salinas, C. N. & Anseth, K. S. Mixed Mode Thiol - Acrylate Photopolymerizations for the Synthesis of PEG - Peptide Hydrogels. *Macromolecules* **41**, 6019–6026 (2008).
36. Zhu, L. & Bratlie, K. M. pH sensitive methacrylated chitosan hydrogels with tunable physical and chemical properties. *Biochem. Eng. J.* **132**, 38–46 (2018).
37. Samorezov, J. E., Morlock, C. M. & Alsberg, E. Dual Ionic and Photo-Crosslinked Alginate Hydrogels for Micropatterned Spatial Control of Material Properties and Cell Behavior. *Bioconjug. Chem.* **26**, 1339–1347 (2015).
38. Marques, P., Gomes, M. E., Khademhosseini, A. & Link, C. Photocrosslinkable Kappa-Carrageenan Hydrogels for Tissue Engineering Applications Accessed. *Adv. Healthc. Mater.* **2**, 895–907 (2018).
39. Tan, H., Li, H., Rubin, P. J. & Marra, K. G. Controlled Gelation and Degradation Rates of Injectable Hyaluronic Acid-based Hydrogels through a Double Crosslinking Strategy. *J. Tissue Eng. Regen. Med.* **5**, 790–797 (2011).
40. Stuart, K. & Panitch, A. Characterization of gels composed of blends of collagen I, collagen III, and chondroitin sulfate. *Biomacromolecules* **10**, 25–31 (2009).
41. Chen, X. G., Wang, Z., Liu, W. S. & Park, H. J. The effect of carboxymethyl-chitosan on proliferation and collagen secretion of normal and keloid skin fibroblasts. *Biomaterials* **23**, 4609–4614 (2002).
42. Boddupalli, A. & Bratlie, K. M. Multimodal imaging of harmonophores and application of high content imaging for early cancer detection. *Mater. Discov.* **1**, 10–20 (2016).
43. P. J. Campagnola & Loew, L. M. Second-harmonic imaging microscopy for visualizing biomolecular arrays in cells, tissues and organisms. *Nat Biotech* **21**, 1356–1360 (2003).
44. Olderøy, M. *et al.* Biochemical and structural characterization of neocartilage formed by mesenchymal stem cells in alginate hydrogels. *PLoS One* **9**, (2014).
45. Chou, A. I. & Nicoll, S. B. Characterization of photocrosslinked alginate hydrogels for nucleus pulposus cell encapsulation. *J. Biomed. Mater. Res. - Part A* **91**, 187–194 (2009).
46. Bygd, H. C. & Bratlie, K. M. The effect of chemically modified alginates on macrophage phenotype and biomolecule transport. *J. Biomed. Mater. Res. - Part A* **104**, 1707–1719 (2016).

47. Hutmacher, D. W. Scaffolds in tissue engineering bone and cartilage. *Biomaterials* **21**, 2529–2543 (2000).
48. Balestrini, J. L., Chaudhry, S., Sarrazy, V., Koehler, A. & Hinz, B. The mechanical memory of lung myofibroblasts. *Integr. Biol.* **4**, 410 (2012).
49. Wells, R. G. The role of matrix stiffness in regulating cell behavior. *Hepatology* **47**, 1394–1400 (2008).
50. Liu, F. *et al.* Feedback amplification of fibrosis through matrix stiffening and COX-2 suppression. *J. Cell Biol.* **190**, 693–706 (2010).
51. Slaughter, B. V., Khurshid, S. S., Fisher, O. Z., Khademhosseini, A. & Peppas, N. A. Hydrogels in Regenerative Medicine. *Adv. Mater.* **21**, 3307–3329 (2009).
52. Anseth, K. S., Bowman, C. N. & Brannon-Peppas, L. Mechanical properties of hydrogels and their experimental determination. *Biomaterials* **17**, 1647–1657 (1996).
53. Podual, K., Doyle, F. J. & Peppas, N. A. Preparation and dynamic response of cationic copolymer hydrogels containing glucose oxidase. *Polymer (Guildf)*. **41**, 3975–3983 (2000).
54. Almeida, C. R. *et al.* Impact of 3-D printed PLA- and chitosan-based scaffolds on human monocyte/macrophage responses: Unraveling the effect of 3-D structures on inflammation. *Acta Biomater.* **10**, 613–622 (2014).
55. Rydholm, A. E., Bowman, C. N. & Anseth, K. S. Degradable thiol-acrylate photopolymers: Polymerization and degradation behavior of an in situ forming biomaterial. *Biomaterials* **26**, 4495–4506 (2005).
56. Kloxin, A. M., Kasko, A. M., Salinas, C. N. & Anseth, K. S. Photodegradable hydrogels for dynamic tuning of physical and chemical properties. *Science* **324**, 59–63 (2009).
57. Holt, D. J., Chamberlain, L. M. & Grainger, D. W. Cell-cell signaling in co-cultures of macrophages and fibroblasts. *Biomaterials* **31**, 9382–9394 (2010).
58. Yasui, T., Tohno, Y. & Araki, T. Characterization of collagen orientation in human dermis by two-dimensional second-harmonic-generation polarimetry. *J. Biomed. Opt.* **9**, 259–64 (2004).
59. Berry, D. P., Harding, K. G., Stanton, M. R., Jasani, B. & Ehrlich, H. P. Human wound contraction: collagen organization, fibroblasts, and myofibroblasts. *Plastic and reconstructive surgery* **102**, 124–131; discussion 132–134 (1998).
60. Conklin, M. W. *et al.* Aligned collagen is a prognostic signature for survival in human breast carcinoma. *Am. J. Pathol.* **178**, 1221–1232 (2011).
61. Provenzano, P. P. *et al.* Collagen reorganization at the tumor-stromal interface facilitates local invasion. *BMC Med.* **4**, 38 (2006).

62. Van Zuijlen, P. P. M. *et al.* Collagen morphology in human skin and scar tissue: No adaptations in response to mechanical loading at joints. *Burns* **29**, 423–431 (2003).
63. Cook, H., Stephens, P., Davies, K. J., Harding, K. G. & Thomas, D. W. Defective extracellular matrix reorganization by chronic wound fibroblasts is associated with alterations in TIMP-1, TIMP-2, and MMP-2 activity. *J. Invest. Dermatol.* **115**, 225–233 (2000).
64. Grinnell, F. Fibroblast-collagen-matrix contraction: growth-factor signalling and mechanical loading. *Trends Cell Biol.* **10**, 362–365 (2000).
65. Huebsch, N. *et al.* Harnessing traction-mediated manipulation of the cell/matrix interface to control stem-cell fate. *Nat. Mater.* **9**, 518–26 (2010).
66. DeForest, C. A. & Tirrell, D. A. A photoreversible protein-patterning approach for guiding stem cell fate in three-dimensional gels. *Nat. Mater.* **14**, 523–531 (2015).
67. Flory, P. J. & Rehner, J. Statistical mechanics of cross-linked polymer networks II. Swelling. *J. Chem. Phys.* **11**, 521–526 (1943).
68. Tomasek, J. J., Gabbiani, G., Hinz, B., Chaponnier, C. & Brown, R. A. Myofibroblasts and mechano-regulation of connective tissue remodelling. *Nat. Rev. Mol. Cell Biol.* **3**, 349–363 (2002).
69. Hinz, B. The myofibroblast: Paradigm for a mechanically active cell. *J. Biomech.* **43**, 146–155 (2010).
70. McAnulty, R. J. Fibroblasts and myofibroblasts: Their source, function and role in disease. *Int. J. Biochem. Cell Biol.* **39**, 666–671 (2007).
71. Chaponnier, C. & Gabbiani, G. Tissue repair , contraction , and the myofibroblast factors involved in myofibroblastic. *Wound Repair Regen.* **13**, 7–12 (2005).
72. Vegas, A. J. *et al.* Combinatorial hydrogel library enables identification of materials that mitigate the foreign body response in primates. *Nat. Biotechnol.* (2016). doi:10.1038/nbt.3462
73. Schneider, L. A., Korber, A., Grabbe, S. & Dissemond, J. Influence of pH on wound-healing: A new perspective for wound-therapy? *Arch. Dermatol. Res.* **298**, 413–420 (2007).
74. Gethin, G. The significance of surface pH in chronic wounds. *Wounds UK* **3**, 52–56 (2007).
75. Schreml, S. *et al.* The impact of the pH value on skin integrity and cutaneous wound healing. *J. Eur. Acad. Dermatology Venereol.* **24**, 373–378 (2010).
76. Lee, K. Y. *et al.* Controlling mechanical and swelling properties of alginate hydrogels independently by cross-linker type and cross-linking density. *Macromolecules* **33**, 4291–4294 (2000).

77. Khare, A. R. & Peppas, N. A. Swelling/deswelling of anionic copolymer gels. *Biomaterials* **16**, 559–567 (1995).
78. Jeong, S. I., Jeon, O., Krebs, M. D., Hill, M. C. & Alsberg, E. Biodegradable photocrosslinked alginate nanofibre scaffolds with tuneable physical properties, cell adhesivity and growth factor release. *Eur. Cells Mater.* **24**, 331–343 (2012).
79. Lokhande, G. *et al.* Nanoengineered injectable hydrogels for wound healing application. *Acta Biomater.* **70**, 35–47 (2018).
80. Leveen, H. H. *et al.* Chemical acidification of wounds. An adjuvant to healing and the unfavorable action of alkalinity and ammonia. *Ann. Surg.* **178**, 745–753 (1973).
81. Phillips, T. J., Kehinde, O., Green, H. & Gilchrist, B. A. Treatment of skin ulcers with cultured epidermal allografts. *J. Am. Acad. Dermatol.* **21**, 191–199 (1989).
82. Eaglstein, W. H. & Falanga, V. Tissue engineering and the development of Apligraf, a human skin equivalent. *Cutis.* **62**, 1–8 (1998).
83. Eiselt, P., Yeh, J., Latvala, R. K., Shea, L. D. & Mooney, D. J. Porous carriers for biomedical applications based on alginate hydrogels. *Biomaterials* **21**, 1921–1927 (2000).
84. Chan, A. W., Whitney, R. A. & Neufeld, R. J. Semisynthesis of a controlled stimuli-responsive alginate hydrogel. *Biomacromolecules* **10**, 609–616 (2009).
85. Cha, C., Kohman, R. E. & Kong, H. Biodegradable polymer crosslinker: independent control of stiffness, toughness, and hydrogel degradation rate. *Adv. Funct. Mater.* **19**, 3056–3062 (2009).
86. Browning, M. B., Cereceres, S. N., Luong, P. T. & Cosgriff-Hernandez, E. M. Determination of the in vivo degradation mechanism of PEGDA hydrogels. *J. Biomed. Mater. Res. - Part A* **102**, 4244–4251 (2014).
87. Coutinho, D. F. *et al.* Modified Gellan Gum hydrogels with tunable physical and mechanical properties. *Biomaterials* **31**, 7494–7502 (2010).
88. Dinnes, D. L. M., Santerre, J. P. & Labow, R. S. Influence of biodegradable and non-biodegradable material surfaces on the differentiation of human monocyte-derived macrophages. *Differentiation* **76**, 232–244 (2008).
89. Jeon, O., Bouhadir, K. H., Mansour, J. M. & Alsberg, E. Photocrosslinked alginate hydrogels with tunable biodegradation rates and mechanical properties. *Biomaterials* **30**, 2724–2734 (2009).
90. Ruskowitz, E. R. & Deforest, C. A. Photoresponsive biomaterials for targeted drug delivery and 4D cell culture. *Nat. Rev. Mater.* **3**, (2018).
91. Nemir, S., Hayenga, H. N. & West, J. L. PEGDA Hydrogels With Patterned Elasticity :

- Novel Tools for the Study of Cell Response to Substrate Rigidity. *Biotechnol. Bioeng.* **105**, 636–644 (2010).
92. Boersema, G. S. A., Grotenhuis, N., Bayon, Y., Lange, J. F. & Bastiaansen-Jenniskens, Y. M. The Effect of Biomaterials Used for Tissue Regeneration Purposes on Polarization of Macrophages. *Biores. Open Access* **5**, 6–14 (2016).
 93. Bygd, H. C., Akilbekova, D., Muñoz, A., Forsmark, K. D. & Bratlie, K. M. Poly-l-arginine based materials as instructive substrates for fibroblast synthesis of collagen. *Biomaterials* **63**, 47–57 (2015).
 94. Anderson, J. M. Biological Responses to Materials. *Annu. Rev. Mater. Res.* **31**, 81–110 (2001).
 95. Salinas, C. N. & Anseth, K. S. The enhancement of chondrogenic differentiation of human mesenchymal stem cells by enzymatically regulated RGD functionalities. *Biomaterials* **29**, 2370–2377 (2008).
 96. Klingberg, F., Hinz, B. & White, E. S. The myofibroblast matrix: Implications for tissue repair and fibrosis. *J. Pathol.* **229**, 298–309 (2013).
 97. English, R. S. & Shenefelt, P. D. Keloids and hypertrophic scars. *Dermatologic Surg.* **25**, 631–638 (1999).
 98. Su, P. J. *et al.* The discrimination of type I and type II collagen and the label-free imaging of engineered cartilage tissue. *Biomaterials* **31**, 9415–9421 (2010).
 99. Meek, K. M. & Boote, C. The organization of collagen in the corneal stroma. *Exp. Eye Res.* **78**, 503–512 (2004).
 100. Linares, H. A., Kischer, C. W., Dobrkovsky, M. & Larson, D. L. The histiotypic organization of collagen of the hypertrophic scar in humans. *J. Invest. Dermatol.* **59**, 323–332 (1972).
 101. Goffin, J. M. *et al.* Focal adhesion size controls tension-dependent recruitment of α -smooth muscle actin to stress fibers. *J. Cell Biol.* **172**, 259–268 (2006).
 102. Trappmann, B. *et al.* Extracellular-matrix tethering regulates stem-cell fate. *Nat. Mater.* **11**, 742–742 (2012).

CHAPTER 8

PHOTOMASK-TUNED AND FIBRONECTIN-MODIFIED ALGINATE HYDROGELS FOR STUDYING FIBROBLAST MORPHOLOGY AND COLLAGEN ORGANIZATION

Methacrylated alginate hydrogels were synthesized across a range of stiffness (6.9 ± 0.4 to $20.2 \pm$ kPa) using photomasks to tune the amount of UV exposure. NIH/3T3 fibroblasts were viable for ten days of culture when surface seeded on these hydrogels. The proliferation of fibroblasts was significantly higher on the stiffer hydrogels, and further surface functionalization of the gel with fibronectin increased cell confluence on these substrates. The cells had a rounded morphology after two days, with stellate morphology observed after four days. After ten days the stiffer substrates were almost completely covered with NIH/3T3 cells that were expressing α -smooth muscle actin. Collagen secretion and organization from the surface-seeded fibroblasts was visualized using second harmonic generation (SHG) microscopy. For both the fibronectin modified and naïve substrates collagen was significantly less organized on the softer substrates and more aligned on stiffer substrates. Cell spreading normalized to secreted collagen on the different hydrogels indicated a clear influence of the stiffness on the cell morphology as well as collagen levels for both four and ten days of culture. This study showed the substantial influence of cell adhesion motifs as well as substrate stiffness on cell morphology and organization of collagen.

8.1. Introduction

The primary aim of tissue engineering is to recapitulate the intricate complexities of natural tissues so they can be used for treating diseased, damaged, or missing tissue.¹⁻³ To develop more effective scaffolds, the role of biomaterials properties on cell-matrix interactions must be understood to develop enhanced design criteria.^{4,5} In the United States alone, it has been reported that over 77 people receive transplants daily which is still does not cover the demand for the same resulting in wait-listing over 98,000 patients for an average of three years or more.^{6,7} Regenerative medicine seeks to cover these shortages by fabricating tunable, biocompatible materials.

Hydrogels fulfil many of the material requirements for tissue scaffolds with their tunable mechanical properties, ease of functionalization, and, in the case of naturally derived materials, their compositional similarity to natural extracellular matrix (ECM).⁸ It is possible to tailor hydrogels with finely tuned scaffold properties to alter cell adhesion and proliferation, as well as degradation kinetics such that they are similar to that of natural tissue growth.^{9,10} The interaction between cells and the ECM is an integral aspect of how tissues maintain homeostasis.¹¹ Through diverse scales of interaction with the ECM, from the molecular to the macroscopic, cells are able to sense dynamic changes in their microenvironment.¹² With such a significant influence of the ECM over cell adhesion, differentiation, and proliferation, there is a need to engineer interactions that can increase the compliance of scaffolds.^{13,14}

Naturally derived hydrogel materials such as alginic acid derived from algae or seaweed can be used as a scaffold for tissue engineering applications.¹⁵⁻¹⁷ Alginate can be crosslinked through ionic binding or through covalent bonds after chemically modifying alginate.^{18,19} Although ionic crosslinking is relatively facile and rapid, ion exchange with monovalent ions in physiological media can result in a loss of mechanical stability.^{20,21} Through methacrylation of these alginate networks, hydrogels can be formed through chain growth polymerization using photocrosslinking.²² By tuning the opacity of photomasks, it is possible to further tune the UV exposure and result in a gradient of hydrogel stiffnesses.²³ To increase the cytocompatibility of such hydrogel gradients, fibronectin (FN), laminin, and collagen have been used to mimic natural tissue environments by providing cell adhesion motifs for better cell attachment.²⁴⁻²⁶ Patterns of such photocrosslinked platforms have been previously used to study the differentiation and mechanotransductive sensitivity of mesenchymal stem cells.^{27,28} These studies showed that both the magnitude and the spatial organization of the stiff regions influenced the differentiation of stem cells to more elongated morphologies. Collagen is a key component of mammalian connective tissue systems.²⁹ Collagen has both organizational and compositional differences in different tissues that dictates the function of the tissue.³⁰⁻³² Previous studies characterizing collagen secreted by cells using molecular biology techniques or expensive dyes have been unable to completely capture the intricacies of the cell-matrix interactions.^{33,34} Second harmonic generation (SHG) microscopy is a powerful tool that can provide detailed mapping of collagen organization in a wide range of tissue samples.³⁵⁻³⁷

In this study, we characterize cell viability, phenotype, and collagen secretion in response to FN-modified as well as naïve alginate scaffolds prepared across a gradient of stiffnesses through photocrosslinking. Fluorescent immunocytochemical staining and live/dead assays provided insight into the biocompatibility and cell morphology of surface-seeded NIH/3T3 fibroblasts. Using the sensitive, dye-less visualization of collagen through SHG imaging, we examined how substrate stiffness influenced collagen secretion and alignment. Through our analysis, we propose design criteria for achieving different collagen organization based on hydrogel stiffness.

8.2. Experimental

8.2.1. Materials

Medium viscosity alginic acid (CAS 9005-38-3) was procured from MP Biomedicals Fisher Scientific (Hampton, NH). Dithiothreitol (DTT) was supplied by VWR Chemicals (Batavia, IL). All other materials used for the experiments were procured from Sigma Aldrich (St. Louis, MO) and used as received, unless otherwise specified. Deionized (DI) water (Milli-Q, Thermo Scientific Nanopure, Waltham, MA) was used throughout these experiments.

8.2.2. Methacrylated Alginate (ALGMA) Synthesis

The medium viscosity alginic acid precursor was used to prepare alginate solutions and methacrylated as described previously.³⁸ Briefly, 2 g of alginic acid powder was dissolved in 200 mL of DI water to prepare a 1 % (w/v) solution. The modification of this solution was initiated by slowly adding 16 mL of methacrylic anhydride. The pH was maintained between 8 and 9 using aliquots of 5 M NaOH at 4 °C. This reaction was stopped after 24h, and the methacrylated alginate (ALGMA) was transferred to molecular weight cutoff membranes of 13,000 Da. The ALGMA was dialyzed against DI water for two days, with the dialysate refreshed twice a day. The final

ALGMA product was lyophilized (4.5 L, Labconco, Kansas City, MO) to obtain a white, foamy powder. NMR spectroscopy was conducted on solutions of the unmodified alginate and ALGMA to characterize the methacrylation extent of the synthesized ALGMA. The ^1H spectra were acquired on a Bruker Avance III Spectrometer at 70°C , a sweep width of 6602.1 Hz, a 90° pulse, and an acquisition time of 2.48 s; 128 repetitive scans with 64 k points were acquired and the data were processed in MNova with 128k points, zero filling, and exponential line broadening of 1.0 Hz.²² Methacrylation % was evaluated through the relative integration of the protons from the methacrylate group (I_{CH_2} at $\delta = 6.0$ and 5.6 ppm) and the methyl group (I_{CH_3} at $\delta = 1.8$ ppm) to the protons from the carbohydrate (I_{polymer}) using equation 1.

$$\% \text{Methacrylation} = \frac{\left(\frac{I_{\text{CH}_2}}{n_{\text{CH}_2}} + \frac{I_{\text{CH}_3}}{n_{\text{CH}_3}} \right)}{\frac{I_{\text{polymer}}}{n_{\text{H}_{\text{polymer}}}}} \quad (1)$$

8.2.3. Hydrogel Fabrication and Characterization

Ionic chain growth crosslinking of the stock solutions was initiated based on protocols previously described.³⁹ The stock hydrogel solution was prepared by dissolving 300 mg ALGMA and 10 mg Irgacure 2959 in 10 mL DI water. This solution was degassed under vacuum. A photomask of varying opacities was applied to the gel and the gel was exposed to UV light (365 nm, 2 W/cm^2) for 10 min. The hydrogels were further exposed to $100\mu\text{L}$ of 0.2 M SrCl_2 to incorporate ionic crosslinks.

The compressive moduli of the different hydrogels across the gradient were measured by testing plugs ($n = 4$) that were 6 mm thick and 16 mm wide. The samples were placed between two glass slides and sequential series of weights were placed on top. Images of measuring the compressive moduli were analyzed using ImageJ (NIH, Bethesda, MD) by evaluating changes in

height and cross-sectional area of the hydrogels. The compressive modulus of each gel was defined as the slope of the linear region over 5-15 % strain, from the stress-strain curve.

8.2.4. Cell Culture and Proliferation Assay

Cell adhesion and proliferation are essential aspects of testing in vitro cytocompatibility of different scaffolds.^{9,40} Proliferation of NIH/3T3 fibroblasts (ATCC, Manassas, VA) was tested on both fibronectin (FN) modified and naïve replicates of all hydrogel surfaces. NIH/3T3 fibroblasts were passaged in Dulbecco's modified Eagle's medium (Cellgro, Thermo Scientific) supplemented with 10% bovine calf serum, penicillin (100 U/L) and streptomycin (100 µg/mL) at 37°C under 5% CO₂. In a 48 well plate, 300 µL of the different hydrogel solutions and were pipetted. For the FN modified surfaces, a solution of 50 µL of 200 µg/mL solution of FN (human FN 95%, AnaSpec, Thermo Fisher) was added to the well and the plates were incubated for 30 min. Glass control surfaces were also incubated at rt for 1 h after addition of the FN. The hydrogels were then exposed to the UV light (365 nm, 2 W/cm²) using the photomask for 10 min to crosslink the gels. To all controls, FN modified hydrogels, and naïve hydrogels, 200 µL cells (1.25×10^5 cells/cm²) was added. Live and dead controls for each plate were prepared by seeding the cells directly on the tissue culture plastic. After 48 h of incubation, the medium in the dead controls was aspirated and 300 µL of 70% ethanol was added for 10 min to lyse the cells. The supernatant in all remaining controls and samples was subsequently aspirated and to each well 150 µL of a Live/Dead working solution (2 µM calcein AM (AnaSpec, Fremont, CA) and 7.5 µM of 7-aminoactinomycin D (Tonbo Biosciences, San Diego, CA) in phosphate buffered saline (PBS)) was added. The plates were incubated for 40 min at 37°C in 5% CO₂. Fluorescence images were obtained using the EVOS Fluid Cell Image Station (Thermo Scientific) with the red (excitation/emission 586/646 nm) and green channels (482/532 nm) to observe the dead and live

cells, respectively. Live cells were quantified using a plate reader (BioTek Synergy HT Multidetector Microplate Reader, Biotek, Winooski, VT) using an excitation/emission of 485/528 nm. The % of live cells was determined using the following equation:

$$\text{Live cells \%} = \frac{F(528)_{\text{sample}} - F(528)_{\text{Dead Control}}}{F(528)_{\text{Live Control}} - F(528)_{\text{Dead Control}}} \times 100\% \quad (3)$$

where $F(528)_{\text{sample}}$ is the fluorescent signal at 528 nm from the cell laden samples, $F(528)_{\text{Dead Control}}$ is the fluorescent signal at 528 nm from the lysed control samples and $F(528)_{\text{Live Control}}$ is the fluorescent signal at 528 nm from the control samples.

8.2.5. Second Harmonic Generation Microscopy of the gels

Cells seeded on hydrogels were prepared as described above. The medium was changed every three days. Cells were preserved using formalin (10% v/v) by aspirating the medium and incubating for 20 min at rt.

A mode-locked Ti: Sapphire laser (100 fs pulse width, 1 kHz repetition rate, Libra, Coherent, Santa Clara, California) with an 800 nm fundamental was used for imaging all samples and controls. The power at the stage was controlled using a half-wave plate and a Glan-Thompson polarizer (Thorlabs, Newton, NJ). The second harmonic signal from the samples was collected in transmission mode. A Nikon Plan Fluorite objective (20 ×, 0.50 NA, 2.1 mm WD, Nikon, Melville, NY) was used to focus the beam to image the samples on an inverted microscope (Amscope, Irvine, CA). The SHG transmission through the sample was collected using a Nikon water immersion objective (40 ×, 0.8 NA, 3.5 mm WD, Nikon, Melville, NY). A dichroic mirror reflected the signal on to the optical path containing two short pass filters <450 nm (FGB37M, Thorlabs) and an 808 nm notch filter (NF-808.0-E-25.0M, Melles Griot, Rochester, NY). This filter combination was used to separate the signal from the fundamental beam prior to detection using an intensified charge-coupled device (iCCD, iStar 334T, Andor, Belfast, United Kingdom). Polarized SHG

imaging was conducted by generating polarized light through a Glan-Thompson polarizer and a half-wave plate mounted on a motor-driven rotational stage (Thorlabs). Samples were imaged at every 10° from 0° to 350°. Images were collected in triplicate for all experimental conditions. Regions of interest (ROIs) were analyzed and fit using MATLAB using the following equation:

$$I_{SHG} = c \cdot \left\{ \left[\sin^2(\theta_e - \theta_o) + \left(\frac{\chi_{zzz}}{\chi_{zxx}} \right) \cos^2(\theta_e - \theta_o) \right]^2 + \left(\frac{\chi_{xzx}}{\chi_{zxx}} \right)^2 \sin^2(2(\theta_e - \theta_o)) \right\} \quad (4)$$

where $\frac{\chi_{zzz}}{\chi_{zxx}}$ and $\frac{\chi_{xzx}}{\chi_{zxx}}$ are the second-order susceptibility tensor element ratios., θ_e and θ_o are the incident polarization angle and collagen fiber angle, respectively, and c is a normalization constant. The orientation of collagen was analyzed in each ROI individually. These orientation angles were then compiled in a histogram. The collagen organization was assessed by measuring the full-width at half-maximum (FWHM) of the Gaussian fit of the histogram. Analysis of the types of collagen was done using previously optimized protocols.⁴¹

8.2.6. Immunocytochemical Staining

Samples preserved for SHG microscopy imaging were processed for immunocytochemical staining. All the samples were blocked (5% dry milk and 0.03% TWEEN-20 in PBS) at rt for 1 h. Cells were stained for α -SMA (1:400, ab5694, Abcam, Cambridge, MA) and actin (phalloidin-iFluor™ 488 conjugate, Cayman Chemicals, Ann Arbor, MI). A secondary antibody was used to visualize α -SMA (1:600, ab150080, Abcam). Nuclei were stained using DAPI (4',6-diamidino-2-phenylindole, 0.1 μ g/mL) for 2 min. Cells were imaged using the Fluid EVOS Fluid Cell Image Station with the blue (excitation/emission 390/446 nm), red (excitation/emission 586/646 nm) and green channels (482/532 nm) tuned to visualize the nuclei, actin cytoskeleton, and α -SMA, respectively.

8.2.7. Statistical Analysis

The data generated was statistically analyzed and reported as mean \pm standard deviation (SD). Statistical significance was determined through mean comparisons via a two-way ANOVA. Pair-wise comparisons were evaluated using Tukey's honest significant different test. Statistically significant differences were identified for $p < 0.05$.

8.3. Results

8.3.1 Compressive Moduli

The ALGMA hydrogel solution crosslinked using chain growth polymerization through a photomask allowing for the opacity to control the level of UV exposure. These gels were further crosslinked using SrCl_2 . The opacity of the photomask was adjusted to generate hydrogels of different Young's moduli ranging from 20.2 ± 0.4 kPa at 0% opacity to 6.9 ± 0.4 kPa at 90% opacity (**Figure 8.1**).

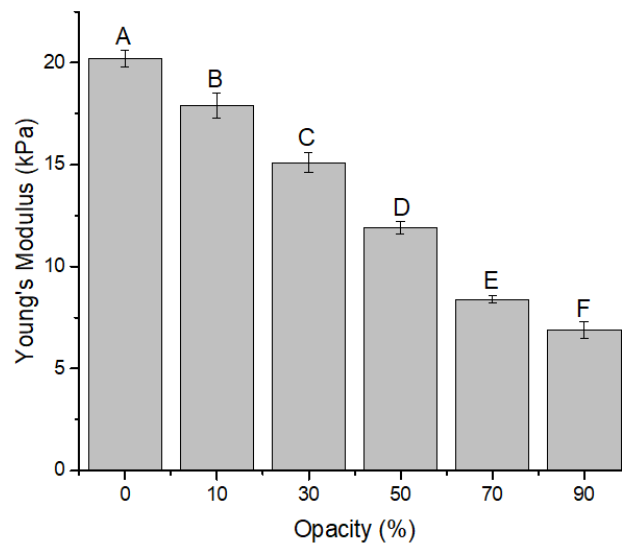


Figure 8.1. Compressive moduli of alginate hydrogels. Compressive moduli of methacrylated alginate hydrogels crosslinked through chain growth after which they were crosslinked by UV

radiation through a photomask across different opacity levels and reinforced by Strontium ions to get discrete hydrogel samples of varying stiffnesses. Data represents the mean \pm SD. $n = 3$. Statistical analysis through two-way ANOVA and Tukey's HSD post-hoc test. * $p < 0.05$.

NIH/3T3 fibroblast transitions to protomyofibroblasts and subsequently myofibroblasts have been observed over the range of 16 kPa, which matches well with these gels.^{42,43} All future discussions on classifying the gradient hydrogels within this manuscript will refer to by the % opacity of the photomask through which they were crosslinked.

8.3.2 Cell Viability

The cytocompatibility of these hydrogels across the gradient of mechanical stiffnesses is a key aspect in their suitability as tissue engineering scaffolds.^{44,45} To enhance cell attachment on these hydrogels, fibronectin (FN) was covalently linked to the surface.^{46,47} Viability of surface seeded NIH/3T3 fibroblasts was assessed through a live/dead assay. Fibroblasts on both naïve and FN-modified surfaces showed no cell death after 48h incubation on the gels (**Figure 8.2**).

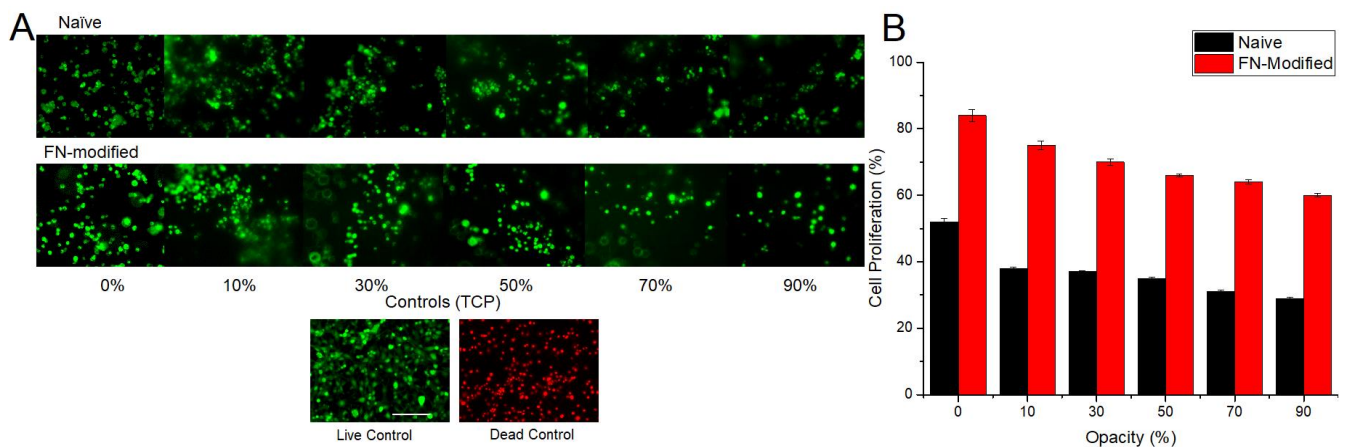


Figure 8.2. Proliferation of NIH/3T3 cells surface-seeded on gradient of alginate hydrogels across FN-modified and naïve conditions. NIH/3T3 fibroblasts were seeded on the both naïve and fibronectin modified, dually crosslinked ALGMA hydrogels across the stiffness gradient. Cells cultured on tissue culture plastic served as controls. (A) Representative micrographs of live

(green) and dead (red) cells cultured for 48 h. (B) Quantification of live and dead cells. Data represents the mean \pm SD. $n = 6$. Statistical analysis through two-way ANOVA and Tukey's HSD post-hoc test. $*p < 0.05$. Scale bar represents 100 μm .

Cell proliferation increased from just $29.0 \pm 0.2\%$ on the softest gel (90%) to $52.0 \pm 1.0\%$ for the stiffest gels (0%). These values were normalized to controls on tissue culture plastic (TCP). As expected, FN-modified substrates significantly increased proliferation with cells on the softer gels (90% FN) at $60.0 \pm 0.5\%$ and cells on the stiffer gels at $84 \pm 1.8\%$, an increase of 1.6 times over the naïve substrates for the same rigidity.

8.3.3 Immunocytochemistry

Immunocytochemistry (ICC) fluorescent staining enabled us to visualize cell morphology and differentiation in response to being seeded on the different hydrogels. Actin filaments were stained with phalloidin and the nuclei was visualized with DAPI. α -smooth muscle actin (α -SMA) was used to show myofibroblast presence. Representative images of the cells show the presence of α -SMA and dense surface coverage of the NIH/3T3 fibroblasts on the stiffer substrates (**Figure 8.3**).

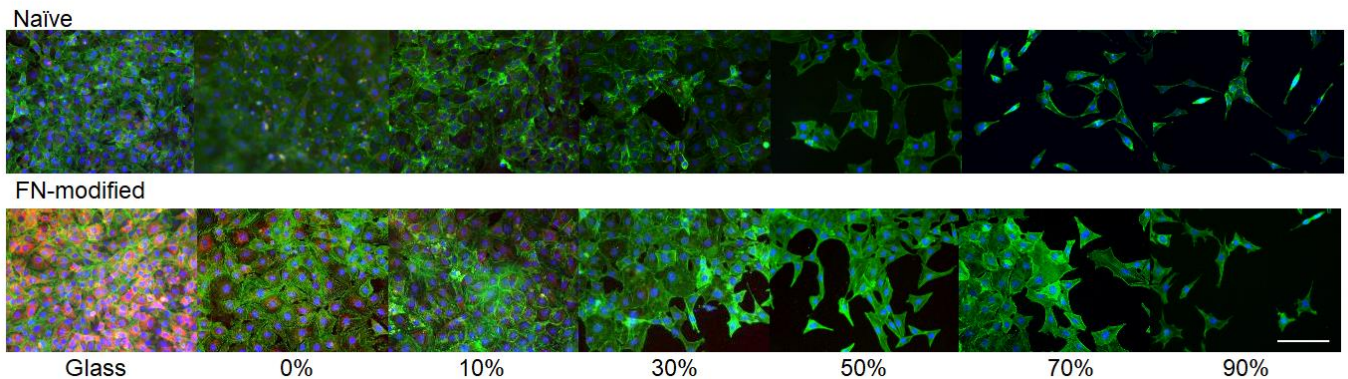


Figure 8.3. Immunocytochemical fluorescent staining of fibroblasts cultured on the ALGMA hydrogels. The representative fluorescent staining images showing fibroblasts proliferating on substrates with varying stiffnesses across the gradient. Fibronectin modified versions of the same hydrogel samples are placed below non-modified, naïve substrates. Here, α -SMA expression is

stained red, the cytoskeletal structure is stained green, and nuclei are blue colored. Scale bar represents 100 μm .

Unlike the live/dead assay, which were carried out after two days, these samples were incubated for ten days. This longer time period allowed for greater cell proliferation on the stiffer, naïve substrates as well as all FN-modified gel surfaces.³² On the softer substrates, the fibroblasts exhibited stellate morphology, indicating their potential ECM remodeling activity which will be discussed further.⁴⁸

8.3.4 Secreted Collagen Levels

We are interested in the influence mechanical stiffness has on collagen secreted by fibroblasts to better understand how materials properties influence the host response⁴⁹ to improve rational design of scaffolds. Collagen is a non-centrosymmetric protein and is SHG active. Here, we quantified collagen secreted by NIH/3T3 fibroblasts in response to these hydrogel substrates. Combining the analysis from ICC staining of the cell-hydrogel samples with the SHG microscopy, the collagen signal was normalized to the number of nuclei stained by DAPI (**Figure 8.5**). This normalization allowed us to gauge the influence of the underlying substrates while controlling for differences in cell numbers on each substrate. For 30% and softer hydrogel samples, more collagen was measured on FN-modified substrates compared with the naïve substrates. There were no differences observed for the stiffer FN and naïve surfaces. Glass controls had significantly more collagen than the softer gels.

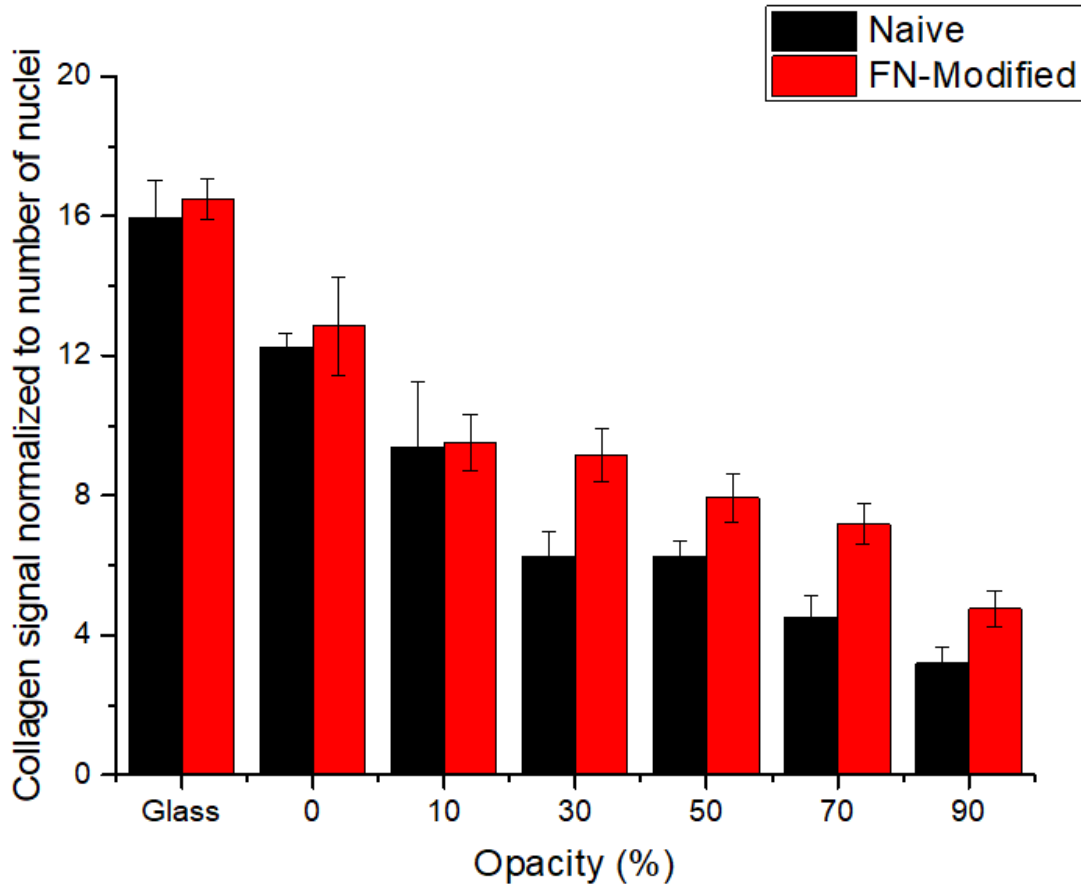


Figure 8.4. Collagen secretion by NIH/3T3 cells seeded on alginate hydrogels was evaluated using SHG microscopy. Surface seeded NIH/3T3 fibroblasts on naïve and FN-modified ALGMA hydrogels were imaged using SHG microscopy after being cultured for 10 days. Collagen signal was normalized to the signal from the respective non-cell seeded hydrogels as well as to the number of nuclei observed from the ICC staining of these samples. Data represents the mean \pm SD. $n = 3$.

8.3.5 Collagen Organization

Remodeling ECM proteins is an important aspect of fibroblast activity at different tissue interfaces.^{50,51} There is a dearth of information on how materials properties influence collagen organization. Here, we studied how alginate-based hydrogels with Young's moduli in the range of ~7 to 20 kPa influences collagen organization by NIH/3T3 fibroblast. Orientation maps are presented in **Figure 8.5** in which the lines illustrate the angle calculated for each individual ROI.

These lines are color coded to better visualize regions of organization. Images with a range of colors indicate that the collagen is disorganized, whereas images with regions of one color are more aligned.

Stiffer substrates resulted in more aligned collagen organization as evidenced by lower FWHM values ($< 60^\circ$). The FWHM increased, indicating collagen was more disordered, on the softest substrates (**Figure 8.6**). Modifying the surface with FN caused collagen to be less aligned (higher FWHM). The ability of FN-modification to increase stochasticity of collagen organization could be pertinent for dermal tissue engineering platforms, in which native tissue is isotropic.⁴¹

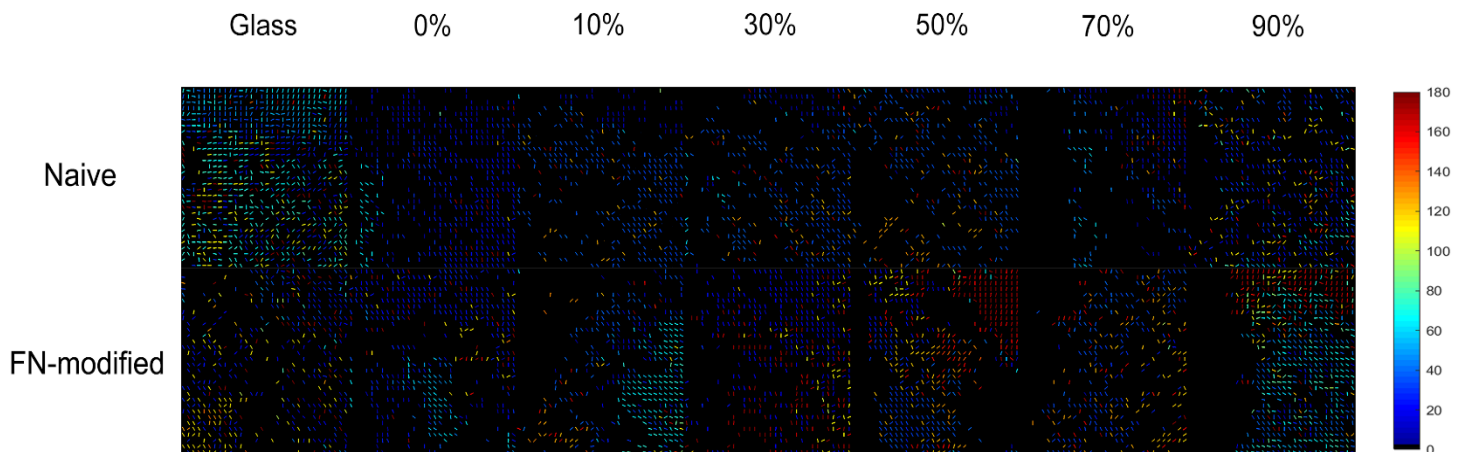


Figure 8.5. Visualizing organization of collagen secreted by fibroblasts on alginate hydrogels. Collagen secreted by NIH/3T3 fibroblasts seeded on the different alginate hydrogels were analyzed using SHG microscopy on day 10. The arrows are placed on areas where collagen signal was detected, and the colors represent collagen organization angle. The legend for the heat map is provided on the right

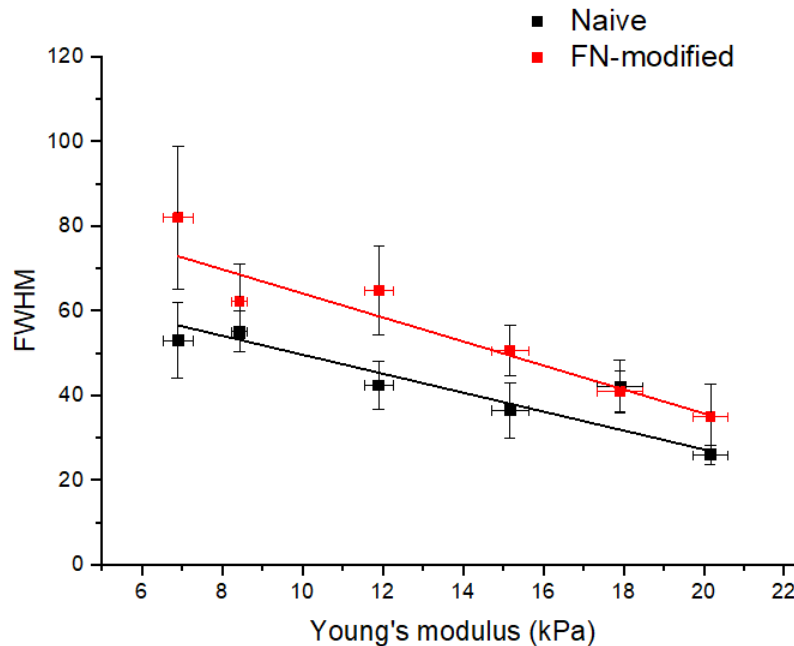


Figure 8.6. Correlating Young's modulus to changes in collagen organization. Collagen organization mapped in terms of the FWHM against the Young's modulus of the gradient hydrogels for both the naïve and FN-modified samples.

Myofibroblast activity indicates remodeling the ECM and is often associated with a fibrotic or scarring response post-wound healing.^{52,53} We analyzed the α -SMA expressing cells to quantify the cell population % that shows possible transition to myofibroblasts. This analysis yielded an interesting observation in which there appears to be a possible threshold stiffness beyond which there is less fibroblast differentiation at the 30% hydrogel (15 kPa) for the FN-modified hydrogels (**Figure 8.8**). The naïve substrates on the other hand showed no significant α -SMA positive cells beyond the glass control and the stiffest 0% hydrogel substrate.

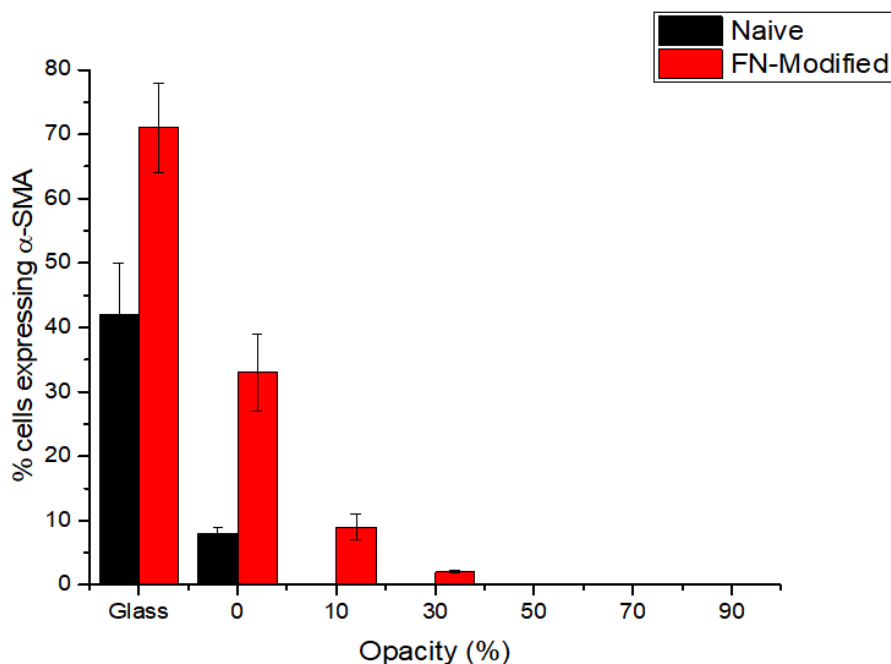


Figure 8.7. Evaluation of α -SMA expression by NIH/3T3 cells seeded on alginate hydrogels. Surface seeded NIH/3T3 fibroblasts on naïve and FN-modified ALGMA hydrogels were imaged using SHG microscopy after being cultured for 10 days. Collagen signal was normalized to the signal from the respective non-cell seeded hydrogels as well as to the number of nuclei observed from the ICC staining of these samples. Data represents the mean \pm SD. n = 3.

8.4. Discussion

The organization of collagen during diverse biological processes such as response to foreign implants,⁵⁴ wound healing,^{29,55} and aging⁵⁶ has a significant impact on tissue properties. Studies have shown strong correlations between the stiffness of a material and the collagen response to it under both *in vivo* and *in vitro* conditions.⁵⁷ In this study, we examine the role played by stiffness of photocrosslinked ALGMA hydrogels across a range of 7 to 20 kPa. Through quantitative as well as qualitative analysis of the cell response to the different mechanical environments, the mechanotransduction of NIH/3T3 fibroblasts was examined to improve design of criteria compliant scaffolds.

The adhesion of cells to solid interfaces is a fascinating process that occurs across a wide variety of conditions both *in vitro* and *in vivo*.^{12,58} We have previously observed how cells sense

the mechanical stiffness of their encapsulating environment of soft³⁸ and relatively stiffer ALGMA hydrogels.³⁹ Here we used a photomask to tune the stiffness of ionic chain growth ALGMA hydrogels from 6.9 ± 0.4 kPa to 20.2 ± 0.4 kPa (**Figure 8.1**). This range allows us to observe the impact of stiffness on the mechanotransduction of cells, particularly their ECM deposition, differentiation, and morphology over a physiologically relevant range.^{59–62} Previous studies have shown the sensitivity of fibroblasts to the stiffness of substrates that they are cultured on, particularly for establishing necessary conditions to avoid senescence.⁶³ We are interested in determining the effect stiffness has not only on fibroblast-to-myofibroblast transitions, but also on collagen organization. Tissues have different collagen organization depending on their function, ranging from disordered structures within healthy dermis⁵⁵ to highly aligned collagen fibers in tendons⁶⁴ and parts of the cornea.⁶⁵ The influence of the collagen organization at the micro-scale has the potential to instigate differentiation of stromal and mesenchymal stem cells, and their subsequent activity at the cell-matrix interface.^{66,67} Fibroblast differentiation to myofibroblasts in particular is clinically relevant in that it is linked to scar tissue.⁶⁸

FN is a well-known surface adhesion protein and was incorporated on the surface of the ALGMA hydrogels to examine the effect of cell adhesion motifs on cell behavior. As expected, there was an increased cell proliferation normalized to TCP on the FN-modified hydrogels compared to naïve substrates (**Figure 8.2**). As the opacity of the photomask increased (stiffness decreased), cell proliferation decreased. Similar studies have used laminin-derived cell adhesion motifs to examine how cell-binding domains influence how cells sense surfaces for attachment.²⁵ Additionally, cell encapsulation within these gradient hydrogel environments will provide closer approximations for the cell response to native tissue which is anticipated as the ideal next step in preparing effective tissue engineering scaffolds.⁶⁹

Visualization of the cell response to diverse underlying substrates allows us to observe changes in morphology.⁷⁰ The sensitivity of fibroblasts to the underlying substrates can be observed by how the cells spread, show actin stress fibers, and exhibit stellate morphology.^{32,71} Even on the softest, naïve 90% hydrogel substrates (~7 kPa), the cultured fibroblasts showed stellate morphology with clear actin stress fibers (**Figure 8.3**). Although cell proliferation itself was significantly lower on the naïve substrates, there were no morphological differences in cell organization. This correlated well with the live/dead images obtained in this study as well as our previous research which showed that the sensitivity of cells on such substrates influences proliferation but not morphology.³⁹ Similar studies on functionalizing alginate hydrogels with FN showed no significant differences in the morphology of encapsulated mesenchymal stem cells regardless of adhesion motifs over a range of mechanical stiffnesses (5 to 110 kPa).⁷² A seminal study on the mechanical memory of lung myofibroblasts showed the cells' preference for stiffer substrates across a similar range of 5 to 100 kPa to TCP with no differences in cell morphology after decoupling proliferation effects.⁶³

ICC staining aided in identifying fibroblast response to the different hydrogel gradient surfaces through the expression of α -SMA. As expected, myofibroblast presence was observed on the FN-modified glass, 0%, and 10% substrates. The amount of α -SMA+ cells decreased exponentially with decreasing stiffness. Very little α -SMA is expressed in the naïve surfaces outside of the glass controls. The presence of actin stress fibers with no α -SMA expression can be interpreted as evidence of protomyofibroblast transitions of the seeded fibroblasts.^{73,74} Previous studies suggested that the protomyofibroblast transition is at 5 to 9 kPa, which is in line with these results. Similarly, these studies have also seen that myofibroblasts differentiate at 16 kPa.⁷⁵ Previous studies have indicated that FN can alter the mechanotransductive signaling of surface-

seeded fibroblasts.⁷⁶ Extra domain-A(ED-A) FN domain was found to be critical for the differentiation of cultured subcutaneous, lung, and dermal fibroblasts when exposed to transforming growth factor-beta1 (TGF- β 1). The ED-A domain FN expression showed a positive correlation with α -SMA levels, with a 5-fold increase over the first 24 h and a 6.5-fold over the next 48-72 h.⁷⁷ This indicated that the expression and binding to FN is an important intermediary step for effectively differentiating fibroblasts which in turn influences ECM remodeling and collagen I expression.⁷⁸

Designing scaffolds for minimal foreign body response necessitates better understanding of how cells secrete ECM proteins in response to different environments.⁷⁹ Our previous studies mapping the differences of secreted collagen levels inside diverse crosslinked hydrogel environments and showed that this aspect can be tuned through different materials properties.³⁸ In this study, we focused on the effect of the compressive modulus of underlying hydrogel substrates for modulating collagen secretion response. The FN-modified surfaces mimicked natural conditions in which cell binding motifs would be readily available.⁸⁰ Collagen secretion was measured using SHG microscopy. Molecules are SHG active if they are non-centrosymmetric. Collagen, by having a triple helix, is non-centrosymmetric and SHG active. The collagen signal was normalized to the number of cells using the DAPI channel in the ICC images. In general, there appeared to be a downward trend for the FN-modified and naïve substrates (**Figure 7.4**), as was expected from comparison to similar studies.²⁴ When comparing the FN-modified and naïve substrates, there were no significant differences for glass, 0%, and 10% substrates. Once the stiffness increases to ~16 kPa (30% opacity), the amount of collagen secreted normalized to cell number is higher on the FN-modified substrates than the naïve surfaces. Differences in the stiffness of surrounding ECM critically influence protein expression. Studies on both epithelial as well as

3T3 cells showed significantly up-regulated integrin on stiffer gels (22 kPa) as compared to very soft gels (< 1 kPa), which concur with our observations.^{81,82} With the integrin expression influencing the effectiveness of TGF- β based differentiation of fibroblasts to myofibroblasts, how fibroblasts sense different substrates is important to understand.^{12,83} These results suggest that there is a continuum transition from fibroblasts to protomyofibroblasts to myofibroblasts based on collagen secretion and α -SMA expression. Depending on the site of activity, different stiffnesses instigate differentiation, which is subsequently followed by increased expression of collagen I.^{78,84} The threshold stiffness for myofibroblast differentiation has confounded researchers, as it is variable based both on location but also the characterization technique applied.^{75,85,86} Substrates as soft as 16 kPa have been sufficient for instigating differentiation.^{75,87} Fibrotic tissues on the other hand have been shown to exhibit stiffnesses of 25 to 50 kPa for differentiation to myofibroblasts with consistent α -SMA expression.^{42,88,89}

Achieving similar collagen organization in tissue engineering scaffolds compared to native tissue would increase compliance of implanted materials.^{90,91} SHG images of the hydrogels were obtained and the angle of collagen in each ROI was calculated using equation 4. These angles were mapped and color coded using a heat map to better illustrate regions of alignment – areas of similar color indicate aligned collagen, whereas areas with many different colors are isotropic (**Figure 8.5**). In general, organization on both FN-modified and naïve substrates decreased with decreasing stiffness. This effect was quantified by generating histograms of orientations maps and fitting them to a Gaussian curve. The FWHM obtained from the fit is plotted in **Figure 8.6** against Young's modulus and shows a negative correlation for both substrates ($R = -0.94$ and $R = -0.93$). By extending the plotted fits for both conditions, it was estimated that they would intersect at a stiffness of 30.7 kPa, where it would be interesting to see if cell binding motifs, in this case FN,

would lose their ability to influence collagen organization at this higher stiffness. In examining glass, which is approximately 3 GPa, the amount of collagen secreted per cell does not appear to be influenced by FN, however, FN does influence the presence of myofibroblasts. Using these experimental observations, we can formulate some basic design principles for achieving the desired collagen organization for a particular application. First, relatively soft hydrogels can be used as dermal wound dressings, which would require isotropic collagen alignment.⁹² Patients suffering from burn wounds in particular show significantly ordered conformation at the surface, which can be treated with scaffolds that instigate stochastic neo-collagen secretion to boost the healing process.^{93,94} On the other hand, one of the critical differences in diseased versus healthy lung tissue has been observed as the increased stiffness of the former.^{78,95} Cartilage tissue is more aligned and would require hydrogels ~ 15 kPa based on collagen alignment, which are significantly softer than the stiffness of cartilage (>0.5 MPa) observed in human subjects.⁹⁶⁻⁹⁸ Collagen organization within tissues such as the cornea is complex as it varies greatly with highly aligned fibers observed in bundles, which on a bigger scale are a part of a dense network of connective tissue.^{67,99,100} Aligned collagen has been observed in mechanically stiffer environments like bones and tendons where relatively rigid scaffolds can be applied to obtain greater compliance of the secreted collagen response to guide tuning of disordered collagen which get deposited upon injury.¹⁰¹ The influence of such tuned hydrogel systems to elicit diverse organization of secreted collagen (**Figure 8.8**) can help inform innovative tissue engineering platforms for diverse biomedical applications.

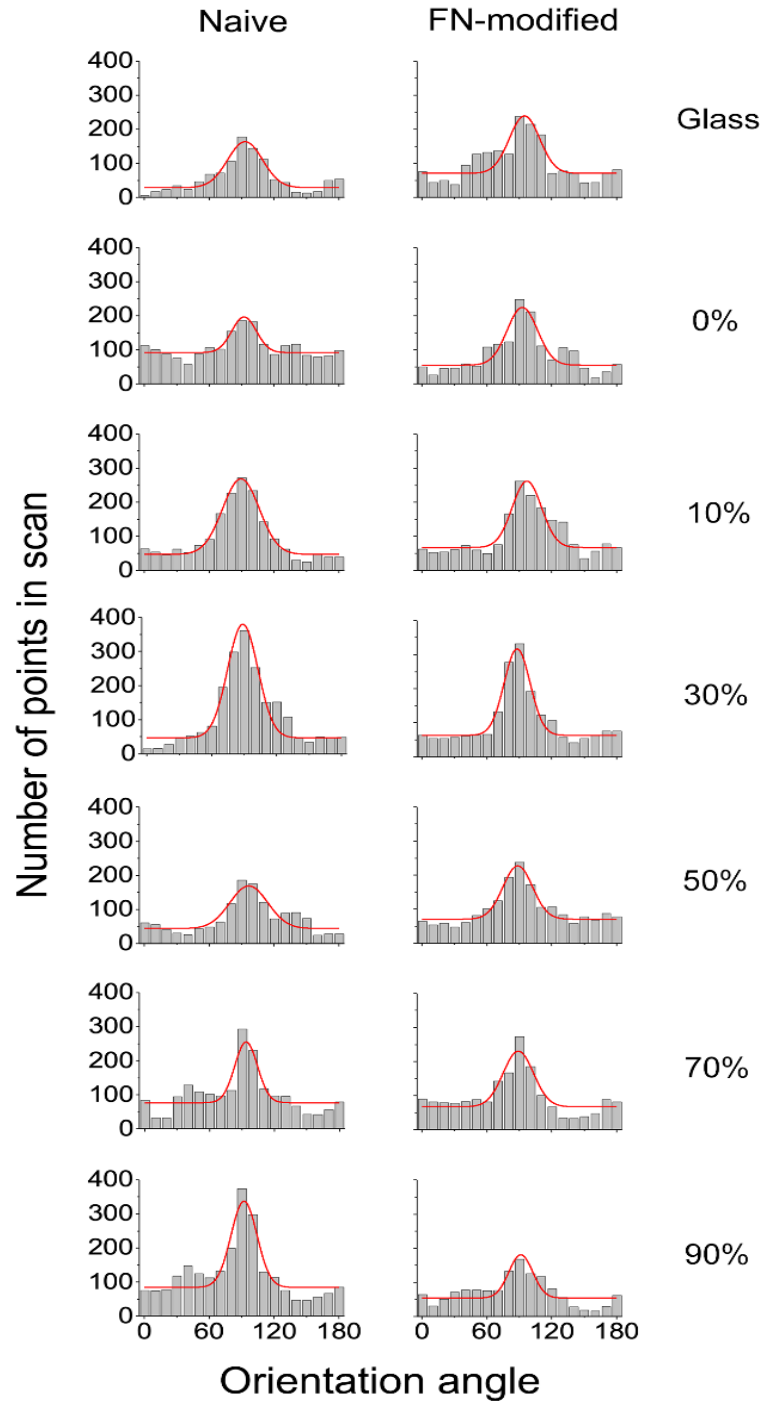


Figure 8.8: Influence of FN on collagen FWHM. Histograms of collagen organization obtained for collagen secreted by NIH 3T3 fibroblasts surface seeded on the ALGMA hydrogel across the naïve and FN-modified substrates. The bars represent experimentally acquired data. The red line is the Gaussian fit to the data.

8.5. Conclusions

In this study, we fabricated ALGMA hydrogels across a range of mechanical stiffnesses (7 – 22 kPa) using photomasks to control the crosslinking density for examining the influence of mechanical cues on cell morphology and collagen secretion. NIH/3T3 fibroblasts showed no cytotoxic response to being seeded on these substrates. FN surface modifications increased cell proliferation across all conditions. A clear influence of the stiffness of the hydrogel gradient substrates on the NIH/3T3 fibroblasts was seen with a positive correlation for secreted collagen levels, as well as cell proliferation. Modifying the surface with FN also increased myofibroblast differentiation as well as the disorder of collagen deposited by these cells. In-depth characterization through the ICC staining and SHG imaging provides design guidelines for effective tissue scaffolds that can be tuned for specific natural implant environments.

Acknowledgments

This work was supported by the Roy J. Carver Charitable Trust Grant No. 13-4265.

8.6 References

1. Khademhosseini, A. & Bong, G. C. Microscale technologies for tissue engineering. *2009 IEEE/NIH Life Sci. Syst. Appl. Work. LiSSA 2009* **103**, 56–57 (2009).
2. Anderson, J. M. & McNally, A. K. Biocompatibility of implants: lymphocyte/macrophage interactions. *Semin. Immunopathol.* **33**, 221–233 (2011).
3. Peppas, N. A., Hilt, J. Z., Khademhosseini, A. & Langer, R. Hydrogels in biology and medicine: From molecular principles to bionanotechnology. *Adv. Mater.* **18**, 1345–1360 (2006).
4. Harrison, R. H., St-Pierre, J.-P. & Stevens, M. M. Tissue Engineering and Regenerative Medicine: A Year in Review. *Tissue Eng. Part B Rev.* **20**, 1–16 (2014).
5. Gailit, J. & Clark, R. A. Wound repair in the context of extracellular matrix. *Curr. Opin. Cell Biol.* **6**, 717–725 (1994).

6. Langer, R. & Peppas, N. A. Advances in Biomaterials, Drug Delivery, and Bionanotechnology. *AIChE J.* **49**, 2990–3006 (2003).
7. Slaughter, B. V., Khurshid, S. S., Fisher, O. Z., Khademhosseini, A. & Peppas, N. A. Hydrogels in Regenerative Medicine. *Adv. Mater.* **21**, 3307–3329 (2009).
8. Rosales, A. M. & Anseth, K. S. The design of reversible hydrogels to capture extracellular matrix dynamics. *Nat. Rev. Mater.* **1**, 1–16 (2016).
9. Kharkar, P. M., Kiick, K. L. & Kloxin, A. M. Designing degradable hydrogels for orthogonal control of cell microenvironments. *Chem. Soc. Rev.* **42**, 7335–7372 (2013).
10. Nicodemus, G. D. & Bryant, S. J. Cell {Encapsulation} in {Biodegradable} {Hydrogels} for {Tissue} {Engineering} {Applications}. *Tissue Eng. Part B. Rev.* **14**, 149–165 (2008).
11. Humphrey, J. D., Dufresne, E. R. & Schwartz, M. A. Mechanotransduction and extracellular matrix homeostasis. *Nat. Rev. Mol. Cell Biol.* **15**, 802–812 (2014).
12. Discher, D. E., Janmey, P. A. & Wang, Y. Tissue Cells Feel and Respond to the Stiffness of Their Substrate. *Science (80-.)*. **310**, 1139–1143 (2005).
13. Reinhart-king, C. A., Dembo, M. & Hammer, D. A. Cell-Cell Mechanical Communication through Compliant Substrates. *Biophys. J.* **95**, 6044–6051 (2008).
14. Trappmann, B. *et al.* Extracellular-matrix tethering regulates stem-cell fate. *Nat. Mater.* **11**, 742–742 (2012).
15. Lee, K. Y. & Mooney, D. J. Alginate: Properties and biomedical applications. *Prog. Polym. Sci.* **37**, 106–126 (2012).
16. Constantinidis, I., Rask, I., Long, R. C. & Sambanis, A. Effects of alginate composition on the metabolic, secretory, and growth characteristics of entrapped β TC3 mouse insulinoma cells. *Biomaterials* **20**, 2019–2027 (1999).
17. Balakrishnan, B., Mohanty, M., Umashankar, P. R. & Jayakrishnan, A. Evaluation of an in situ forming hydrogel wound dressing based on oxidized alginate and gelatin. *Biomaterials* **26**, 6335–6342 (2005).
18. Chou, A. I., Akintoye, S. O. & Nicoll, S. B. Photo-crosslinked alginate hydrogels support enhanced matrix accumulation by nucleus pulposus cells in vivo. *Osteoarthr. Cartil.* **17**, 1377–1384 (2009).
19. Sun, J. & Tan, H. Alginate-based biomaterials for regenerative medicine applications. *Materials (Basel)*. **6**, 1285–1309 (2013).
20. Kuo, C. K. & Ma, P. X. Ionically crosslinked alginate hydrogels as scaffolds for tissue engineering : Part 1 . Structure , gelation rate and mechanical properties. *Biomaterials* **22**, 511–521 (2001).

21. Baer, A. E., Wang, J. Y., Kraus, V. B. & Setton, L. A. Collagen gene expression and mechanical properties of intervertebral disc cell-alginate cultures. *J. Orthop. Res.* **19**, 2–10 (2001).
22. Chou, A. I. & Nicoll, S. B. Characterization of photocrosslinked alginate hydrogels for nucleus pulposus cell encapsulation. *J. Biomed. Mater. Res. - Part A* **91**, 187–194 (2009).
23. Samorezov, J. E., Morlock, C. M. & Alsberg, E. Dual Ionic and Photo-Crosslinked Alginate Hydrogels for Micropatterned Spatial Control of Material Properties and Cell Behavior. *Bioconjug. Chem.* **26**, 1339–1347 (2015).
24. Marin-Pareja, N. *et al.* Different Organization of Type I Collagen Immobilized on Silanized and Nonsilanized Titanium Surfaces Affects Fibroblast Adhesion and Fibronectin Secretion. *ACS Appl. Mater. Interfaces* **7**, 20667–20677 (2015).
25. Zhu, Y. *et al.* Potent laminin-inspired antioxidant regenerative dressing accelerates wound healing in diabetes. *Proc. Natl. Acad. Sci.* **115**, 6816–6821 (2018).
26. Saeidi, N. *et al.* Disorganized collagen scaffold interferes with fibroblast mediated deposition of organized extracellular matrix in vitro. *Biotechnol. Bioeng.* **109**, 2683–2698 (2012).
27. Yang, C. *et al.* Spatially patterned matrix elasticity directs stem cell fate. *Proc. Natl. Acad. Sci.* **113**, E4439–E4445 (2016).
28. Mellati, A. *et al.* Microengineered 3D cell-laden thermoresponsive hydrogels for mimicking cell morphology and orientation in cartilage tissue engineering. *Biotechnol. Bioeng.* **114**, 1–15 (2017).
29. Verhaegen, P. D. H. M. *et al.* Differences in collagen architecture between keloid, hypertrophic scar, normotrophic scar, and normal skin: An objective histopathological analysis. *Wound Repair Regen.* **17**, 649–656 (2009).
30. Jikko, A., Harris, S. E., Chen, D., Mendrick, D. L. & Damsky, C. H. Collagen Integrin Receptors Regulate Early Osteoblast Differentiation Induced by BMP-2. *J. Bone Miner. Res.* **14**, 1075–1083 (1999).
31. Wenzel G.I., Anvari B., Mazhar A., Pikkula B., O. J. S. . & Wenzel, Gentiana I., Bahman Anvari, Amaan, Mazhar, Brian, Pikkula, J. S. O. Laser-induced collagen remodeling and deposition within the basilar membrane of the mouse cochlea. *J Biomed Opt* **12**, 021007 (2007).
32. Beningo, K. A., Dembo, M. & Wang, Y. -I. Responses of fibroblasts to anchorage of dorsal extracellular matrix receptors. *Proc. Natl. Acad. Sci.* **101**, 18024–18029 (2004).
33. Stuart, K. & Panitch, A. Characterization of gels composed of blends of collagen I, collagen III, and chondroitin sulfate. *Biomacromolecules* **10**, 25–31 (2009).

34. Chen, X. G., Wang, Z., Liu, W. S. & Park, H. J. The effect of carboxymethyl-chitosan on proliferation and collagen secretion of normal and keloid skin fibroblasts. *Biomaterials* **23**, 4609–4614 (2002).
35. Tilbury, K. & Campagnola, P. J. Applications of second-harmonic generation imaging microscopy in ovarian and breast cancer. *Perspect. Medicin. Chem.* **7**, 21–32 (2015).
36. Chen, X., Nadiarynk, O., Plotnikov, S. & Campagnola, P. J. Second harmonic generation microscopy for quantitative analysis of collagen fibrillar structure. *Nat. Protoc.* **7**, 654–69 (2012).
37. Nadiarynk, O., LaComb, R. B., Brewer, M. a & Campagnola, P. J. Alterations of the extracellular matrix in ovarian cancer studied by Second Harmonic Generation imaging microscopy. *BMC Cancer* **10**, 94 (2010).
38. Boddupalli, A. & Bratlie, K. M. Collagen organization deposited by fibroblasts encapsulated in pH responsive methacrylated alginate hydrogels. *J. Biomed. Mater. Res. Part A* (2018). doi:10.1002/jbm.a.36482
39. Boddupalli, A. & Bratlie, K. M. Second harmonic generation microscopy of collagen organization in tunable, environmentally responsive alginate hydrogels. *Comple. Manusc.* (2018).
40. Ji, C., Khademhosseini, A. & Deghani, F. Enhancing cell penetration and proliferation in chitosan hydrogels for tissue engineering applications. *Biomaterials* **32**, 9719–29 (2011).
41. Akilbekova, D. & Bratlie, K. M. Quantitative characterization of collagen in the fibrotic capsule surrounding implanted polymeric microparticles through second harmonic generation imaging. *PLoS One* **10**, 1–17 (2015).
42. Hinz, B. The myofibroblast: Paradigm for a mechanically active cell. *J. Biomech.* **43**, 146–155 (2010).
43. Goffin, J. M. *et al.* Focal adhesion size controls tension-dependent recruitment of ??-smooth muscle actin to stress fibers. *J. Cell Biol.* **172**, 259–268 (2006).
44. Kloxin, A. M., Kasko, A. M., Salinas, C. N. & Anseth, K. S. Photodegradable hydrogels for dynamic tuning of physical and chemical properties. *Science* **324**, 59–63 (2009).
45. Hao, Y., Shih, H., Muñoz, Z., Kemp, A. & Lin, C. C. Visible light cured thiol-vinyl hydrogels with tunable degradation for 3D cell culture. *Acta Biomater.* **10**, 104–114 (2014).
46. Keselowsky, B. G., Collard, D. M. & García, A. J. Surface chemistry modulates fibronectin conformation and directs integrin binding and specificity to control cell adhesion. *J. Biomed. Mater. Res. Part A* **66A**, 247–259 (2003).

47. Wang, H., Haeger, S. M., Kloxin, A. M., Leinwand, L. A. & Anseth, K. S. Redirecting valvular myofibroblasts into dormant fibroblasts through light-mediated reduction in substrate modulus. *PLoS One* **7**, (2012).
48. Li, Z. *et al.* Transforming growth factor- β and substrate stiffness regulate portal fibroblast activation in culture. *Hepatology* **46**, 1246–1256 (2007).
49. Kastellorizios, M., Tipnis, N. & Burgess, D. J. *Foreign body reaction to subcutaneous implants. Advances in Experimental Medicine and Biology* **865**, (2015).
50. Wang, J. *et al.* Degradation and Remodeling of Epitaxially Grown Collagen Fibrils. *Cell. Mol. Bioeng.* (2018). doi:10.1007/s12195-018-0547-6
51. Bellows, C. G., Melcher, A. H. & Aubin, J. E. Contraction and organization of collagen gels by cells cultured from periodontal ligament, gingiva and bone suggest functional differences between cell types. *J Cell Sci* **50**, 299–314 (1981).
52. Petrov, V. V, Fagard, R. H. & Lijnen, P. J. Stimulation of collagen production by transforming growth factor-beta1 during differentiation of cardiac fibroblasts to myofibroblasts. *Hypertension* **39**, 258–63 (2002).
53. Li, B. & Wang, J. H. C. Fibroblasts and myofibroblasts in wound healing: Force generation and measurement. *J. Tissue Viability* **20**, 108–120 (2011).
54. Stephan, S. B. *et al.* Biopolymer implants enhance the efficacy of adoptive T-cell therapy. *Nat. Biotechnol.* **33**, 97–101 (2015).
55. Linares, H. A., Kischer, C. W., Dobrkovsky, M. & Larson, D. L. The histiotypic organization of collagen of the hypertrophic scar in humans. *J. Invest. Dermatol.* **59**, 323–332 (1972).
56. Cicchi, R. *et al.* Scoring of collagen organization in healthy and diseased human dermis by multiphoton microscopy. *J. Biophotonics* **3**, 34–43 (2010).
57. Marinucci, L. *et al.* Biocompatibility of collagen membranes crosslinked with glutaraldehyde or diphenylphosphoryl azide: an in vitro study. *J. Biomed. Mater. Res. A* **67**, 504–509 (2003).
58. Stevens, M. M. & George, J. H. Exploring and Engineering the Cell Surface Interface. *Science (80-.)*. **310**, 1135–1138 (2005).
59. Boddupalli, A., Zhu, L. & Bratlie, K. M. Methods for Implant Acceptance and Wound Healing: Material Selection and Implant Location Modulate Macrophage and Fibroblast Phenotypes. *Adv. Healthc. Mater.* **5**, (2016).
60. Young, J. L., Holle, A. W. & Spatz, J. P. Nanoscale and mechanical properties of the physiological cell-ECM microenvironment. *Exp. Cell Res.* **343**, 3–6 (2016).

61. Schrader, J. *et al.* Matrix stiffness modulates proliferation, chemotherapeutic response, and dormancy in hepatocellular carcinoma cells. *Hepatology* **53**, 1192–1205 (2011).
62. Bott, K. *et al.* The effect of matrix characteristics on fibroblast proliferation in 3D gels. *Biomaterials* **31**, 8454–8464 (2010).
63. Balestrini, J. L., Chaudhry, S., Sarrazy, V., Koehler, A. & Hinz, B. The mechanical memory of lung myofibroblasts. *Integr. Biol.* **4**, 410 (2012).
64. Stoller, P. C., Celliers, P. M., Reiser, K. M. & Rubenchik, A. M. Imaging collagen orientation using polarization-modulated second harmonic generation. *Multiphot. Microsc. Biomed. Sci. II* **4620**, 157–165 (2002).
65. Latour, G., Gusachenko, I., Kowalczyk, L., Lamarre, I. & Schanne-Klein, M. In vivo structural imaging of the cornea by polarization-resolved second harmonic microscopy. *Biomed. Opt. Express* **3**, 1 (2012).
66. Johnson, C. & Galis, Z. S. Matrix Metalloproteinase-2 and -9 Differentially Regulate Smooth Muscle Cell Migration and Cell-Mediated Collagen Organization. *Arterioscler. Thromb. Vasc. Biol.* **24**, 54–60 (2004).
67. Cicchi, R. *et al.* From molecular structure to tissue architecture: Collagen organization probed by SHG microscopy. *J. Biophotonics* **6**, 129–142 (2013).
68. Sarrazy, V., Billet, F., Micallef, L., Coulomb, B. & Desmoulière, A. Mechanisms of pathological scarring: Role of myofibroblasts and current developments. *Wound Repair Regen.* **19**, 10–15 (2011).
69. Weber, L. M. & Anseth, K. S. Hydrogel encapsulation environments functionalized with extracellular matrix interactions increase islet insulin secretion. *Matrix Biol.* **27**, 667–673 (2008).
70. Fahrenholtz, M. *et al.* Characterization of Dermal Fibroblasts as a Cell Source for Pediatric Tissue Engineered Heart Valves. *J. Cardiovasc. Dev. Dis.* **1**, 146–162 (2014).
71. Discher, D. E., Discher, D. E., Janmey, P. & Wang, Y. Tissue Cells Feel and Respond to the Stiffness of Their Substrate. *Science (80-.)*. **310**, 1139–1143 (2005).
72. Huebsch, N. *et al.* Harnessing traction-mediated manipulation of the cell/matrix interface to control stem-cell fate. *Nat. Mater.* **9**, 518–26 (2010).
73. Chaponnier, C. & Gabbiani, G. Tissue repair , contraction , and the myofibroblast factors involved in myofibroblastic. *Wound Repair Regen.* **13**, 7–12 (2005).
74. McAnulty, R. J. Fibroblasts and myofibroblasts: Their source, function and role in disease. *Int. J. Biochem. Cell Biol.* **39**, 666–671 (2007).

75. Goffin, J. M. *et al.* Focal adhesion size controls tension-dependent recruitment of α -smooth muscle actin to stress fibers. *J. Cell Biol.* **172**, 259–268 (2006).
76. Serini, G. *et al.* The fibronectin domain ED-A is crucial for myofibroblastic phenotype induction by transforming growth factor- β 1. *J. Cell Biol.* **142**, 873–881 (1998).
77. Serini, G. & Gabbiani, G. Mechanisms of myofibroblast activity and phenotypic modulation. *Exp. Cell Res.* **250**, 273–83 (1999).
78. Zhang, K., Rekhter, M. D., Gordon, D. & Phan, S. H. Myofibroblasts and their role in lung collagen gene expression during pulmonary fibrosis. A combined immunohistochemical and in situ hybridization study. *Am J Pathol* **145**, 114–125 (1994).
79. Avula, M. N., Rao, A. N., McGill, L. D., Grainger, D. W. & Solzbacher, F. Foreign body response to subcutaneous biomaterial implants in a mast cell-deficient Kitw-Sh murine model. *Acta Biomater.* **10**, 1856–1863 (2014).
80. Grotendorst, G. R., Seppä, H. E., Kleinman, H. K. & Martin, G. R. Attachment of smooth muscle cells to collagen and their migration toward platelet-derived growth factor. *Proc. Natl. Acad. Sci. U. S. A.* **78**, 3669–72 (1981).
81. Yeung, T. *et al.* Effects of substrate stiffness on cell morphology, cytoskeletal structure, and adhesion. *Cell Motil. Cytoskeleton* **60**, 24–34 (2005).
82. Von Der Mark, K., Park, J., Bauer, S. & Schmuki, P. Nanoscale engineering of biomimetic surfaces: Cues from the extracellular matrix. *Cell Tissue Res.* **339**, 131–153 (2010).
83. Wells, R. G. Tissue mechanics and fibrosis. *Biochim. Biophys. Acta - Mol. Basis Dis.* **1832**, 884–890 (2013).
84. Gabbiani, M. Le Lous, A. J. Bailey, Delaunay, A., S. B. Collagen and Myofibroblasts of Granulation Tissue A Chemical, Ultrastructural and Immunologic Study. *Virchows Arch. B Cell Path.* **21**, 133–145 (1976).
85. Tomasek, J. J., Gabbiani, G., Hinz, B., Chaponnier, C. & Brown, R. a. Myofibroblasts and mechano-regulation of connective tissue remodelling. *Nat. Rev. Mol. Cell Biol.* **3**, 349–63 (2002).
86. Hinz, B. *et al.* The Myofibroblast. *Am. J. Pathol.* **170**, 1807–1816 (2007).
87. Kim, D. H. *et al.* Mechanosensitivity of fibroblast cell shape and movement to anisotropic substratum topography gradients. *Biomaterials* **30**, 5433–5444 (2009).
88. Darby, I. A., Laverdet, B., Bonté, F. & Desmoulière, A. Fibroblasts and myofibroblasts in wound healing. *Clin. Cosmet. Investig. Dermatol.* **7**, 301–311 (2014).

89. Hinz, B. Tissue stiffness, latent TGF- β 1 Activation, and mechanical signal transduction: Implications for the pathogenesis and treatment of fibrosis. *Curr. Rheumatol. Rep.* **11**, 120–126 (2009).
90. Ghanaati, S. *et al.* Evaluation of the tissue reaction to a new bilayered collagen matrix in vivo and its translation to the clinic. *Biomed. Mater.* **6**, (2011).
91. Battiston, K. G., Labow, R. S., Simmons, C. A. & Santerre, J. P. Immunomodulatory polymeric scaffold enhances extracellular matrix production in cell co-cultures under dynamic mechanical stimulation. *Acta Biomater.* **24**, 74–86 (2015).
92. Yasui, T., Tohno, Y. & Araki, T. Determination of collagen fiber orientation in human tissue by use of polarization measurement of molecular second-harmonic-generation light. *Appl. Opt.* **43**, 2861 (2004).
93. Yasui, T., Tanaka, R., Hase, E., Fukushima, S. & Araki, T. In vivo time-lapse imaging of skin burn wound healing using second-harmonic generation microscopy. *Proc. SPIE* **8948**, 89480B (2014).
94. Ribeiro, M. S. *et al.* Effects of low-intensity polarized visible laser radiation on skin burns: a light microscopy study. *J. Clin. Laser Med. Surg.* **22**, 59–66 (2004).
95. Liu, F. *et al.* Feedback amplification of fibrosis through matrix stiffening and COX-2 suppression. *J. Cell Biol.* **190**, 693–706 (2010).
96. Herzog, W. *et al.* Material and functional properties of articular cartilage and patellofemoral contact mechanics in an experimental model of osteoarthritis. *J. Biomech.* **31**, 1137–1145 (1998).
97. Mansfield, J. C., Winlove, C. P., Moger, J. & Mather, S. J. Collagen fiber arrangement in normal and diseased cartilage studied by polarization sensitive nonlinear microscopy. *J. Biomed. Opt.* **13**, 044020 (2008).
98. Chen, T., Hilton, M. J., Brown, E. B., Zuscik, M. J. & Awad, H. A. Engineering superficial zone features in tissue engineered cartilage. *Biotechnol. Bioeng.* **110**, 1476–86 (2013).
99. Boote, C., Hayes, S., Abahussin, M. & Meek, K. M. Mapping collagen organization in the human cornea: Left and right eyes are structurally distinct. *Investig. Ophthalmol. Vis. Sci.* **47**, 901–908 (2006).
100. Tenboll, A. *et al.* Controlled deposition of highly oriented type I collagen mimicking In Vivo collagen structures. *Langmuir* **26**, 12165–12172 (2010).
101. Fung, D. T. *et al.* Second harmonic generation imaging and fourier transform spectral analysis reveal damage in fatigue-loaded tendons. *Ann. Biomed. Eng.* **38**, 1741–1751 (2010).

CHAPTER 9

GENERAL CONCLUSION

Over the course of this research, detailed insight into the complex nature of cell-matrix interaction was obtained. Particularly from the perspective of tuning soft, biocompatible materials into physiologically relevant approximations of natural tissue environments, it was possible to evaluate cell proliferation and ECM secretion that is critical to wound healing, foreign body response and synthesis of bioactive scaffolds. Methacrylated alginate hydrogels were observed to swell significantly more under basic pH conditions, and demonstrate a range of viable crosslinking mechanisms, and thereby considered appropriate for responsive tissue engineering scaffolds. The collaborative studies with 3M provided a wide variety of wound healing tests that contributed to understanding the complexity of wound healing processes, particularly those relevant to reduction of scarring responses. Decoupling the influence of covalent crosslinking chemistry from the cell-matrix interactions, provided insight into fibroblast differentiation and collagen fiber organization that will inform future studies on making extracellular matrices more compliant to the natural microenvironments. The overall goal of these studies on cell-laden hydrogels, animal tissue samples was achieved on the basis of the insight that has been obtained on the significant role played by collagen organization that needs to be considered for diverse biomaterial scaffolds.